

JULY 2023

AJNR

VOLUME 44 • PP 749-878

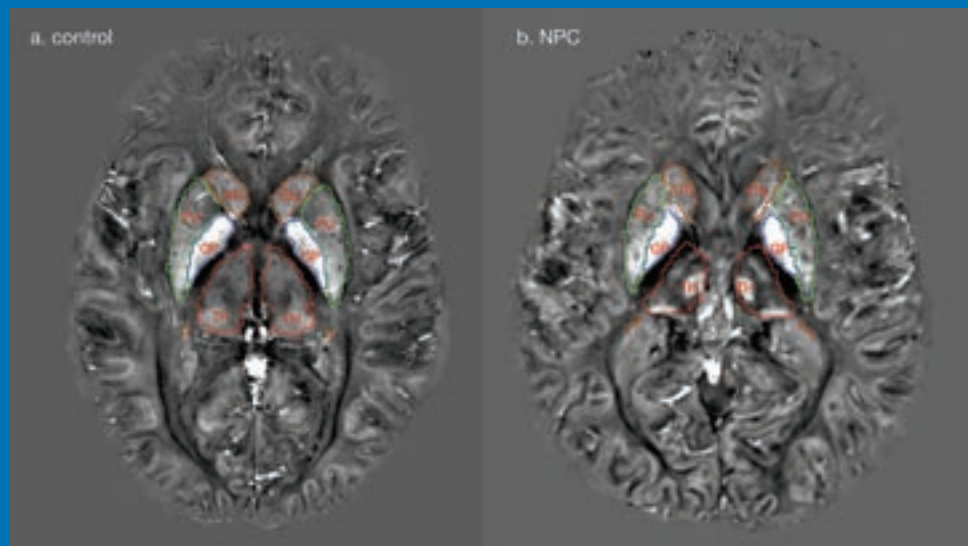
AJNR

AMERICAN JOURNAL OF NEURORADIOLOGY

JULY 2023
VOLUME 44
NUMBER 7
WWW.AJNR.ORG

THE JOURNAL OF DIAGNOSTIC AND
INTERVENTIONAL NEURORADIOLOGY

Advances in acute ischemic stroke
QSM of Niemann-Pick type C
Imaging findings of autoimmune encephalitis
T2-FLAIR mismatch in pediatric low-grade glioma
Long-term follow-up of prenatal myelomeningocele repair
Official Journal ASNR • ASFNR • ASHNR • ASPNR • ASSR



FRED™ X™

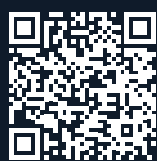
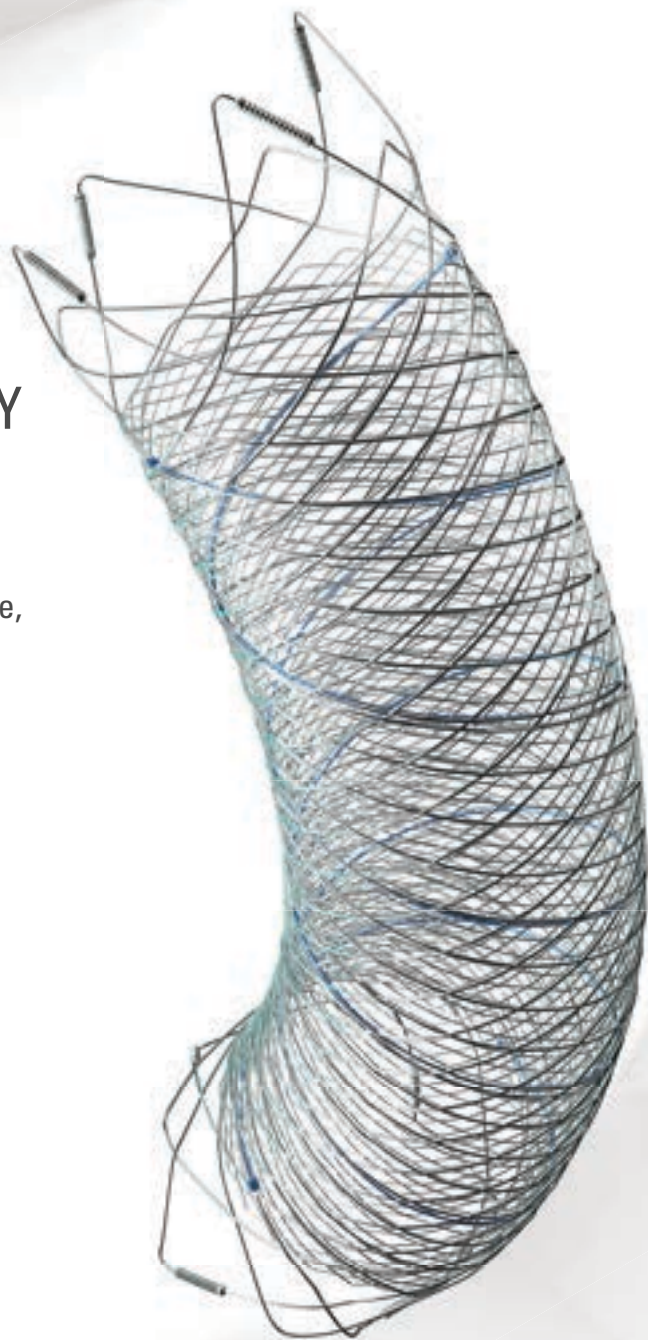
Flow Diverter Stent

THE NEXT ADVANCEMENT IN FLOW DIVERSION TECHNOLOGY

The FRED™ X Flow Diverter features the same precise placement and immediate opening of the FRED™ Device, now with X Technology. X Technology is a covalently bonded, nanoscale surface treatment, designed to:

- **REDUCE MATERIAL THROMBOGENICITY¹**
- **MAINTAIN NATURAL VESSEL HEALING RESPONSE^{2,3,4}**
- **IMPROVE DEVICE DELIVERABILITY AND RESHEATHING¹**

The only FDA PMA approved portfolio with a 0.021" delivery system for smaller device sizes, and no distal lead wire.



For more information, contact your local MicroVention sales representative or visit our website. www.microvention.com



^{*} Data is derived from in vivo and ex vitro testing and may not be representative of clinical performance.

¹ Data on file

² Tanaka M et al. Design of biocompatible and biodegradable polymers based on intermediate water concept. Polymer Journal. 2015;47:114-121.

³ Tanaka M et al. Blood compatible aspects of poly(2-methoxyethylacrylate) (PMEA) – relationship between protein adsorption and platelet adhesion on PMEAs surface. Biomaterials. 2000;21:1471-1481.

⁴ Schiel L et al. X Coating™: A new biopassive polymer coating. Canadian Perfusion Canadienne. June 2001;11(2):9.

Indications for Use: The FRED X System is indicated for use in the internal carotid artery from the petrous segment to the terminus for the endovascular treatment of adult patients (22 years of age or older) with wide-necked (neck width 4 mm or dome-to-neck ratio < 2) saccular or fusiform intracranial aneurysms arising from a parent vessel with a diameter 2.0 mm and 5.0 mm.

Rx Only: Federal (United States) law restricts this device to sale by or on the order of a physician. For Healthcare professionals intended use only.

MICROVENTION, FRED and HEADWAY are registered trademarks of MicroVention, Inc. in the United States and other jurisdictions. Stylized X is a trademark of MicroVention, Inc. © 2022 MicroVention, Inc. MM1222 US 03/22

WEB™ 17

Aneurysm Embolization System

LOWER PROFILE



NEW SIZES



MORE ACCESS OPTIONS



INDICATIONS FOR USE:

The WEB Aneurysm Embolization System is intended for the endovascular embolization of ruptured and unruptured intracranial aneurysms and other neurovascular abnormalities such as arteriovenous fistulae (AVF). The WEB Aneurysm Embolization System is also intended for vascular occlusion of blood vessels within the neurovascular system to permanently obstruct blood flow to an aneurysm or other vascular malformation.

POTENTIAL COMPLICATIONS:

Potential complications include but are not limited to the following: hematoma at the site of entry, aneurysm rupture, emboli, vessel perforation, parent artery occlusion, hemorrhage, ischemia, vasospasm, clot formation, device migration or misplacement, premature or difficult device detachment, non-detachment, incomplete aneurysm filling, revascularization, post-embolization syndrome, and neurological deficits including stroke and death. For complete indications, potential complications, warnings, precautions, and instructions, see instructions for use (IFU provided with the device).

VIA 21, 27, 33 - The VIA Microcatheter is intended for the introduction of interventional devices (such as the WEB device/stents/flow diverters) and infusion of diagnostic agents (such as contrast media) into the neuro, peripheral, and coronary vasculature.

VIA 17,17 Preshaped - The VIA Microcatheter is intended for the introduction of interventional devices (such as the WEB device/stents/flow diverters) and infusion of diagnostic agents (such as contrast media) into the neuro, peripheral, and coronary vasculature.

The VIA Microcatheter is contraindicated for use with liquid embolic materials, such as n-butyl 2-cyanoacrylate or ethylene vinyl alcohol & DMSO (dimethyl sulfoxide).

The device should only be used by physicians who have undergone training in all aspects of the WEB Aneurysm Embolization System procedure as prescribed by the manufacturer.

RX Only: Federal law restricts this device to sale by or on the order of a physician.

For healthcare professional intended use only.



MicroVention Worldwide
Innovation Center PH +1.714.247.8000

35 Enterprise
Aliso Viejo, CA 92656 USA
MicroVention UK Limited PH +44 (0) 191 258 6777
MicroVention Europe, S.A.R.L. PH +33 (1) 39 21 77 46
MicroVention Deutschland GmbH PH +49 211 210 798-0
Website microvention.com



WEB™ and VIA™ are registered trademarks
of Sequent Medical, Inc. in the United States.

©2021 MicroVention, Inc. MM1184 WW 11/2021

LIFE IS FULL OF COMPROMISES.
IT'S TIME TO TAKE A STAND.

NO COMPROMISE

HIGH RELAXIVITY, HIGH STABILITY:^{1,2}
I CHOOSE BOTH.

The individual who appears is for illustrative purposes. The person depicted is a model and not a real healthcare professional. Please see Brief Summary of Prescribing Information including Boxed Warning on adjacent page.

VUEWAY™ (gadopiclenol) solution for injection

Indications

VUEWAY injection is indicated in adults and children aged 2 years and older for use with magnetic resonance imaging (MRI) to detect and visualize lesions with abnormal vascularity in:

- the central nervous system (brain, spine and surrounding tissues),
- the body (head and neck, thorax, abdomen, pelvis, and musculoskeletal system).

IMPORTANT SAFETY INFORMATION

WARNING: NEPHROGENIC SYSTEMIC FIBROSIS (NSF)

Gadolinium-based contrast agents (GBCAs) increase the risk for NSF among patients with impaired elimination of the drugs. Avoid use of GBCAs in these patients unless the diagnostic information is essential and not available with non-contrast MRI or other modalities. NSF may result in fatal or debilitating fibrosis affecting the skin, muscle and internal organs.

- **The risk for NSF appears highest among patients with:**
 - **Chronic, severe kidney disease (GFR < 30 mL/min/1.73 m²), or**
 - **Acute kidney injury.**
- **Screen patients for acute kidney injury and other conditions that may reduce renal function. For patients at risk for chronically reduced renal function (e.g. age > 60 years,**

hypertension, diabetes), estimate the glomerular filtration rate (GFR) through laboratory testing.

- **For patients at highest risk for NSF, do not exceed the recommended VUEWAY dose and allow a sufficient period of time for elimination of the drug from the body prior to any re-administration.**

Contraindications

VUEWAY injection is contraindicated in patients with history of hypersensitivity reactions to VUEWAY.

Warnings

Risk of **nephrogenic systemic fibrosis** is increased in patients using GBCA agents that have impaired elimination of the drugs, with the highest risk in patients chronic, severe kidney disease as well as patients with acute kidney injury. Avoid use of GBCAs among these patients unless the diagnostic information is essential and not available with non-contrast MRI or other modalities.

Hypersensitivity reactions, including serious hypersensitivity reactions, could occur during use or shortly following VUEWAY administration. Assess all patients for any history of a reaction to contrast media, bronchial asthma and/or allergic disorders, administer VUEWAY only in situations where trained personnel and therapies are promptly available for the treatment of hypersensitivity reactions, and observe patients for signs and symptoms of hypersensitivity reactions after administration.



MR Suite

IN MRI

INTRODUCING


Vueway™
(gadopiclenol) injection
485.1 mg/mL

HALF THE GADOLINIUM DOSE COMPARED TO OTHER
MACROCYCLIC GBCAs IN APPROVED INDICATIONS.^{1,3-6}
FROM BRACCO, YOUR TRUSTED PARTNER IN MRI.



LIFE FROM INSIDE

Gadolinium retention can be for months or years in several organs after administration. The highest concentrations (nanomoles per gram of tissue) have been identified in the bone, followed by other organs (brain, skin, kidney, liver and spleen). Minimize repetitive GBCA imaging studies, particularly closely spaced studies, when possible.

Acute kidney injury requiring dialysis has occurred with the use of GBCAs in patients with chronically reduced renal function. The risk of acute kidney injury may increase with increasing dose of the contrast agent.

Ensure catheter and venous patency before injecting as **extravasation** may occur, and cause tissue irritation.

VUEWAY may **impair the visualization of lesions** seen on non-contrast MRI. Therefore, caution should be exercised when Vueway MRI scans are interpreted without a companion non-contrast MRI scan.

The most common adverse reactions (incidence \geq 0.5%) are injection site pain (0.7%), and headache (0.7%).

You are encouraged to report negative side effects of prescription drugs to the FDA. Visit www.fda.gov/medwatch or call 1-800-FDA-1088.

Please see BRIEF SUMMARY of Prescribing Information for VUEWAY, including BOXED WARNING on Nephrogenic Systemic Fibrosis.

Manufactured for Bracco Diagnostics Inc. by Liebel-Flarsheim Company LLC - Raleigh, NC, USA 27616.

VUEWAY is a trademark of Bracco Imaging S.p.A.

References: **1.** Vueway™ (gadopiclenol) Injection Full Prescribing Information. Monroe Twp., NJ: Bracco Diagnostics Inc.; September 2022. **2.** Robic C, Port M, Rousseaux O, et al. Physicochemical and Pharmacokinetic Profiles of Gadopiclenol: A New Macrocytic Gadolinium Chelate With High T1 Relaxivity. *Invest Radiol.* 2019 Aug;54: 475–484. **3.** GADAVIST® (gadobutrol) Injection. Full Prescribing Information. Bayer HealthCare Pharmaceuticals Inc. Whippany, NJ; April 2022. **4.** DOTAREM® (gadoterate meglumine) Injection. Full Prescribing Information. Guerbet LLC. Princeton, NJ; April 2022. **5.** CLARISCAN™ (gadoterate meglumine) injection for intravenous use. Full Prescribing Information. GE Healthcare. Marlborough, MA; February 2020. **6.** ProHance® (Gadoteridol) Injection. Full Prescribing Information and Patient Medication Guide. Monroe Twp., NJ: Bracco Diagnostics Inc.; December 2020.

Bracco Diagnostics Inc.
259 Prospect Plains Road, Building H
Monroe Township, NJ 08831 USA
Phone: 609-514-2200
Toll Free: 1-877-272-2269 (U.S. only)
Fax: 609-514-2446
© 2022 Bracco Diagnostics Inc.
All Rights Reserved. US-VW-2200012 10/22

VISIT
VUEWAY.COM
FOR MORE
INFORMATION



Vueway™

(gadopiclenol) injection, for intravenous use

BRIEF SUMMARY: Please see package insert of full prescribing information.

WARNING: NEPHROGENIC SYSTEMIC FIBROSIS (NSF)
Gadolinium-based contrast agents (GBCAs) increase the risk for NSF among patients with impaired elimination of the drugs. Avoid use of GBCAs in these patients unless the diagnostic information is essential and not available with non-contrast MRI or other modalities. NSF may result in fatal or debilitating fibrosis affecting the skin, muscle and internal organs.

- The risk for NSF appears highest among patients with:
 - Chronic, severe kidney disease (GFR <30 mL/min/1.73 m²), or
 - Acute kidney injury.
- Screen patients for acute kidney injury and other conditions that may reduce renal function. For patients at risk for chronically reduced renal function (e.g. age >60 years, hypertension, diabetes), estimate the glomerular filtration rate (GFR) through laboratory testing.
- For patients at highest risk for NSF, do not exceed the recommended Vueway dose and allow a sufficient period of time for elimination of the drug from the body prior to any re-administration [see Warnings and Precautions (5.1) in the full Prescribing Information].

INDICATIONS AND USAGE

Vueway™ (gadopiclenol) is a gadolinium-based contrast agent indicated in adult and pediatric patients aged 2 years and older for use with magnetic resonance imaging (MRI) to detect and visualize lesions with abnormal vascularity in:

- the central nervous system (brain, spine, and associated tissues),
- the body (head and neck, thorax, abdomen, pelvis, and musculoskeletal system).

CONTRAINDICATIONS

Vueway is contraindicated in patients with history of hypersensitivity reactions to gadopiclenol.

WARNINGS AND PRECAUTIONS

Nephrogenic Systemic Fibrosis Gadolinium-based contrast agents (GBCAs) increase the risk for nephrogenic systemic fibrosis (NSF) among patients with impaired elimination of the drugs. Avoid use of GBCAs among these patients unless the diagnostic information is essential and not available with non-contrast MRI or other modalities. The GBCA-associated NSF risk appears highest for patients with chronic, severe kidney disease (GFR <30 mL/min/1.73 m²) as well as patients with acute kidney injury. The risk appears lower for patients with chronic, moderate kidney disease (GFR 30-59 mL/min/1.73 m²) and little, if any, for patients with chronic, mild kidney disease (GFR 60-89 mL/min/1.73 m²). NSF may result in fatal or debilitating fibrosis affecting the skin, muscle, and internal organs. Report any diagnosis of NSF following Vueway administration to Bracco Diagnostics Inc. (1-800-257-5181) or FDA (1-800-FDA-1088 or www.fda.gov/medwatch).

Screen patients for acute kidney injury and other conditions that may reduce renal function. Features of acute kidney injury consist of rapid (over hours to days) and usually reversible decrease in kidney function, commonly in the setting of surgery, severe infection, injury or drug-induced kidney toxicity. Serum creatinine levels and estimated GFR may not reliably assess renal function in the setting of acute kidney injury. For patients at risk for chronically reduced renal function (e.g., age >60 years, diabetes mellitus or chronic hypertension), estimate the GFR through laboratory testing.

Among the factors that may increase the risk for NSF are repeated or higher than recommended doses of a GBCA and the degree of renal impairment at the time of exposure. Record the specific GBCA and the dose administered to a patient. For patients at highest risk for NSF, do not exceed the recommended Vueway dose and allow a sufficient period of time for elimination of the drug prior to re-administration. For patients receiving hemodialysis, physicians may consider the prompt initiation of hemodialysis following the administration of a GBCA in order to enhance the contrast agent's elimination [see Use in Specific Populations (8.6) and Clinical Pharmacology (12.3) in the full Prescribing Information]. The usefulness of hemodialysis in the prevention of NSF is unknown.

Hypersensitivity Reactions With GBCAs, serious hypersensitivity reactions have occurred. In most cases, initial symptoms occurred within minutes of GBCA administration and resolved with prompt emergency treatment.

- Before Vueway administration, assess all patients for any history of a reaction to contrast media, bronchial asthma and/or allergic disorders. These patients may have an increased risk for a hypersensitivity reaction to Vueway.
- Vueway is contraindicated in patients with history of hypersensitivity reactions to Vueway [see Contraindications (4) in the full Prescribing Information].
- Administer Vueway only in situations where trained personnel and therapies are promptly available for the treatment of hypersensitivity reactions, including personnel trained in resuscitation.
- During and following Vueway administration, observe patients for signs and symptoms of hypersensitivity reactions.

Gadolinium Retention Gadolinium is retained for months or years in several organs. The highest concentrations (nanomoles per gram of tissue) have been identified in the bone, followed by other organs (e.g. brain, skin, kidney, liver, and spleen). The duration of retention also varies by tissue and is longest in bone. Linear GBCAs cause more retention than macrocyclic GBCAs. At equivalent doses, gadolinium retention varies among the linear agents with gadodiamide causing greater retention than other linear agents such as gadoxetate disodium, and gadobenate dimeglumine. Retention is lowest and similar

among the macrocyclic GBCAs such as gadoterate meglumine, gadobutrol, gadoteridol, and gadopiclenol.

Consequences of gadolinium retention in the brain have not been established. Pathologic and clinical consequences of GBCA administration and retention in skin and other organs have been established in patients with impaired renal function [see Warnings and Precautions (5.1) in the full Prescribing Information]. There are rare reports of pathologic skin changes in patients with normal renal function. Adverse events involving multiple organ systems have been reported in patients with normal renal function without an established causal link to gadolinium.

While clinical consequences of gadolinium retention have not been established in patients with normal renal function, certain patients might be at higher risk. These include patients requiring multiple lifetime doses, pregnant and pediatric patients, and patients with inflammatory conditions. Consider the retention characteristics of the agent when choosing a GBCA for these patients. Minimize repetitive GBCA imaging studies, particularly closely spaced studies, when possible.

Acute Kidney Injury in patients with chronically reduced renal function, acute kidney injury requiring dialysis has occurred with the use of GBCAs. The risk of acute kidney injury may increase with increasing dose of the contrast agent. Do not exceed the recommended dose.

Extravasation and Injection Site Reactions Injection site reactions such as injection site pain have been reported in the clinical studies with Vueway [see Adverse Reactions (6.1) in the full Prescribing Information]. Extravasation during Vueway administration may result in tissue irritation [see Nonclinical Toxicology (13.2) in the full Prescribing Information]. Ensure catheter and venous patency before the injection of Vueway.

Interference with Visualization of Lesions Visible with Non-Contrast MRI As with any GBCA, Vueway may impair the visualization of lesions seen on non-contrast MRI. Therefore, caution should be exercised when Vueway MRI scans are interpreted without a companion non-contrast MRI scan.

ADVERSE REACTIONS

The following serious adverse reactions are discussed elsewhere in labeling:

- Nephrogenic Systemic Fibrosis [see Warnings and Precautions (5.1) in the full Prescribing Information]
- Hypersensitivity Reactions [see Contraindications (4) and Warnings and Precautions (5.2) in the full Prescribing Information]

Clinical Trials Experience Because clinical trials are conducted under widely varying conditions, adverse reaction rates observed in the clinical trials of a drug cannot be directly compared to rates in the clinical trials of another drug and may not reflect the rates observed in clinical practice.

The safety of Vueway was evaluated in 1,047 patients who received Vueway at doses ranging from 0.025 mmol/kg (one half the recommended dose) to 0.3 mmol/kg (six times the recommended dose). A total of 708 patients received the recommended dose of 0.05 mmol/kg. Among patients who received the recommended dose, the average age was 51 years (range 2 years to 88 years) and 56% were female. The ethnic distribution was 79% White, 10% Asian, 7% American Indian or Alaska native, 2% Black, and 2% patients of other or unspecified ethnic groups.

Overall, approximately 4.7% of subjects receiving the labeled dose reported one or more adverse reactions.

Table 1 lists adverse reactions that occurred in >0.2% of patients who received 0.05 mmol/kg Vueway.

TABLE 1. ADVERSE REACTIONS REPORTED IN >0.2% OF PATIENTS RECEIVING VUEWAY IN CLINICAL TRIALS	
Adverse Reaction	Vueway 0.05 mmol/kg (n=708) (%)
Injection site pain	0.7
Headache	0.7
Nausea	0.4
Injection site warmth	0.4
Injection site coldness	0.3
Dizziness	0.3
Local swelling	0.3

Adverse reactions that occurred with a frequency < 0.2% in patients who received 0.05 mmol/kg Vueway included: maculopapular rash, vomiting, worsened renal impairment, feeling hot, pyrexia, oral paresthesia, dysgeusia, diarrhea, pruritus, allergic dermatitis, erythema, injection site paresthesia, Cystatin C increase, and blood creatinine increase.

Adverse Reactions in Pediatric Patients

One study with a single dose of Vueway (0.05 mmol/kg) was conducted in 80 pediatric patients aged 2 years to 17 years, including 60 patients who underwent a central nervous system (CNS) MRI and 20 patients who underwent a body MRI. One adverse reaction (maculopapular rash of moderate severity) in one patient (1.3%) was reported in the CNS cohort.

USE IN SPECIFIC POPULATIONS

Pregnancy Risk Summary There are no available data on Vueway use in pregnant women to evaluate for a drug-associated risk of major birth defects, miscarriage or other adverse maternal or fetal outcomes. GBCAs cross the human placenta and result in fetal exposure and gadolinium retention. The available human data on GBCA exposure during pregnancy and adverse fetal outcomes are limited and inconclusive (see Data). In animal reproduction studies, there were no adverse developmental effects observed in rats or rabbits with intravenous administration of Vueway during organogenesis (see Data). Because of the potential risks of gadolinium to the fetus, use Vueway only if imaging is essential during pregnancy and cannot be delayed. The estimated background risk of major birth defects and miscarriage for the indicated population(s) are unknown. All pregnancies have a background risk of birth defect, loss, or other adverse outcomes. In the U.S. general population, the estimated background risk of major birth defects and miscarriage in clinically recognized pregnancies is 2% to 4% and 15% to 20% respectively. Data Human Data Contrast enhancement is visualized in the placenta and fetal tissues after maternal GBCA administration. Cohort studies and case reports on exposure to GBCAs during pregnancy have not reported a clear association between GBCAs and adverse effects in the exposed neonates. However, a retrospective cohort study comparing pregnant women who had a GBCA MRI to pregnant women who did not have an MRI reported a higher occurrence of stillbirths and neonatal deaths in the group receiving GBCA MRI. Limitations of this study include a lack of comparison with non-contrast MRI and lack of information about the maternal indication for MRI. Overall, these data preclude

a reliable evaluation of the potential risk of adverse fetal outcomes with the use of GBCAs in pregnancy.

Animal Data Gadolinium Retention: GBCAs administered to pregnant non-human primates (0.1 mmol/kg on gestational days 85 and 135) result in measurable gadolinium concentration in the offspring in bone, brain, skin, liver, kidney, and spleen for at least 7 months. GBCAs administered to pregnant mice (2 mmol/kg daily on gestational days 16 through 19) result in measurable gadolinium concentrations in the pups in bone, brain, kidney, liver, blood, muscle, and spleen at one-month postnatal age.

Reproductive Toxicology: Animal reproduction studies conducted with gadopiclenol showed some signs of maternal toxicity in rats at 10 mmol/kg and rabbits at 5 mmol/kg (corresponding to 52 times and 57 times the recommended human dose, respectively). This maternal toxicity was characterized in both species by swelling, decreased activity, and lower gestation weight gain and food consumption.

No effect on embryo-fetal development was observed in rats at 10 mmol/kg (corresponding to 52 times the recommended human dose). In rabbits, a lower mean fetal body weight was observed at 5 mmol/kg (corresponding to 57 times the recommended human dose) and this was attributed as a consequence of the lower gestation weight gain.

Lactation Risk Summary There are no data on the presence of gadopiclenol in human milk, the effects on the breastfed infant, or the effects on milk production. However, published lactation data on other GBCAs indicate that 0.01% to 0.04% of the maternal gadolinium dose is excreted in breast milk. Additionally, there is limited GBCA gastrointestinal absorption in the breast-fed infant. Gadopiclenol is present in rat milk. When a drug is present in animal milk, it is likely that the drug will be present in human milk (see Data). The developmental and health benefits of breastfeeding should be considered along with the mother's clinical need for Vueway and any potential adverse effects on the breastfed infant from Vueway or from the underlying maternal condition. Data In lactating rats receiving single intravenous injection of [¹⁵²Gd]-gadopiclenol, 0.3% and 0.2% of the total administered radioactivity was transferred to the pups via maternal milk at 6 hours and 24 hours after administration, respectively. Furthermore, in nursing rat pups, oral absorption of gadopiclenol was 3.6%.

Pediatric Use The safety and effectiveness of Vueway for use with MRI to detect and visualize lesions with abnormal vascularity in the CNS (brain, spine, and associated tissues), and the body (head and neck, thorax, abdomen, pelvis, and musculoskeletal system) have been established in pediatric patients aged 2 years and older.

Use of Vueway in this age group is supported by evidence from adequate and well-controlled studies in adults with additional pharmacokinetic and safety data from an open-label, uncontrolled, multicenter, single dose study of Vueway (0.05 mmol/kg) in 80 pediatric patients aged 2 to 17 years. The 80 patients consisted of 60 patients who underwent a CNS MRI and 20 patients who underwent a body MRI [see Adverse Reactions (6.1) and Clinical Pharmacology (12.3) in the full Prescribing Information].

The safety and effectiveness of Vueway have not been established in pediatric patients younger than 2 years of age.

Geriatric Use Of the total number of Vueway-treated patients in clinical studies, 270 (26%) patients were 65 years of age and over, while 62 (6%) patients were 75 years of age and over. No overall differences in safety or efficacy were observed between these subjects and younger subjects.

This drug is known to be substantially excreted by the kidney, and the risk of adverse reactions to this drug may be greater in patients with impaired renal function. Because elderly patients are more likely to have decreased renal function, it may be useful to monitor renal function.

Renal Impairment in patients with renal impairment, the exposure of gadopiclenol is increased compared to patients with normal renal function. This may increase the risk of adverse reactions such as nephrogenic systemic fibrosis (NSF). Avoid use of GBCAs among these patients unless the diagnostic information is essential and not available with non-contrast MRI or other modalities. No dose adjustment of Vueway is recommended for patients with renal impairment. Vueway can be removed from the body by hemodialysis [see Warnings and Precautions (5.1, 5.3, 5.4) and Clinical Pharmacology (12.3) in the full Prescribing Information].

OVERDOSAGE

Among subjects who received a single 0.3 mmol/kg intravenous dose of gadopiclenol (6 times the recommended dose of Vueway), headache and nausea were the most frequently reported adverse reactions. Gadopiclenol can be removed from the body by hemodialysis [see Clinical Pharmacology (12.3) in the full Prescribing Information].

PATIENT COUNSELING INFORMATION Advise the patient to read the FDA-approved patient labeling (Medication Guide).

Nephrogenic Systemic Fibrosis Inform the patient that Vueway may increase the risk for NSF among patients with impaired elimination of the drugs and that NSF may result in fatal or debilitating fibrosis affecting the skin, muscle and internal organs.

Instruct the patients to contact their physician if they develop signs or symptoms of NSF following Vueway administration, such as burning, itching, swelling, scaling, hardening and tightening of the skin; red or dark patches on the skin; stiffness in joints with trouble moving, bending or straightening the arms, hands, legs or feet; pain in the hip bones or ribs; or muscle weakness [see Warnings and Precautions (5.1) in the full Prescribing Information].

Gadolinium Retention Advise patients that gadolinium is retained for months or years in brain, bone, skin, and other organs following Vueway administration even in patients with normal renal function. The clinical consequences of retention are unknown. Retention depends on multiple factors and is greater following administration of linear GBCAs than following administration of macrocyclic GBCAs [see Warnings and Precautions (5.3) in the full Prescribing Information].

Injection Site Reactions Inform the patient that Vueway may cause reactions along the venous injection site, such as mild and transient burning or pain or feeling of warmth or coldness at the injection site [see Warnings and Precautions (5.5) in the full Prescribing Information].

Pregnancy Advise pregnant women of the potential risk of fetal exposure to Vueway [see Use in Specific Populations (8.1) in the full Prescribing Information].

Rx only

US Patent No. 10,973,934
Manufactured for Bracco Diagnostics Inc. by Liebel-Flarsheim Company LLC
- Raleigh, NC, USA 27616.
Toll Free: 1-877-272-2269 (U.S. only)
Revised November 2022



The ASNR Career Center

The Go-To Job Site for Neuroradiology Employers and Job Seekers

For Job Seekers

- Access to an expanded network of jobs via the National Healthcare Career Network
- Confidential resume posting
- Professional online profile

For Employers

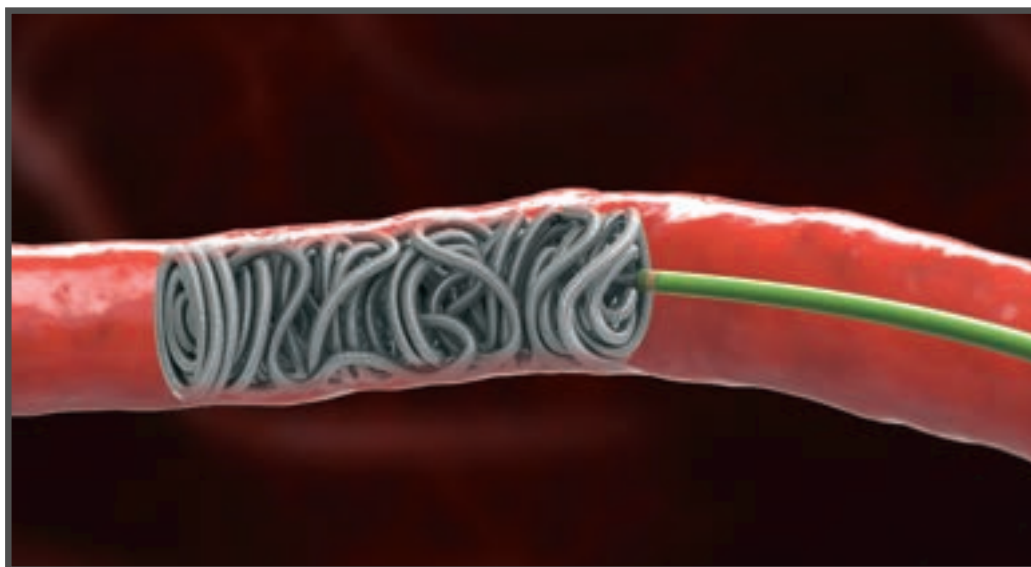
- Employer resources to help you recruit top talent
- Multiple pricing options, including free Fellowship listings
- Resume search

Start here: careers.asnr.org

OPTIBLOCK™

COIL

PRECISION PLACEMENT



EFFICIENT OCCLUSION

- Precision Anchoring
- Concise, Dense Pack
- Unique Design and Long Lengths
- $\geq .0165$ Microcatheter Compatible

Visit our products page at baltgroup.com for more information.

Balt USA
29 Parker, Irvine, CA 92618 • tel 949.788.1443 fax 949.788.1444
baltgroup.com

© 2023 BALT USA MKTG-370 Rev. A



AJNR

AMERICAN JOURNAL OF NEURORADIOLOGY

JULY 2023
VOLUME 44
NUMBER 7
WWW.AJNR.ORG

Publication Preview at www.ajnr.org features articles released in advance of print. Visit www.ajnrblog.org to comment on AJNR content and chat with colleagues and AJNR's News Digest at <http://ajnrdigest.org> to read the stories behind the latest research in neuroimaging.

749 **PERSPECTIVES** *A. Arora*

REVIEW ARTICLE

-   750 **Advances in Acute Ischemic Stroke Treatment: Current Status and Future Directions** *G. Bathla, et al.*

ADULT BRAIN

EDITORIAL

-  759 **Realistic Productivity in Academic Neuroradiology: A National Survey of Neuroradiology Division Chiefs** *M. Wintermark, et al.*

GENERAL CONTENTS

-  762 **Crowd-Sourced Deep Learning for Intracranial Hemorrhage Identification: Wisdom of Crowds or Laissez-Faire** *E.I.S. Hofmeijer, et al.* **ADULT BRAIN**
-    768 **Investigation of Brain Iron in Niemann-Pick Type C: A 7T Quantitative Susceptibility Mapping Study** *P. Ravanfar, et al.* **ADULT BRAIN FUNCTIONAL**
-    776 **Choroid Plexus Calcification Correlates with Cortical Microglial Activation in Humans: A Multimodal PET, CT, MRI Study** *T. Butler, et al.* **ADULT BRAIN FUNCTIONAL**
-    783 **Cost-Effectiveness Analysis of ⁶⁸Ga-DOTATATE PET/MRI in Radiotherapy Planning in Patients with Intermediate-Risk Meningioma** *J. Rodriguez, et al.* **ADULT BRAIN**
-  792 **Sex-Specific Patterns of Cerebral Atrophy and Enlarged Perivascular Spaces in Patients with Cerebral Amyloid Angiopathy and Dementia** *J. Pinho, et al.* **ADULT BRAIN**
-   799 **MR Imaging Findings in a Large Population of Autoimmune Encephalitis** *S. Gillon, et al.* **ADULT BRAIN**
-  807 **Early Detection of Underlying Cavernomas in Patients with Spontaneous Acute Intracerebral Hematomas** *A. Bani-Sadr, et al.* **ADULT BRAIN**
-  814 **Perifocal Edema in Patients with Meningioma is Associated with Impaired Whole-Brain Connectivity as Detected by Resting-State fMRI** *V.M. Stoecklein, et al.* **FUNCTIONAL**
-   820 **Exploratory Multisite MR Spectroscopic Imaging Shows White Matter Neuroaxonal Loss Associated with Complications of Type 1 Diabetes in Children** *L.Y. Cai, et al.* **PEDIATRICS FUNCTIONAL**

AJNR (Am J Neuroradiol ISSN 0195–6108) is a journal published monthly, owned and published by the American Society of Neuroradiology (ASNR), 820 Jorie Boulevard, Oak Brook, IL 60523. Annual dues for the ASNR include approximately 19% for a journal subscription. The journal is printed by Intellicor Communications, 330 Eden Road, Lancaster, PA 17601; Periodicals postage paid at Oak Brook, IL and additional mailing offices. Printed in the U.S.A. POSTMASTER: Please send address changes to American Journal of Neuroradiology, P.O. Box 3000, Denville, NJ 07834, U.S.A. Subscription rates: nonmember \$452 (\$530 foreign) print and online, \$320 online only; institutions \$520 (\$594 foreign) print and basic online, \$1029 (\$1103 foreign) print and extended online, \$380 online only (basic), \$825 online only (extended); single copies are \$35 each (\$40 foreign). Indexed by PubMed/MEDLINE, BIOSIS Previews, Current Contents (Clinical Medicine and Life Sciences), EMBASE, Google Scholar, HighWire Press, Q-Sensei, RefSeek, Science Citation Index, SCI Expanded, ReadCube, and Semantic Scholar. Copyright © American Society of Neuroradiology.

- 828** Association of Lower Age and Cardiorespiratory Events during Intra-Arterial Chemotherapy for Retinoblastoma: A Prospective Observational Study *M.F. Lima, et al.*
PEDIATRICS
INTERVENTIONAL
- 833** Correlation between Multiparametric MR Imaging and Molecular Genetics in Pontine Pediatric High-Grade Glioma *V. Rameh, et al.*
PEDIATRICS
FUNCTIONAL
- 841** T2-FLAIR Mismatch Sign in Pediatric Low-Grade Glioma *M.W. Wagner, et al.*
PEDIATRICS
- 846** Development of an Ultrasound Scoring System to Describe Brain Maturation in Preterm Infants *A. Stein, et al.*
PEDIATRICS
- 853** Predicting Drug Treatment Outcomes in Childrens with Tuberous Sclerosis Complex–Related Epilepsy: A Clinical Radiomics Study *Z. Hu, et al.*
PEDIATRICS
FUNCTIONAL
- 861** Long-Term Imaging Follow-up from the Management of Myelomeningocele Study *E. George, et al.*
PEDIATRICS
- 867** Validation of a New Semiautomated Segmentation Pipeline Based on the Spinal Cord Toolbox DeepSeg Algorithm to Estimate the Cervical Canal Area *N. Mongay-Ochoa, et al.*
SPINE
- 873** The Development and Application of a Cost-Effective Cervical Spine Phantom for Use in Fluoroscopically Guided Lateral C1–C2 Spinal Puncture Training *V. Risner, et al.*
SPINE

ONLINE FEATURES

E32 **ERRATUM**

BOOK REVIEWS *R.M. Quencer, Section Editor*

Please visit www.ajnrblog.org to read and comment on Book Reviews.



Representative QSM images from control and Niemann-Pick type groups from Ravanfar, et al, in this issue.



Indicates Editor's Choices selection



Indicates Fellows' Journal Club selection



Indicates open access to non-subscribers at www.ajnr.org



Indicates article with supplemental online data



Indicates article with supplemental online video



Evidence-Based Medicine Level 1



Evidence-Based Medicine Level 2



Title: Aerial view of the majestic old Delhi through the lancet window of one of the minarets in Jama Masjid, New Delhi, which is one of the most powerful archaic monuments testifying to the Mughal rule's legacy in India. The timeless architecture recalls the ardent talent of architects of yesteryear.

Ankit Arora, Training Neuroradiologist, National Institute of Mental Health and Neuro Science, Bengaluru, India

Advances in Acute Ischemic Stroke Treatment: Current Status and Future Directions

G. Bathla, P. Ajmera, P.M. Mehta, J.C. Benson, C.P. Derdeyn, G. Lanzino, A. Agarwal, and W. Brinjikji



ABSTRACT

SUMMARY: The management of acute ischemic stroke has undergone a paradigm shift in the past decade. This has been spearheaded by the emergence of endovascular thrombectomy, along with advances in medical therapy, imaging, and other facets of stroke care. Herein, we present an updated review of the various stroke trials that have impacted and continue to transform stroke management. It is critical for the radiologist to stay abreast of the ongoing developments to provide meaningful input and remain a useful part of the stroke team.

ABBREVIATIONS: AHA/ASA = American Heart Association/American Stroke Association; ACS = anterior circulation stroke; AIS = acute ischemic stroke; COR = class of recommendation; eTICI = expanded TICI; EVT = endovascular thrombectomy; ICAD = intracranial atherosclerotic disease; ICH = intracranial hemorrhage; LOE = level of evidence; LVO = large-vessel occlusion; mTICI = modified TICI; PCS = posterior circulation strokes; RCT = randomized controlled trial; SMM = standard medical management; TNK = tenecteplase

Every year, around 800,000 individuals experience new or recurrent strokes, with most of these being new cases. Approximately 87% are ischemic, 10% reflect intracranial hemorrhage (ICH), and 3% are SAH. Despite a general decrease in stroke incidence during the past 30 years, it is projected that by 2030, an additional 3.4 million US adults will have had a stroke.¹

The management of acute ischemic stroke (AIS) has undergone a remarkable transformation in the past decade, largely led by endovascular thrombectomy (EVT), with contributions through improvements in thrombectomy devices, medical management, and stroke workflows. Recent trials have also demonstrated improved outcomes with EVT in posterior circulation strokes (PCS) and larger strokes, which will continue to impact stroke care in the future. Additionally, various aspects of stroke therapy are currently being studied, including the role of EVT in distal occlusions and clinically mild strokes with large-vessel occlusion (LVO). It is crucial for radiologists and the medical community to stay informed about these developments to provide

meaningful information that positively impacts patient outcomes. To this end, a review of recent studies related to AIS is presented.

Before proceeding, it is important for the reader to understand 3 commonly used terms in stroke care: the mRS, the NIHSS, and the modified TICI (mTICI) scale. The mRS is a 7-point scale that ranges from 0 (no symptoms) to 6 (death) and covers the entire range of functional outcomes in stroke. It is easy to administer, correlates with measures of stroke, and is useful in evaluating the efficacy of acute stroke therapies. A single-point change in the mRS score is considered clinically relevant.² In all trials conducted to assess stroke outcomes, at least one of the primary end points is typically the mRS, due to its high validity and reliability as well as its requirement for a smaller sample size compared with other measures of stroke outcomes.³

The NIHSS is a 15-item neurologic examination scale to assess stroke severity and changes in clinical status. The score ranges from 0 to 42, with higher scores indicating greater stroke severity. A recent meta-analysis noted that an NIHSS score of ≥ 10 is 73% sensitive and 74% specific for predicting underlying LVO.⁴ The 2019 update to the 2018 American Heart Association/American Stroke Association (AHA/ASA) guidelines also recommend the use of a stroke scale, preferably the NIHSS to assess stroke severity.⁵

Finally, the mTICI was derived from the original TICI grading in 2013 and measures the degree of reperfusion.⁶ The score ranges from 0 to 3 with grade 0 indicating no reperfusion, grade 1 indicating limited distal filling past the initial occlusion, grade 2 indicating further reperfusion with subdivisions based on the amount of reperfused MCA territory (2a: $< 50\%$; 2b: $> 50\%$; 2c: 90%–99%), and grade 3 indicating complete reperfusion. The current AHA/ASA guidelines recommend a score of $\geq 2b$ as the

Received March 5, 2023; accepted after revision April 3.

From the Department of Radiology (G.B., P.M.M., J.C.B., G.L., W.B.), Mayo Clinic, Rochester, Minnesota; Department of Radiology (P.A.), University College of Medical Sciences, Delhi, India; Department of Radiology (C.P.D.), University of Iowa Hospitals and Clinics, Iowa City, Iowa; and Department of Radiology (A.A.), Mayo Clinic, Jacksonville, Florida.

Please address correspondence to Girish Bathla, MBBS, FRCR, Department of Radiology, Mayo Clinic, 200 1st st SW, Rochester, Minnesota, 55905; e-mail: Bathla.Girish@mayo.edu; @GBathlaMD; @CPDerdeyn; @WBrinjikji; @AmitAgarwalMD

Indicates open access to non-subscribers at www.ajnr.org

Indicates article with online supplemental data.

<http://dx.doi.org/10.3174/ajnr.A7872>

angiographic goal of EVT.⁵ More recently, an expanded TICI (eTICI) scale has also been proposed, which encompasses a 7-point score, with eTICI grade 0 implying no reperfusion and grade 1 implying thrombus reduction without distal reperfusion. eTICI 2 is further subdivided to define the extent of reperfusion more precisely (2a: 1%–49%; 2b50: 50%–66%; 2b67: 67%–89%; 2c: 90%–99%), while eTICI 3 implies complete reperfusion, similar to TICI 3.⁷ The authors noted that despite adjacent categories of reperfusion in eTICI 2, the outcomes were significantly different, and they argued that eTICI 2b67 could be considered the ideal threshold for defining successful reperfusion.

Thrombolytics

IV-tPA was first approved by the FDA for the treatment of AIS within 3 hours of symptom onset in 1995, based on the results of the for National Institute of Neurological Disorders and Stroke tPA (NINDS tPA) trial.⁸ In 2008, the treatment window for IV tPA was expanded to 4.5 hours, after the European Cooperative Acute Stroke Study III demonstrated sustained treatment benefits.⁹ More recently, the European Cooperative Acute Stroke Study (ECASS) IV and Extending the Time for Thrombolysis in Emergency Neurological Deficits (EXTEND) trials evaluated IV tPA efficacy between the 4.5- and 9-hour window in patients who were not EVT eligible and had a perfusion-to-diffusion mismatch ratio of ≥ 1.2 . Although ECASS IV did not show significantly improved 90-day outcomes, EXTEND demonstrated better functional independence when adjusted for age and stroke severity. Both studies were, however, terminated early. Enrollment in ECASS IV declined post publication of extended window EVT trials, and EXTEND was stopped because the results from the Efficacy and Safety of the MRI-Based Thrombolysis in Wake-Up Stroke (WAKE-UP) trial led to loss of equipoise.^{10,11}

The safety and efficacy of IV tPA in AIS of unknown onset, which accounted for 14%–27% of strokes, was evaluated in the WAKE-UP and A Study of Intravenous Thrombolysis With Alteplase in MRI-Selected Patients (MR WITNESS) trials.^{12,13} Of note, MR WITNESS was primarily designed to assess the safety rather than the efficacy of IV tPA administration. WAKE-UP used DWI-FLAIR mismatch criteria (ischemic lesion visible on DWI without corresponding FLAIR signal change), while MR WITNESS further quantified the FLAIR signal change (FLAIR signal intensity in ischemic region/contralateral normal brain ≤ 1.15) as a criterion for IV tPA administration. Even though WAKE-UP was terminated early due to lack of funding, analysis of the 503 enrolled patients revealed that 53.5% of the IV tPA group achieved a 90-day mRS of 0–1 compared with 41.8% in the placebo group ($P = .02$).

Tenecteplase (TNK) is a bioengineered form of alteplase with higher fibrin selectivity and a longer half-life, allowing administration as a single bolus dose, unlike alteplase, which is given initially as a bolus (10% dose) followed by slow infusion (90% dose) for 1 hour. The Tenecteplase versus Alteplase before Endovascular Therapy for Ischemic Stroke (EXTEND-IA TNK) showed that TNK administration before EVT resulted in improved revascularization and 90-day outcomes, compared with alteplase.^{14,15} More recently, Tenecteplase versus Alteplase in Acute Ischaemic Cerebrovascular

Events (TRACE-2) (1430 patients) and Alteplase compared to Tenecteplase in Patients With Acute Ischemic Stroke (AcT) (1600 patients) showed TNK to be noninferior to alteplase in patients presenting within 4.5 hours of AIS.¹⁶ TNK is, however, currently not FDA-approved for AIS, though this may change in the future, given the accumulating evidence.

Thrombolytics, however, have limitations such as a narrow treatment window and modest recanalization rates for LVO, prompting a search for alternate methods to achieve timely recanalization.

EVT in Anterior Circulation Stroke

In 2015, five randomized controlled trials (RCTs) showed the efficacy of EVT over standard medical management (SMM) in patients with anterior circulation stroke (ACS) with proximal LVO. The Multicenter Randomized Clinical Trial of Endovascular Treatment for Acute Ischemic Stroke in the Netherlands (MR CLEAN) found that 32% of patients treated with EVT had better outcomes (90-day mRS 0–2) compared with 19% in the SMM group.¹⁷ Endovascular Treatment for Small Core and Proximal Occlusion Ischemic Stroke (ESCAPE) trial ended early after MR CLEAN study results were released, with the interim analysis showing higher functional independence rates with EVT (53%) compared with SMM (29%). The ESCAPE trial focused on efficient workflow, emphasized the use of CTA over MR imaging, and achieved a median NCCT-to-reperfusion time of 84 minutes.¹⁸ Similar positive results were also noted with the Solitaire With the Intention for Thrombectomy as Primary Endovascular Treatment (SWIFT PRIME), Extending the Time for Thrombolysis in Emergency Neurological Deficits Intra-Arterial (EXTEND-IA), Endovascular Revascularization With Solitaire Device Versus Best Medical Therapy in Anterior Circulation Stroke Within 8 Hours (REVASCAT), and the Trial and Cost Effectiveness Evaluation of Intra-Arterial Thrombectomy in Acute Ischemic Stroke (THRACE studies) (Figure).^{19–22}

A meta-analysis of the 5 major EVT trials, conducted in 2016 by the HERMES collaboration, found that the effectiveness of EVT declined with each passing hour and concluded that treatment within the first 7 hours is likely to produce the best results.²³ The number needed to treat was 2.6.²⁴ Subsequently, the Clinical Mismatch in the Triage of Wake Up and Late Presenting Strokes Undergoing Neurointervention With Trevo (DAWN) and Endovascular Therapy Following Imaging Evaluation for Ischemic Stroke (DEFUSE 3) trials were undertaken and demonstrated the effectiveness of EVT in delayed time windows (up to 24 hours).^{25,26} The DAWN trial showed increased functional independence in patients in the 6- to 24-hour window who had a clinical-imaging mismatch. The DEFUSE 3 trial, on the other hand, showed improved outcomes with EVT for patients presenting in the 6- to 16-hour time window who met certain imaging criteria (ACS with LVO involving the ICA or proximal MCA, core infarct of < 70 mL, and ratio of ischemic tissue to infarct of > 1.8), regardless of clinical-imaging mismatch. Of note, about 40% of patients in DEFUSE 3 would not have met the clinical-imaging mismatch criteria of the DAWN trial. The DEFUSE 3 trial was terminated early after an early interim analysis established EVT superiority.

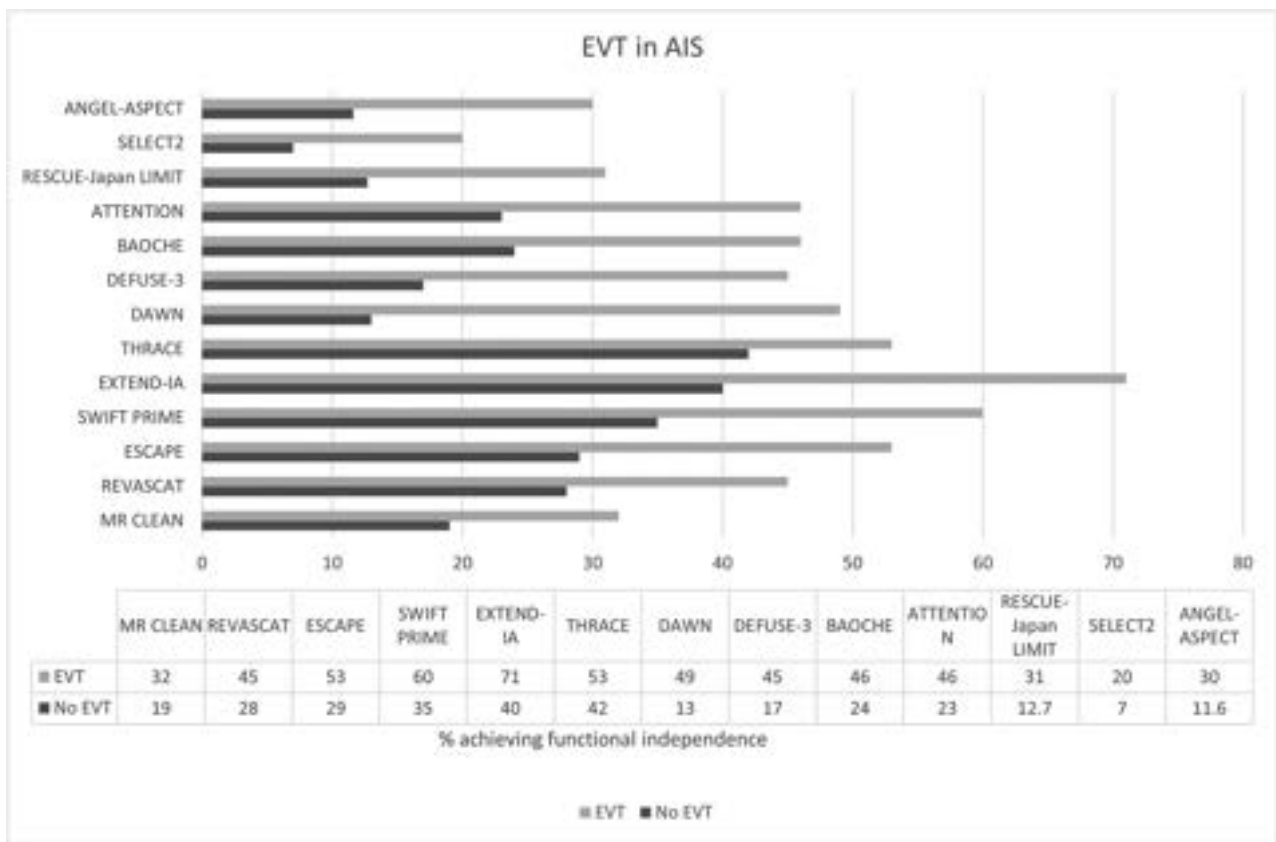


FIGURE 1. Barplot showing the differences in functional outcomes with (gray) and without EVT (black) in select trials. The first 3 trials evaluated EVT with large infarct, and BAOICHE and ATTENTION assessed EVT in PCS, while the rest assessed EVT in ACS.

More recently, a few trials have evaluated the role of combined IV tPA and EVT compared with EVT alone. The Direct Intra-Arterial Thrombectomy in Order to Revascularize AIS Patients With Large Vessel Occlusion Efficiently in Chinese Tertiary Hospitals (DIRECT-MT) and Effect of Endovascular Treatment Alone Versus Intravenous Alteplase Plus Endovascular Treatment on Functional Independence in Patients with Acute Ischemic Stroke (DEVIT) trials (China) showed noninferiority of EVT compared with combined therapy.^{27,28} However, the Randomized study of endovascular therapy with versus without intravenous tissue plasminogen activator in acute stroke with ICA and M1 occlusion (SKIP) trial (Japan) failed to show noninferiority, while the Solitaire With the Intention for Thrombectomy plus Intravenous tPA Versus DIRECT Solitaire Stent-Retriever Thrombectomy in Acute Anterior Circulation Stroke (SWIFT-DIRECT) trial (Europe and Canada) noted that EVT alone was not noninferior and resulted in reduced reperfusion rates compared with combined therapy.^{29,30} The Multicenter MR CLEAN-NO IV trial (Europe) also noted that EVT was neither superior nor noninferior to combined therapy.³¹ More recently, A Randomized Controlled Trial of DIRECT Endovascular Clot Retrieval versus Standard Bridging Thrombolysis With Endovascular Clot Retrieval (DIRECT-SAFE) again did not show noninferiority of EVT. Most interesting, the authors noted better outcomes in Asian patients with combined therapy.³² Currently, Endovascular Treatment With versus Without Intravenous rhTNK-tPA in Stroke (BRIDGE-TNK, NCT04733742) is currently evaluating a combination of TNK and EVT compared with EVT alone.

EVT in Large Core Infarcts

In the past, most trials excluded patients with ASPECTS of < 5 or a core infarct volume of >70 mL. These patients, however, have poor outcomes. Recently, the RCT of Recovery by Endovascular Salvage for Cerebral Ultra-acute Embolism Japan Large Ischemic core Trial (RESCUE-Japan LIMIT), a prospective RCT that enrolled patients with ASPECTS between 3 and 5, showed improved functional outcomes (90-day mRS 0–3) in patients who additionally received EVT compared with SMM.³³ Although the EVT group had a higher incidence of ICH, the incidence of symptomatic ICH was not significantly different between groups. A secondary analysis suggested that improved functional outcomes were mainly seen in patients with ASPECTS of 4 or 5, whereas those with ASPECTS of ≤ 3 did not have significantly improved outcomes.³⁴ Earlier in 2023, two additional trials, A Randomized Controlled Trial to Optimize Patient’s Selection for Endovascular Treatment in Acute Ischemic Stroke (SELECT2) and Endovascular Therapy in Acute Anterior Circulation Large Vessel Occlusive Patients with a large infarct core (ANGEL-ASPECT) evaluated patients with ASPECTS between 3 and 5 and large-core infarct (ANGEL-ASPECT, 70–100 mL, and SELECT2, ≥ 50 mL). Both trials were stopped early due to overwhelmingly improved outcomes with EVT.^{35,36} Currently, at least 3 more trials are evaluating EVT in large infarcts, including the Large Stroke Therapy Evaluation (LASTE), Efficacy and Safety of Thrombectomy in Stroke With Extended Lesion and Extended Time Window (TENSION), and Thrombectomy for

Emergent Salvage of Large Anterior Circulation Ischemic Stroke (TESLA).³⁷

Tandem Occlusions

Tandem lesions, defined as anterior circulation LVOs with concurrent high-grade stenosis or occlusion of the ipsilateral ICA secondary to atherosclerosis or vascular dissection, may be seen in up to 10%–20% of patients with AIS. Their optimal management remains unclear. A subgroup analysis of the Safety and Efficacy of Nerinetide (NA-1) in Subjects Undergoing Endovascular Thrombectomy for Stroke (ESCAPE-NA1) data showed that a concurrent tandem lesion did not lower the odds of a good functional outcome, regardless of stent placement.³⁸ However, because the trial enrolled only patients with moderate collaterals and smaller infarcts, the confounding effect of these variables remains unclear. A recent meta-analysis reviewing the effect of acute carotid stent placement in patients undergoing EVT noted that stent placement was associated with favorable outcomes without increased mortality or ICH.³⁹ Ongoing RCTs, the Endovascular Acute Stroke Intervention–Tandem Occlusion Trial (EASI-TOC) (NCT04261478), Proximal Internal Carotid Artery Acute Stroke Secondary to Tandem or Local Occlusion Thrombectomy Trial (PICASSO, NCT05611242), and Thrombectomy In TANdem Occlusion (TITAN, NCT03978988), will prospectively evaluate the role of carotid stent placement in AIS with tandem lesions.³⁸

EVT in PCS

Posterior circulation LVOs may account for 7%–12% of all intracranial LVOs in AIS, and up to 80% of patients with basilar artery occlusion presenting with moderate-to-severe deficits die or have severe disability despite SMM.^{40–42} The most frequent causes of posterior circulation LVOs in the MR CLEAN registry were large-artery atherosclerosis and cardioembolism.⁴³ Four recent RCTs evaluated the role of EVT in PCS. The Acute Basilar Artery Occlusion: Endovascular Interventions vs Standard Medical Treatment (BEST) trial was discontinued due to poor recruitment and high crossover rates between the treatment arms.⁴⁴ The Basilar Artery International Cooperation Study (BASICS) did not demonstrate any significant additional benefit with EVT.⁴⁵ However, the study had nonconsecutive enrollment, and a third of eligible patients were treated outside the trial, most of whom received EVT, which may have biased the study conclusions.

More recently, the Basilar Artery Occlusion Chinese Endovascular (BAOCHE) and Endovascular Treatment For Acute Basilar Artery Occlusion (ATTENTION) trials, both conducted in Chinese patients, showed improved outcomes with EVT in PCS presenting between 6 and 24 hours and <12 hours of last known well, respectively.^{41,46} Of note, both trials used posterior circulation ASPECTS as one of the exclusion criteria, with BAOCHE excluding patients with a score of <6, and ATTENTION excluding patients with a score of <6 if younger than 80 years of age and a score of <8 if older than 80 years of age.

Thrombectomy Devices

The mechanical embolus removal in cerebral ischemia (Merci) device (Stryker) was the first successful clot-retrieval device, achieving recanalization in 48% of patients.⁴⁷ This was followed by the

Penumbra system (Penumbra), which achieved Thrombolysis in Myocardial Infarction scores of 2–3 in 81.6% of patients.⁴⁸ However, early studies raised concerns about the efficacy of EVT, failing to show any additional benefit compared with SMM. Importantly, these studies did not require LVO confirmation for enrollment into the treatment arm.^{49,50}

It was only after the publication of MR CLEAN and subsequent trials in 2015 that there was renewed interest in EVT.^{17,18,20–22} Most of these trials used second-generation thrombectomy devices known as stent retrievers.

Stent retriever and clot aspiration are the 2 most used EVT techniques, with continued improvements leading to reperfusion rates exceeding 90% in LVO thrombectomy.⁵¹ Stent retrievers are inserted within the thrombus and re-establish blood flow once expanded, while simultaneously binding the thrombus. Subsequent stent retrieval extracts the clot. Aspiration devices, on the other hand, connect to an external aspiration pump that creates a negative suction to aspirate the clot. The Contact Aspiration vs Stent Retriever for Successful Revascularization (ASTER) trial, a multicenter, randomized blinded-end-point superiority trial conducted in France failed to show superiority of first-line contact aspiration compared with a first-line stent retriever in AIS.⁵² The COMPASS Trial: a Direct Aspiration First Pass Technique (COMPASS) trial, on the other hand, was designed as a noninferiority trial and conducted in a multicenter setting in North America. The study compared the 2 techniques and showed that contact aspiration was noninferior to stent retrievers.⁵³ Currently, the choice of technique is primarily based on user preference and expertise.

AIS Secondary to Intracranial Atherosclerotic Disease

Intracranial atherosclerotic disease (ICAD) accounts for about 10%–15% of AIS cases in the West but has higher prevalence in Asia where it may account for up to 46.6% of AIS cases.⁵⁴ These patients have an especially higher risk of recurrent stroke and often have acute vessel re-occlusion despite repeat recanalization during EVT.^{51,54} The Wingspan stent (Stryker) was the first self-expanding stent designed specifically for ICAD and is the only FDA-approved stent for symptomatic ICAD.⁵⁵ A few trials have evaluated the role of stent placement versus aggressive medical therapy in preventing recurrent strokes in this cohort. The Stenting versus Aggressive Medical Management for Preventing Recurrent Stroke in Intracranial Stenosis (SAMMPRIS) trial was terminated early due to a significantly higher complication rate in the stented group.⁵⁶ Similarly, the Vitesse Intracranial Stent Study for Ischemic Therapy (VISSIT) trial was also terminated early after an interim analysis showed increased stroke risk with stent placement.⁵⁷ More recently, the China Angioplasty and Stenting for Symptomatic Intracranial Severe Stenosis (CASSISS) trial again showed no additional benefit of stent placement over medical management.⁵⁴ However, 2 recent postmarketing surveillance studies (Post Market Surveillance Study of the Wingspan Stent System [WEAVE] trial and the Post Market Surveillance of Percutaneous Transluminal Angioplasty and Wingspan Stenting for Intracranial Atherosclerotic Disease [WICAD] study) demonstrated an excellent safety profile when used by experienced interventionalists following on-label guidelines. Functional independence (mRS

0–2) was achieved in 88.9% of patients in the WICAD group with a mortality rate of 3%.^{58,59}

Role of Imaging in AIS

The current AHA/ASA guidelines recommend that all patients suspected of having AIS undergo brain imaging on first arrival (class of recommendation [COR] I; level of evidence [LOE] A). Both NCCT (COR-I; LOE-A) and MR imaging (COR-I; LOE-B) are effective in excluding ICH before IV tPA.⁵ Of note, a post hoc analysis of the THRACE data using 401 patients (299 MR imaging and 102 CT) did not note any differences in clinical outcomes despite the slightly longer duration of the MR imaging scans (median MR imaging duration, 13 minutes; CT, 9 minutes).⁶⁰

For patients with AIS presenting between 6 and 24 hours, the guidelines recommend CTA with CT perfusion or MRA with DWI with or without MR perfusion for selecting EVT candidates (COR-I; LOE-A). However, in patients presenting <6 hours from last known well and having an ASPECTS of >6, EVT eligibility may be determined on the basis of NCCT and CTA/MR imaging and MRA without additional perfusion studies (COR-I; LOE-B). In patients with AIS who awake with stroke symptoms or have an unclear time of onset of >4.5 hours from last known well or a baseline state, MR imaging to detect DWI-FLAIR mismatch may be useful in selecting IV tPA-eligible patients (COR-IIa; LOE-B).

The guidelines also recommend noninvasive intracranial vascular imaging for patients who otherwise meet the EVT criteria or when LVO is suspected (COR-I; LOE-A). Extracranial carotid and vertebral artery imaging may be reasonable to provide information on eligibility and treatment-planning (COR-IIb; LOE-C). Incorporating the collateral status into decision-making for potential EVT is also considered reasonable (COR-IIb; LOE-C).

Several post hoc analyses of published RCTs and larger patient registries have evaluated the role of imaging markers in the assessment of stroke. Boodt et al,⁶¹ in an analysis of 1429 consecutive patients from the MR CLEAN registry, noted that noncardioembolic strokes were associated with the presence of the hyperdense artery sign (OR = 2.2; 95% CI, 1.6–3.0) and a more proximal thrombus location (common OR = 0.2; 95% CI, 0.2–0.3), findings based on univariable analysis. Additionally, thrombus characteristics in strokes with undetermined etiology were similar to those of cardioembolic strokes, suggesting that most cryptogenic strokes may be cardioembolic. A secondary analysis of the DIRECT-MT trial noted that the hyperdense artery sign at baseline indicated improved outcomes with the addition of IV tPA to EVT, while its absence correlated with worse outcomes.⁶²

Both the hyperdense artery sign and increased susceptibility of the thrombus on T2* images (positive susceptibility vessel sign) are secondary to an increased amount of red blood cells, which can favorably interfere with stent retriever struts during EVT.^{61,63} A subgroup analysis of the THRACE data noted that smaller DWI volumes, the presence of a positive susceptibility vessel sign, and a short susceptibility vessel sign length were associated with excellent outcomes (90-day mRS ≤1) with IV tPA alone.⁶⁴

A post hoc analysis of the DEFUSE 3 data noted that nearly half of the penumbral tissue with a time-to-maximum of >6 seconds may remain viable in untreated patients at 24 hours, while about 74% of the penumbral tissue with time-to-maximum

of >10 seconds may remain viable after TICI 3 recanalization. Similar effects on penumbral tissue were, however, not seen with incomplete recanalization (TICI 0–2b).⁶⁵ Another secondary analysis of the DEFUSE 3 data noted that patients with favorable collaterals had smaller 24-hour infarct volumes than initially predicted, suggesting that collateral status may impact final infarct volumes.⁶⁶

In terms of functional outcomes, a post hoc analysis of the ESCAPE-NA1 using 1026 patients noted that infarction confined to gray matter, sparing of the corticospinal tract, and scattered infarct structure were highly predictive of good 90-day outcome.⁶⁷ Hemorrhagic transformation, regardless of severity, is associated with worse functional outcomes, though the effect appears more pronounced with hemorrhage of >30% of the infarct volume.⁶⁸ A substudy of THRACE data noted that pretreatment infarct volume is an independent predictor of functional outcome. The efficacy of EVT decreases with increasing infarct volume, with the number of patients needed to treat to achieve functional independence increasing from 10 patients for a volume of 80 mL to 15 patients for a volume of 135 mL.⁶⁹ The Online Supplemental Data outline imaging-based inclusion and exclusion criteria of select stroke trials based on thrombolytics and EVT, respectively.

Stroke Workflow and Perioperative Management

Because the most critical component in AIS is timely re-establishment of perfusion, several studies have evaluated the impact of different workflows and perioperative management on overall outcomes.

The Direct Transfer to an Endovascular Center Compared to Transfer to the Closest Stroke Center in Acute Stroke Patients With Suspected Large Vessel Occlusion (RACECAT) study, which evaluated differences in outcomes in nonurban areas between patients who were transferred directly to an EVT-capable center compared with patients who were initially transferred to a local stroke center (capable of imaging, IV tPA, but not EVT), followed by transfer to an EVT-capable center if LVO was confirmed, was halted for futility after the second interim analysis showed no differences in outcomes.⁷⁰ The best approach, therefore, may be based on the availability of local resources and achievable workflow metrics, and a “drip and ship” approach may still be acceptable, especially in remote settings.

Because multiple prior studies have demonstrated improved patient outcomes with earlier treatment initiation, considerable effort has been made to reduce door-to-needle times.^{23,71} More recent studies have demonstrated that door-to-needle times of <60 minutes are achievable in most patients.⁷² Another recent study noted that for patients with ACS undergoing EVT, the addition of 100% oxygen through a face mask led to significantly reduced infarct volumes at 24–48 hours (median, 20.1 versus 37.7 mL; $P < .01$) and improved 90-day mRS.⁷³ Two recent trials evaluated the safety and efficacy of intensive blood pressure control after EVT. The Blood Pressure Target in Acute Stroke to Reduce Hemorrhage After Endovascular Therapy (BP-TARGET) trial did not find a difference in radiographic intraparenchymal hemorrhage, while the Second ENhanced Control of Hypertension ANd Thrombectomy stroke stuDY (ENCHANTED2/MT) trial was stopped early after outcome data revealed that more intensive blood pressure control was associated with poor functional outcomes and early neurologic deterioration.^{74,75}

In terms of sedation during EVT, the General Or Local Anaesthesia in Intra Arterial Therapy (GOLIATH), Anesthesia during Stroke (AnStroke), Sedation vs Intubation for Endovascular Stroke Treatment Trial (SIESTA), and General Anesthesia vs Sedation During Intra-arterial Treatment for Stroke (GASS) studies showed that both conscious sedation and general anesthesia were equally effective in terms of neurologic improvement and 90-day functional outcomes.⁷⁶⁻⁷⁹ However, 3 of these are single-center studies and had smaller sample sizes.^{76,78,79} A recent meta-analysis of 7 RCTs with a total of 980 patients (487 general anesthesia, 493 non-general anesthesia) showed that general anesthesia was associated with higher rates of recanalization, resulting in 8.4% absolute improvement in the rate of good functional outcome.⁸⁰ The current AHA/ASA guidelines recommend technique selection based on individualized assessment, clinical characteristics, and technical performance of the procedure.⁵

Future Directions

Despite the advances, multiple aspects of stroke treatment should be further addressed. As discussed earlier, ongoing trials will further refine the role of EVT in large infarcts. An LVO may be seen in up to 28% of patients with AIS and an NIHSS score of ≤ 4 , and the best LVO treatment strategy in clinically mild stroke (NIHSS score of ≤ 5) is unclear. The Endovascular Therapy for Low NIHSS Ischemic Strokes (ENDOLOW, NCT04167527) and Minor Stroke Therapy Evaluation (MOSTE, NCT03796468) trials are currently underway to study this issue.

Similarly, treatment strategies in distal medium-vessel occlusions remain unclear. Medium vessels (defined as A2/A3 ACA, M2/M3 MCA, and P2/P3 PCA vessels) were generally excluded from prior EVT trials but can result in substantial neurologic deficits. Meta-analysis of the HERMES group data noted that patients with M2 MCA occlusions would benefit from EVT (adjusted OR = 2.39; 95% CI 1.08–5.28; $P = .03$), with the number needed to treat for 1 patient to achieve functional independence being 5.4.⁸¹ Rescue Thrombolysis for medium vessel occlusion (RESCUE-TNK, NCT05657470) is currently evaluating the role of intra-arterial TNK in both primary (de novo) and secondary (to EVT) medium-vessel occlusions. The effect of EVT in distal occlusions is also currently being evaluated in prospective studies: Distal Ischemic Stroke Treatment with Adjustable Low-profile Stentriever (DISTALS, NCT05152524) and Evaluation of Mechanical Thrombectomy in Acute Ischemic Stroke Related to a Distal Arterial Occlusion (DISCOUNT) (NCT05030142).

Patients who achieve reperfusion during the first attempt of EVT have improved functional outcomes, known as the first-pass effect. A recent meta-analysis comprising 2747 patients noted that patients with a first-pass effect had better outcomes and lower mortality, especially if they achieved mTICI 3 recanalization.⁸² This finding has increasingly led to comparison of catheter performance in terms of achieving a first-pass effect mTICI $\geq 2b$.⁵¹ The use of balloon-guided catheters during EVT is also being explored to reduce the chances of clot fragmentation and distal embolization.⁸³

In terms of thrombolytic therapies, the Norwegian Tenecteplase Stroke Trial 2 (NOR-TEST 2, NCT03854500) is evaluating TNK within 4.5 hours of stroke onset. The Tenecteplase in Stroke Patients Between 4.5 and 24 Hours (TIMELESS, NCT03785678) study is a

Phase III trial evaluating TNK in the late-therapy time window, while Randomization to Extend Stroke Intravenous Thrombolysis In Evolving Non-Large Vessel Occlusion With TNK [RESILIENT EXTEND-IV, NCT05199662] is assessing TNK in patients with AIS without LVO within the 4.5- to 12-hour window. The Extending the Time Window for Tenecteplase by Effective Reperfusion in Patients With Large Vessel Occlusion (ETERNAL-LVO, NCT04454788) is similarly evaluating the role of TNK in EVT-eligible patients presenting within 24 hours, while the Extending the Time Window for Tenecteplase by Recanalization of Basilar Artery Occlusion in Posterior Circulation Stroke (POST-ETERNAL, NCT05105633) trial is evaluating the same for PCS.

Finally, even though no neuroprotective agents are currently approved by the US FDA, there is increasing focus on both pharmacologic and nonpharmacologic therapies, which reduce excitotoxicity, oxidative stress, inflammation, or cellular apoptosis in AIS. Initial studies using uric acid and nerinetide have shown improved neuroprotection, especially in patients undergoing EVT. Multiple prospective trials are ongoing to further identify and refine the role of neuroprotective agents in AIS.⁸⁴

CONCLUSIONS

The past decade has seen a paradigm shift in the management of AIS. These trends will likely continue, and ongoing trials are expected to further refine AIS care, with likely a much more nuanced and granular approach in individual cases. The radiologist will need to stay abreast of these developments to provide a meaningful contribution to patient care and remain an important part of the care team.

Disclosure forms provided by the authors are available with the full text and PDF of this article at www.ajnr.org.

REFERENCES

- Virani SS, Alonso A, Aparicio HJ, et al; American Heart Association Council on Epidemiology and Prevention Statistics Committee and Stroke Statistics Subcommittee. **Heart Disease and Stroke Statistics-2021 Update: a report from the American Heart Association.** *Circulation* 2021;143:e254–43 CrossRef Medline
- Broderick JP, Adeoye O, Elm J. **Evolution of the modified Rankin scale and its use in future stroke trials.** *Stroke* 2017;48:2007–12 CrossRef Medline
- Banks JL, Marotta CA. **Outcomes validity and reliability of the modified Rankin scale: implications for stroke clinical trials: a literature review and synthesis.** *Stroke* 2007;38:1091–96 CrossRef Medline
- Smith EE, Kent DM, Bulsara KR, et al; American Heart Association Stroke Council. **Accuracy of prediction instruments for diagnosing large vessel occlusion in individuals with suspected stroke: a systematic review for the 2018 Guidelines for the Early Management of Patients With Acute Ischemic Stroke.** *Stroke* 2018;49:e111–22 CrossRef Medline
- Powers WJ, Rabinstein AA, Ackerson T, et al. **Guidelines for the Early Management of Patients With Acute Ischemic Stroke: 2019 Update to the 2018 Guidelines for the Early Management of Acute Ischemic Stroke—A Guideline for Healthcare Professionals from the American Heart Association/American Stroke Association.** *Stroke* 2019;50:e344–418 CrossRef Medline
- Zaidat OO, Yoo AJ, Khatri P, et al; STIR Thrombolysis in Cerebral Infarction (TICI) Task Force. **Recommendations on angiographic**

- revascularization grading standards for acute ischemic stroke: a consensus statement. *Stroke* 2013;44:2650–63 CrossRef Medline
7. Liebeskind DS, Bracard S, Guillemin F, et al; HERMES Collaborators. eTICI reperfusion: defining success in endovascular stroke therapy. *J Neurointerv Surg* 2019;11:433–38 CrossRef Medline
 8. National Institute of Neurological Disorders and Stroke rt-PA Stroke Study Group. Tissue plasminogen activator for acute ischemic stroke. *N Engl J Med* 1995;333:1581–87 CrossRef Medline
 9. Hacke W, Kaste M, Bluhmki E, et al; ECASS Investigators. Thrombolysis with alteplase 3 to 4.5 hours after acute ischemic stroke. *N Engl J Med* 2008;359:1317–29 CrossRef Medline
 10. Hollist M, Morgan L, Cabatbat R, et al. Acute stroke management: overview and recent updates. *Aging Dis* 2021;12:1000–09 CrossRef Medline
 11. Ma H, Campbell BC, Parsons MW, et al; EXTEND Investigators. Thrombolysis guided by perfusion imaging up to 9 hours after onset of stroke. *N Engl J Med* 2019;380:1795–803 CrossRef Medline
 12. Schwamm LH, Wu O, Song SS, et al; MR WITNESS Investigators. Intravenous thrombolysis in unwitnessed stroke onset: MR WITNESS trial results. *Ann Neurol* 2018;83:980–93 CrossRef Medline
 13. Thomalla G, Simonsen CZ, Boutitie F, et al; WAKE-UP Investigators. MRI-guided thrombolysis for stroke with unknown time of onset. *N Engl J Med* 2018;379:611–22 CrossRef Medline
 14. Campbell BC, Mitchell PJ, Churilov L, et al; EXTEND-IA TNK Investigators. Tenecteplase versus alteplase before endovascular thrombectomy (EXTEND-IA TNK): a multicenter, randomized, controlled study. *Int J Stroke* 2018;13:328–34 CrossRef Medline
 15. Menon BK, Buck BH, Singh N, et al; AcT Trial Investigators. Intravenous tenecteplase compared with alteplase for acute ischaemic stroke in Canada (AcT): a pragmatic, multicentre, open-label, registry-linked, randomised, controlled, non-inferiority trial. *Lancet* 2022;400:161–69 CrossRef Medline
 16. Wang Y, Li S, Pan Y, et al; TRACE-2 Investigators. Tenecteplase versus Alteplase in Acute Ischaemic Cerebrovascular Events (TRACE-2): a Phase 3, multicentre, open-label, randomised controlled, non-inferiority trial. *Lancet* 2023;401:645–54 CrossRef Medline
 17. Berkhemer OA, Fransen PS, Beumer D, et al; MR CLEAN Investigators. A randomized trial of intraarterial treatment for acute ischemic stroke. *N Engl J Med* 2015;372:11–20 CrossRef Medline
 18. Goyal M, Demchuk AM, Menon BK, et al; ESCAPE Trial Investigators. Randomized assessment of rapid endovascular treatment of ischemic stroke. *N Engl J Med* 2015;372:1019–30 CrossRef Medline
 19. Bracard S, Ducrocq X, Mas JL, et al; THRACE Investigators. Mechanical thrombectomy after intravenous alteplase versus alteplase alone after stroke (THRACE): a randomised controlled trial. *Lancet Neurol* 2016;15:1138–47 CrossRef Medline
 20. Campbell BC, Mitchell PJ, Kleinig TJ, et al; EXTEND-IA Investigators. Endovascular therapy for ischemic stroke with perfusion-imaging selection. *N Engl J Med* 2015;372:1009–18 CrossRef Medline
 21. Jovin TG, Chamorro A, Cobo E, et al; REVASCAT Trial Investigators. Thrombectomy within 8 hours after symptom onset in ischemic stroke. *N Engl J Med* 2015;372:2296–306 CrossRef Medline
 22. Saver JL, Goyal M, Bonafe A, et al; SWIFT PRIME Investigators. Stent-retriever thrombectomy after intravenous t-PA vs. t-PA alone in stroke. *N Engl J Med* 2015;372:2285–95 CrossRef Medline
 23. Saver JL, Goyal M, van der Lugt A, et al; HERMES Collaborators. Time to treatment with endovascular thrombectomy and outcomes from ischemic stroke: a meta-analysis. *JAMA* 2016;316:1279–88 CrossRef Medline
 24. Goyal M, Menon BK, van Zwam WH, et al; HERMES Collaborators. Endovascular thrombectomy after large-vessel ischaemic stroke: a meta-analysis of individual patient data from five randomised trials. *Lancet* 2016;387:1723–31 CrossRef Medline
 25. Albers GW, Marks MP, Kemp S, et al; DEFUSE 3 Investigators. Thrombectomy for stroke at 6 to 16 hours with selection by perfusion imaging. *N Engl J Med* 2018;378:708–18 CrossRef Medline
 26. Nogueira RG, Jadhav AP, Haussen DC, et al. DAWN Trial Investigators. Thrombectomy 6 to 24 hours after stroke with a mismatch between deficit and infarct. *N Engl J Med* 2018;378:11–21 CrossRef Medline
 27. Yang P, Zhang Y, Zhang L, et al; DIRECT-MT Investigators. Endovascular thrombectomy with or without intravenous alteplase in acute stroke. *N Engl J Med* 2020;382:1981–93 CrossRef Medline
 28. Zi W, Qiu Z, Li F, et al; DEVT Trial Investigators. Effect of endovascular treatment alone vs intravenous alteplase plus endovascular treatment on functional independence in patients with acute ischemic stroke: the DEVT randomized clinical trial. *JAMA* 2021;325:234–43 CrossRef Medline
 29. Fischer U, Kaesmacher J, Strbian D, et al; SWIFT DIRECT Collaborators. Thrombectomy alone versus intravenous alteplase plus thrombectomy in patients with stroke: an open-label, blinded-outcome, randomised non-inferiority trial. *Lancet* 2022;400:104–15 CrossRef Medline
 30. Suzuki K, Matsumaru Y, Takeuchi M, et al; SKIP Study Investigators. Effect of mechanical thrombectomy without vs with intravenous thrombolysis on functional outcome among patients with acute ischemic stroke: the SKIP randomized clinical trial. *JAMA* 2021;325:244–53 CrossRef Medline
 31. LeCouffe NE, Kappelhof M, Treurniet KM, et al; MR CLEAN-NO IV Investigators. A randomized trial of intravenous alteplase before endovascular treatment for stroke. *N Engl J Med* 2021;385:1833–44 CrossRef Medline
 32. Mitchell PJ, Yan B, Churilov L, et al; DIRECT-SAFE Investigators. DIRECT-SAFE: a randomized controlled trial of DIRECT endovascular clot retrieval versus standard bridging therapy. *J Stroke* 2022;24:57–64 CrossRef Medline
 33. Yoshimura S, Sakai N, Yamagami H, et al. Endovascular therapy for acute stroke with a large ischemic region. *N Engl J Med* 2022;386:1303–13 CrossRef Medline
 34. Uchida K, Shindo S, Yoshimura S, et al; RESCUE-Japan LIMIT Investigators. Association between Alberta Stroke Program Early Computed Tomography Score and efficacy and safety outcomes with endovascular therapy in patients with stroke from large-vessel occlusion: a secondary analysis of the Recovery by Endovascular Salvage for Cerebral Ultra-acute Embolism-Japan Large Ischemic Core Trial (RESCUE-Japan LIMIT). *JAMA Neurol* 2022;79:1260–66 CrossRef Medline
 35. Huo X, Ma G, Tong X, et al; ANGEL-ASPECT Investigators. Trial of endovascular therapy for acute ischemic stroke with large infarct. *N Engl J Med* 2023;388:1272–83 CrossRef Medline
 36. Sarraj A, Hassan AE, Abraham MG, et al; SELECT2 Investigators. Trial of endovascular thrombectomy for large ischemic strokes. *N Engl J Med* 2023;388:1259–71 CrossRef Medline
 37. Ren Z, Huo X, Kumar J, et al. Review of current large core volume stroke thrombectomy clinical trials: controversies and progress. *Stroke Vasc Interv Neurol* 2022;2:e000330 CrossRef
 38. Marko M, Cimflova P, Poppe AY, et al; ESCAPE-NA1 investigators. Management and outcome of patients with acute ischemic stroke and tandem carotid occlusion in the ESCAPE-NA1 trial. *J Neurointerv Surg* 2022;14:429–33 CrossRef Medline
 39. Dufort G, Chen BY, Jacquin G, et al. Acute carotid stenting in patients undergoing thrombectomy: a systematic review and meta-analysis. *J Neurointerv Surg* 2021;13:141–45 CrossRef Medline
 40. Huo X, Gao F, Ma N, et al; ANGEL Investigators. Characteristic and prognosis of acute large vessel occlusion in anterior and posterior circulation after endovascular treatment: the ANGEL registry real world experience. *J Thromb Thrombolysis* 2020;49:527–32 CrossRef Medline
 41. Tao C, Nogueira RG, Zhu Y, et al; ATTENTION Investigators. Trial of endovascular treatment of acute basilar-artery occlusion. *N Engl J Med* 2022;387:1361–72 CrossRef Medline
 42. Pirson FAV, Boedt N, Brouwer J, et al; MR CLEAN Registry Investigators. Endovascular treatment for posterior circulation stroke in routine clinical practice: results of the multicenter randomized clinical trial of endovascular treatment for acute ischemic stroke in the Netherlands Registry. *Stroke* 2022;53:758–68 CrossRef Medline

43. Pirson F, Boodt N, Brouwer J, et al; MR CLEAN Registry Investigators. **Etiology of large vessel occlusion posterior circulation stroke: results of the MR CLEAN Registry.** *Stroke* 2022;53:2468–77 CrossRef Medline
44. Liu X, Dai Q, Ye R, et al; BEST Trial Investigators. **Endovascular Treatment versus Standard Medical Treatment for Vertebrobasilar Artery Occlusion (BEST): an open-label, randomised controlled trial.** *Lancet Neurol* 2020;19:115–22 CrossRef Medline
45. Langezaal LCM, van der Hoeven E, Mont'Alverne FJ, et al; BASICS Study Group. **Endovascular therapy for stroke due to basilar-artery occlusion.** *N Engl J Med* 2021;384:1910–20 CrossRef Medline
46. Jovin TG, Li C, Wu L, et al; BAOCHE Investigators. **Trial of thrombectomy 6 to 24 hours after stroke due to basilar-artery occlusion.** *N Engl J Med* 2022;387:1373–84 CrossRef Medline
47. Smith WS, Sung G, Starkman S, et al; MERCI Trial Investigators. **Safety and efficacy of mechanical embolectomy in acute ischemic stroke: results of the MERCI trial.** *Stroke* 2005;36:1432–38 CrossRef Medline
48. Penumbra Pivotal Stroke Trial Investigators. **The Penumbra Pivotal Stroke Trial: safety and effectiveness of a new generation of mechanical devices for clot removal in intracranial large vessel occlusive disease.** *Stroke* 2009;40:2761–68 CrossRef Medline
49. Ciccone A, Valvassori L, Nichelatti M, et al; SYNTHESIS Expansion Investigators. **Endovascular treatment for acute ischemic stroke.** *N Engl J Med* 2013;368:904–13 CrossRef Medline
50. Kidwell CS, Jahan R, Gornbein J, et al; MR RESCUE Investigators. **A trial of imaging selection and endovascular treatment for ischemic stroke.** *N Engl J Med* 2013;368:914–23 CrossRef Medline
51. Yeo LL, Jing M, Bhogal P, et al. **Evidence-based updates to thrombectomy: targets, new techniques, and devices.** *Front Neurol* 2021;12:712527 CrossRef Medline
52. Lapergue B, Blanc R, Gory B, et al; ASTER Trial Investigators. **Effect of endovascular contact aspiration vs stent retriever on revascularization in patients with acute ischemic stroke and large vessel occlusion: the ASTER randomized clinical trial.** *JAMA* 2017;318:443–52 CrossRef Medline
53. Turk AS 3rd, Siddiqui A, Fifi JT, et al. **Aspiration Thrombectomy versus Stent Retriever Thrombectomy as First-Line Approach for Large Vessel Occlusion (COMPASS): a multicentre, randomised, open label, blinded outcome, non-inferiority trial.** *Lancet* 2019;393:998–1008 CrossRef Medline
54. Gao P, Wang T, Wang D, et al; CASSISS Trial Investigators. **Effect of stenting plus medical therapy vs medical therapy alone on risk of stroke and death in patients with symptomatic intracranial stenosis: the CASSISS randomized clinical trial.** *JAMA* 2022;328:534–42 CrossRef Medline
55. Barnard ZR, Alexander MJ. **Update in the treatment of intracranial atherosclerotic disease.** *Stroke Vasc Neurol* 2020;5:59–64 CrossRef Medline
56. Chimowitz MI, Lynn MJ, Derdeyn CP, et al; SAMMPRIS Trial Investigators. **Stenting versus aggressive medical therapy for intracranial arterial stenosis.** *N Engl J Med* 2011;365:993–1003 CrossRef Medline
57. Zaidat OO, Fitzsimmons BF, Woodward BK; et al; VISSIT Trial Investigators. **Effect of a balloon-expandable intracranial stent vs medical therapy on risk of stroke in patients with symptomatic intracranial stenosis: the VISSIT randomized clinical trial.** *JAMA* 2015;313:1240–48 CrossRef Medline
58. Alexander MJ, Zauner A, Chaloupka JC, et al; WEAVE Trial Sites and Interventionalists. **WEAVE trial: final results in 152 on-label patients.** *Stroke* 2019;50:889–94 CrossRef Medline
59. Imamura H, Sakai N, Sakai C, et al. **Japanese postmarket surveillance of percutaneous transluminal angioplasty and Wingspan stenting for intracranial atherosclerotic disease.** *World Neurosurg* 2023 Jan 28. [Epub ahead of print] CrossRef Medline
60. Provost C, Soudant M, Legrand L, et al. **Magnetic resonance imaging or computed tomography before treatment in acute ischemic stroke.** *Stroke* 2019;50:659–64 CrossRef Medline
61. Boodt N, Compagne KJ, Dutra BG, et al; Coinvestigators MR CLEAN Registry. **Stroke etiology and thrombus computed tomography characteristics in patients with acute ischemic stroke: a MR CLEAN Registry substudy.** *Stroke* 2020;51:1727–35 CrossRef Medline
62. Zhou Y, Jing Y, Ospel J, et al; DIRECT-MT Investigators. **CT hyperdense artery sign and the effect of alteplase in endovascular thrombectomy after acute stroke.** *Radiology* 2022;305:410–18 CrossRef Medline
63. Bourcier R, Hassen WB, Soize S, et al. **Susceptibility vessel sign on MRI predicts better clinical outcome in patients with anterior circulation acute stroke treated with stent retriever as first-line strategy.** *J Neurointerv Surg* 2019;11:328–33 CrossRef Medline
64. Riou-Comte N, Gory B, Soudant M, et al; THRACE Investigators. **Clinical imaging factors of excellent outcome after thrombolysis in large-vessel stroke: a THRACE subgroup analysis.** *Stroke Vasc Neurol* 2021;6:631–39 CrossRef Medline
65. Yaghi S, Raz E, Dehkharghani S, et al. **Penumbra consumption rates based on time-to-maximum delay and reperfusion status: a post hoc analysis of the DEFUSE 3 trial.** *Stroke* 2021;52:2690–93 CrossRef Medline
66. Rao VL, Mlynash M, Christensen S, et al. **Collateral status contributes to differences between observed and predicted 24-h infarct volumes in DEFUSE 3.** *J Cereb Blood Flow Metab* 2020;40:1966–74 CrossRef Medline
67. Ospel JM, Menon BK, Qiu W, et al; ESCAPE-NA1 Investigators. **A detailed analysis of infarct patterns and volumes at 24-hour non-contrast CT and diffusion-weighted MRI in acute ischemic stroke due to large vessel occlusion: results from the ESCAPE-NA1 trial.** *Radiology* 2021;300:152–59 CrossRef Medline
68. van Kranendonk KR, Treurniet KM, Boers AM, et al; MR CLEAN Investigators. **Hemorrhagic transformation is associated with poor functional outcome in patients with acute ischemic stroke due to a large vessel occlusion.** *J Neurointerv Surg* 2019;11:464–68 CrossRef Medline
69. Xie Y, Oppenheim C, Guillemin F, et al; THRACE Investigators. **Pretreatment lesional volume impacts clinical outcome and thrombectomy efficacy.** *Ann Neurol* 2018;83:178–85 CrossRef Medline
70. Pérez de la Ossa N, Abilleira S, Jovin TG, et al; RACECAT Trial Investigators. **Effect of direct transportation to thrombectomy-capable center vs local stroke center on neurological outcomes in patients with suspected large-vessel occlusion stroke in nonurban areas: the RACECAT randomized clinical trial.** *JAMA* 2022;327:1782–94 CrossRef Medline
71. Saver JL, Fonarow GC, Smith EE, et al. **Time to treatment with intravenous tissue plasminogen activator and outcome from acute ischemic stroke.** *JAMA* 2013;309:2480–88 CrossRef Medline
72. Xian Y, Xu H, Lytle B, et al. **Use of strategies to improve door-to-needle times with tissue-type plasminogen activator in acute ischemic stroke in clinical practice: findings from target: stroke.** *Circ Cardiovasc Qual Outcomes* 2017;10:e003227 CrossRef Medline
73. Li W, Qi Z, Ma Q, et al. **Normobaric hyperoxia combined with endovascular treatment for patients with acute ischemic stroke: a randomized controlled clinical trial.** *Neurology* 2022;99:e824–34 CrossRef Medline
74. Mazighi M, Richard S, Lapergue B, et al; BP-TARGET Investigators. **Safety and efficacy of intensive blood pressure lowering after successful endovascular therapy in acute ischaemic stroke (BP-TARGET): a multicentre, open-label, randomised controlled trial.** *Lancet Neurol* 2021;20:265–74 CrossRef Medline
75. Yang P, Song L, Zhang Y, et al; ENCHANTED2/MT Investigators. **Intensive blood pressure control after endovascular thrombectomy for acute ischaemic stroke (ENCHANTED2/MT): a multicentre, open-label, blinded-endpoint, randomised controlled trial.** *Lancet* 2022;400:1585–96 CrossRef Medline
76. Lowhagen Henden P, Rentzos A, Karlsson JE, et al. **General anesthesia versus conscious sedation for endovascular treatment of acute ischemic stroke: the AnStroke trial (Anesthesia During Stroke).** *Stroke* 2017;48:1601–07 CrossRef Medline
77. Maurice A, Eugène F, Ronzière T, et al; GASS (General Anesthesia versus Sedation for Acute Stroke Treatment) Study Group and the

- French Society of Anesthesiologists (SFAR) Research Network. **General anesthesia versus sedation, both with hemodynamic control, during intraarterial treatment for stroke: the GASS randomized trial.** *Anesthesiology* 2022;136:567–76 CrossRef Medline
78. Schonenberger S, Uhlmann L, Hacke W, et al. **Effect of conscious sedation vs general anesthesia on early neurological improvement among patients with ischemic stroke undergoing endovascular thrombectomy: a randomized clinical trial.** *JAMA* 2016;316:1986–96 CrossRef Medline
79. Simonsen CZ, Yoo AJ, Sørensen LH, et al. **Effect of general anesthesia and conscious sedation during endovascular therapy on infarct growth and clinical outcomes in acute ischemic stroke: a randomized clinical trial.** *JAMA Neurol* 2018;75:470–77 CrossRef Medline
80. Campbell D, Butler E, Campbell RB, et al. **General anesthesia compared to non-GA in endovascular thrombectomy for ischemic stroke: a systematic review and meta-analysis of randomized controlled trials.** *Neurology* 2023;100:e1655–63 CrossRef Medline
81. Menon BK, Hill MD, Davalos A, et al. **Efficacy of endovascular thrombectomy in patients with M2 segment middle cerebral artery occlusions: meta-analysis of data from the HERMES Collaboration.** *J Neurointerv Surg* 2019;11:1065–69 CrossRef Medline
82. Rizvi A, Seyedsaadat SM, Murad MH, et al. **Redefining ‘success’: a systematic review and meta-analysis comparing outcomes between incomplete and complete revascularization.** *J Neurointerv Surg* 2019;11:9–13 CrossRef Medline
83. Goyal M, Kappelhof M, Ospel JM, et al. **Balloon guide catheters: use, reject, or randomize?** *Neuroradiology* 2021;63:1179–83 CrossRef Medline
84. Vos EM, Geraedts VJ, van der Lugt A, et al. **Systematic review: combining neuroprotection with reperfusion in acute ischemic stroke.** *Front Neurol* 2022;13:840892 CrossRef Medline

Realistic Productivity in Academic Neuroradiology: A National Survey of Neuroradiology Division Chiefs

M. Wintermark, V. Gupta, C. Hess, R. Lee, J. Maldjian, S. Mukherjee, S. Mukherji, D. Seidenwurm, and T. Kennedy

The productivity of academic neuroradiologists is typically measured by using relative value units (RVUs). RVUs are the basic component of the resource-based relative value scale, a methodology used by the Centers for Medicare & Medicaid Services (CMS) to determine the payment of physicians. RVUs define the value of a service or procedure relative to all clinical services and procedures. This measure of value is based on the time and intensity of physicians' work, expertise, as well as clinical and nonclinical resources required to deliver the health care service to patients. RVUs ultimately determine the compensation of physicians when the conversion factor, dollars per RVU, is applied to the total RVU. Private payer contracts are typically negotiated as a percentage of the CMS payment; therefore, RVUs serve as the base payment for all physicians' payment.

Organizations such as the Association of Administrators in Academic Radiology (AAARAD) and the Society of Chairs of Academic Radiology Departments maintain annual statistics about the clinical productivity of academic radiologists across North America. These statistics include the mean, median, and percentile distribution of RVUs, stratified by the radiology subspecialty and rank.¹ During the past decade, the median RVU productivity by academic neuroradiologists has grown considerably. This growth comes as the result of academic departments increasing RVU targets in step with these national norms to the 60th, 70th, and 75th percentiles of the AAARAD statistics as their goal each year so that the 60th, 70th, and 75th percentiles of 1 year become the new median of the following year.

The median RVU productivity for such statistics has reached levels that are likely not sustainable. They may jeopardize patient safety, as illustrated by a recent study showing that errors were associated with higher-volume shifts.² Also, these excessive targets compromise other crucial missions at academic institutions, such as education and research.

Survey

With such background in mind, we conducted a Web-based survey of the academic neuroradiology division chiefs listed by the American Society of Neuroradiology. We sent e-mail correspondence to all academic neuroradiology division chiefs in the United States, discussing the intent of the project and encouraging participation, with 3 follow-up e-mails for nonrespondents.

The responding division chiefs (Figure) reported a median of 9 faculty (interquartile range, 6–13; range, 3–60), for a total of 563 neuroradiology faculty across these 42 sites. At the time of the survey (October 2022), they were recruiting for a median of 1 open position (interquartile range, 0–2, range, 0–5), for a total of 68 open positions across these 42 sites. Of interest, there was no correlation between the number of open positions and the size of the neuroradiology division.

The 42 academic neuroradiology division chiefs reported that their faculty interprets imaging studies independently in 45% of the cases (median, 45% interquartile range, 27%–52%), with a junior trainee (first- or second-year resident) in 25% of the cases (median, 25% interquartile range, 15%–30%), and with a senior trainee (third- or fourth-year resident or fellow) in 30% of the cases (median, 30% interquartile range, 18%–50%).

On the basis of their daily expertise and experience, the 42 academic neuroradiology division chiefs were asked to estimate the number of cross-sectional studies (CT and MR imaging) a neuroradiology faculty member can reasonably and safely interpret in a regular full clinical day (excluding calls, evening coverage, and moonlighting work), considering the time taken for answering calls from technologists and consulting with clinicians. The median estimated number was 32 cross-sectional studies when reading independently (interquartile range, 23–36 studies), 25 when reading with a junior trainee (first- or second-year resident) (interquartile range, 19–30 studies), and 33 when reading with a senior trainee (third- or fourth-year resident or fellow) (interquartile range, 25–41 studies).

When asked about their division's current workload, 22% of the academic neuroradiology division chiefs thought that they were currently at capacity; 37%, that they were working above capacity; and 41%, that they were working well above capacity.

Detailed results can be found in the Online Supplemental Data.

Reflections

The median number of 32 cross-sectional studies on a standard clinical day should be considered with caution. There are many local factors that can influence the optimal number for any given academic practice. These factors include the technique-mix of cross-sectional imaging studies (a noncontrast head CT typically takes less time to interpret than a complex brain MR imaging with and without contrast, including advanced neuroimaging), the complexity of the pathology in the imaging studies (eg, an unremarkable spine MR imaging versus a complex postoperative neck cancer imaging study), as well as the number of comparison studies that need to be reviewed to provide an accurate interpretation, just to name a few. The median number of 32 is, however, helpful as a general target with appropriate adjustments to incorporate individual practice variations.

In addition, there are inherent differences among the workflows of academic neuroradiologists at different institutions, including for noninterpretive work. For example, expectations related to the protocoling of studies (preservice period of

Indicates article with online supplemental data.
<http://dx.doi.org/10.3174/ajnr.A7912>



FIGURE. Geographic location of the forty-two academic neuroradiology division chiefs responded to this survey.

radiologist work) and to multidisciplinary conference and tumor board preparations and presentations (postservice period of radiologist work) are often performed on nonclinical rotations.^{3,4} The addition of these noninterpretative tasks to the clinical workday may influence the radiologist's workload capacity for image interpretation.

Our survey indirectly addressed other critical missions of academic neuroradiology practices, including the time required for teaching trainees. Education is a critical mission for academic institutions but takes additional time and effort and should be factored into the overall expectations for clinical productivity.

CONCLUSIONS

Thirty-two represents a reasonable reference to guide the number of cross-sectional imaging studies (CT and MR imaging) that can be safely interpreted in a day by a typical academic neuroradiologist. This target may need to be adjusted on the basis of local practice patterns, case complexity, noninterpretative task expectations, and teaching requirements.

ACKNOWLEDGMENTS

The academic neuroradiology division chiefs of the following institutions responded to our survey:

- Baystate Medical Center/Baystate Health
- Boston Children's Hospital
- Boston Medical Center
- Cedars Sinai
- Duke University
- Emory University
- Harbor UCLA Medical Center
- Johns Hopkins University

- Loma Linda University Medical Center
- Mallinckrodt Institute of Radiology/Washington University in St. Louis
- Mayo Clinic Florida
- Mayo Clinic Rochester
- Medical College of Wisconsin
- Medical University of South Carolina
- Medstar Georgetown University Hospital
- Montefiore Medical Center/Albert Einstein College of Medicine
- Mount Sinai Hospital
- New York University Langone Medical Center
- Northwestern University
- Oregon Health & Science University
- Penn State Health Medical Center
- San Diego VA Healthcare System
- Stanford
- University Hospitals Case Western
- University of California Davis
- University of California Los Angeles
- University of California San Francisco
- University of California San Diego
- University of Cincinnati
- University of Colorado
- University of Florida Jacksonville
- University of Illinois at Chicago
- University of Iowa
- University of Maryland
- University of Miami
- University of Mississippi Medical Center
- University of Missouri
- University of Nebraska

- University of New Mexico
- University of North Carolina at Chapel Hill
- University of Rochester
- University of Texas MD Anderson Cancer Center
- University of Texas San Antonio
- University of Texas Southwestern Medical Center
- University of Utah
- University of Virginia
- Valleywise Health

Disclosure forms provided by the authors are available with the full text and PDF of this article at www.ajnr.org.

REFERENCES

1. Lu Y, Arenson RL. **The academic radiologist's clinical productivity: an update.** *Acad Radiol* 2005;12:1211–23 CrossRef Medline
2. Ivanovic V, Paydar A, Chang YM, et al. **Impact of shift volume on neuroradiology diagnostic errors at a large tertiary academic center.** *Acad Radiol* 2022 Sept 27. [Epub ahead of print] CrossRef Medline
3. Allen B Jr, Donovan WD, McGinty G, et al. **Professional component payment reductions for diagnostic imaging examinations when more than one service is rendered by the same provider in the same session: an analysis of relevant payment policy.** *J Am Coll Radiol* 2011;8:610–16 CrossRef Medline
4. Wintermark M, Zeineh M, Zaharchuk G, et al. **Non-relative value unit-generating activities represent one-fifth of academic neuroradiologist productivity.** *AJNR Am J Neuroradiol* 2016;37:1206–08 CrossRef Medline

Crowd-Sourced Deep Learning for Intracranial Hemorrhage Identification: Wisdom of Crowds or Laissez-Faire

E.I.S. Hofmeijer, C.O. Tan, F. van der Heijden, and R. Gupta



ABSTRACT

BACKGROUND AND PURPOSE: Researchers and clinical radiology practices are increasingly faced with the task of selecting the most accurate artificial intelligence tools from an ever-expanding range. In this study, we sought to test the utility of ensemble learning for determining the best combination from 70 models trained to identify intracranial hemorrhage. Furthermore, we investigated whether ensemble deployment is preferred to use of the single best model. It was hypothesized that any individual model in the ensemble would be outperformed by the ensemble.

MATERIALS AND METHODS: In this retrospective study, de-identified clinical head CT scans from 134 patients were included. Every section was annotated with “no-intracranial hemorrhage” or “intracranial hemorrhage,” and 70 convolutional neural networks were used for their identification. Four ensemble learning methods were researched, and their accuracies as well as receiver operating characteristic curves and the corresponding areas under the curve were compared with those of individual convolutional neural networks. The areas under the curve were compared for a statistical difference using a generalized U-statistic.

RESULTS: The individual convolutional neural networks had an average test accuracy of 67.8% (range, 59.4%–76.0%). Three ensemble learning methods outperformed this average test accuracy, but only one achieved an accuracy above the 95th percentile of the individual convolutional neural network accuracy distribution. Only 1 ensemble learning method achieved a similar area under the curve as the single best convolutional neural network (Δ area under the curve = 0.03; 95% CI, -0.01 – 0.06 ; $P = .17$).

CONCLUSIONS: None of the ensemble learning methods outperformed the accuracy of the single best convolutional neural network, at least in the context of intracranial hemorrhage detection.

ABBREVIATIONS: AUC = area under the curve; CNN = convolutional neural network; ICH = intracranial hemorrhage; SVM = support vector machine

As clinical support systems in radiology evolve, artificial intelligence has become prevalent for supporting myriad operations ranging from order entry, computer-aided diagnosis, clinical decision support, triage, to back-end analytics. With the development of new tools for design, implementation, and deployment of artificial intelligence-based systems, many in-

house support tools are more accessible to clinicians as well as researchers.¹ In fact, many radiology practices are continuously developing and deploying their internal artificial intelligence tools and support systems, and the use of these tools has increased exponentially.

At the same time, researchers and clinical radiology practices are increasingly faced with the task of selecting the most accurate tools from an ever-expanding range. With multiple methods available for the same task, combining the results of multiple tools presents an intriguing possibility. Such “crowd-sourcing” may be able to achieve better performance than any individual method. At the same time, there is the risk of corrupting the results of better-performing methods with those from weaker ones.

For example, while multiple artificial intelligence methods for segmentation of intracranial hemorrhage (ICH) have been very successful,^{2,3} those for identification and progression of ICH can have variable accuracy.^{4,5} Part of this variability derives from differences in the characteristics of the data used for training and the

Received December 15, 2022; accepted after revision May 7, 2023.

From the Department of Robotics and Mechatronics (E.I.S.H., C.O.T., F.v.d.H.), Faculty of Electrical Engineering, Mathematics and Computer Science, University of Twente, Enschede, the Netherlands; and Department of Radiology (C.O.T., R.G.), Massachusetts General Hospital, Boston, Massachusetts.

The position of E.I.S.H. is supported by a ZonMw Innovative Medical Devices Initiative (IMDI) subsidy for the B3CARE project (Dossier number: 10-10400-98-008). The funder had no role in study design, data collection and analysis, decision to publish, or preparation of the manuscript.

Please address correspondence to Elfi Hofmeijer, MSc, Robotics and Mechatronics, Faculty of Electrical Engineering, Mathematics & Computer Science, P.O. Box 217, 7500 AE Enschede, the Netherlands; e-mail: e.i.s.hofmeijer@utwente.nl



Indicates article with online supplemental data.

<http://dx.doi.org/10.3174/ajnr.A7902>

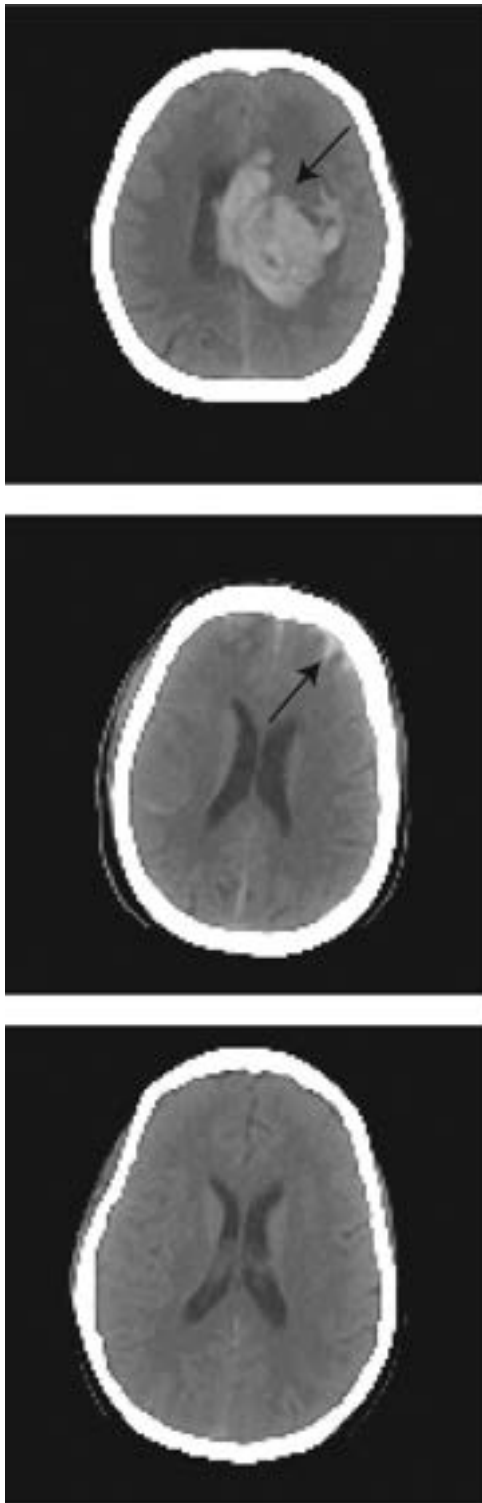


FIG 1. Head CT scan slices annotated as ICH (upper and middle, arrows) and annotated as no-ICH (bottom).

population encountered in practice. It is tempting to use the best-performing method, but best performance on one specific data set does not necessarily guarantee best performance on another.

Ensemble learning may mitigate this high variability by pooling multiple methods. Since its introduction >2 decades ago,^{6,7} ensemble learning has garnered substantial attention as a tool for improving the performance, accuracy, and robustness of existing

medical image-interpretation methods.⁸ It relies on a meta-algorithmic technique wherein multiple machine learning methods are trained individually and aggregated together. This approach has been successfully applied to multiple medical problems, including identification of lung cancer cells,⁹ colon polyp detection,¹⁰ automated classification of pulmonary bronchovascular anatomy in CT scans,¹¹ and the differential diagnosis of focal liver lesions detected on CT scans.¹²

In this study, we sought to test the utility of ensemble learning for determining the best combination of models from a set of 70 models that were individually trained to identify ICH (in all intracranial compartments). Furthermore, we investigated whether ensemble deployment is preferred over the use of the single best model. We tested the hypothesis that an ensemble of different models, developed using a single training set, will outperform each individual model in the ensemble.

MATERIALS AND METHODS

Data

We used a retrospective data set of de-identified clinical head CT scans from 134 unique patients treated at the Massachusetts General Hospital (institutional review board protocol 2015P000607). Written consent was not required by the institutional review board, given the retrospective use of existing clinically available data. The clinical images were acquired under standard clinical protocols in our tertiary care hospital from January 2015 to September 2018. Patients were excluded if external hardware was visible in the scan. Images were obtained (Somatom Force; Siemens) with an exposure time of 1000 ms and a section thickness of 1 mm. Each section in the axial plane in the CT data set was annotated by the treating neuroradiologists, not part of this study, as “no-ICH” or “ICH” (Fig 1), and annotations were verified by a neuroradiologist with 20 years of experience (R.G.). Images were then down-sampled to 128×128 pixels. The intensity of each image was clipped between -15 and 155 HU¹³ and rescaled to $[0, 1]$ for normalization. Consequently, slices were saved as TIFF images for further processing. Visible head support was removed from the images to prevent any bias due to extraneous input and to constrain the variability introduced by the head holder. Slices from the upper part and bottom of the scan FOV were excluded if they contained no or very limited parts of the head. These slices were either completely black or were at the very top of the head. The final data set included 4287 slices of which 34.4% were labeled as containing ICH.

The data set was split into 4 sets. Data sets 1 (48%) and 2 (12%) were used, respectively, as training and validation sets for the individual convolutional neural networks (CNNs). Data set 3 (28%) was used as a training set for the ensemble learning methods. All the remaining slices (data set 4; 12%, test set) were used to independently test the accuracy of individual CNNs as well as that of ensemble learning methods to evaluate the final performance. These steps are described in detail below.

All subsets were created at the patient level (as opposed to individual section level) to avoid superfluous correlation between images that belong to the same patient. Models were trained and their performance was evaluated on the section level, while grouping slices within each patient before partitioning to avoid bias due to overrepresentation of slices from a single patient. This

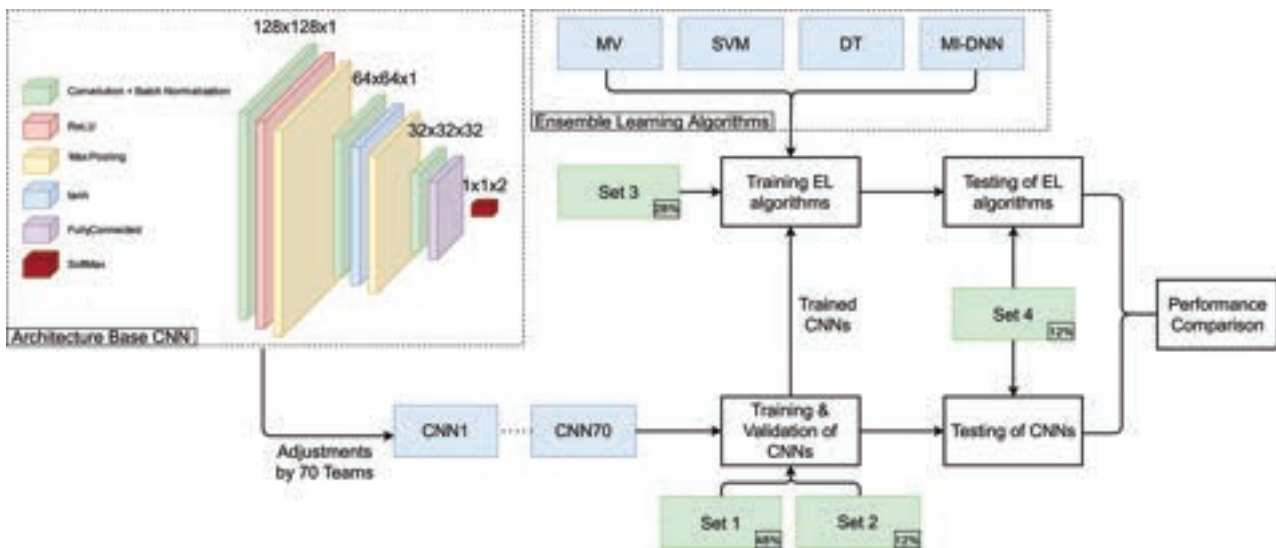


FIG 2. Flowchart of the study. The upper left corner shows the base architecture underlying all 70 CNNs, which was then structurally optimized by the 70 teams, resulting in 70 different CNNs. These were trained on data sets 1 and 2 and were used to train the 4 ensemble learning methods (MV indicates majority voting; DT, decision tree; MI-DNN, multi-input deep neural network; see text) on data set 3. Both the 70 trained CNNs and the trained ensemble methods were tested on data set 4. ReLU indicates rectified linear unit; tanh, hyperbolic tangent; EL, ensemble learning.

partitioning resulted in 61 cases and 2034 slices in data set 1, 16 cases and 516 slices in data set 2, 38 cases and 1208 slices in data set 3, and 17 cases and 529 slices in data set 4. The slices in each set included approximately the same proportion (~34%, varying between 32.9% and 38.8%) with ICH.

CNNs

CNNs to classify slices as ICH or no-ICH were implemented by graduate students as a part of a course taught by the authors. In 2 different courses, offered between 2019 and 2021, one hundred forty students with comparable experience and education were divided into teams of 2 students each. These teams developed 70 CNNs for detecting the presence or absence of ICH in each section. Each CNN was built on the same base architecture (Fig 2), designed to provide a minimum accuracy (~67%) and was modified, trained, and tested independently by each team on a virtual machine running on Amazon Web Services (<https://aws.amazon.com/>) using Matlab R2020a (MathWorks).

Each team customized the base architecture (Fig 2, left) to improve the accuracy on identical data sets. Customization included switching, adding, or removing layers and/or changing layer parameters. Parameters other than those associated with individual layers (ie, hyperparameters) were not varied so that only variations in architecture and random initialization impacted the performance during testing. Each team trained their CNN model on data set 1 for 50 epochs with a batch size of 32. They used stochastic gradient descent with a momentum optimizer with a learning rate of 0.001. Each CNN was then validated on data set 2. The final accuracy of each CNN was evaluated on data set 4 (Fig 2).

Ensemble Learning Method Training

We tested 4 different ensemble methods to explore whether the collective accuracy of 70 CNNs is higher than that of individual models. Ensemble learning methods included majority voting,

decision tree, support vector machine (SVM), and the multi-input deep neural network.

In majority voting, the final prediction of the ensemble was determined to be that class predicted by the majority of CNNs. For the remaining ensemble learning methods, the probability scores for the no-ICH class were collected from each of the 70 CNNs for every image in data set 3 and were used as input. In decision tree,¹⁴ a treelike model was created in which every end branch represents a decision. One final predicted class label will be given as output. Similarly, the SVM¹⁵ also returned 1 predicted class label, and training was performed with a linear kernel. The last ensemble learning method we tested was a multi-input deep neural network. Unlike the ensemble learning methods described earlier, the multi-input deep neural network requires an additional input, namely, a CT image. The multi-input deep neural network provides a probability score for the no ICH and ICH classifications as output. A more elaborate description of these ensemble learning methods can be found in the Online Supplemental Data.

Each ensemble learning method was trained on data set 3 and tested on data set 4 (Fig 2). Test accuracy was assessed via receiver operating characteristic curves and the corresponding areas under the curve (AUCs). The code for processing of data and training of CNNs and ensemble learning methods can be found on: https://github.com/UT-RAM-AIM/Ensemble_Learning.

Statistical Analysis

By design, each CNN had a different accuracy, resulting in a normal distribution of individual accuracies across 70 individual CNNs (see Results). Thus, the accuracy of each of the 4 ensemble learning methods was compared with the distribution of individual CNNs. For this comparison, an accuracy of >95% of the individual accuracy distribution, ie, larger than 2 SDs, was considered statistically significant. We also used the minimum redundancy maximum relevance algorithm to rank the 70 CNNs in a way that optimizes the amount of information each contained. This use allowed us to determine the CNN that provides the most

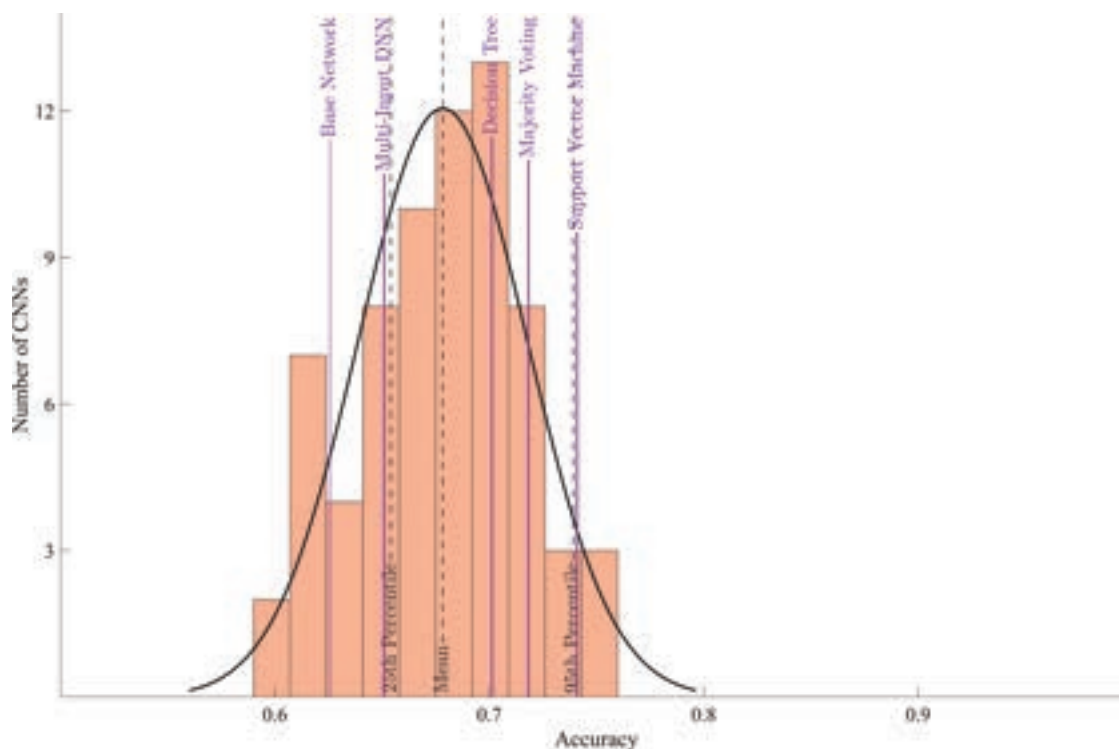


FIG 3. Accuracy of individual CNNs and ensemble learning methods. The purple solid vertical lines show the accuracy achieved by each ensemble learning method, and the black dashed vertical lines show means and lower and upper 95% confidence intervals for the distribution of accuracy of individual CNNs. Additionally, the first purple solid line indicates the accuracy of the base network. DNN indicates deep neural network.

information to predict the correct classification while having the least amount of redundant information.¹⁶ The individual CNN with the largest relevance was ranked first, and the previous steps were repeated to determine the individual CNN with the second highest relevance and least redundancy. This process was repeated until all individual CNNs were ranked. Thus, minimum redundancy maximum relevance provided insight into the added value that each CNN contributed to the ensemble. The difference between AUCs across different ensemble methods was tested for statistical significance using a generalized U-statistic, analogous to the Mann-Whitney statistic.¹⁷

RESULTS

The base architecture achieved an accuracy of 62.6% on data set 4. Individual CNNs had an average test accuracy of 67.8% with a range of 59.4% to 76.0% (Fig 3).

All except 1, the multi-input deep neural network, ensemble learning method outperformed the average accuracy of individual networks. However, of these, only SVM resulted in a statistically significant improvement in accuracy (ie, above the 95th percentile of the accuracy distribution from individual CNNs). None of the ensemble learning methods resulted in an accuracy greater than the individual CNN with highest accuracy (76.0%). The base architecture achieved an AUC of 0.66 (95% CI, 0.61–0.70). The AUCs attained by SVM, majority voting, and the single best CNN were, respectively, 0.79 (95% CI, 0.75–0.83), 0.79 (95% CI, 0.75–0.83), and 0.82 (95% CI, 0.78–0.85) (Fig 4).

The CNN with the best accuracy had a minimum redundancy maximum relevance score of 0.15, while the second one scored only 0.0006—that is, the relevance of the single best CNN model

contributed most to the ensemble learning model while the contribution of the rest was effectively zero. Additional exploration of the SVM method confirmed this observation. Training the SVM with only the network with the highest minimum redundancy maximum relevance score led to a test accuracy of 73.9%, while adding the second most relevant CNN increased the accuracy only by 0.2%–74.1%.

Statistical Analysis

The AUC for each ensemble model was statistically different from that of the base model (Fig 4; base versus decision tree, $\Delta\text{AUC} = 0.05$; 95% CI, -0.00008 – 0.11 ; $P = .05$; base versus majority voting, $\Delta\text{AUC} = 0.14$; 95% CI, 0.10 – 0.17 ; $P < .001$; base versus multi-input deep neural network, $\Delta\text{AUC} = 0.05$; 95% CI, 0.0004 – 0.09 ; $P = .05$; and base versus SVM, $\Delta\text{AUC} = 0.13$; 95% CI, 0.09 – 0.18 ; $P < .001$). The AUC for majority voting and SVM was statistically different from that of the CNN with average accuracy (average versus majority voting, $\Delta\text{AUC} = 0.07$; 95% CI, 0.04 – 0.10 ; $P < .001$; and average versus SVM, $\Delta\text{AUC} = 0.07$; 95% CI, 0.02 – 0.12 ; $P = .001$). All except the SVM method, including the CNN with average accuracy, were statistically different from the best-performing CNN (best CNN versus SVM, $\Delta\text{AUC} = 0.03$; 95% CI, -0.01 – 0.06 ; $P = .17$). Thus, the SVM method performed better than the base model and CNN with average accuracy, but comparable with the best-performing CNN.

DISCUSSION

As mentioned earlier, many artificial intelligence–based support tools are available for a wide variety of tasks, and researching radiology practices are faced with the task of how to develop the

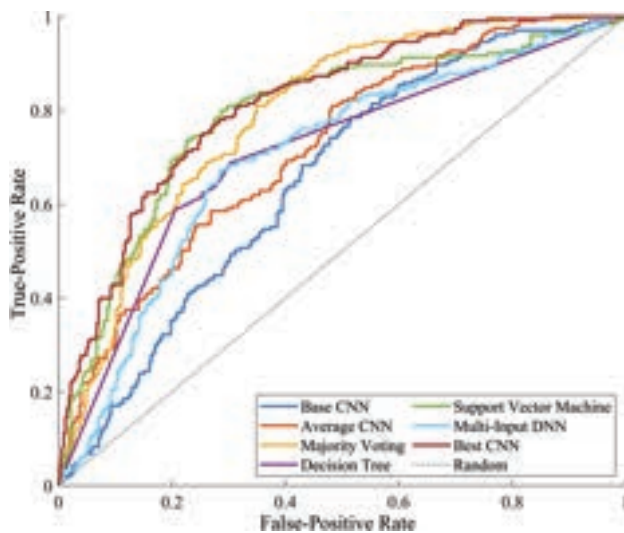


FIG 4. Receiver operating characteristic curves of the base network (dark blue) and the single best CNN (dark red), the curve of the average performing CNN (orange), and ensemble learning methods. The dashed black line indicates the performance of a random classifier (ie, accuracy of 50%). DNN indicates deep neural network.

most accurate ones for internal deployment. Ensemble learning was suggested to mitigate the high variability between multiple tools by pooling them. Our results affirm that all ensemble learning methods, with the notable exception of the multi-input deep neural network, outperform the average of different crowdsourced CNN models. Thus, the “wisdom of crowds” can exceed the average wisdom of individuals, at least in the context of ICH identification. It was surprising that only the SVM resulted in a statistically significant improvement in accuracy. Our most important finding, however, is that none of the other methods outperformed the CNN with the highest accuracy. Thus, our study provides several important lessons for crowdsourcing.

There was a relatively large variation in accuracy of individual models, ranging from ~ 0.60 to ~ 0.75 . However, this variability does not necessarily imply variation in information; in the context of our study, the magnitude of redundancy between the individual CNNs is high. In fact, our results show that individual models contribute little, if at all, to the overall performance of the ensemble beyond the model with the best accuracy. Uncorrelated models contribute to the ensemble most, because they can reflect features that other models do not. Consequently, a combination of different models that include different, uncorrelated features is likely to result in a better-performing ensemble.

We have adopted a “laissez-faire” approach (leaving people to take their own course, without interfering) as opposed to direct guidance. This indicates that a simple agglomeration of all models may be counterproductive and may drive the model toward the average accuracy. For example, the poorly performing models may corrupt the overall performance of the ensemble rather than collaborating to improve accuracy. In fact, it can be seen in the Results that the worst-performing single CNN achieves an accuracy (59%) lower than that of the base model (63%) accuracy. The effort of the team to improve the base architecture actually had the opposite effect in this CNN, and it most likely did not aid in improving ensemble performance. For ensemble learning over

multiple individually trained models, the assumption of holistic performance from crowdsourcing may not hold, unless some basic conditions about model independence can be ensured. To that end, analysis of an ensemble of models with a feature-selection algorithm, such as minimum redundancy maximum relevance, is an essential step toward finding the optimal model.

In general but more specifically for our use case ICH identification, the apparent impact of the size of the used data set is underestimated. If the data set is not large enough, the CNNs might be unable to learn different mappings, ie, the problem does not have many solutions. Ultimately, this issue also results in redundancy within the individual CNNs. Especially in our case, ICH comprises roughly 15%¹⁸ of

all cases of stroke and is, therefore, not as common in stroke. It can be difficult to acquire enough variation in a data set to allow the CNNs to learn different mappings. It may be more useful to examine safe ways of sharing data and consequently training 1 best tool with this method.

The relevant literature includes multiple studies using ensemble learning that found a positive effect from its application. For example, in their research into skin lesion classification from dermoscopic images, Shahin et al¹⁹ found that by averaging the predictions of the trained ResNet-50 (accuracy 87.1%) and Inception-V3 (accuracy 89.7%) models, their accuracy improved to 89.9%. Furthermore, Rajaraman et al²⁰ reported an accuracy increase by weighted averaging (90.97%) of their trained ResNet-18 (89.58%, highest), MobileNetV2, and DenseNet-121, to detect coronavirus disease 2019 (COVID-19) on chest radiographs. Most interesting, adding 2 more models to the ensemble in fact deteriorated the accuracy slightly. Most similar in approach to our case is the research by Zabihollahy et al,²¹ who trained 7 U-Nets for the localization of prostate peripheral tumors. The U-Nets differed in the depth and number of filters used in the convolution layers and were pooled using majority voting. Pooling 3 U-Nets was optimal, but this did not outperform the single best U-Net in terms of sensitivity or specificity. However, it did find the best trade-off between the two.

In contrast to the cases above, many more networks were pooled together in our study to improve the performance via ensemble learning methods. Additionally, our results did not show that an ensemble learning method outperformed the single best CNN model. However, as was also found in the research by Zabihollahy et al²¹ and Rajaraman et al,²⁰ using multiple models in the ensemble learning method does not necessarily increase the performance. While Zabihollahy et al found that the overall performance did not improve when adding >3 models, in our case that point was reached at 2. Combining fewer, but structurally different, models might be more efficient as is shown in Rajaraman et al.²⁰

CONCLUSIONS

Using ICH identification as a use case, we sought to identify the best combination from a set of 70 CNNs. Furthermore, we investigated whether an ensemble of the CNNs is preferred over using the single best CNN. It was hypothesized that an ensemble of different models, optimized from a base model, would outperform each individual CNN. While the SVM ensemble learning method did perform statistically better than the average CNN, its performance was comparable with that of the single best CNN. Even though this classroom experiment does not represent a real-world scenario when multiple artificial intelligence tools are at your disposal, it may be preferable to search for structurally different models and analyze them with a feature-selection algorithm before applying an ensemble learning method. Otherwise, a focus on the single best model may be more productive.

Disclosure forms provided by the authors are available with the full text and PDF of this article at www.ajnr.org.

REFERENCES

1. Korot E, Guan Z, Ferraz D, et al. **Code-free deep learning for multi-modality medical image classification.** *Nat Mach Intell* 2021;3:288–98 CrossRef
2. Wang T, Song N, Liu L, et al. **Efficiency of a deep learning-based artificial intelligence diagnostic system in spontaneous intracerebral hemorrhage volume measurement.** *BMC Med Imaging* 2021;21:125 CrossRef Medline
3. Sharrock MF, Mould WA, Ali H, et al. **3D deep neural network segmentation of intracerebral hemorrhage: development and validation for clinical trials.** *Neuroinformatics* 2021;19:403–15 CrossRef Medline
4. Teng L, Ren Q, Zhang P, et al. **Artificial intelligence can effectively predict early hematoma expansion of intracerebral hemorrhage analyzing noncontrast computed tomography image.** *Front Aging Neurosci* 2021;13:632138 CrossRef Medline
5. Dhar R, Falcone GJ, Chen Y, et al. **Deep learning for automated measurement of hemorrhage and perihematomal edema in supratentorial intracerebral hemorrhage.** *Stroke* 2020;51:648–51 CrossRef Medline
6. Hastie T, Tibshirani R, Friedman J. **Boosting and Additive Trees.** In: Hastie T, Tibshirani R, Friedman J. *The Elements of Statistical Learning: Data Mining, Inference, and Prediction.* Springer-Verlag; 2009:337–87
7. Hastie T, Tibshirani R, Friedman J. **Model Inference and Averaging.** In: Hastie T, Tibshirani R, Friedman J. *The Elements of Statistical Learning: Data Mining, Inference, and Prediction.* Springer-Verlag; 2009:261–94
8. Dietterich TG. **Ensemble Methods in Machine Learning.** In: Kittler J, Roli F, eds. *Multiple Classifier Systems.* Vol 12. Springer-Verlag; 2000;1857:1–15
9. Zhou ZH, Jiang Y, Yang YB, et al. **Lung cancer cell identification based on artificial neural network ensembles.** *Artif Intell Med* 2002;24:25–36 CrossRef Medline
10. Jerebko AK, Malley JD, Franaszek M, et al. **Support vector machines committee classification method for computer-aided polyp detection in CT colonography.** *Acad Radiol* 2005;12:479–86 CrossRef Medline
11. Ochs R, Goldin J, Abtin F, et al. **Automated classification of lung bronchovascular anatomy in CT using AdaBoost.** *Med Image Anal* 2007;11:315–24 CrossRef Medline
12. Mougialakou SG, Valavanis IK, Nikita A, et al. **Differential diagnosis of CT focal liver lesions using texture features, feature selection and ensemble driven classifiers.** *Artif Intell Med* 2007;41:25–37 CrossRef Medline
13. Abujudeh HH. *Emergency Radiology.* Oxford University Press; 2016
14. Swain PH, Hauska H. **The decision tree classifier: design and potential.** *IEEE Transactions on Geoscience Electronics* 1977;15:142–47 CrossRef
15. Vapnik VN. *The Nature of Statistical Learning Theory.* 2nd ed. Springer-Verlag; 2000
16. Ding C, Peng H. **Minimum redundancy feature selection from microarray gene expression data.** *J Bioinform Comput Biol* 2005;3:185–205 CrossRef Medline
17. DeLong ER, DeLong DM, Clarke-Pearson DL. **Comparing the areas under two or more correlated receiver operating characteristic curves: a nonparametric approach.** *Biometrics* 1988;44:837–45 CrossRef Medline
18. Andrews CM, Jauch EC, Hemphill JC, et al. **Emergency neurological life support: intracerebral hemorrhage.** *Neurocrit Care* 2012;17 (Suppl 1):37–46 CrossRef Medline
19. Shahin AH, Kamal A, Elattar MA. **Deep Ensemble Learning for Skin Lesion Classification from Dermoscopic Images.** In: *Proceedings of the 9th Cairo International Biomedical Engineering Conference (CIBEC),* Cairo, Egypt. December 20–22, 2018 CrossRef
20. Rajaraman S, Sornapudi S, Alderson PO, et al. **Analyzing inter-reader variability affecting deep ensemble learning for COVID-19 detection in chest radiographs.** *PLoS One* 2020;15:e0242301 CrossRef Medline
21. Zabihollahy F, Ukwatta E, Krishna S, et al. **Fully automated localization of prostate peripheral zone tumors on apparent diffusion coefficient map MR images using an ensemble learning method.** *J Magn Reson Imaging* 2020;51:1223–34 CrossRef Medline

Investigation of Brain Iron in Niemann-Pick Type C: A 7T Quantitative Susceptibility Mapping Study

P. Ravanfar, W.T. Syeda, R.J. Rushmore, B. Moffat, A.E. Lyall, A.H. Merritt, G.A. Devenyi, M.M. Chakravarty, P. Desmond, V.L. Cropley, N. Makris, M.E. Shenton, A.I. Bush, D. Velakoulis, C. Pantelis, and M. Walterfang



ABSTRACT

BACKGROUND AND PURPOSE: While brain iron dysregulation has been observed in several neurodegenerative disorders, its association with the progressive neurodegeneration in Niemann-Pick type C is unknown. Systemic iron abnormalities have been reported in patients with Niemann-Pick type C and in animal models of Niemann-Pick type C. In this study, we examined brain iron using quantitative susceptibility mapping MR imaging in individuals with Niemann-Pick type C compared with healthy controls.

MATERIALS AND METHODS: A cohort of 10 patients with adolescent- and adult-onset Niemann-Pick type C and 14 age- and sex-matched healthy controls underwent 7T brain MR imaging with T1 and quantitative susceptibility mapping acquisitions. A probing whole-brain voxelwise comparison of quantitative susceptibility mapping between groups was conducted. Mean quantitative susceptibility mapping in the ROIs (thalamus, hippocampus, putamen, caudate nucleus, and globus pallidus) was further compared. The correlations between regional volume, quantitative susceptibility mapping values, and clinical features, which included disease severity on the Iturriaga scale, cognitive function, and the Social and Occupational Functioning Assessment Scale, were explored as secondary analyses.

RESULTS: We observed lower volume in the thalamus and voxel clusters of higher quantitative susceptibility mapping in the pulvinar nuclei bilaterally in patients with Niemann-Pick type C compared with the control group. In patients with Niemann-Pick type C, higher quantitative susceptibility mapping in the pulvinar nucleus clusters correlated with lower volume of the thalamus on both sides. Moreover, higher quantitative susceptibility mapping in the right pulvinar cluster was associated with greater disease severity.

CONCLUSIONS: Our findings suggest iron deposition in the pulvinar nucleus in Niemann-Pick type C disease, which is associated with thalamic atrophy and disease severity. This preliminary evidence supports the link between iron and neurodegeneration in Niemann-Pick type C, in line with existing literature on other neurodegenerative disorders.

ABBREVIATIONS: ANTs = Advanced Normalization Tools; GRE = gradient recalled-echo; MABS = Multi-Atlas Brain Segmentation; NPC = Niemann-Pick type C; NUCOG = Neuropsychiatry Unit Cognitive Assessment Tool; QSM = quantitative susceptibility mapping; QSMART = Quantitative Susceptibility Mapping Artifact Reduction Technique; SOFAS = Social and Occupational Functioning Assessment Scale

Niemann-Pick type C (NPC) is a rare genetic lysosomal storage disease characterized by defective intracellular lipid transport mechanisms, which result in the intracellular accumulation of cholesterol and glycosphingolipids, primarily in the

brain, spleen, and liver. Brain involvement in NPC gives rise to numerous neurologic and neuropsychiatric presentations such as developmental delay, movement disorders, progressive cognitive decline, and psychosis.¹ Neuroimaging studies have reported

Received January 30, 2023; accepted after revision May 3.

From Melbourne Neuropsychiatry Centre (P.R., W.T.S., A.H.M., V.L.C., D.V., C.P., M.W.), the Department of Psychiatry, The University of Melbourne and Melbourne Health, Carlton South, Victoria, Australia; Psychiatry Neuroimaging Laboratory (P.R., R.J.R., A.E.L., N.M., M.E.S.), Department of Psychiatry (A.E.L., M.E.S.), and Department of Radiology (M.E.S.), Brigham and Women's Hospital and Harvard Medical School, Boston, Massachusetts; Center for Morphometric Analysis (R.J.R., N.M.), Massachusetts General Hospital, Charlestown, Massachusetts; Department of Anatomy and Neurobiology (R.J.R.), Boston University School of Medicine, Boston, Massachusetts; Melbourne Brain Centre Imaging Unit (B.M.), Department of Radiology, University of Melbourne, Parkville, Victoria, Australia; Department of Psychiatry (A.E.L., M.E.S.), Massachusetts General Hospital, Harvard Medical School, Boston, Massachusetts; Cerebral Imaging Center (G.A.D., M.M.C.), Douglas Research Centre, Montreal, Quebec, Canada; Departments of Psychiatry (G.A.D., M.M.C.) and Biomedical Engineering (M.M.C.), McGill University, Montreal, Quebec, Canada; Departments of Radiology (P.D.) and Neuropsychiatry (D.V., M.W.), Royal Melbourne Hospital, University of Melbourne, Parkville, Victoria, Australia; Melbourne Dementia

Research Centre (A.I.B.), and The Florey Institute of Neuroscience and Mental Health (C.P.), The University of Melbourne, Parkville, Victoria, Australia.

C. Pantelis and M. Walterfang are joint senior authors.

This research was enabled, in part, by support provided by Digital Research Alliance of Canada (<https://alliancecan.ca/en/services/advanced-research-computing>), the MASSIVE high performance computing facility (www.massive.org.au), National Imaging Facility of Australia (<https://anif.org.au/>), and Siemens Healthcare for providing the MP2RAGE sequence pre-release as part of the works in progress package (WIP).

The study was supported by a Royal Melbourne Hospital grant-in-aid (GIA-030H2016) to C.P., V.L.C., B.M., P.D.) and the National Health and Medical Research Council program grant to C.P. (ID: 1150083). V.L.C. is supported by a National Health and Medical Research Council Investigator Grant (1177370) and a University of Melbourne Dame Kate Campbell Fellowship. N.M. is supported by National Institute of Health grants: R01MH125860, R01MH112748, R01MH11917, K24MH116366, R01AG042512, R21DA042271. A.I.B. is supported by a National Health and Medical Research Council L3

marked volume loss in the cerebellum, thalamus, hippocampus, and basal ganglia in NPC. Widespread defects in myelination and reduced fractional anisotropy have also been observed in the brains of individuals with NPC.¹ The exact pathophysiologic processes through which the gene mutations in NPC lead to neurodegeneration are not as yet fully understood. Possible mechanisms that have been proposed include oxidative stress,²⁻⁴ neuroinflammation,⁵ and Tau pathology.⁶⁻⁸ A clearer understanding of the intrinsic drivers of neuropathology in NPC is needed to provide avenues for the development of therapeutic interventions.

One possible pathophysiologic mediator of brain changes in NPC is the dysregulation of iron. Iron is a crucial element in myelin synthesis, neurotransmitter production, and mitochondrial energy metabolism,⁹ in addition to serving a central role in neurodevelopment.¹⁰ Excessive iron, however, has been shown to be neurotoxic by contributing to oxidative stress and ferroptosis.^{11,12} In fact, a recent review summarized the existing neuroimaging evidence demonstrating iron accumulation in the specific brain regions that are most implicated in the pathology of neurodegenerative disorders (for a review see Ravanfar et al,¹³ in 2021). In NPC, there is evidence suggesting abnormal systemic and brain iron regulation. More specifically, histochemical examinations have identified diminished ferritin, the main iron storage unit, in various tissue types in individuals with NPC,^{14,15} which can lead to abnormal distribution of iron throughout the body. Furthermore, Hung et al¹⁶ reported a lower concentration of iron in the CSF in individuals with NPC and a trend toward increased iron content in postmortem cerebellar tissue in patients with NPC and healthy controls. Most important, in mouse models of NPC, Hung et al found an increased iron concentration in the brain along with decreased iron in the liver and spleen, suggesting that the abnormalities in systemic iron may involve the brain. However, due to the limitations in conducting human in vivo studies to examine iron in the central nervous system, the existing literature is limited in this area.

Technological advancements in neuroimaging, such as quantitative susceptibility mapping (QSM), have provided the tools for the in vivo evaluation of brain iron. Accordingly, in this study, we conducted an in vivo investigation of brain iron in individuals with NPC compared with healthy controls using QSM at ultra-high-field 7T MR imaging. Most important, this ultra-high-field imaging provides an increased contrast-to-noise ratio in QSM and enables the identification of smaller effect sizes compared with lower field strengths.¹⁷

Following from the available animal and human data, we hypothesized that individuals with NPC would evince altered levels of iron in key brain regions that undergo neurodegeneration in

NPC, specifically the thalamus, striatum, and the hippocampus.¹⁸ Furthermore, we hypothesized that such alterations would be associated with volume loss in these brain regions and the severity of clinical symptoms in patients with NPC.

MATERIALS AND METHODS

Standard Protocol Approvals, Registrations, and Patient Consents

This study was approved by the Melbourne Health Human Research Ethics Committees (HREC2012.066) and the Australian Research Infrastructure Network (ARIN – 7T-2015.005, CFMS No. MRI495000045). Written informed consent was obtained from all participants and/or their legal guardians before their enrollment in the study.

Study Population

This study was conducted as a prospective case-control study from April 2019 to December 2019. Ten individuals diagnosed with adolescent- and adult-onset NPC based on clinical features and confirmed with genetic testing for *NPC1* disease-causing mutations were enrolled at the Royal Melbourne Hospital. Because there are no existing neuroimaging studies of brain iron in NPC and considering the rarity of this disease, a study population of 10 for the NPC group was deemed an achievable sample size for this study. Fourteen age- and sex-matched healthy individuals were recruited from the general community in the local metropolitan area through online advertisement. A history of any other neurologic conditions (including head injury and seizures), systemic diseases (eg, inflammatory disorders, diabetes, and impaired thyroid function), current pregnancy, breastfeeding, and MR imaging contraindications (eg, magnetic metal implants and claustrophobia) were considered exclusion criteria for both healthy and NPC groups. A personal or family (first degree relative) history of any psychiatric and neurologic illness, psychopathology that impacts functioning, and past or current use of any psychoactive medication were considered as additional exclusion criteria for the control group.

Imaging Methods

MR imaging was performed using a 7T MR imaging scanner (Magnetom Terra 7T; Siemens) with a 1TX / 32Rx head coil (Nova Medical). For the T1 structural images, an MP2RAGE sequence was obtained with the following parameters: TE = 2.89 ms, TR = 4900 ms, matrix size = 256 × 232 × 192, voxel size = 0.9 mm isotropic, acquisition time = 5:25 minutes. For QSM reconstruction, a multiecho gradient recalled-echo (GRE) sequence was acquired with the following parameters: number of echoes = 9, first TE = 5.1 ms, ΔTE = 2.04 ms, TR = 24 ms, flip angle = 13°, matrix size = 280 × 242 × 192, voxel size = 0.75 mm isotropic, acquisition time = 8:42 minutes.

Processing of Neuroimaging Data

Structural T1. T1 images were used for anatomic labeling and segmentation of the ROIs. Brain masks were constructed using the Multi-Atlas Brain Segmentation (MABS) tool (<https://github.com/pnlbwh/PNL-manual#multi-atlas-brain-segmentation-mabs>). Generated binary masks were visually assessed and manually

Investigator Grant (1194028) and by the generous donation of Mr Douglas Stutt to the University of Melbourne. C.P. is supported by National Health and Medical Research Council L3 Investigator Grant (1196508). A.E.L. is supported by National Institute of Health grants, National Institute of Mental Health 1 K01 MH15247-01A1 and 1K24MH110807-01A1, a Brain and Behavior Research Foundation Young Investigator Award, and a Brigham and Women's Department of Psychiatry Internal Funding Award. R.J.R. is supported by National Institute of Mental Health grant R01MH112748. M.E.S. is supported by the National Institute of Health grant 5 U01MH109977.

Please address correspondence to Parsa Ravanfar, MD, Melbourne Neuropsychiatry Centre, Level 3, Alan Gilbert Building, 161 Barry St, Carlton South, VIC 3053, Australia; e-mail: sravanfar@student.unimelb.edu.au; @ParsaRVN

 Indicates open access to non-subscribers at www.ajnr.org

 Indicates article with online supplemental data.

<http://dx.doi.org/10.3174/ajnr.A7894>

corrected using ITK-SNAP, Version 3.8 (<http://www.itksnap.org/>)¹⁹ by an investigator blinded to participant groups.

The striatum (the putamen and caudate nucleus), hippocampus, and thalamus were selected as the ROIs for the ROI-based comparison of mean QSM values between groups. The putamen, caudate nucleus, and thalamus were automatically segmented using the Multiple Automatically Generated Templates Brain Segmentation (MAGeT-Brain; <https://github.com/CobraLab/MAGeTbrain>) pipeline²⁰ with the CIT168 atlas.²¹ Automatic segmentation of the hippocampus was performed using FreeSurfer, Version 7.1.0 (<http://surfer.nmr.mgh.harvard.edu>). Label maps generated by MAGeT-Brain and FreeSurfer for the study ROIs were merged into single files for each subject, visually inspected, and manually corrected in all cases using 3D Slicer, Version 4.11 (<https://www.slicer.org>)²² by an investigator under the guidance and quality assessment of 2 senior neuroanatomists, all of whom were blinded to participant groups.

QSM Processing. The Quantitative Susceptibility Mapping Artifact Reduction Technique (QSMART) pipeline²³ was used to construct QSM maps using the phase and magnitude components of the GRE sequence. Briefly, a brain mask was generated using the FSL Brain Extraction Tool (<http://fsl.fmrib.ox.ac.uk/fsl/fslwiki/BET>).²⁴ After phase unwrapping using a Laplacian-based method²⁵ for each echo, multiecho data were combined using a magnitude-weighted least squares echo fitting method. A 3D spatially dependent filtering²⁶ and iterative least-squares (iLSQR) decomposition were subsequently used for background field removal and field-to-source inversion, respectively. Details of this method were further explained in Yaghmaie et al,²³ in 2021. In QSM processing, magnetic susceptibility is commonly estimated and reported relative to a reference region in the brain that is assumed to be unaffected by disease pathology and, therefore, expected to have similar QSM across study groups.²⁷ In NPC, we expect a generalized involvement of the brain regions by disease pathology. Hence, in this study, we did not use a reference region for QSM processing. Magnetic susceptibility values reported by the QSMART pipeline are inherently referenced to the magnetic susceptibility of water.

Voxelwise QSM Comparison between Groups. To compare the QSM values in the entire brain between the 2 groups, we performed a probing voxelwise comparison of QSM between groups. To transform all QSM images to a common template, we first created a study template from all participants' skull-stripped T1 images using the `antsMultivariateTemplateConstruction2` tool from Advanced Normalization Tools, Version 2.3.5 (ANTs; <https://github.com/ANTsX/ANTs/>).²⁸ For each subject, affine and nonlinear transformations were constructed from the subject T1 to the study template using `antsRegistrationSyN` tool from ANTs. Additionally, for each subject, we conducted a rigid transformation from the non-skull-stripped first-echo magnitude image of the GRE sequence to the T1 image using ANTs. The "GRE-to-T1" rigid transform and the "subject-to-study template" affine + nonlinear transforms were sequentially applied to each participant's QSM to warp it to the common study template.

ROI-Based QSM Comparison. To compare mean QSM values in the putamen, caudate nucleus, globus pallidus, thalamus, and

hippocampus between groups, we overlaid the label maps generated from the brain segmentation step onto the QSM images by inversely applying the rigid transform from the GRE-to-T1 acquisitions generated in the previous step. Mean intensity values on QSM images (magnetic susceptibility) were extracted in each ROI for comparison between groups.

Clinical Assessments. For individuals with NPC, the treating physician conducted and reported clinical evaluations of disease severity using the Iturriaga scale,²⁹ cognitive performance using the Neuropsychiatry Unit Cognitive Assessment Tool (NUCOG),³⁰ and global functioning capacity using the Social and Occupational Functioning Assessment Scale (SOFAS).³¹

Statistical Analysis. We tested groups for age and sex differences using an independent samples *t* test and a χ^2 test, respectively. To compare ROI volumes between groups, we used the ANCOVA test with total brain volume as a covariate and 5000 bootstraps. We used skull-stripped brain images as inputs for FreeSurfer to improve the accuracy of segmentations. Therefore, the total intracranial volume was not obtainable from the FreeSurfer outputs. Total brain volume was calculated by the summation of all gray and white matter volumes from the label maps provided by FreeSurfer, to exclude any intracranial space occupied by the CSF.

Voxelwise comparison of QSM between groups was conducted using the Randomize tool in FSL (<http://fsl.fmrib.ox.ac.uk/fsl/fslwiki/Randomise/UserGuide>), with age as covariate, 5000 permutations, and threshold-free cluster enhancement³² family-wise error rate correction.³³ ROI-based between-group comparison of QSM was performed using ANCOVA, with age and volume of each ROI as covariates with 5000 bootstraps. To limit the number of covariates in the statistical models and considering that most of the QSM studies have not observed an effect of sex on brain iron,^{34,35} we did not include sex as a covariate in our models. In these analyses, correction for multiple comparisons was performed using the Benjamini-Hochberg method,³⁶ with a false detection rate of 0.05. An $\alpha = .05$ was considered the significance threshold. All the above statistical tests were performed using SPSS (Version 24; SPSS Statistics for Mac; IBM).

As secondary analyses, we examined the partial correlation between volume and QSM in the brain regions that showed a significant difference between groups, controlling for the effect of age. Furthermore, we explored the partial correlation between mean QSM (controlling for age) and volume (controlling for total brain volume) in the ROIs with clinical assessments. We conducted these analyses using the Pearson correlation test. Data preparation, statistical analyses, and data visualization were conducted using R Studio (<http://rstudio.org/download/desktop>) 2021.09.0 Build 351 "Ghost Orchid" Release³⁷ operating on R version 4.1.2, using the `psych` 2.1.9,³⁸ `corrplot` 0.92,³⁹ `corx` 1.0.6.1,⁴⁰ `tidyverse` 1.3.1,⁴¹ `readxl` 1.3,⁴² `ggplot2`,⁴³ and `dplyr` 1.0.7⁴⁴ packages.

Data Availability. Data sets extracted from study participants' MR imaging acquisitions will be shared by request from any qualified investigator. Raw de-identified neuroimaging data can be made available on requests from investigators, subject to

Table 1: Demographic description and comparison of the study population

	Control (n = 14)	NPC (n = 10)	P Value
Age (mean) (SD) (yr)	32.6 (9.2)	33.1 (12.1)	.92
Sex (male/female)	6:8	4:6	.89
Iturriaga score (mean) (SD)	NA	9.1 (3)	NA
NUCOG (mean) (SD)	NA	63.9 (18)	NA
SOFAS (mean) (SD)	NA	42 (22.7)	NA
Miglustat dose	NA	7 Patients taking 200 mg TID	NA

Note:—NA indicates not applicable; TID, 3 times per day.

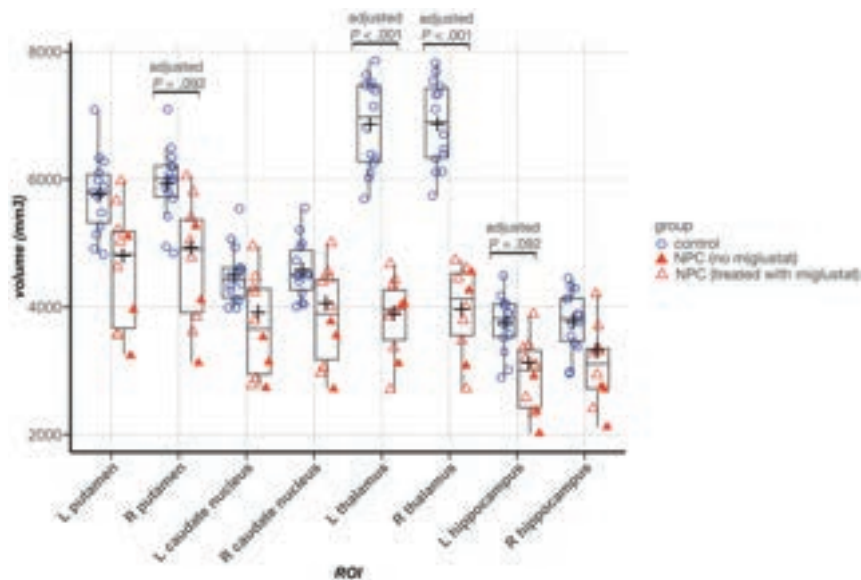


FIG 1. Between-group comparison of volume in the ROIs. In the Tukey boxplots, the *middle line* of each box indicates the median, upper and lower boundaries of the boxes show the upper and lower quartiles, respectively; the upper and lower *whiskers* show the maximum and minimum data points; and the *cross signs* indicate the mean in each group. *Filled triangles* represent data points from patients with NPC who were not taking miglustat. *Error bars* indicate SDs. L indicates left; R, right.

approval from the Human Research Ethics Committee and signing a data-sharing agreement.

RESULTS

Demographic, clinical, and neuroimaging data were analyzed from all 10 individuals with NPC and 14 healthy control participants. All patients with NPC had mutations in the *NPC1* gene. Seven of 10 patients in the NPC group were on active treatment with miglustat. Data sets from all participants were complete and met the required quality for analysis. Table 1 presents a summary of the demographic and clinical information of the study population. Age and sex were not statistically different between groups.

ROI Volumetric Comparisons

In individuals with NPC, the volume of the thalamus was significantly lower bilaterally (left: 3846.4 versus 6861.1 mm³, adjusted $P = .002$, $\eta^2_p = 0.85$; right: 3964.6 versus 6866.3 mm³, adjusted $P = .002$, $\eta^2_p = 0.82$), and there was a trend toward lower volume in the left hippocampus (2916.7 versus 3741.7 mm³, adjusted $P = .08$, $\eta^2_p = 0.20$). In all other ROIs, although average volumes were lower in the NPC group, the differences were not statistically significant (Online Supplemental Data and Fig 1).

Voxelwise QSM Comparison

In NPC, whole-brain voxelwise comparison of QSM between groups showed clusters of significantly higher QSM in the posterior segment of the right (223 voxels, center of mass in Montreal Neurological Institute 152 space: $X = 17.2$ mm, $Y = -28.7$ mm, $Z = 3.37$ mm) and left (245 voxels, center of mass in Montreal Neurological Institute 152 space: $X = -17.2$ mm, $Y = -29.9$ mm, $Z = 2.47$ mm) thalamus, consistent with the anatomic location of the pulvinar nucleus. Furthermore, we observed a large cluster (30,764 voxels) of lower QSM in the NPC group, spread across the white matter, including the bilateral parietal lobes, corpus callosum, and white matter surrounding the hippocampi (Fig 2).

ROI-Based QSM Comparison

Between-group comparison of mean QSM values in the ROIs showed significantly lower magnetic susceptibility in the right hippocampus in the NPC group after correction for multiple comparisons. In the other ROIs, we did not find any significant difference between groups. In the thalamus, despite the presence of clusters with higher and lower QSM, the mean QSM value was not significantly different between groups and was lower in NPC (Table 2).

Figure 3 provides representative QSM images from subjects in the NPC and control groups. In Fig 4, treatment status with miglustat is demonstrated on each of the data points. Due to the limited number of patients in the treatment subgroups, statistical analysis based on treatment status was not pursued. As a qualitative observation, patients who were not treated with miglustat showed higher QSM values in the thalamus compared with those on treatment. Such a distinction was not noticeable in other ROIs (Fig 4).

Correlation between QSM and Volume

The results are shown in Figure 5 for our exploratory test of correlations between QSM and volume in the thalamus and hippocampus, 2 regions that showed a significant difference between groups.

In the control group, a higher whole-ROI mean QSM value was associated with higher volume in the left thalamus ($r = 0.73$; 95% CI, 0.19–0.93) and left hippocampus ($r = 0.66$; 95% CI, 0.05–0.91). In the NPC group, in contrast, these correlations were not strong, and the confidence intervals contained the neutral (zero) value. However, the mean QSM value of clusters within the thalamus that showed significantly higher QSM compared with controls (not the whole thalamus) correlated with a smaller

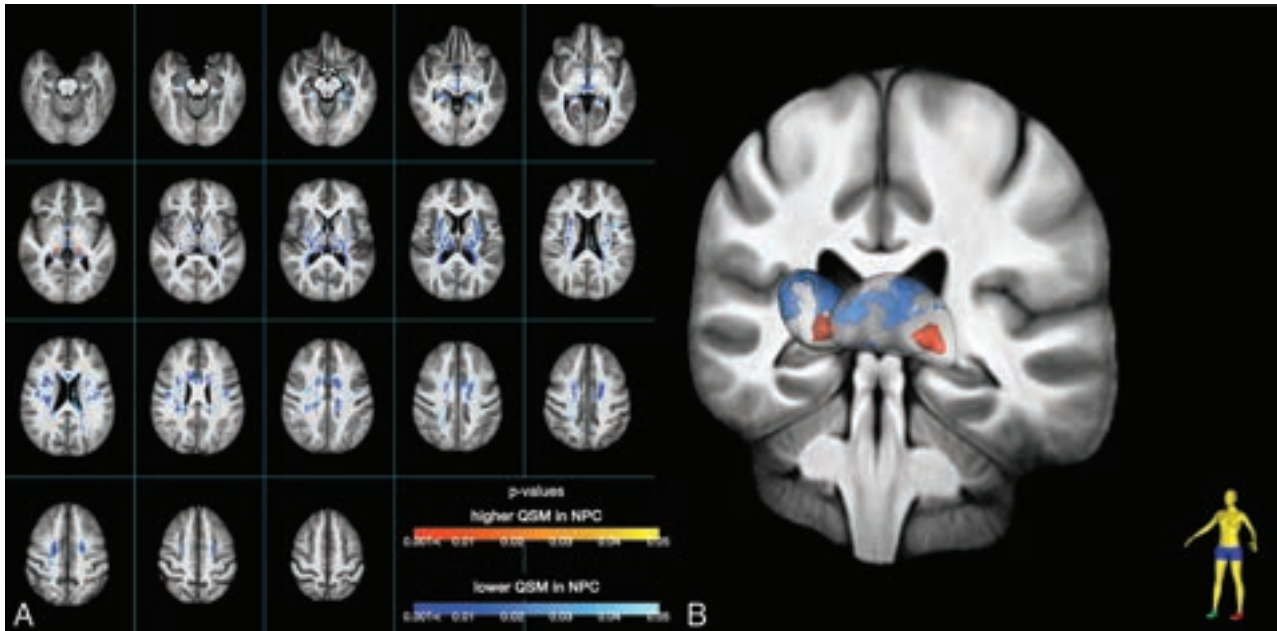


FIG 2. Voxelwise between-group comparison of QSM. *A*, Lightbox axial view with 4-mm section spacing. The yellow-red spectrum indicates clusters with higher QSM, and the blue-to-light blue spectrum shows clusters with lower QSM values in the NPC group compared with healthy controls. *B*, A visualization of the thalamus with clusters that show significant between-group QSM difference. Red and blue indicate higher and lower QSM in the NPC group compared with the control group, respectively. Clusters with increased QSM in NPC, depicted in red, are in the posterior part of the thalamus, consistent with the anatomic location of the pulvinar nucleus.

Table 2: ROI-based between-group comparison of mean QSM values with age and ROI volume as covariates

ROI	Control (Mean) (SD) (ppb)	NPC (Mean) (SD) (ppb)	FDR-Adjusted P Value	Effect Size (η^2_p)
Putamen				
Left	17 (5)	17.01 (9)	.56	0.03
Right	15.6 (3.5)	15.8 (7.4)	.79	0.003
Caudate				
Left	22.6 (3.4)	22 (7.7)	.56	0.02
Right	22.2 (4.3)	20.4 (5.9)	.63	0.01
Globus pallidus				
Left	81.3 (20.8)	95.1 (23)	.56	0.06
Right	84.9 (16.6)	102.7 (19.5)	.51	0.12
Thalamus				
Left	2.4 (4)	2.2 (6.1)	.31	0.1
Right	1.5 (3.5)	1 (6.2)	.56	0.04
Hippocampus				
Left	-1.6 (2.2)	-8.2 (3.6)	.10	0.3
Right	-1.9 (2.1)	-5.7 (3.3)	.04	0.2

Note:—ppb indicates parts per billion; FDR, false detection rate

volume of the whole thalamus bilaterally (left: $r = -0.8$; 95% CI, -0.95 to -0.34 ; right: $r = -0.7$; 95% CI, -0.92 to -0.13).

Correlations between Neuroimaging and Clinical Assessments

In the NPC group, QSM in the left hippocampus correlated with the NUCOG score ($r = 0.73$; 95% CI, 0.13 – 0.94). In the clusters within the left thalamus that showed significantly higher QSM in NPC, mean QSM values were associated with the Iturriaga disease severity score ($r = 0.69$; 95% CI, 0.1 – 0.92). Volume in the thalamus and right hippocampus (ROIs with

significant between-group volume differences) did not correlate with any of the clinical measures (Online Supplemental Data).

DISCUSSION

In the present study, we used QSM MR imaging at ultra-high field (7T) to examine brain iron in patients with NPC. QSM accurately estimates magnetic susceptibility at a voxel level and provides an indirect measurement of iron, a strong paramagnetic element with large positive magnetic susceptibility that increases the QSM signal.^{45,46} In contrast, cholesterol and sphingomyelin, which pathologically accumulate in the brain in NPC, have weak negative magnetic susceptibility and reduce QSM.⁴⁷ In the presence of abnormal lipid deposition that has an opposing effect on QSM than iron, a finding of higher QSM in NPC indicates greater iron content, but lower QSM in NPC can result from the negative magnetic susceptibility of lipid aggregates along with decreased, unchanged, or (slightly) increased iron. In the right hippocampus and scattered areas within the white matter, QSM was lower in the NPC group, consistent with the effect of lipid accumulation. In the thalamus, however, QSM differences were heterogeneous; while there was a widespread cluster of lower QSM in the thalamus, there were bilateral foci of higher QSM in the pulvinar nuclei, indicating a regional accumulation of iron. Furthermore, the volume of the thalamus was markedly lower in the NPC group.

Our secondary analyses demonstrated that excess iron in the pulvinar is associated with a reduced volume of the thalamus in the NPC group (Table 3). In the left pulvinar nucleus, iron content was also associated with higher disease severity scores. In fact, disease severity showed greater correlation with QSM in the

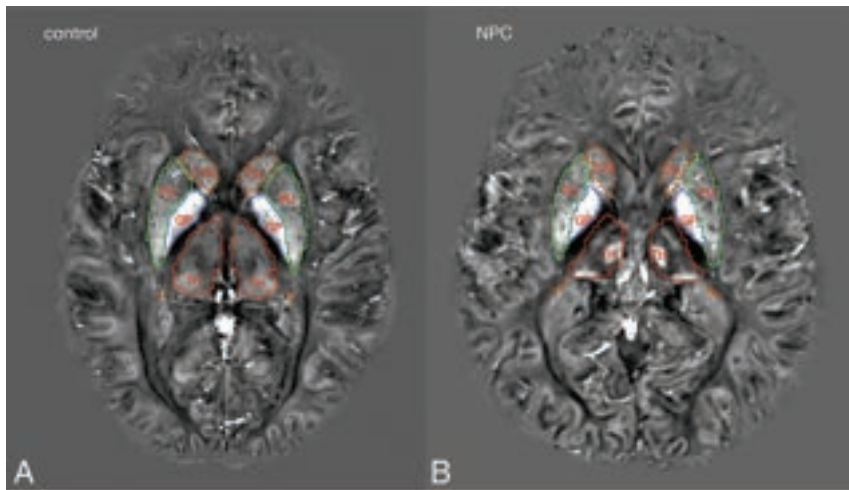


FIG 3. Representative QSM images from control and NPC groups. Colored lines mark the borders of segmentation labels: green, putamen; brown, caudate nucleus; red, thalamus; blue, globus pallidus.

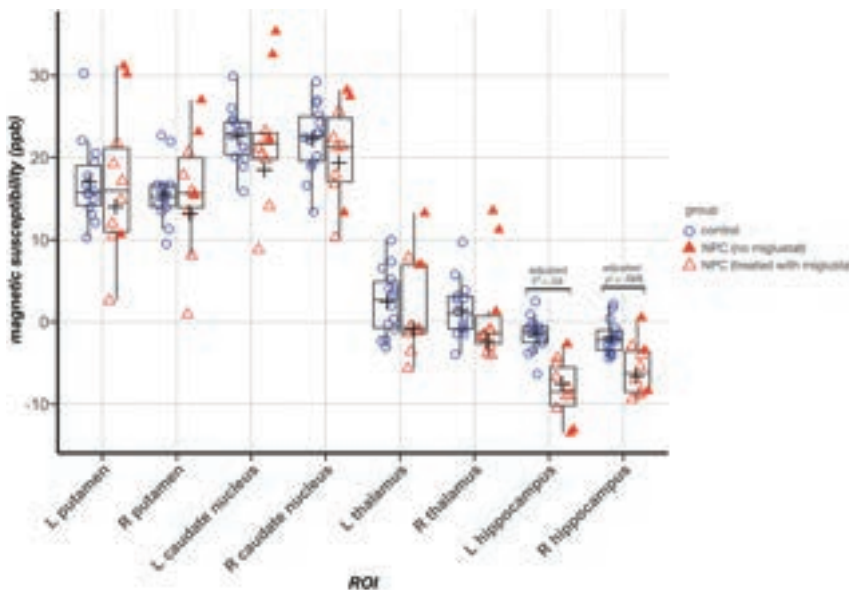


FIG 4. ROI-based between-group comparison of mean QSM values. In the Tukey boxplots, the middle line of each box indicates the median, upper, and lower boundaries of the boxes and shows the upper and lower quartiles, respectively; the upper and lower whiskers show the maximum and minimum data points; and the cross signs indicate the mean in each group. Filled triangles represent data points from patients with NPC who were not taking miglustat. Error bars indicate SDs in the entire control and NPC groups. In the thalamus, patients with NPC who were not taking miglustat had higher mean QSM values than those who were prescribed miglustat. L indicates left; R, right.

left pulvinar cluster than with the volume of the thalamus (Online Supplemental Data). Taken together, these findings point to a preferential deposition of iron in the pulvinar nucleus in association with disease severity and atrophy of the thalamus. The thalamus is centrally involved by the pathology of NPC. Previous structural studies have demonstrated the second highest levels of neuronal loss in the thalamus in NPC, after the cerebellum.^{1,5,48,49} In the present study, in addition to the marked atrophy in the thalamus, we identified a marked heterogeneity in

thalamic iron distribution, suggested by clusters of higher and lower QSM in NPC, which might link iron to the neuropathology of NPC. The pulvinar nucleus, through its connectivity to the visual cortical areas, is believed to play an important role in the regulation of visual attention and oculomotor functions.⁵⁰ One of the characteristic neurologic findings in NPC is supranuclear vertical gaze palsy,⁵¹ which we speculate could be associated with our finding of increased iron concentration and the previously reported atrophy in the pulvinar nucleus.⁴⁸

The link between the NPC genotype and our observation of a regional increase in brain iron content can be found in genetic studies. In NPC, in addition to the mutation of the *NPC* gene, coexisting upregulation of multiple genes involved in iron homeostasis⁵² and diminished expression of ferritin¹⁵ have been reported. Ferritin is the main intracellular iron storage, which sequesters and prevents iron from participating in reactions that generate oxidative stress. These genetic alterations are potentially associated with the elevated brain iron and oxidative stress observed in animal models of NPC.^{4,16} While the abnormal accumulation of cholesterol and sphingolipids is believed to be the underlying pathologic mechanism for neurodegeneration in NPC, oxidative stress associated with iron burden can be a mediating factor for neurotoxicity in this disorder. QSM, in its current state, is unable to differentiate various biologic forms of iron such as ferritin-bound, neuromelanin, or free labile iron (which contributes to oxidative stress and cytotoxicity). Protein-bound forms of iron (ferritin and neuromelanin) have stronger paramagnetic properties and make the greatest contribution to QSM signal. It is possible that the higher QSM in the pulvinar nucleus

observed in this study partly or wholly originates from an elevation in these stable forms of iron. However, an increase in protein-bound iron would also be associated with or reflect an increase in labile iron because the labile and protein-bound forms of iron exist in an equilibrium in which an increase on either side elevates (or is caused by the elevation of) the other side. By demonstrating regional accumulation of iron in NPC using advanced in vivo neuroimaging, this pilot study provides a promising approach for understanding the neurobiologic changes in NPC that warrant further investigations.

mean QSM value	volume	hemisphere	control	NPC
			correlation (95% CI)	correlation (95% CI)
thalamus cluster	whole	left	0.16 (-0.52, 0.72)	-0.8 (-0.95, -0.34)
	thalamus	right	0.28 (-0.42, 0.77)	-0.7 (-0.92, -0.13)
whole thalamus	whole	left	0.73 (0.19, 0.93)	0.13 (-0.55, 0.7)
	thalamus	right	0.46 (-0.24, 0.85)	0.16 (-0.52, 0.72)
hippocampus	hippocampus	left	0.66 (0.05, 0.91)	0.01 (-0.62, 0.64)
		right	0.29 (-0.41, 0.78)	0.13 (-0.55, 0.7)

FIG 5. Pearson correlation between volume and QSM in the brain regions that showed a difference in volume or QSM values between groups. Cells containing correlation coefficients are color-coded according to the value of the correlation coefficient. Blue indicates negative correlation, and red indicates positive correlation. Color intensities correspond to the value of the coefficient.

This knowledge has implications in the development of new therapeutic modalities for patients with NPC.

Miglustat is a glucosylceramide synthase inhibitor that is an approved treatment for NPC1, for which it shows modest efficacy. Seven of the 10 participants in the NPC group were on active treatment with miglustat. Whereas this small number precludes a subset analysis, we show these instances in the data (Fig 3), in which patients who were not receiving miglustat showed higher QSM values in the thalamus. It is unclear whether miglustat would have an impact on the homeostasis of iron in the brain. Considering its mechanism of action, treatment with miglustat would be expected to increase QSM secondary to lower lipid accumulation, while in the thalamus, patients who were not treated with miglustat had the highest QSM values. Iron chelation has recently gained attention as a potential medical treatment of neurodegenerative disorders such as Alzheimer disease and Parkinson disease.⁵³ In a previous animal study however, iron chelation with deferiprone did not rescue a mouse model of NPC,⁵⁴ so pharmacologic strategies to correct the abnormal distribution of iron may need to target iron trafficking indirectly.

This study has potential limitations. One limitation is the small sample size, which restricted the power to observe statistical significance in small-to-medium effect sizes. Considering the rarity of the disorder, the small study population was expected, and we tailored the statistical methods to limit the number of primary comparisons to our central hypothesis, supported by previous reports and our probing voxelwise analysis. However, we tested the associations among regional iron, brain volume, and clinical measures as secondary tests to inform future hypotheses and investigations. Furthermore, we used an ultra-high-field MR imaging scanner (7T), which enhances the magnetization of paramagnetic particles, increasing the tissue-phase perturbation and amplifying the detection power for smaller effect sizes of difference among groups compared with 3T or 1.5T scanners.

A second limitation is the inability of our QSM method to estimate paramagnetic and diamagnetic contributions of iron and lipid moieties to the QSM signal. Such a distinction would allow us to detect potential alterations in iron distribution that could be masked by the abnormal lipid accumulation in NPC.

Recently, new methods have been proposed to enable the decomposition of positive and negative magnetic susceptibility sources.⁵⁵ However, in our experience, we found the biexponential model that aims to disentangle positive and negative susceptibilities to be mathematically unstable, and we were not able to incorporate it into our QSM pipeline.

CONCLUSIONS

The present study provides in vivo evidence consistent with previous human and animal reports suggesting the disturbance of brain iron in NPC, in association with clinical features and structural brain changes. Further studies are required to investigate a potential link between iron dysregulation and neurodegeneration of NPC, ideally using a longitudinal design. Uncovering a possible role for iron in the neurotoxicity of NPC can be an avenue for treatment of individuals with NPC.

ACKNOWLEDGMENTS

The authors acknowledge the facilities and scientific and technical assistance of the National Imaging Facility, a National Collaborative Research Infrastructure Strategy capability, at the Melbourne Brain Centre Imaging Unit, University of Melbourne, Victoria, Australia. The authors acknowledge the statistical analysis support received from Mr Peter Summers at Melbourne Statistical Consulting Platform, The University of Melbourne. The authors thank Enterprise Research Infrastructure and Services at Partners HealthCare for their in-depth support.

Disclosure forms provided by the authors are available with the full text and PDF of this article at www.ajnr.org.

REFERENCES

1. Rego T, Farrand S, Goh AM, et al. **Psychiatric and cognitive symptoms associated with Niemann-Pick Type C disease: neurobiology and management.** *CNS Drugs* 2019;33:125–42 CrossRef Medline
2. Adibhatla RM, Hatcher JF. **Lipid oxidation and peroxidation in CNS health and disease: from molecular mechanisms to therapeutic opportunities.** *Antioxid Redox Signal* 2010;12:125–69 CrossRef Medline
3. Fu R, Yanjanin NM, Bianconi S, et al. **Oxidative stress in Niemann-Pick disease, type C.** *Mol Genet Metab* 2010;101:214–18 CrossRef Medline
4. Vázquez MC, Balboa E, Alvarez AR, et al. **Oxidative stress: a pathogenic mechanism for Niemann-Pick Type C disease.** *Oxid Med Cell Longev* 2012;2012:205713 CrossRef Medline
5. Walterfang M, Di Biase MA, Cropley VL, et al. **Imaging of neuroinflammation in adult Niemann-Pick type C disease: a cross-sectional study.** *Neurology* 2020;94:e1716–25 CrossRef Medline
6. Love S, Bridges LR, Case CP. **Neurofibrillary tangles in Niemann-Pick disease type C.** *Brain J Neurol* 1995;118:19–29 CrossRef Medline
7. Suzuki K, Parker CC, Pentchev PG, et al. **Neurofibrillary tangles in Niemann-Pick disease type C.** *Acta Neuropathol* 1995;89:227–38 CrossRef Medline
8. Villemagne VL, Velakoulis D, Doré V, et al. **Imaging of tau deposits in adults with Niemann-Pick type C disease: a case-control study.** *Eur J Nucl Med Mol Imaging* 2019;46:1132–38 CrossRef Medline
9. Hare D, Ayton S, Bush A, et al. **A delicate balance: iron metabolism and diseases of the brain.** *Front Aging Neurosci* 2013;5:34 CrossRef Medline
10. Georgieff MK. **The role of iron in neurodevelopment: fetal iron deficiency and the developing hippocampus.** *Biochem Soc Trans* 2008;36:1267–71 CrossRef Medline

11. Donley DW, Realing M, Gigley JP, et al. **Iron activates microglia and directly stimulates indoleamine-2,3-dioxygenase activity in the N171-82Q mouse model of Huntington's disease.** *PLoS One* 2021;16:e0250606 CrossRef Medline
12. Nnah IC, Wessling-Resnick M. **Brain iron homeostasis: a focus on microglial iron.** *Pharmaceuticals (Basel)* 2018;11:129 CrossRef Medline
13. Ravanfar P, Loi SM, Syeda W, et al. **Systematic review; quantitative susceptibility mapping (QSM) of brain iron profile in neurodegenerative diseases.** *Front Neurosci* 2021;15:618435 CrossRef Medline
14. Christomanou H, Kellermann J, Linke RP, et al. **Deficient ferritin immunoreactivity in visceral organs from four patients with Niemann-Pick disease type C.** *Biochem Mol Med* 1995;55:105–15 CrossRef Medline
15. Christomanou H, Vanier MT, Santambrogio P, et al. **Deficient ferritin immunoreactivity in tissues from Niemann-Pick type C patients: extension of findings to fetal tissues, H and L ferritin isoforms, but also one case of the rare Niemann-Pick C2 complementation group.** *Mol Genet Metab* 2000;70:196–202 CrossRef Medline
16. Hung YH, Faux NG, Killilea DW, et al. **Altered transition metal homeostasis in Niemann-Pick disease, type C1.** *Metallomics* 2014;6:542–53 CrossRef Medline
17. Ladd ME, Bachert P, Meyerspeer M, et al. **Pros and cons of ultra-high-field MRI/MRS for human application.** *Prog Nucl Magn Reson Spectrosc* 2018;109:1–50 CrossRef Medline
18. Benussi A, Cotelli MS, Padovani A, et al. **Recent neuroimaging, neurophysiological, and neuropathological advances for the understanding of NPC.** *F1000Res* 2018;7:194 CrossRef Medline
19. Yushkevich PA, Piven J, Hazlett HC, et al. **User-guided 3D active contour segmentation of anatomical structures: significantly improved efficiency and reliability.** *Neuroimage* 2006;31:1116–28 CrossRef Medline
20. Chakravarty MM, Steadman P, van Eede MC, et al. **Performing label-fusion-based segmentation using multiple automatically generated templates.** *Hum Brain Mapp* 2013;34:2635–54 CrossRef Medline
21. Pauli WM, Nili AN, Tyszka JM. **A high-resolution probabilistic in vivo atlas of human subcortical brain nuclei.** *Sci Data* 2018;5:180063 CrossRef Medline
22. Fedorov A, Beichel R, Kalpathy-Cramer J, et al. **3D Slicer as an image computing platform for the Quantitative Imaging Network.** *Magn Reson Imaging* 2012;30:1323–41 CrossRef Medline
23. Yaghmaie N, Syeda WT, Wu C, et al. **QSMART: quantitative susceptibility mapping artifact reduction technique.** *Neuroimage* 2021;231:117701 CrossRef Medline
24. Jenkinson M, Beckmann CF, Behrens TE, et al. **FSL.** *Neuroimage* 2012;62:782–90 CrossRef Medline
25. Li W, Wu B, Liu C. **Quantitative susceptibility mapping of human brain reflects spatial variation in tissue composition.** *Neuroimage* 2011;55:1645–56 CrossRef Medline
26. Ng A, Johnston L, Chen Z, et al. **Spatially dependent filtering for removing phase distortions at the cortical surface.** *Magn Reson Med* 2011;66:784–93 CrossRef Medline
27. Fazlollahi A, Ayton S, Bourgeat P, et al. **A normalisation framework for quantitative brain imaging; application to quantitative susceptibility mapping.** In: *2017 IEEE 14th International Symposium on Biomedical Imaging (ISBI 2017)*, Melbourne, Australia. April 18–21, 2017:97–100 CrossRef
28. Avants BB, Tustison NJ, Song G, et al. **A reproducible evaluation of ANTs similarity metric performance in brain image registration.** *Neuroimage* 2011;54:2033–44 CrossRef Medline
29. Iturriaga C, Pineda M, Fernández-Valero EM, et al. **Niemann-Pick C disease in Spain: clinical spectrum and development of a disability scale.** *J Neurol Sci* 2006;249:1–6 CrossRef Medline
30. Walterfang M, Siu R, Velakoulis D. **The NUCOG: validity and reliability of a brief cognitive screening tool in neuropsychiatric patients.** *Aust N Z J Psychiatry* 2006;40:995–1002 CrossRef Medline
31. Rush AJ Jr, First MB, Blacker D, eds. *Handbook of Psychiatric Measures*. 2nd ed. American Psychiatric Publishing; 2008:84–86
32. Smith SM, Nichols TE. **Threshold-free cluster enhancement: addressing problems of smoothing, threshold dependence and localisation in cluster inference.** *Neuroimage* 2009;44:83–98 CrossRef Medline
33. Winkler AM, Ridgway GR, Webster MA, et al. **Permutation inference for the general linear model.** *Neuroimage* 2014;92:381–97 CrossRef Medline
34. Spence H, McNeil CJ, Waiter GD. **The impact of brain iron accumulation on cognition: a systematic review.** *PLoS One* 2020;15:e0240697 CrossRef Medline
35. Khattar N, Triebswetter C, Kiely M, et al. **Investigation of the association between cerebral iron content and myelin content in normative aging using quantitative magnetic resonance neuroimaging.** *Neuroimage* 2021;239:118267 CrossRef Medline
36. Benjamini Y, Hochberg Y. **Controlling the false discovery rate: a practical and powerful approach to multiple testing.** *Royal Statistical Society: Series B (Methodological)* 1995;57:289–300 CrossRef
37. RStudio Team. **RStudio: Integrated Development Environment for R.** 2020. <http://www.rstudio.com/>. Accessed December 6, 2021
38. Revelle W. **psych: Procedures for Psychological, Psychometric, and Personality Research.** September 22, 2021. <https://CRAN.R-project.org/package=psych>. Accessed December 6, 2021
39. Wei T, Simko V, Levy M, et al. **corrplot: Visualization of a Correlation Matrix.** November 18, 2021. <https://CRAN.R-project.org/package=corrplot>. Accessed December 6, 2021
40. Conigrave J. **corx: Create and Format Correlation Matrices.** June 30, 2020. <https://CRAN.R-project.org/package=corx>. Accessed December 6, 2021
41. Wickham H, Averick M, Bryan J, et al. **Welcome to the tidyverse.** *J Open Source Softw* 2019;4:1686 CrossRef
42. Wickham H, Bryan J. **readxl: Read Excel Files.** 2019. <https://CRAN.R-project.org/package=readxl>. Accessed December 6, 2021
43. Wickham H. **ggplot2: Elegant Graphics for Data Analysis.** 2016. <https://ggplot2.tidyverse.org>. Accessed December 6, 2021
44. Wickham H, François R, Henry L, et al. **dplyr: A Grammar of Data Manipulation.** 2021. <https://CRAN.R-project.org/package=dplyr>. Accessed December 6, 2021
45. Deistung A, Schweser F, Reichenbach JR. **Overview of quantitative susceptibility mapping.** *NMR Biomed* 2017;30:e3569 CrossRef Medline
46. Langkammer C, Schweser F, Krebs N, et al. **Quantitative susceptibility mapping (QSM) as a means to measure brain iron? A post mortem validation study.** *Neuroimage* 2012;62:1593–99 CrossRef Medline
47. Duyn JH, Schenck J. **Contributions to magnetic susceptibility of brain tissue.** *NMR Biomed* 2017;30:23546 CrossRef
48. Walterfang M, Patenaude B, Abel LA, et al. **Subcortical volumetric reductions in adult Niemann-Pick disease type C: a cross-sectional study.** *AJNR Am J Neuroradiol* 2013;34:1334–40 CrossRef Medline
49. Walterfang M, Fahey M, Desmond P, et al. **White and gray matter alterations in adults with Niemann-Pick disease type C: a cross-sectional study.** *Neurology* 2010;75:49–56 CrossRef Medline
50. Benarroch EE. **Pulvinar.** *Neurology* 2015;84:738–47 CrossRef Medline
51. Salsano E, Umeh C, Rufa A, et al. **Vertical supranuclear gaze palsy in Niemann-Pick type C disease.** *Neurol Sci* 2012;33:1225–32 CrossRef Medline
52. Reddy JV, Ganley IG, Pfeffer SR. **Clues to neuro-degeneration in Niemann-Pick type C disease from global gene expression profiling.** *PLoS One* 2006;1:e19 CrossRef Medline
53. Devos D, Cabantchik ZI, Moreau C, et al; FAIRPARK-II and FAIRALS-II studygroups. **Conservative iron chelation for neurodegenerative diseases such as Parkinson's disease and amyotrophic lateral sclerosis.** *J Neural Transm (Vienna)* 2020;127:189–203 CrossRef Medline
54. Hung YH, Lotan A, Yeshurun S, et al. **Iron chelation by deferiprone does not rescue the Niemann-Pick disease type C1 mouse model.** *Biomaterials* 2020;33:87–95 CrossRef Medline
55. Chen J, Gong NJ, Chaim KT, et al. **Decompose quantitative susceptibility mapping (QSM) to sub-voxel diamagnetic and paramagnetic components based on gradient-echo MRI data.** *Neuroimage* 2021;242:118477 CrossRef Medline

Choroid Plexus Calcification Correlates with Cortical Microglial Activation in Humans: A Multimodal PET, CT, MRI Study

T. Butler, X.H. Wang, G.C. Chiang, Y. Li, L. Zhou, K. Xi, N. Wickramasuriya, E. Tanzi, E. Spector, I. Ozsahin, X. Mao, Q.R. Razlighi, E.K. Fung, J.P. Dyke, T. Maloney, A. Gupta, A. Raj, D.C. Shungu, P.D. Mozley, H. Rusinek, and L. Glodzik



ABSTRACT

BACKGROUND AND PURPOSE: The choroid plexus (CP) within the brain ventricles is well-known to produce cerebrospinal fluid (CSF). Recently, the CP has been recognized as critical in modulating inflammation. MRI-measured CP enlargement has been reported in neuroinflammatory disorders like MS as well as with aging and neurodegeneration. The basis of MRI-measured CP enlargement is unknown. On the basis of tissue studies demonstrating CP calcification as a common pathology associated with aging and disease, we hypothesized that previously unmeasured CP calcification contributes to MRI-measured CP volume and may be more specifically associated with neuroinflammation.

MATERIALS AND METHODS: We analyzed 60 subjects (43 healthy controls and 17 subjects with Parkinson's disease) who underwent PET/CT using ¹¹C-PK11195, a radiotracer sensitive to the translocator protein expressed by activated microglia. Cortical inflammation was quantified as nondisplaceable binding potential. Choroid plexus calcium was measured via manual tracing on low-dose CT acquired with PET and automatically using a new CT/MRI method. Linear regression assessed the contribution of choroid plexus calcium, age, diagnosis, sex, overall volume of the choroid plexus, and ventricle volume to cortical inflammation.

RESULTS: Fully automated choroid plexus calcium quantification was accurate (intraclass correlation coefficient with manual tracing = .98). Subject age and choroid plexus calcium were the only significant predictors of neuroinflammation.

CONCLUSIONS: Choroid plexus calcification can be accurately and automatically quantified using low-dose CT and MRI. Choroid plexus calcification—but not choroid plexus volume—predicted cortical inflammation. Previously unmeasured choroid plexus calcium may explain recent reports of choroid plexus enlargement in human inflammatory and other diseases. Choroid plexus calcification may be a specific and relatively easily acquired biomarker for neuroinflammation and choroid plexus pathology in humans.

ABBREVIATIONS: AD = Alzheimer disease; BMI = body mass index; Bpnd = nondisplaceable binding potential; CP = choroid plexus; HU = Hounsfield units; ICC = intraclass correlation coefficient; PD = Parkinson disease; PK = ¹¹C-PK11195; TSPO = translocator protein

The choroid plexus (CP), a highly vascularized filamentous structure within the brain ventricular system, is well-known to produce CSF. Recently, additional, important CP functions

have been recognized, including the regulation of inflammation. The CP both initiates and modulates neuroinflammation, and CP dysfunction is considered highly relevant to the pathophysiology of disorders characterized by excess inflammation such as MS¹⁻⁶ and Alzheimer disease (AD)⁷⁻⁹ as well as normal aging.¹⁰

Unlike virtually all brain parenchymal structures, which atrophy in association with aging and dysfunction, CP enlargement appears to be pathologic, and recent MRI studies have demonstrated larger CP volume in patients with neuropsychiatric disorders, including MS,⁴⁻⁶ AD,^{7,8} depression,¹¹ and stroke,¹² and normal aging.¹⁰ The basis of CP enlargement remains uncertain, but on the basis of postmortem and animal studies, it has been posited to relate to CP basement membrane thickening and fibrous stroma expansion with protein, inflammatory cells, and deposition of metal, in particular calcium.¹³⁻¹⁶ While most of these CP components are detectable and quantifiable only through direct examination of tissue, the assessment of calcium using in

Received January 11, 2023; accepted after revision May 4.

From the Brain Health Imaging Institute (T.B., X.H.W., G.C.C., Y.L., L.Z., K.X., N.W., E.T., E.S., I.O., X.M., Q.R.R., T.M., A.G., L.G.), and Department of Radiology (X.M., E.K.F., J.P.D., D.C.S., P.D.M.), Weill Cornell Medicine, New York, New York; Department of Radiology (A.R.), University of California, San Francisco, San Francisco, California; and Department of Radiology (H.R.), New York University, New York, New York.

This work was funded by National Institutes of Health grants K23NS057579, R01NS105541, R01NS092802, R01AG072753 and a Department of Defense grant W81XWH-15-1-0437.

Please address correspondence to Tracy Butler, MD, Weill Cornell Medicine, Brain Health Imaging Institute, 407 East 61st St, 2nd Floor, New York, NY 10065; e-mail: tab2006@med.cornell.edu

Indicates open access to non-subscribers at www.ajnr.org

Indicates article with online supplemental data.

<http://dx.doi.org/10.3174/ajnr.A7903>

vivo neuroimaging is relatively simple because of its vastly higher photon attenuation compared with water and brain, making it easily visible on CT.

For decades, CP calcification has been recognized as a normal phenomenon, with gradually increasing calcification noted with increasing age. CP calcification may have been the first age-related brain change ever detected in living humans. In 1930, Cornelius Dyke, considered the world's first neuroradiologist, noticed that CP calcification on skull radiographs was rare in children but common in the elderly.¹⁷ This finding was demonstrated in 1980 using CT.¹⁸ Markedly increased calcification of the CP, basal ganglia, and other brain structures in association with neuropsychiatric decline constitutes the still-poorly-understood and underdiagnosed syndrome of Fahr disease.¹⁹ CP calcification has received less research attention in recent years, in large part because MRI, with its submillimeter spatial resolution and lack of radiation has supplanted CT as the technique of choice for human neuroimaging research, and the variable signal of calcium on typical MRI makes calcium quantification on MRI challenging^{20,21} (though novel quantitative susceptibility mapping sequences under development may, in the future, support MRI quantification of calcium with an accuracy approaching that of CT²²).

To our knowledge, decades-old recognition of increasing CP calcification with aging and certain diseases has not been linked to the more recent understanding that CP has important roles beyond CSF production, in particular the regulation of neuroinflammation.¹⁻⁶ Neuroinflammation can currently be measured in vivo in humans using PET with radiotracers sensitive to the translocator protein (TSPO) expressed by activated microglia, the resident immune cell type of the brain.²³⁻²⁵ Increased regional TSPO PET signal has been demonstrated in a number of human neuroinflammatory and neurodegenerative disorders.^{23,25} However, despite the development of several new TSPO radiotracers during the past 15 years, there remain significant challenges associated with TSPO PET implementation, quantification, and interpretation, motivating research to identify additional biomarkers for neuroinflammation appropriate for human use.^{25,26} Intriguingly, 2 recent PET studies showed that cortical TSPO expression correlated with MRI-measured CP volume in patients with MS⁶ and depression.¹¹ On the basis of neuropathologic evidence that calcium deposition is associated with CP basement membrane thickening and fibrous stroma expansion in aging and disease,¹³⁻¹⁶ we wondered whether this correlation between CP volume and TSPO PET-measured neuroinflammation could be due to calcium. If so, CP calcium, which is easily detectable using CT, could represent a simple biomarker of neuroinflammation.

We, therefore, took a multimodal imaging approach, combining CT, MRI, and TSPO PET to measure the relationship between CP calcium and cortical neuroinflammation in a convenience sample of subjects (healthy controls and patients with Parkinson disease [PD]) who had undergone PET using the TSPO radiotracer ¹¹C-PK11195 (PK) at our institution and who had agreed to their data being included in a local neuroimage repository.

We developed an automated method for measuring CP calcium volume using low-dose CT (routinely acquired during PET/CT studies) and MRI, which we validated against semimanual tracing.

We hypothesized that the volume of calcium within the CP would be an independent predictor of PET-measured neuroinflammation.

Although the purpose of this study was to assess the contribution of CP calcium to cortical neuroinflammation as a general phenomenon, rather than as a function of disease, we also assessed the possible effects of the diagnosis (PD or control) on CP calcium, TSPO PET, and their interaction.

MATERIALS AND METHODS

Subjects

Subjects ($n = 60$) who underwent PK PET for several different studies conducted on a single PET/CT scanner between 2013 and 2019 were included in this analysis. This was a convenience sample based on available scan data. Subjects were either healthy controls ($n = 43$) or had been diagnosed with PD without dementia ($n = 17$) on the basis of standard criteria.²⁷ Most subjects with PD were taking ≥ 1 medication for PD. Healthy subjects were free from serious medical or neurologic disease including substance abuse. Common medical conditions in older subjects such as hypertension and hypercholesterolemia and medications to treat these conditions were not exclusionary. No subjects were taking anti-inflammatory medication. All subjects provided informed consent to participate in a disease-focused research study and for their data to be included in a registry for future analyses such as this one.

PET and MR Image Acquisition

PET images were acquired during 1 hour in list mode, starting at the time of injection of ~ 370 MBq of PK on a Biograph PET/CT scanner (Siemens) (voxel size: $1.0182 \times 1.0182 \times 2.025$ mm³). Low-dose CT was acquired immediately before the PET acquisition (voxel size: $0.488 \times 0.488 \times 1.5$ mm³). 3D volumetric T1-weighted BRAVO (GE Healthcare) (voxel size: $0.9375 \times 0.9375 \times 1.5$ mm³) or MPRAGE (voxel size: 1 mm³ isotropic) MR images were acquired using a Discovery MR750 (GE Healthcare) or Tim Trio 3T (Siemens) scanner, respectively.

PET Image Processing

PET images were reconstructed into 22 frames and motion-corrected using MCFLIRT²⁸ (<https://fsl.fmrib.ox.ac.uk/fsl/fslwiki/MCFLIRT>) in FSL (<http://www.fmrib.ox.ac.uk/fsl>).²⁹ Nondisplaceable binding potential (BPnd) images reflecting the concentration of TSPO expressed by activated microglia, irrespective of tracer delivery and blood flow, were generated from dynamic PET using a multilinear reference tissue model³⁰ implemented in the freely available software package FireVoxel (<https://firevoxel.org>). The reference tissue time-activity curve was identified via optimized supervised cluster analysis,³¹ which is considered the method of choice for analyzing PK PET scans.³²

MR Image Processing

FreeSurfer, Version 7 (<http://surfer.nmr.mgh.harvard.edu>),³³ was used to segment MR images for 3 purposes: to define the bilateral cortical ROI as well as other regions for quantifying PET signal; to segment the bilateral lateral ventricles for the automated calcium-quantification method described below; and to quantify CP and lateral ventricle volume to be included as predictors of cortical inflammation. For this latter purpose, CP and ventricular volumes

were divided by each subject's whole-brain volume, calculated using SPM 12 (<http://www.fil.ion.ucl.ac.uk/spm/software/spm12>), to account for head size. To quantify inflammation (average BPnd) over the cortical ROI, each subject's T1-weighted MRI was linearly coregistered to his or her summed PET image with rigid body transformation in FSL.²⁹ ROIs were transformed to PET space with the inverse transformation matrix from the coregistration step and eroded 1 mm in-plane to minimize partial volume effects.

Semimanual Quantification of CP Calcium on CT

Using FireVoxel, CT images were windowed at width = 100 Hounsfield units (HU) and level = 50 HU to clearly visualize CP calcifications, which typically have a signal of >100 HU.³⁴ 3D ROIs of CP calcification within all horns of the bilateral lateral ventricles were drawn using an electronic paint brush on contiguous axial images. ROIs were then thresholded at 60 HU to exclude any noncalcified voxels. Semimanual tracing was performed by one rater on a random subset of scans ($n = 44$).

Automated Quantification of CP Calcium Using MRI and CT

T1 MRI and FreeSurfer segmentations were coregistered to CT using rigid transformation with the Advanced Normalization Tools software package (<http://stnava.github.io/ANTs/>).³⁵ An ROI mask consisting of the bilateral CPs and the posterior portion of the bilateral lateral ventricles (posterior to the most anterior extent of the CP) was generated. Excluding the most anterior portion of this mask prevented erroneous misidentification of parenchymal voxels as calcified and was found to improve correlation with manual tracing. Voxels with Hounsfield units of >100 within this combined CP/posterior lateral ventricle mask were used as seeds to build a weighted image based on the intensity difference. This weighted image was segmented into background and foreground using the fast marching method.³⁶ Clusters from the segmentation were then divided into 2 groups using k-means clustering,³⁷ and the one with higher signal was selected as the calcified CP voxels.

Statistical Analyses

Analyses were performed in SPSS, Version 26 (IBM). Results were considered significant at $P < .05$.

Subject demographic factors were summarized using means and SDs. Although between-group differences were not the focus of this study, possible demographic differences between subjects with PD and controls were assessed using 2-sample t test (age) and χ^2 test (sex).

The intraclass correlation coefficient (ICC) assessed agreement between semimanual and automated CP calcium volumes.

Multiple linear regression was used to assess the contribution of CP calcium, CP overall volume, ventricle volume, age, sex, body mass index (BMI; previously shown to affect TSPO PET³⁸), and diagnosis (control or PD) to the dependent variable of cortical BPnd. Because disease effects on these measures are unknown, we also assessed whether the interaction between diagnosis and any of these variables contributed significantly to cortical BPnd.

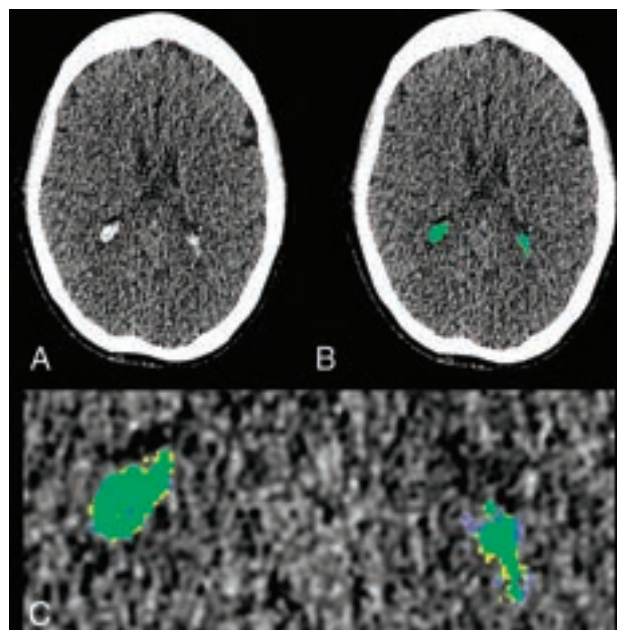


FIG 1. Example of CP calcification segmentation. A, Axial section from a low-dose CT acquired with PET/CT shows CP calcification in the occipital horn of the lateral ventricles bilaterally. B, Semimanually traced CP calcification is shown in yellow; fully-automated segmentation, in blue; and the overlap, in green. C, Magnified view of B shows close correspondence between semimanual and automated CP calcification segmentation.

In exploratory analyses using Mann-Whitney tests, we assessed whether any measured neuroimaging parameters differed between subjects with PD and controls.

RESULTS

Subject Demographics

Subjects ($n = 60$) ranged in age from 23 to 78 (mean, 57.0 [SD, 14.3]) years and included 24 (40%) women. The 2 types of subjects included in our convenience sample (PD [$n = 17$] and control [$n = 43$]) did not differ significantly by age, sex, or BMI. Details of subject demographics are presented in the Online Supplemental Data.

Comparison between Semimanual and Automated CP Calcium Measurements

There was excellent absolute agreement between semimanual and automated calcium measurements (ICC = 0.982, $F[43, 43] = 71.42$, $P < .001$). On the basis of this agreement, for all subsequent analyses, CP calcium refers to the automated value. Figure 1 shows an example of CP semimanual and automated segmentation.

Association of CP Calcium, CP Overall Volume, Ventricle Volume, Age, Sex, BMI, and Diagnosis with Cortical BPnd

A multiple regression model ($R^2 = 0.298$, adjusted $R^2 = 0.203$ $F[7, 52] = 3.15$, $P = .008$; details provided in the Table and Fig 2) showed that only age ($P = .017$) and CP calcium ($P = .017$) were significant predictors of cortical BPnd. Neither CP volume, ventricle volume, sex, nor diagnosis (control versus PD) was a

Linear regression model predicting cortical BPnd in 60 subjects^a

Variable	Unstandardized β	Standardized β	P Value
CP calcium volume	2.77E ⁻⁵	0.324	.017
Age	0.001	0.336	.017
CP volume	-1.78E ⁻⁵	-0.256	.181
Ventricle volume	4.97E ⁻⁷	0.219	.230
Sex	0.006	0.127	.310
BMI	-0.001	-0.145	.267
Diagnosis (control or PD)	0.002	0.041	.751

^a Only CP calcium and age were significant predictors.

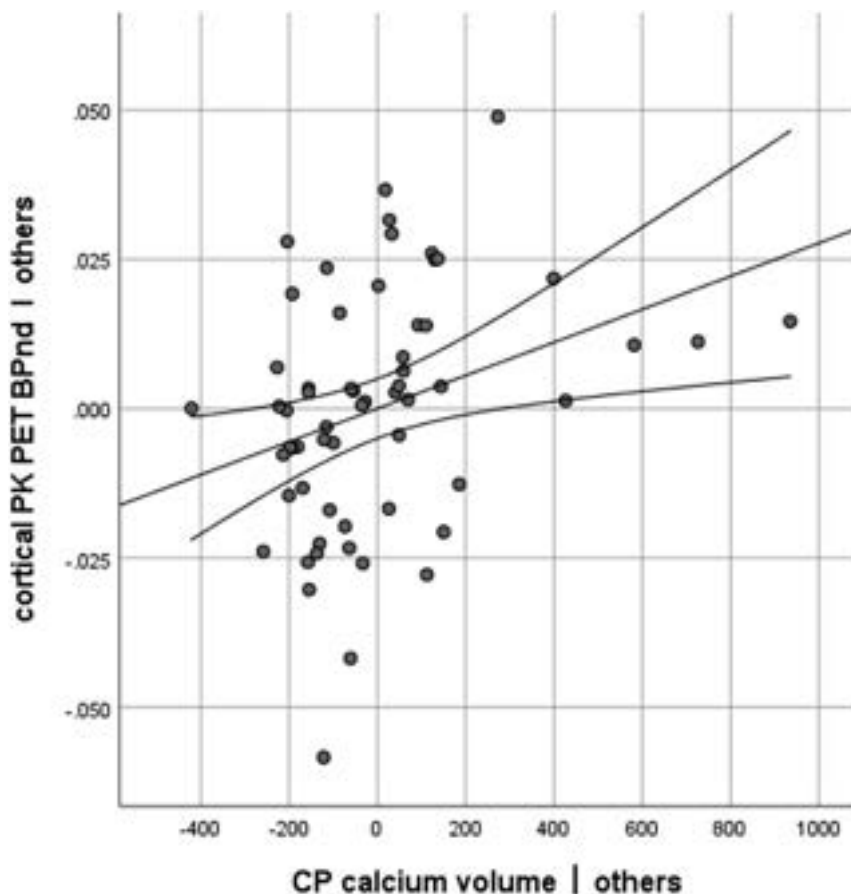


FIG 2. Partial regression plot showing the relation of CP calcium to PK BPnd in 60 subjects when controlling for the other variables (CP overall volume, ventricle volume, age, sex, BMI, and diagnosis [PD or control]).

significant predictor of cortical BPnd, and no interaction terms were significant.

Exploratory Group Differences

As shown in the Online Supplemental Data, there were no significant differences in the neuroimaging parameters of interest (CP calcium volume, CP overall volume, PK PET cortical BPnd) between subjects with PD and controls, though there was a nonsignificant trend ($P = .078$) for subjects with PD to have greater cortical BPnd than controls. BPnd in other brain regions also did not differ between subjects with PD and controls (all $P > .1$). These results are shown in the Online Supplemental Data, along with an example of a PK PET scan with normal findings illustrating typical regional TSPO expression.

DISCUSSION

We show that the volume of calcium within CP—but not CP overall volume—is associated with TSPO PET-measured cortical neuroinflammation and provides a method for accurately and automatically measuring CP calcium volume using MRI and low-dose CT. This method was highly congruent ($ICC = 0.98$) with the gold standard of manual tracing. We discuss implications of these findings as well as important limitations.

CP Calcification May Account for Prior Findings of CP Enlargement in Association with Neuroinflammatory Disease

Our results shed light on the basis of pathologic CP enlargement increasingly recognized in association with human inflammatory and neurodegenerative diseases.^{6-8,10,11} It is possible that unmeasured CP calcium can explain prior findings of CP enlargement in human aging and disease, including highly relevant recent findings of CP enlargement in association with TSPO PET-measured inflammation in MS and depression.^{6,11} Additional work, including studies linking in vivo or ex vivo neuroimaging of the human CP to direct tissue assessment, would be needed to determine more precisely the contribution of calcium and other CP histologic features to MRI-measured volume of the CP and its relation with neuroinflammation. It will also be important to determine whether our finding that CP calcification but not CP overall volume predicts cortical TSPO expression, which we have demonstrated in subjects without known neuroinflammatory disease, holds true in

subjects with more prominent neuroinflammation as occurs in MS.

CP Calcification as a Potential Biomarker for Neuroinflammation

Assessing neuroinflammation in humans is challenging, and current methods are limited to TSPO PET, which has well-known limitations, including a low SNR and poor availability outside academic medical centers.^{25,26} Our finding that CP calcification correlated significantly with cortical TSPO expression, coupled with our automated method for quantifying CP calcification using low-dose CT, suggests the potential for CP calcification to serve as a relatively easily acquired biomarker or proxy for neuroinflammation.

Because our results are based on a convenience sample of subjects and do not include subjects with overt neuroinflammatory disease, additional work would be needed to determine whether CP calcification correlates with TSPO PET in diseases associated with more severe neuroinflammation like MS. It would also be important to determine whether CP calcification changes in response to anti-inflammatory therapy. While brain calcium deposits are often considered permanent and life-long, a recent study using [¹⁸F]-NaF PET showed that the calcium in the CP may be uniquely metabolically active and potentially dynamic.³⁹ Furthermore, parenchymal calcification associated with neonatal toxoplasmosis has been shown to diminish with antimicrobial treatment.⁴⁰

CP Calcification Explains Interindividual Variability in TSPO PET

Wide and unexplained interindividual variability in TSPO PET is a known limitation of this technique, making detection of disease-specific alterations challenging.^{25,26} Our multiple regression model including age and CP calcium explained 30% of the variability in cortical TSPO expression. While this explanatory power may seem modest, it is similar to the effect of the TSPO gene rs6971 polymorphism that defines high-, low-, and mixed-affinity binders in studies using second-generation TSPO PET tracers (but not studies like this one using the first-generation tracer PK).^{41,42} Studies using second-generation TSPO tracers must genetically screen all subjects because accounting for this polymorphism is essential for data interpretation. Similarly, accounting for CP calcification would be expected to reduce unexplained variability in TSPO PET studies, improving interpretability and facilitating detection of effects of interest.

No Significant Differences between Subjects with PD and Controls

Although not the focus of this study, in exploratory analyses, we assessed CP calcification, CP volume, and cortical neuroinflammation in subjects with PD compared with controls and did not find any significant differences. Normal CP volume in PD is in accord with 1 prior study.⁸ There was a trend ($P = .078$) for subjects with PD to have greater cortical TSPO expression than controls. Prior TSPO PET studies of PD have provided variable results: Some show increased TSPO expression in regions including the cortex, basal ganglia, and midbrain compared with controls,^{43,44} though others show no significant differences.⁴⁵ Current negative results in this relatively small sample of subjects with PD cannot resolve the controversy over this issue. Our finding that subject diagnosis did not affect the correlation between CP calcification and cortical neuroinflammation suggests that this correlation may be a general phenomenon, potentially broadly relevant in human health and disease. Additional work in larger and more diagnostically diverse groups of subjects is needed.

Usefulness of Low-Dose CT Acquired with PET to Measure CP Calcification

Because most human PET studies are currently performed using PET/CT machines, an association of CP calcification with any type of PET-measured molecular information can be assessed with no additional cost or radiation exposure. For example, CP dysfunction

has been posited to play an early etiologic role in AD.⁷⁻⁹ Whether CP calcification predicts AD protein deposition could be assessed using existing longitudinal neuroimage repositories if the CT portion of the PET/CT were recognized as valuable and made available.

Limitations

This study has several important limitations.

This is a cross-sectional study demonstrating a correlation between CP calcification and cortical neuroinflammation. Results suggest that CP calcification, which is simple to measure, could serve as a biomarker for cortical inflammation, which is much more difficult to measure. However, this study cannot clarify causality, the mechanism linking these 2 measures, nor whether increased cortical TSPO expression may be detrimental or beneficial. While PET-measured TSPO expression has traditionally been considered to reflect an activated, proinflammatory, detrimental microglial phenotype termed M2 (versus a resting M1 phenotype associated with the maintenance of homeostasis), it is now recognized that this bimodal scheme is an oversimplification and that microglial phenotypes and functions cannot be fully characterized using a probe for a single molecule.⁴⁶ A recent study using an animal model of Fahr disease found that activated microglia were beneficial in regulating calcification and preventing neurodegeneration.⁴⁷ The question of whether such homeostatic interplay between microglia and calcification occurs in humans and whether it may be altered in diseases such as MS and AD associated with microglial dysfunction^{1-6,48} requires additional longitudinal study.

Another limitation of this study is that TSPO is expressed in the brain not just by microglia but by several cell types including other brain macrophages, astrocytes, vascular endothelial cells, and possibly neurons.^{24,49,50} Meningeal macrophages⁵¹ bordering the cortical ROI in this study may contribute to the cortical signal. Because of these limitations of TSPO PET imaging, there is intense interest in identifying new neuroimaging methods to quantify neuroinflammation in vivo in humans.²⁴⁻²⁶ However, currently, TSPO PET remains the only available research option, and we apply optimal image processing and analysis methods in this study.³²

It is a limitation that our analysis is retrospective and based on a relatively small convenience sample of heterogeneous subjects (controls and subjects with PD) scanned for different projects and that we did not include subjects with a definite neuroinflammatory disease like MS. Future prospective studies including additional patient populations are needed to determine whether the association of CP calcification with cortical TSPO expression that we have demonstrated holds true when the range of neuroinflammation across subjects is greater. Replication and extension of our findings in greater numbers of subjects and in different disease states is necessary and would be facilitated by the inclusion of the CT portion of PET/CT studies in public neuroimage repositories. Our results show that information about CP calcification present in low-dose CT is valuable and should not be discarded.

CONCLUSIONS

CP calcification volume can be reliably quantified using semiautomated tracing on low-dose CT acquired with PET/CT and fully

automatically using our new, accurate (ICC with semimanual tracing = 0.98) CT/MRI method. CP calcification and age—but not overall CP volume—significantly predicted PK PET-measured cortical neuroinflammation in this study. CP calcification is a relatively easily assessed, previously overlooked potential biomarker for neuroinflammation and CP pathology.

ACKNOWLEDGMENT

We are grateful to Steve Poulin, PhD, for assistance with statistical analyses.

Disclosure forms provided by the authors are available with the full text and PDF of this article at www.ajnr.org.

REFERENCES

1. Reboldi A, Coisne C, Baumjohann D, et al. **C-C chemokine receptor 6-regulated entry of TH-17 cells into the CNS through the choroid plexus is required for the initiation of EAE.** *Nat Immunol* 2009;10:514–23 CrossRef Medline
2. Kunis G, Baruch K, Rosenzweig N, et al. **IFN- γ -dependent activation of the brain's choroid plexus for CNS immune surveillance and repair.** *Brain* 2013;136:3427–40 CrossRef Medline
3. Schwartz M, Baruch K. **The resolution of neuroinflammation in neurodegeneration: leukocyte recruitment via the choroid plexus.** *EMBO J* 2014;33:7–22 CrossRef Medline
4. Manouchehri N, Stuve O. **Choroid plexus volumetrics and brain inflammation in multiple sclerosis.** *Proc Natl Acad Sci U S A* 2021;118:e2115221118 CrossRef Medline
5. Fleischer V, Gonzalez-Escamilla G, Ciolac D, et al. **Translational value of choroid plexus imaging for tracking neuroinflammation in mice and humans.** *Proc Natl Acad Sci U S A* 2021;118:e2025000118 CrossRef Medline
6. Ricigliano VA, Morena E, Colombi A, et al. **Choroid plexus enlargement in inflammatory multiple sclerosis: 3.0-T MRI and translocator protein PET evaluation.** *Radiology* 2021;301:166–77 CrossRef Medline
7. Choi JD, Moon Y, Kim HJ, et al. **Choroid plexus volume and permeability at brain MRI within the Alzheimer disease clinical spectrum.** *Radiology* 2022;304:635–45 CrossRef Medline
8. Tadayon E, Pascual-Leone A, Press D, et al; Alzheimer's Disease Neuroimaging Initiative. **Choroid plexus volume is associated with levels of CSF proteins: relevance for Alzheimer's and Parkinson's disease.** *Neurobiol Aging* 2020;89:108–17 CrossRef Medline
9. Alvira-Botero X, Carro EM. **Clearance of amyloid-beta peptide across the choroid plexus in Alzheimer's disease.** *Curr Aging Sci* 2010;3:219–29 CrossRef Medline
10. Alisch JS, Kiely M, Triebswetter C, et al. **Characterization of age-related differences in the human choroid plexus volume, microstructural integrity, and blood perfusion using multiparameter magnetic resonance imaging.** *Front Aging Neurosci* 2021;13:734992 CrossRef Medline
11. Althubaity N, Schubert J, Martins D, et al. **Choroid plexus enlargement is associated with neuroinflammation and reduction of blood brain barrier permeability in depression.** *Neuroimage Clin* 2022;33:102926 CrossRef Medline
12. Egorova N, Gottlieb E, Khlif MS, et al. **Choroid plexus volume after stroke.** *Int J Stroke* 2019;14:923–30 CrossRef Medline
13. Živković VS, Stanojković MM, Antić MM. **Psammoma bodies as signs of choroid plexus ageing: a morphometric analysis.** *Vojnosanitetski Pregled* 2017;74:1054–59 CrossRef
14. Alcolado JC, Moore IE, Weller RO. **Calcification in the human choroid plexus, meningiomas and pineal gland.** *Neuropathol Appl Neurobiol* 1986;12:235–50 CrossRef Medline
15. Wolburg H, Paulus W. **Choroid plexus: biology and pathology.** *Acta Neuropathol* 2010;119:75–88 CrossRef Medline
16. Emerich DF, Skinner SJ, Borlongan CV, et al. **The choroid plexus in the rise, fall and repair of the brain.** *Bioessays* 2005;27:262–74 CrossRef Medline
17. Dyke CG. **Indirect signs of brain tumor as noted in routine roentgen examinations: displacement of the pineal shadow (a survey of 3000 consecutive skull examinations).** *AJR Am J Roentgenol* 1930;23:598–606
18. Modic M, Weinstein M, Rothner A, et al. **Calcification of the choroid plexus visualized by computed tomography.** *Radiology* 1980;135:369–72 CrossRef Medline
19. Nicolas G, Charbonnier C, Campion D, et al. **Estimation of minimal disease prevalence from population genomic data: application to primary familial brain calcification.** *Am J Med Genet B Neuropsychiatr Genet* 2018;177:68–74 CrossRef Medline
20. Adams LC, Bressemer K, Böker SM, et al. **Diagnostic performance of susceptibility-weighted magnetic resonance imaging for the detection of calcifications: a systematic review and meta-analysis.** *Sci Rep* 2017;7:15506 CrossRef Medline
21. Wehrli FW. **Magnetic resonance of calcified tissues.** *J Magn Reson* 2013;229:35–48 CrossRef Medline
22. Wen Y, Spincemaille P, Nguyen T, et al. **Multiecho complex total field inversion method (mcTFI) for improved signal modeling in quantitative susceptibility mapping.** *Magn Reson Med* 2021;86:2165–78 CrossRef Medline
23. Kreisl WC, Kim MJ, Coughlin JM, et al. **PET imaging of neuroinflammation in neurological disorders.** *Lancet Neurol* 2020;19:940–50 CrossRef Medline
24. Guilarte TR, Rodichkin AN, McGlothlan JL, et al. **Imaging neuroinflammation with TSPO: a new perspective on the cellular sources and subcellular localization.** *Pharmacol Ther* 2022;234:108048 CrossRef Medline
25. Jain P, Chaney AM, Carlson ML, et al. **Neuroinflammation PET imaging: current opinion and future directions.** *J Nucl Med* 2020;61:1107–12 CrossRef Medline
26. Janssen B, Vugets DJ, Windhorst AD, et al. **PET imaging of microglial activation: beyond targeting TSPO.** *Molecules* 2018;23:607 CrossRef Medline
27. Hughes AJ, Daniel SE, Kilford L, et al. **Accuracy of clinical diagnosis of idiopathic Parkinson's disease: a clinico-pathological study of 100 cases.** *J Neurol Neurosurg Psychiatry* 1992;55:181–84 CrossRef Medline
28. Jenkinson M, Bannister P, Brady M, et al. **Improved optimization for the robust and accurate linear registration and motion correction of brain images.** *Neuroimage* 2002;17:825–41 CrossRef Medline
29. Smith SM, Jenkinson M, Woolrich MW, et al. **Advances in functional and structural MR image analysis and implementation as FSL.** *Neuroimage* 2004;23:S208–19 CrossRef Medline
30. Butler T, Li Y, Tsui W, et al. **Transient and chronic seizure-induced inflammation in human focal epilepsy.** *Epilepsia* 2016;57:e191–94 CrossRef Medline
31. Schubert J, Tonietto M, Turkheimer F, et al. **Supervised clustering for TSPO PET imaging.** *Eur J Nucl Med Mol Imaging* 2021;49:257–68 CrossRef Medline
32. Wimberley C, Lavis S, Hillmer A, et al. **Kinetic modeling and parameter estimation of TSPO PET imaging in the human brain.** *Eur J Nucl Med Mol Imaging* 2021;49:246–56 CrossRef Medline
33. Fischl B, Salat DH, Busa E, et al. **Whole brain segmentation: automated labeling of neuroanatomical structures in the human brain.** *Neuron* 2002;33:341–55 CrossRef Medline
34. Yalcin A, Ceylan M, Bayraktutan OF, et al. **Age and gender related prevalence of intracranial calcifications in CT imaging; data from 12,000 healthy subjects.** *J Chem Neuroanat* 2016;78:20–24 CrossRef Medline
35. Avants BB, Tustison NJ, Song G, et al. **A reproducible evaluation of ANTs similarity metric performance in brain image registration.** *Neuroimage* 2011;54:2033–44 CrossRef Medline

36. Sethian JA. *Level Set Methods and Fast Marching Methods: Evolving interfaces in computational geometry, fluid mechanics, computer vision, and materials science*. Cambridge University Press; 1999
37. Arthur D, Vassilvitskii S. **k-means++ the advantages of careful seeding**. Proceedings of the eighteenth annual ACM-SIAM symposium on Discrete algorithms (2007, January, pp 1027–1035).
38. Tuisku J, Plavén-Sigra P, Gaiser EC, et al; HRRRT [¹¹C] PBR28 Study Group. **Effects of age, BMI and sex on the glial cell marker TSPO: a multicentre [¹¹C] PBR28 HRRRT PET study**. *Eur J Nucl Med Mol Imaging* 2019;46:2329–38 CrossRef Medline
39. Al-Zaghal A, Seraj SM, Werner TJ, et al. **Assessment of physiologic intracranial calcification in healthy adults using 18F-NaF PET/CT**. *J Nucl Med* 2018 Jul 12. [Epub ahead of print] CrossRef
40. Patel DV, Holfels EM, Vogel NP, et al. **Resolution of intracranial calcifications in infants with treated congenital toxoplasmosis**. *Radiology* 1996;199:433–40 CrossRef Medline
41. Suridjan I, Rusjan P, Voineskos AN, et al. **Neuroinflammation in healthy aging: a PET study using a novel translocator protein 18 kDa (TSPO) radioligand, [18F]-FEPPA**. *Neuroimage* 2014;84:868–75 CrossRef Medline
42. Owen DR, Yeo AJ, Gunn RN, et al. **An 18-kDa translocator protein (TSPO) polymorphism explains differences in binding affinity of the PET radioligand PBR28**. *J Cereb Blood Flow Metab* 2012;32:1–5 CrossRef Medline
43. Gerhard A. **TSPO imaging in parkinsonian disorders**. *Clin Transl Imaging* 2016;4:183–90 CrossRef Medline
44. Zhang PF, Gao F. **Neuroinflammation in Parkinson's disease: a meta-analysis of PET imaging studies**. *J Neurol* 2022;269:2304–14 CrossRef Medline
45. Ghadery C, Koshimori Y, Coakeley S, et al. **Microglial activation in Parkinson's disease using [18 F]-FEPPA**. *J Neuroinflammation* 2017;14:8 CrossRef Medline
46. Salter MW, Stevens B. **Microglia emerge as central players in brain disease**. *Nat Med* 2017;23:1018–27 CrossRef Medline
47. Zarb Y, Sridhar S, Nassiri S, et al. **Microglia control small vessel calcification via TREM2**. *Sci Adv* 2021;7:eabc4898 CrossRef Medline
48. Hansen DV, Hanson JE, Sheng M. **Microglia in Alzheimer's disease**. *J Cell Biol* 2018;217:459–72 CrossRef Medline
49. Gui Y, Marks JD, Das S, et al. **Characterization of the 18 kDa translocator protein (TSPO) expression in post-mortem normal and Alzheimer's disease brains**. *Brain Pathol* 2020;30:151–64 CrossRef Medline
50. Notter T, Schalbetter SM, Clifton NE, et al. **Neuronal activity increases translocator protein (TSPO) levels**. *Mol Psychiatry* 2021;26:2025–37 CrossRef Medline
51. Mildenerger W, Stifter SA, Greter M. **Diversity and function of brain-associated macrophages**. *Curr Opin Immunol* 2022;76:102181 CrossRef Medline

Cost-Effectiveness Analysis of ⁶⁸Ga-DOTATATE PET/MRI in Radiotherapy Planning in Patients with Intermediate-Risk Meningioma

J. Rodriguez, G. Martinez, S. Mahase, M. Roytman, A. Haghdel, S. Kim, G. Madera, R. Magge, P. Pan, R. Ramakrishna, T.H. Schwartz, S.C. Pannullo, J.R. Osborne, E. Lin, J.P.S. Knisely, P.C. Sanelli, and J. Ivanidze



ABSTRACT

BACKGROUND AND PURPOSE: While contrast-enhanced MR imaging is the criterion standard in meningioma diagnosis and treatment response assessment, gallium ⁶⁸Ga-DOTATATE PET/MR imaging has increasingly demonstrated utility in meningioma diagnosis and management. Integrating ⁶⁸Ga-DOTATATE PET/MR imaging in postsurgical radiation planning reduces the planning target volume and organ-at-risk dose. However, ⁶⁸Ga-DOTATATE PET/MR imaging is not widely implemented in clinical practice due to higher perceived costs. Our study analyzes the cost-effectiveness of ⁶⁸Ga-DOTATATE PET/MR imaging for postresection radiation therapy planning in patients with intermediate-risk meningioma.

MATERIALS AND METHODS: We developed a decision-analytical model based on both recommended guidelines on meningioma management and our institutional experience. Markov models were implemented to estimate quality-adjusted life-years (QALY). Cost-effectiveness analyses with willingness-to-pay thresholds of \$50,000/QALY and \$100,000/QALY were performed from a societal perspective. Sensitivity analyses were conducted to validate the results. Model input values were based on published literature.

RESULTS: The cost-effectiveness results demonstrated that ⁶⁸Ga-DOTATATE PET/MR imaging yields higher QALY (5.47 versus 5.05) at a higher cost (\$404,260 versus \$395,535) compared with MR imaging alone. The incremental cost-effectiveness ratio analysis determined that ⁶⁸Ga-DOTATATE PET/MR imaging is cost-effective at a willingness to pay of \$50,000/QALY and \$100,000/QALY. Furthermore, sensitivity analyses showed that ⁶⁸Ga-DOTATATE PET/MR imaging is cost-effective at \$50,000/QALY (\$100,000/QALY) for specificity and sensitivity values above 76% (58%) and 53% (44%), respectively.

CONCLUSIONS: ⁶⁸Ga-DOTATATE PET/MR imaging as an adjunct imaging technique is cost-effective in postoperative treatment planning in patients with meningiomas. Most important, the model results show that the sensitivity and specificity cost-effective thresholds of ⁶⁸Ga-DOTATATE PET/MR imaging could be attained in clinical practice.

ABBREVIATIONS: CTCAE = Common Terminology Criteria for Adverse Events; EBRT = external beam radiotherapy; GTR = gross total resection; PFS = progression-free survival; QALY = quality-adjusted life-years; RT = radiotherapy; SRS = stereotactic radiosurgery; SSTR2A = somatostatin receptor 2A; WHO = World Health Organization; WTP = willingness to pay

Meningiomas are the most common primary benign brain neoplasms.¹ Surgery is the primary management, particularly for larger or symptomatic tumors. The World Health Organization (WHO) classification stratifies patients on the basis

of histopathologic features (number of mitotic figures per high-power field), and it is used in prognostication and postoperative radiation therapy planning. While most meningiomas are grade 1, approximately 15%–20% are grade 2 or 3, demonstrating more

Received November 8, 2022; accepted after revision May 7, 2023.

From the Department of Radiology (J.R., M.R., A.H., S.K., G. Madera, J.R.O., E.L., J.I.), Brain Tumor Center, (R.M.), Department of Neurological Surgery (R.R., T.H.S., S.C.P.), and Department of Radiation Oncology (J.P.S.K.), Weill Cornell Medicine, New York, New York; Siemens Healthineers (G. Martinez), Malvern, Pennsylvania; Department of Radiation Oncology (S.M.), Penn State Health, Mechanicsburg, Pennsylvania; Department of Neurology (P.P.), Columbia University Medical Center, New York, New York; Meinig School of Biomedical Engineering (S.C.P.), Cornell University, Ithaca, New York; Department of Radiology (P.C.S.), Donald and Barbara Zucker School of Medicine at Hofstra/Northwell, Hempstead, New York; and Imaging Clinical Effectiveness and Outcomes Research Program (G. Martinez, P.C.S.), Health System Science, Feinstein Institutes for Medical Research, Manhasset, New York.

J. Rodriguez and G. Martinez contributed equally to this work.

This work was partially supported by Novartis Pharmaceuticals, No.: CAAA501A0U505T, investigator-initiated trial grant; Principal Investigator: J. Ivanidze; Radiological Society of North America Resident Research Grant; Principal Investigator: M. Roytman; Radiological Society of North America Medical Student Research Grant; Principal Investigator: S. Kim; as well as the Clinical and Translational Science Center National Institutes of Health Predoctoral Training Award, Principal Investigator: A. Haghdel.

Please address correspondence to Jana Ivanidze, MD, PhD, Department of Diagnostic Radiology, Weill Cornell Medicine, 525 East 68th St, Starr 2, Office ST205, New York, NY 10065; e-mail: jai9018@med.cornell.edu; @jana_ivanidze; @JoseA_Rodr; @MGabriela_ML

Indicates open access to non-subscribers at www.ajnr.org

Indicates article with online supplemental data.

<http://dx.doi.org/10.3174/ajnr.A7901>

aggressive behavior and worse prognosis. Gross total resection (GTR) is not achieved in up to 50%, with resulting lower rates of progression-free survival (PFS).²

Surgery is the standard of care for meningiomas. Current postoperative management, especially in intermediate risk meningiomas, is currently not based on level 1 evidence. Patients with WHO grades 2 and 3 meningiomas are treated with a combination of surgery and postoperative irradiation.³ Treatment choice (radiotherapy [RT], re-operation, and active surveillance) is highly individualized and depends on tumor location, degree of progression, associated clinical symptoms, and the preference of the patient and treating physician.^{3,4} While re-operation can be an option in selected patients, overall patients undergoing re-operation for recurrent meningioma have been shown to have higher rates of postoperative complications and worse clinical outcomes.^{5,6} External beam radiation therapy (EBRT) and stereotactic radiosurgery (SRS) may improve clinical outcomes in patients with a higher risk of recurrence, including high-grade and recurring meningiomas.⁷ However, the role of EBRT for meningiomas is currently being evaluated.⁸ The NRG Oncology RTOG 0539 trial is an international Phase II trial assessing the benefits of RT in intermediate risk meningiomas, defined as recurrent WHO grade 1 meningiomas after either GTR or subtotal resection and new WHO grade 2 meningiomas after GTR. Rogers et al³ reported a 3-year PFS rate of 93.7% with minimal radiation-induced adverse events, validating the use of postoperative RT for intermediate-risk meningiomas. These results emphasize the importance of optimizing target delineation in postoperative RT planning of intermediate-risk meningiomas.

Accurate tumor delineation is critical for optimal radiation planning, as well as to minimize radiation-induced complications. Contrast-enhanced MR imaging is the standard of care for postoperative RT planning.³ However, MR imaging has many limitations regarding tumor delineation, particularly in the context of infiltrative or en plaque lesions, lesions with osseous or parenchymal invasion, and in differentiating residual tumor from postsurgical scarring or inflammation.^{7,9}

Somatostatin receptor 2A (SSTR2A) is overexpressed in meningiomas and is a highly sensitive and specific meningioma biomarker.^{10,11} Gallium ⁶⁸Ga-DOTATATE is a PET radiotracer binding SSTR2A with high affinity. It is widely used clinically for gastrointestinal neuroendocrine tumors, which also overexpress SSTR2A.¹² ⁶⁸Ga-DOTATATE PET/CT demonstrated marked improvement in the sensitivity for detection of osseous involvement of meningiomas compared with MR imaging (98.5% versus 53.7%), while maintaining a high specificity (86.7% versus 93.3%).¹³ Most important, the improved sensitivity of ⁶⁸Ga-DOTATATE PET for differentiating residual meningiomas from postsurgical dural thickening and enhancement may improve RT target volume delineation, thereby improving clinical outcomes. Improved tumor delineation reduces RT doses and RT burden to surrounding tissue and organs at risk by allowing more accurate targeting of tumors, thereby improving PFS while decreasing radiation-induced toxicity and tumor recurrence.^{7,14-18}

PET/MR imaging has been increasingly used clinically during the past decade. PET/MR imaging exposes patients to less

radiation because MR imaging is used for attenuation correction obviating the need to acquire a CT scan. Additional key advantages include increased soft-tissue contrast and increased patient convenience and resource use, given that PET/MR imaging obviates the need for 2 separate studies.

We hypothesize that ⁶⁸Ga-DOTATATE PET/MR imaging reduces health care costs due to a lower risk of both meningioma progression and radiation-induced complications after RT. To examine our hypothesis, we conducted a model-based cost-effectiveness analysis of ⁶⁸Ga-DOTATATE PET/MR imaging for RT planning of intermediate-risk meningiomas in the US health care setting.

MATERIALS AND METHODS

Study Cohort

The modeled cohort represents patients with nonmalignant meningioma who are status post resection, with a mean age of 58 years based on the published mean age at diagnosis.¹⁵ The cohort was divided in our model into 2 broad groups based on treatment eligibility as recommended in the European Association of Neuro-Oncology (EANO): 1) RT-eligible patients: intermediate-risk meningioma defined in accordance to the RTOG 0539 ongoing Phase II clinical trial as patients with either newly diagnosed and completely resected (as assessed by MR imaging) WHO grade 2 meningiomas or recurrent WHO grade 1 meningiomas; and 2) patients under active surveillance: nonrecurrent WHO grade 1 meningioma.

WHO grade 3 meningiomas were not included in our study, given the lack of literature data specifically analyzing WHO grade 3 outcomes.

Decision-Analytic Model

We developed a decision-analytic model from a societal perspective in TreeAge Pro 2021 (TreeAge Software) to compare adjunct ⁶⁸Ga-DOTATATE PET/MR imaging (“new strategy”) with MR imaging alone (“standard strategy”) for postresection meningioma evaluation and RT planning of intermediate-risk nonmalignant meningioma in terms of clinical outcomes and costs.

Treatment and management decisions followed the EANO guidelines on postresection RT for nonmalignant meningiomas.⁴ Patients in the model undergo tumor delineation and are selected for RT or active surveillance on the basis of the MR imaging or ⁶⁸Ga-DOTATATE PET/MR imaging results as follows: 1) Patients with imaging findings showing the presence of residual intermediate-risk meningioma after subtotal resection are selected for RT with the EBRT or SRS technique;¹⁹ 2) patients with imaging findings showing gross total resection are selected for active surveillance. Given the present lack of level 1 evidence for RT versus active surveillance in meningioma, we modeled the outcomes of these patients on the basis of the cohort in the study of Mirimanoff et al,²⁰ reporting the recurrence and progression of patients with nonmalignant meningiomas following an operation.

The follow-up imaging used in both strategies follows the main recommendations endorsed by the National Comprehensive Cancer Network, consisting of imaging follow-up every 6 months for the first 2 years and every year thereafter.²¹

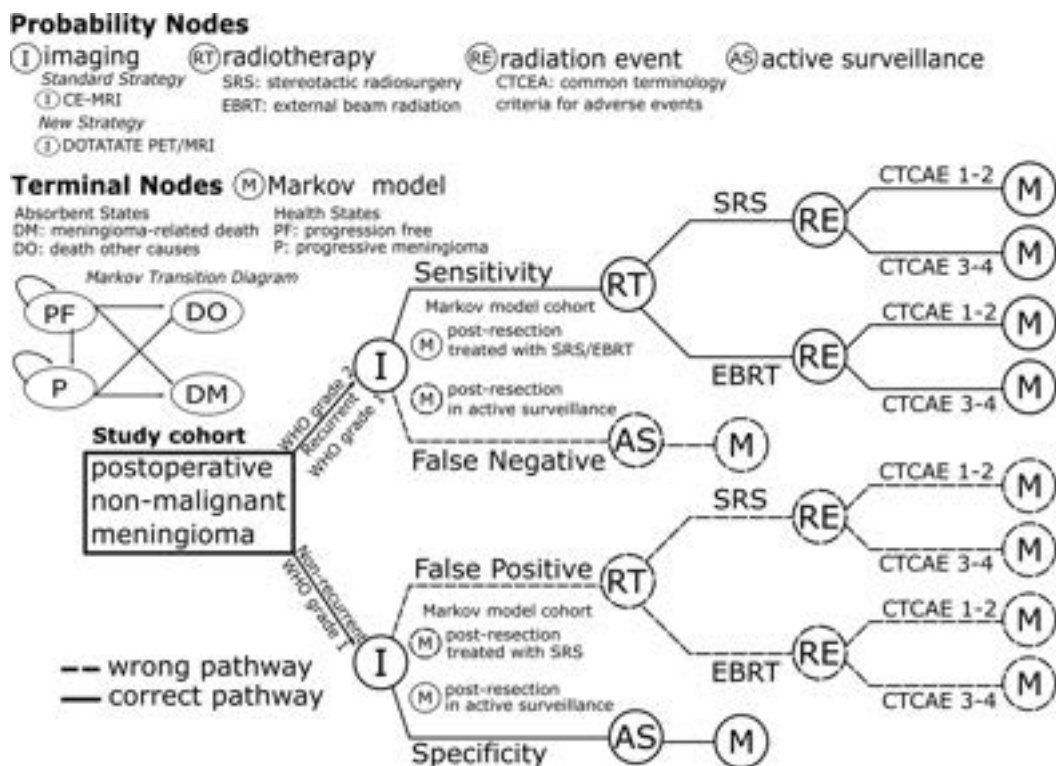


FIG 1. Schematic representation of the decision-analytic model structure. The study cohort represents patients with nonmalignant meningioma status post resection. Patients with imaging findings of residual disease undergo RT. Following RT with either SRS or EBRT, the model accounts for the risk of toxicity as defined by the CTCAE classified as CTCAE 1–2 or CTCAE 3–4. The terminal nodes of the decision tree are Markov models with health states representing the status of the meningioma: progression-free, progression, or death (meningioma or other causes). The initial transition in the Markov models is determined by the assigned subcohort to a treatment plan (RT or active surveillance) based on the imaging results. Sensitivity and specificity were incorporated in the clinical pathways to properly assess the downstream effects of the imaging results on patients’ outcomes and costs, as illustrated in the diagram by the wrong and correct pathways. For example, patients with intermediate-risk nonmalignant meningiomas should be triaged to RT with either SRS or EBRT per the recommended guidelines (pathway represented by the *solid-line* branches). However, on the basis of the sensitivity of imaging (standard strategy: MR imaging; new strategy: ^{68}Ga -DOTATATE PET-MR imaging), a proportion of these patients could be managed with active surveillance (pathway represented by the *dashed-line* branches), increasing their risk of progression in the Markov model. CE indicates contrast-enhanced.

We incorporated the sensitivity and specificity of residual/recurrent meningioma detection following surgical resection for ^{68}Ga -DOTATATE PET/MR imaging and MR imaging in the clinical pathways to assess the downstream effects of the treatment plan on the basis of the imaging results as illustrated in Fig 1.

Health Outcomes and Time Horizon

A Markov model was incorporated in the decision-analytic model to estimate the health outcomes and health care costs after intervention (RT or active surveillance). The health states of the Markov model were based on meningioma status and patient survival as follows: 1) stable (progression-free meningioma), 2) progression (worsened tumor burden), and 3) death (meningioma-related or other causes).

The Markov transitions were estimated with 1-year cycles. The initial transition corresponds to the observed health state after 1 year following intervention. Furthermore, the National Cancer Institute Common Terminology Criteria for Adverse Events (CTCAE)²² was used to model radiation risks at 1 year following radiation therapy. Radiation risks were categorized as CTCAE 1–2 in severity and CTCAE 3–4 in severity, and values were based on reported data for SRS and EBRT in meningiomas.^{7,23–26}

During the following 1-year cycles, patients could remain in the same health state (stable or progression), transition to a worse state (progression or meningioma-related death), or die (due to natural causes not associated with meningioma). The Markov transition probabilities were calculated with the PFS, overall survival, and mortality data of patients undergoing SRS or EBRT selected with MR imaging reported in the studies of Dohm et al²⁶ and Pollock et al,²⁵ respectively. Markov transitions for patients undergoing RT in the new strategy were based on the study by Zollner et al.²³ Markov transitions for patients with intermediate-risk and nonrecurrent WHO 1 meningiomas following active surveillance were based on the studies of Dohm et al²⁶ and Mirimanoff et al,²⁰ respectively.

At every Markov transition, health outcomes were measured with utility weights representing the quality of life at each health state. The utilities for stable and progression states were based on a cost-effectiveness analysis of RT for high-risk, low-grade gliomas due to limited meningioma-specific published data.²⁷ Costs included in the initial transition correspond to the cost of imaging, intervention and radiation-induced toxicity. Following the initial transition, the costs incorporated the cost of follow-up care (accounting for a visit to a physician and MR imaging every 6 months during the first 2 years and annually thereafter), progressive disease, and loss of

productivity caused by premature meningioma-related death. Indirect costs were calculated with the retirement age at 72 years.²⁸ A 3% discount rate was applied to both costs and utilities following the initial transition.²⁹

The age-based mortality risk was obtained from the US Social Security Administration for the general population.³⁰ Mortality hazard ratios were used in the model to adjust the mortality risk, given the presence of a meningioma.³¹ On the basis of data availability, a 10-year time horizon was implemented in the Markov model to assess the impact of the new strategy for treatment planning on the basis of the projected costs and outcomes.^{23,25,26,32}

Input Parameters

The probabilities of experiencing a CTCAE 1–2 or 3–4 event for patients treated with SRS and EBRT in the new strategy were derived from the studies of Mahase et al⁷ and Zollner et al,²³ respectively. Data from the studies of Dohm et al²⁶ and Pollock et al²⁵ were used in the standard strategy. The cost of ⁶⁸Ga-DOTATATE was based on the tracer costs of neuroendocrine tumors established by the Centers for Medicare and Medicaid Services. The costs of PET/MR imaging, MR imaging, SRS, and EBRT were based on Current Procedural Terminology codes and the Centers for Medicare and Medicaid Services data. The input parameter values and sources can be found in the Online Supplemental Data. All costs are reported in US dollars.

Cost-Effectiveness and Sensitivity Analyses

The base case analysis was conducted for the modeled cohort with the model input values listed in the Online Supplemental Data. The quality-adjusted life-years (QALY) was selected to measure the effectiveness of the strategies,³³ representing the projected quality of life, and it was estimated with the Markov model. Incremental cost-effectiveness ratio analyses were conducted to compare the strategies in which the society's willingness to pay (WTP) for QALY gained were used to define cost-effectiveness. The US recommended WTP threshold values of \$50,000/QALY and \$100,000/QALY were implemented in our analyses.^{29,34}

To evaluate the robustness of our results, we performed 1-way sensitivity and probabilistic sensitivity analyses to identify the key variables affecting the results in our model. The net monetary benefit metric was used in the 1-way sensitivity analyses.³¹ Probability distributions for the key model parameters were derived from conventional standards for the health utilities, probabilities, and costs. Furthermore, we evaluated the uncertainty of the results with respect to WTP thresholds ranging from \$40,000/QALY to \$400,000/QALY.^{35,36} The distribution type for the model input parameters is shown in the Online Supplemental Data.

RESULTS

Base Case Analyses

The cost-effectiveness results showed that the new strategy yields higher QALY (5.47 versus 5.05) at a higher cost (\$404,260 versus \$395,535) compared with the standard strategy, with an incremental cost-effectiveness ratio of \$20,877 per QALY (Table). Consequently, the new strategy is cost-effective at a WTP of \$50,000/QALY and \$100,000/QALY (Fig 2).

Sensitivity Analyses

One-way sensitivity analyses indicated that the key variables contributing to variations in the net monetary values at both a WTP of \$50,000/QALY (Fig 3) and \$100,000/QALY are the proportion of intermediate-risk meningiomas in the modeled cohort, the utility for the stable and progressive health states, and the specificity of ⁶⁸Ga-DOTATATE PET/MR imaging. Furthermore, the analyses identified that the new strategy is cost-effective at a WTP of \$50,000/QALY (\$100,000/QALY) when the proportion of intermediate-risk meningiomas of the modeled cohort is >12% (7%), the specificity of ⁶⁸Ga-DOTATATE PET/MR imaging is >76% (58%), and the sensitivity of ⁶⁸Ga-DOTATATE PET/MR imaging is >53% (44%); otherwise, the standard strategy is cost-effective.

We conducted a probabilistic sensitivity analysis accounting for the collective variation of the input-model values with 100,000 iterations. The results (Fig 4) indicated that the new strategy is cost-effective at a WTP of \$50,000/QALY (\$100,000/QALY) with a probability of 91% (96%). Furthermore, the cost-effectiveness acceptability curve showed that the new strategy is cost-effective at WTP values ranging from \$40,000/QALY to \$200,000/QALY, with a probability of 88%–99%, respectively. These results highlight the robustness of the cost-effectiveness results (Fig 5).

DISCUSSION

Recent studies support adjunct ⁶⁸Ga-DOTATATE PET use in RT planning for patients with intermediate-risk meningiomas.^{5,13–16} However, there is a dearth of literature exploring the cost-effectiveness of using ⁶⁸Ga-DOTATATE for this purpose. Consequently, we analyzed the cost-effectiveness of ⁶⁸Ga-DOTATATE PET/MR imaging to evaluate the practicality of incorporating it into clinical practice. Our study indicated that although the use of adjunct ⁶⁸Ga-DOTATATE PET/MR imaging as part of the imaging work-up for postoperative RT planning in patients with intermediate-risk meningioma is associated with higher health care costs, its use is cost-effective from a societal perspective. More specifically, the difference in health benefits between the use of adjunct ⁶⁸Ga-DOTATATE PET/MR imaging and MR imaging alone is 0.42 QALY, which translates to 5 additional months in perfect health.^{33,37} Moreover, the incremental cost-effectiveness ratio analysis indicated that ⁶⁸Ga-DOTATATE PET/MR imaging is cost-effective at a WTP of >\$20,877/QALY.

The sensitivity analyses established that the use of adjunct ⁶⁸Ga-DOTATATE PET/MR imaging is cost-effective at a WTP of \$50,000/QALY (\$100,000/QALY) as long as the specificity of ⁶⁸Ga-DOTATATE PET/MR imaging is >76% (58%) and the sensitivity of ⁶⁸Ga-DOTATATE PET/MR imaging is >53% (44%). A recent diagnostic accuracy analysis of ⁶⁸Ga-DOTATATE PET/MR imaging in 62 patients with meningiomas demonstrated a sensitivity and specificity of 86.7% and 80.5%, respectively, when using the standard uptake value ratio of the target lesion to superior sagittal sinus method.¹⁵ Therefore, the sensitivity and specificity in this published clinical cohort exceeded the thresholds needed to render PET/MR imaging cost-effective in our analysis. Most important, the probabilistic sensitivity analysis showed that ⁶⁸Ga-DOTATATE PET/MR imaging is cost-effective with a

probability of 91% (96%) at a WTP of \$50,000/QALY (\$100,000/QALY) when simultaneously varying the model input values according to their probability distribution.

Another insight from our analysis is that ^{68}Ga -DOTATATE PET/MR imaging is cost-effective at a WTP of \$50,000/QALY (\$100,000/QALY) when the proportion of intermediate-risk meningiomas is >12% (7%). Population-based studies have shown that the proportion of WHO grade 2 meningiomas varies from 15% to 20%.³⁸ Furthermore, recent studies have identified the increasing incidence trend of WHO grade 2 meningiomas, highlighting the importance of our results.³⁹

Our model-based cost-effectiveness findings were similar to published results on ^{68}Ga -DOTATATE PET/CT in patients with neuroendocrine tumors. A cost-effectiveness study performed by Froelich et al⁴⁰ determined that ^{68}Ga -DOTATATE PET/CT is cost-effective for detecting neuroendocrine tumors compared with Indium 111-pentetreotide SPECT/CT and CT alone, respectively. Froelich et al deemed it the most beneficial imaging approach for a diagnostic work-up of neuroendocrine tumors. The cost-consequence analysis conducted by Schreiter et al⁴¹ showed that the use of ^{68}Ga -DOTATOC PET/CT for staging

Cost-effectiveness analysis summary for the base case

	QALY	Cost (US \$)	ICER (US \$/QALY)
New strategy	5.47	404,260	20,877
Standard strategy	5.05	395,535	–

Note:—ICER indicates incremental cost-effectiveness ratio; the en dash indicates the reference strategy.

enteropancreatic neuroendocrine tumors reduces the overall use of health care resources.

Optimal radiosurgical planning relies on high-precision target volume delineation. In meningiomas, the gross target volume and clinical target volume are delineated on the basis of multimodal imaging. Although MR imaging is currently commonly used in clinical practice for tumor delineation, its accuracy is compromised in tumors located at high-contrast-enhancement areas or in tumors infiltrating the bone.¹³ Adjunct ^{68}Ga -DOTATATE PET/CT and PET/MR imaging allow more accurate delineation of meningiomas,^{9,13,15-18} particularly in the postoperative setting, thereby improving gross target volume and clinical target volume delineation and reducing RT-associated toxicity. In a recently published pilot study, ^{68}Ga -DOTATATE PET/MR imaging-based RT planning significantly reduced mean planning tumor volume to 11.12 cm³ from 71.39 cm³ on the basis of MR imaging alone.⁵ Moreover, the ^{68}Ga -DOTATATE PET maximum standard uptake value correlated with the tumor growth rate in meningiomas, providing additional information related to tumor biology compared with MR imaging alone, probably of importance for the design of future therapeutic trials.⁴² Allocating resources to perform such trials is further supported if clinical validation leads to implementing a cost-effective management change that improves patient outcomes.

The main limitation of our model design is the lack of long-term data regarding the use of ^{68}Ga -DOTATATE PET/MR imaging in patients with intermediate-risk meningiomas. Therefore, data

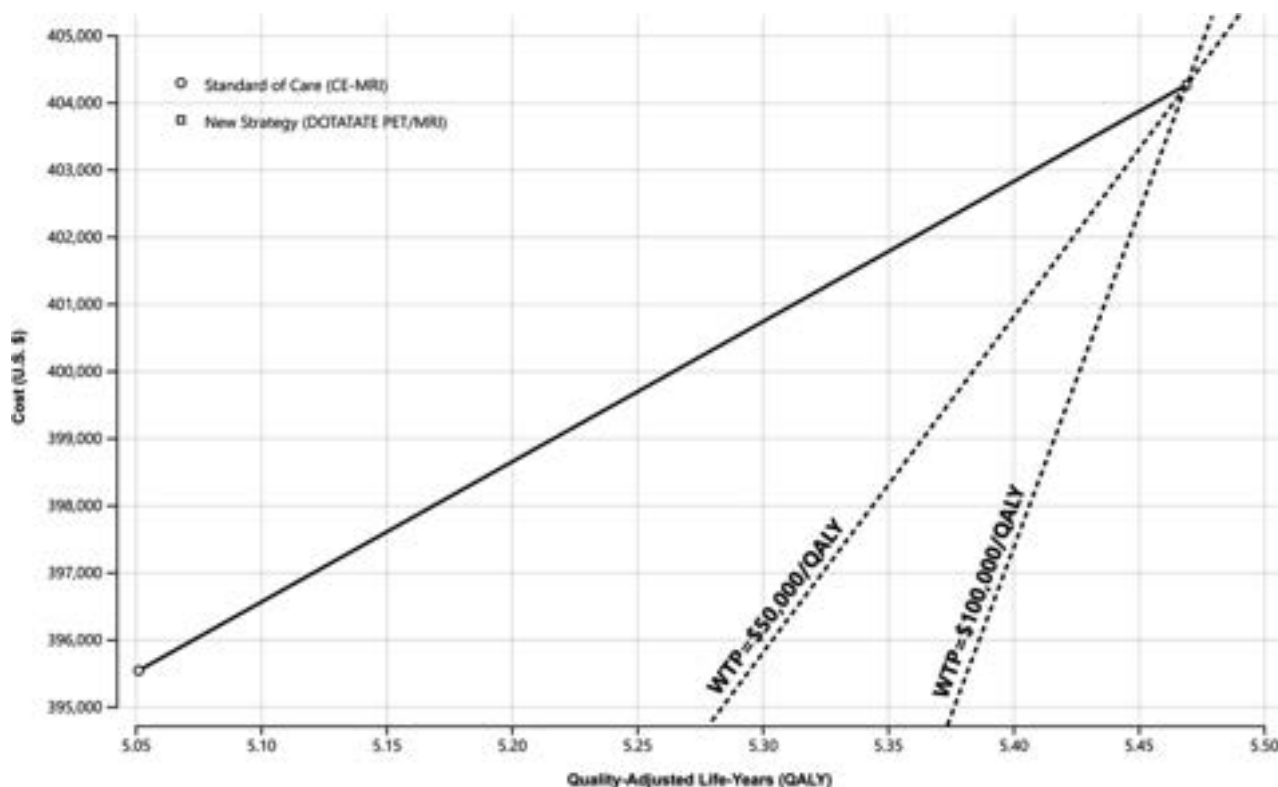


FIG 2. Cost-effectiveness analysis. The new strategy (^{68}Ga -DOTATATE PET/MR imaging) yields higher QALY at a higher cost compared with the standard strategy (MR imaging). Furthermore, the new strategy is cost-effective at \$50,000/QALY and \$100,000/QALY. CE indicates contrast-enhanced.

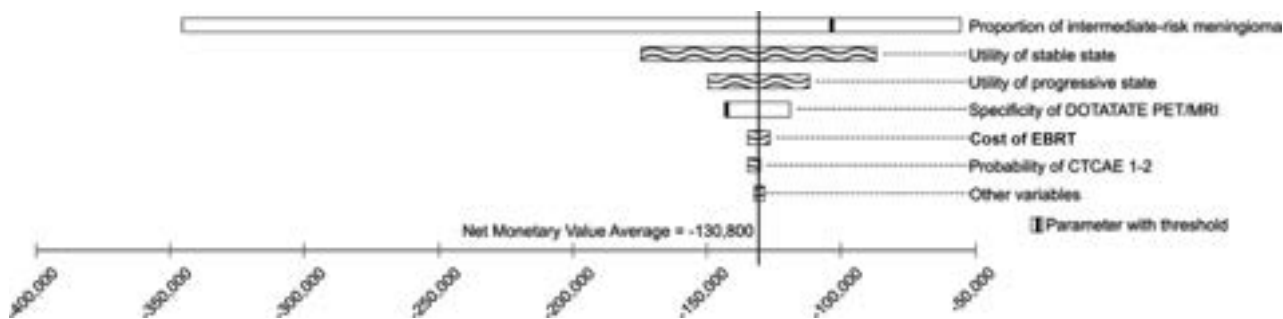


FIG 3. Tornado analysis demonstrating the set of model parameters that play a role in the variation of the results measured with a net monetary benefit at a WTP of \$50,000/QALY. Net monetary benefit = QALY × WTP – Cost.

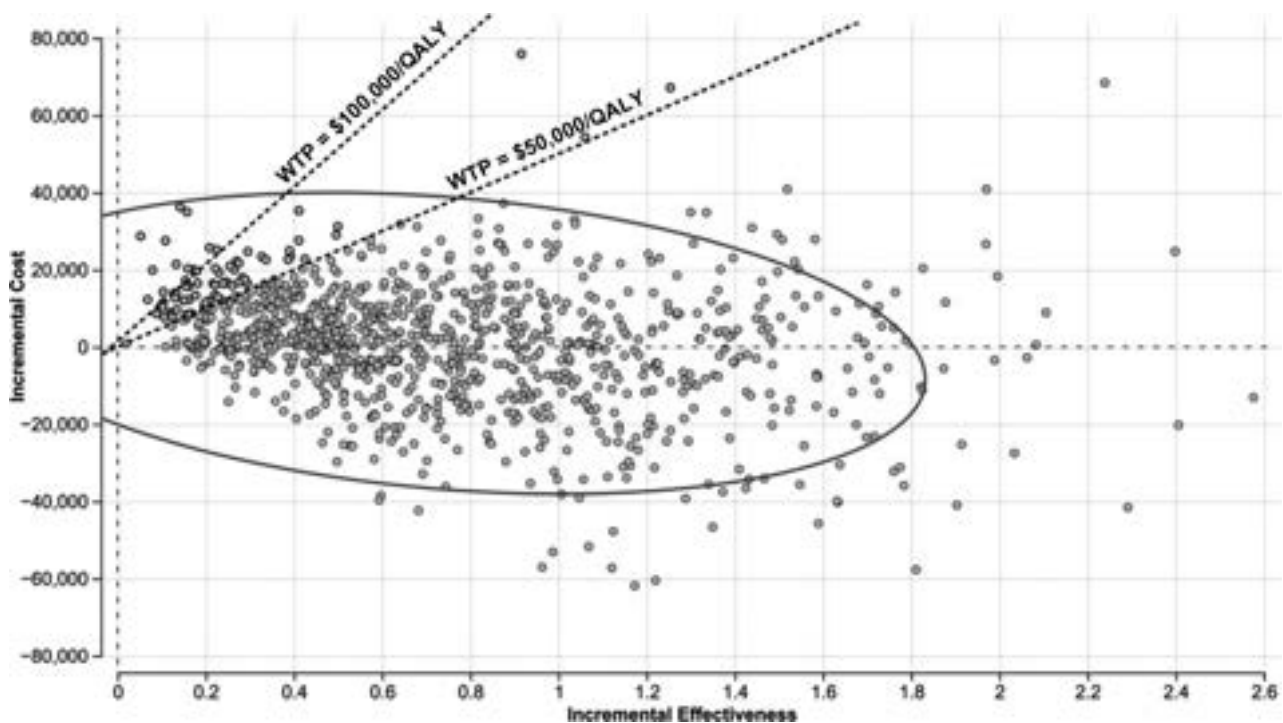


FIG 4. Probabilistic sensitivity analysis considering the collective variation of costs, utilities, imaging parameters, and radiation-induced toxicity risk with 100,000 iterations. The probabilistic sensitivity analysis showed that the new strategy is cost-effective in 91% of the 100,000 iterations, demonstrating its cost-effectiveness at WTP = \$50,000/QALY.

extrapolations were required for modeling the Markov model transitions. Some of our input parameters were taken from studies using ^{68}Ga -DOTATATE PET/CT rather than PET/MR imaging. Most important, prior studies regarding somatostatin analog PET radiotracers (such as ^{68}Ga -DOTATATE, ^{68}Ga -DOTA-TOC, ^{68}Ga -DOTANOC) for other SSTR2A-positive neoplasms demonstrated that there is no significant difference in the detection rate between PET/CT and PET/MR imaging for a given radiotracer.^{43,44} In our model, we had to make assumptions such as considering that all patients with gross total resection were treated with active surveillance only. This may not always be the case in clinical practice because many radiation oncologists consider the use of RT following complete resection of WHO grade 2 meningiomas.³ Our model did not account for uncertain scenarios such as clinical situations with inconclusive imaging results as well as for meningioma location, which can affect clinical management

and outcomes.²⁴ Furthermore, there are extremely rare cases with MR imaging-positive, SSTR2A-negative findings and therefore ^{68}Ga -DOTATATE PET-negative meningiomas.⁴⁵ In clinical practice, information derived from ^{68}Ga -DOTATATE PET/MR imaging has to be evaluated in conjunction with MR imaging findings and placed in the context of the individual patient. We assumed that radiation-associated toxicities would occur only in the first year postirradiation. Furthermore, we assumed that CTCAE 1–2 events would not transition to CTCAE 3–4 events due to data limitations. While delayed radiation toxicity can occur, such events tend to be very rare and it is unlikely that CTCAE 1–2 events will convert to CTCAE 3–4 events after 1 year of completion of radiation. The indirect costs were calculated assuming maximum retirement benefits, which occur at a retirement age of 72 years.⁴⁶ Due to lack of data, we used standardized mortality ratios for meningiomas without the distinction of grade. Furthermore, for the

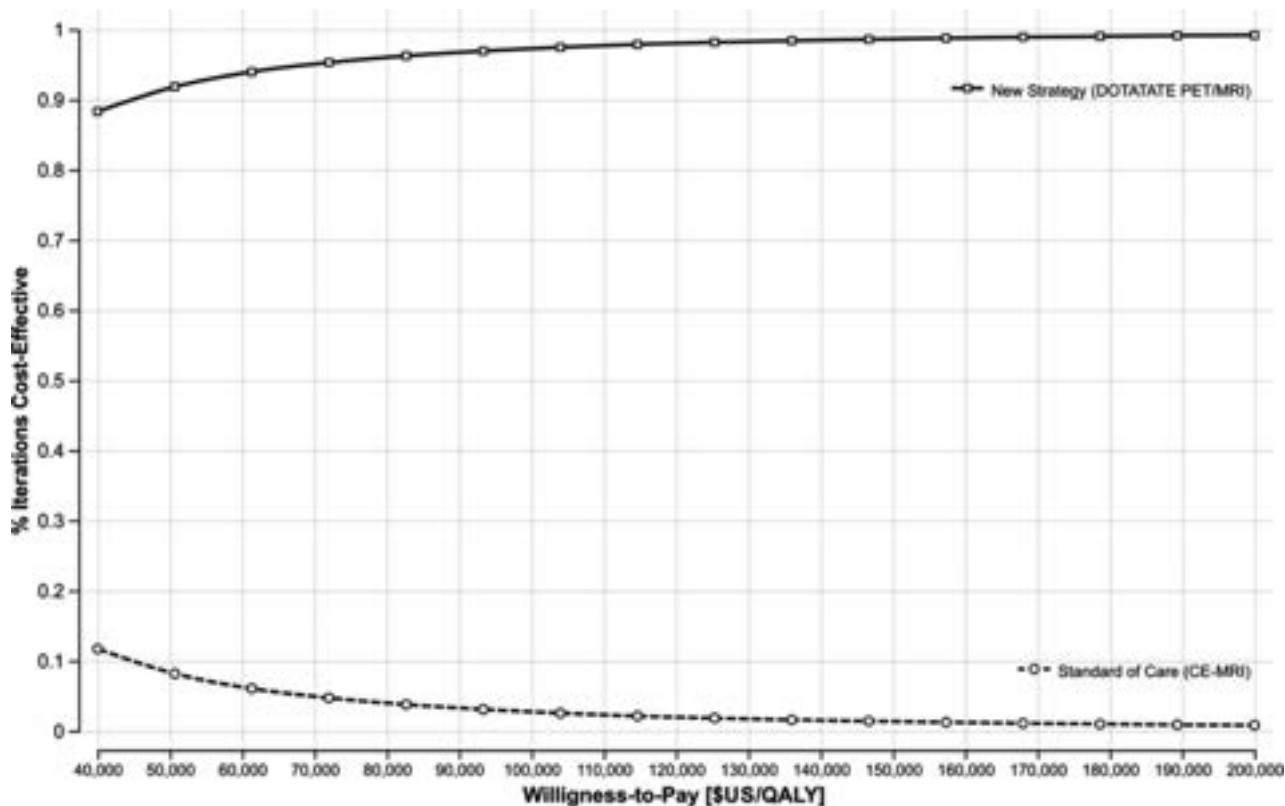


FIG 5. Cost-effectiveness acceptability curve with WTP values between \$40,000/QALY and \$200,000/QALY. The new strategy is consistently cost-effective across the WTP values used in our analysis. CE indicates contrast-enhanced.

surveillance cohort in our model, the Markov model was based on the study of Mirimanoff et al.²⁰ While this study is older and not specifically limited to intermediate-risk meningiomas compared with later retrospective analyses such as that by Aghi et al,⁴⁷ it has the largest sample size (225 patients) and has the needed data availability to model the transitions between health states (Fig 1). Given inclusion of all meningioma grades (except malignant meningiomas), the Mirimanoff et al cohort likely represents a closer approximation of the general clinical population of patients with meningiomas requiring postoperative management. Moreover, given that the limitations of MR imaging in the evaluation of meningiomas mostly pertain to the clinical context of postoperative recurrence and an invasive growth pattern,⁹ our model results are likely more conservative.

In this study, health care costs were based on a US setting. Thus, our findings may not be directly applied to other countries. However, our model can be adopted to other countries or regions by substituting region-specific parameters.

Significant advancements in molecular profiling of meningiomas have uncovered genetic and epigenetic biomarkers allowing more accurate prediction of tumor behavior compared with classic histopathologic approaches, including the mitotic rate and cytomorphologic criteria applied in the WHO classification scheme.⁴⁸ Future studies may determine the need to incorporate molecular classifiers into decision-making regarding surveillance versus RT and may benefit from incorporating ⁶⁸Ga-DOTATATE PET/MR imaging.⁴⁹

Future studies, such as a cost-consequence analysis should be conducted for a comprehensive evaluation of the cost implications

of ⁶⁸Ga-DOTATATE PET/MR imaging in clinical practice. Future work should further incorporate molecular profiling data, which has recently demonstrated utility in predicting clinical outcomes in patients with meningiomas.⁵⁰⁻⁵³

CONCLUSIONS

Incorporating ⁶⁸Ga-DOTATATE PET/MR imaging for meningioma management is cost-effective from a societal perspective and may improve RT planning, thereby improving clinical outcomes and reducing long-term costs due to RT-related complications.

Disclosure forms provided by the authors are available with the full text and PDF of this article at www.ajnr.org.

REFERENCES

- Ostrom QT, Price M, Ryan K, et al. **CBTRUS Statistical Report: Pediatric Brain Tumor Foundation Childhood and Adolescent Primary Brain and Other Central Nervous System Tumors Diagnosed in the United States in 2014-2018.** *Neuro Oncol* 2022;24:iii1-38 CrossRef Medline
- Rogers L, Barani I, Chamberlain M, et al. **Meningiomas: knowledge base, treatment outcomes, and uncertainties: a RANO review.** *J Neurosurg* 2015;122:4-23 CrossRef Medline
- Rogers L, Zhang P, Vogelbaum MA, et al. **Intermediate-risk meningioma: initial outcomes from NRG Oncology RTOG 0539.** *J Neurosurg* 2018;129:35-47 CrossRef Medline
- Goldbrunner R, Stavrinou P, Jenkinson MD, et al. **EANO guideline on the diagnosis and management of meningiomas.** *Neuro Oncol* 2021;23:1821-34 CrossRef Medline

5. Magill ST, Dalle Ore CL, Diaz MA, et al. **Surgical outcomes after reoperation for recurrent non-skull base meningiomas.** *J Neurosurg* 2018;130:876–83 CrossRef Medline
6. Magill ST, Lee DS, Yen AJ, et al. **Surgical outcomes after reoperation for recurrent skull base meningiomas.** *J Neurosurg* 2018;130:876–83 CrossRef Medline
7. Mahase SS, Roth O'Brien DA, No D, et al. **[⁶⁸Ga]-DOTATATE PET/MRI as an adjunct imaging modality for radiation treatment planning of meningiomas.** *Neurooncol Adv* 2021;3:vdab012 CrossRef Medline
8. Halliday J, Fernandes H. **Meningioma recurrence: the efficacy and cost-effectiveness of current screening.** *Br J Neurosurg* 2010;24:55–61 CrossRef Medline
9. Ivanidze J, Roytman M, Lin E, et al. **Gallium-68 DOTATATE PET in the evaluation of intracranial meningiomas.** *J Neuroimaging* 2019;29:650–56 CrossRef Medline
10. Reubi JC, Schar JC, Waser B, et al. **Affinity profiles for human somatostatin receptor subtypes SST1-SST5 of somatostatin radiotracers selected for scintigraphic and radiotherapeutic use.** *Eur J Nucl Med* 2000;27:273–82 CrossRef Medline
11. Silva CB, Ongaratti BR, Trott G, et al. **Expression of somatostatin receptors (SSTR1-SSTR5) in meningiomas and its clinicopathological significance.** *Int J Clin Exp Pathol* 2015;8:13185–92 Medline
12. Hofman MS, Lau WF, Hicks RJ. **Somatostatin receptor imaging with ⁶⁸Ga DOTATATE PET/CT: clinical utility, normal patterns, pearls, and pitfalls in interpretation.** *Radiographics* 2015;35:500–16 CrossRef Medline
13. Kunz WG, Jungblut LM, Kazmierczak PM, et al. **Improved detection of transosseous meningiomas using ⁶⁸Ga-DOTATATE PET/CT compared with contrast-enhanced MRI.** *J Nucl Med* 2017;58:1580–87 CrossRef Medline
14. Graf R, Plotkin M, Steffen IG, et al. **Magnetic resonance imaging, computed tomography, and ⁶⁸Ga-DOTATOC positron emission tomography for imaging skull base meningiomas with intracranial extension treated with stereotactic radiotherapy: a case series.** *Head Face Med* 2012;8:1 CrossRef Medline
15. Kim SH, Roytman M, Madera G, et al. **Evaluating diagnostic accuracy and determining optimal diagnostic thresholds of different approaches to [⁶⁸Ga]-DOTATATE PET/MRI analysis in patients with meningioma.** *Sci Rep* 2022;12:9256 CrossRef Medline
16. Ivanidze J, Roytman M, Skafida M, et al. **Dynamic ⁶⁸Ga-DOTATATE PET/MRI in the diagnosis and management of intracranial meningiomas.** *Radiol Imaging Cancer* 2022;4:e210067 CrossRef Medline
17. Perlow HK, Siedow M, Gokun Y, et al. **⁶⁸Ga-DOTATATE PET-based radiation contouring creates more precise radiation volumes for patients with meningioma.** *Int J Radiat Oncol Biol Phys* 2022;113:859–65 CrossRef Medline
18. Kowalski ES, Khairnar R, Gryaznov AA, et al. **⁶⁸Ga-DOTATATE PET-CT as a tool for radiation planning and evaluating treatment responses in the clinical management of meningiomas.** *Radiat Oncol* 2021;16:151 CrossRef Medline
19. Sun SQ, Cai C, Murphy RK, et al. **Radiation therapy for residual or recurrent atypical meningioma: the effects of modality, timing, and tumor pathology on long-term outcomes.** *Neurosurgery* 2016;79:23–32 CrossRef Medline
20. Mirimanoff RO, Dosoretz DE, Linggood RM, et al. **Meningioma: analysis of recurrence and progression following neurosurgical resection.** *J Neurosurg* 1985;62:18–24 CrossRef Medline
21. Brem SS, Bierman PJ, Black P, et al; National Comprehensive Cancer Network. **Central nervous system cancers: clinical practice guidelines in oncology.** *J Natl Compr Canc Netw* 2005;3:644–90 CrossRef Medline
22. U.S. Department of Health and Human Services. **Common Terminology Criteria for Adverse Events (CTCAE).** November 27, 2017. https://ctep.cancer.gov/protocoldevelopment/electronic_applications/docs/CTCAE_v5_Quick_Reference_5x7.pdf. Accessed May 23, 2021
23. Zollner B, Ganswindt U, Maihofer C, et al. **Recurrence pattern analysis after [⁶⁸Ga]-DOTATATE-PET/CT-planned radiotherapy of high-grade meningiomas.** *Radiat Oncol* 2018;13:110 CrossRef Medline
24. Pan PC, Pisapia DJ, Ramakrishna R, et al. **Outcomes following upfront radiation versus monitoring in atypical meningiomas: 16-year experience at a tertiary medical center.** *Neurooncol Adv* 2021;3:vdab094 CrossRef Medline
25. Pollock BE, Stafford SL, Link MJ, et al. **Stereotactic radiosurgery of World Health Organization grade II and III intracranial meningiomas: treatment results on the basis of a 22-year experience.** *Cancer* 2012;118:1048–54 CrossRef Medline
26. Dohm A, McTyre ER, Chan MD, et al. **Early or late radiotherapy following gross or subtotal resection for atypical meningiomas: clinical outcomes and local control.** *J Clin Neurosci* 2017;46:90–98 CrossRef Medline
27. Qian Y, Maruyama S, Kim H, et al. **Cost-effectiveness of radiation and chemotherapy for high-risk low-grade glioma.** *Neuro Oncol* 2017;19:1651–60 CrossRef Medline
28. Knoll MA, Olsen A. **Incentivizing delayed claiming of social security retirement benefits before reaching the full retirement age.** *Social Security Bulletin* 2014;74:23
29. Sanders GD, Neumann PJ, Basu A, et al. **Recommendations for conduct, methodological practices, and reporting of cost-effectiveness analyses: Second Panel on Cost-Effectiveness in Health and Medicine.** *JAMA* 2016;316:1093–103 CrossRef Medline
30. Arias E, Xu J. **United States Life Tables, 2018.** *Natl Vital Stat Rep* 2020;69:1–45 Medline
31. Cea-Soriano L, Wallander MA, García Rodríguez LA. **Epidemiology of meningioma in the United Kingdom.** *Neuroepidemiology* 2012;39:27–34 CrossRef Medline
32. Cohen DJ, Reynolds MR. **Interpreting the results of cost-effectiveness studies.** *J Am Coll Cardiol* 2008;52:2119–26 CrossRef Medline
33. Whitehead SJ, Ali S. **Health outcomes in economic evaluation: the QALY and utilities.** *Br Med Bull* 2010;96:5–21 CrossRef Medline
34. Neumann PJ, Cohen JT, Weinstein MC. **Updating cost-effectiveness: the curious resilience of the \$50,000-per-QALY threshold.** *N Engl J Med* 2014;371:796–97 CrossRef Medline
35. Hiroiwa T, Sung YK, Fukuda T, et al. **International survey on willingness-to-pay (WTP) for one additional QALY gained: what is the threshold of cost effectiveness?** *Health Econ* 2010;19:422–37 CrossRef Medline
36. Ryen L, Svensson M. **The willingness to pay for a quality adjusted life year: a review of the empirical literature.** *Health Econ* 2015;24:1289–301 CrossRef Medline
37. Wouters OJ, Naci H, Samani NJ. **QALYs in cost-effectiveness analysis: an overview for cardiologists.** *Heart* 2015;101:1868–73 CrossRef Medline
38. Wilson TA, Huang L, Ramanathan D, et al. **Review of atypical and anaplastic meningiomas: classification, molecular biology, and management.** *Front Oncol* 2020;10:565582 CrossRef Medline
39. Recker MJ, Kuo CC, Prasad D, et al. **Incidence trends and survival analysis of atypical meningiomas: a population-based study from 2004 to 2018.** *J Neurooncol* 2022;160:13–22 CrossRef Medline
40. Froelich MF, Schnitzer ML, Holzgreve A, et al. **Cost-effectiveness analysis of ⁶⁸Ga DOTA-TATE PET/CT, ¹¹¹In-Pentetreotide SPECT/CT and CT for diagnostic workup of neuroendocrine tumors.** *Diagnostics (Basel)* 2021;11:334 CrossRef Medline
41. Schreiter NF, Brenner W, Nogami M, et al. **Cost comparison of ¹¹¹In-DTPA-octreotide scintigraphy and ⁶⁸Ga-DOTATOC PET/CT for staging enteropancreatic neuroendocrine tumours.** *Eur J Nucl Med Mol Imaging* 2012;39:72–82 CrossRef Medline
42. Sommerauer M, Burkhardt JK, Frontzek K, et al. **⁶⁸Gallium-DOTATATE PET in meningioma: a reliable predictor of tumor growth rate?** *Neuro Oncol* 2016;18:1021–27 CrossRef Medline
43. Berzaczy D, Giraudo C, Haug AR, et al. **Whole-body ⁶⁸Ga-DOTANOC PET/MRI versus ⁶⁸Ga-DOTANOC PET/CT in patients with neuroendocrine tumors: a prospective study in 28 patients.** *Clin Nucl Med* 2017;42:669–74 CrossRef Medline

44. Afshar-Oromieh A, Wolf MB, Kratochwil C, et al. **Comparison of ⁶⁸Ga-DOTATOC-PET/CT and PET/MRI hybrid systems in patients with cranial meningioma: initial results.** *Neuro Oncol* 2015;17:312–19 CrossRef Medline
45. Roytman M, Pisapia DJ, Liechty B, et al. **Somatostatin receptor-2 negative meningioma: pathologic correlation and imaging implications.** *Clin Imaging* 2020;66:18–22 CrossRef Medline
46. Kunz WG, Hunink MG, Dimitriadis K, et al. **Cost-effectiveness of endovascular therapy for acute ischemic stroke: a systematic review of the impact of patient age.** *Radiology* 2018;288:518–26 CrossRef Medline
47. Aghi MK, Carter BS, Cosgrove GR, et al. **Long-term recurrence rates of atypical meningiomas after gross total resection with or without postoperative adjuvant radiation.** *Neurosurgery* 2009;64:56–60; discussion 60 CrossRef Medline
48. Louis DN, Perry A, Wesseling P, et al. **The 2021 WHO Classification of Tumors of the Central Nervous System: a summary.** *Neuro Oncol* 2021;23:1231–51 CrossRef Medline
49. Prasad RN, Perlow HK, Bovi J, et al. **⁶⁸Ga-DOTATATE PET: the future of meningioma treatment.** *Int J Radiat Oncol Biol Phys* 2022;113:868–71 CrossRef Medline
50. Maas SL, Stichel D, Hielscher T, et al; German Consortium on Aggressive Meningiomas (KAM). **Integrated molecular-morphologic meningioma classification: a multicenter retrospective analysis, retrospectively and prospectively validated.** *J Clin Oncol* 2021;39:3839–52 CrossRef Medline
51. Nassiri F, Liu J, Patil V, et al. **A clinically applicable integrative molecular classification of meningiomas.** *Nature* 2021;597:119–25 CrossRef Medline
52. Raleigh D, Chen W, Choudhury A, et al. **Targeted gene expression profiling predicts meningioma outcomes and radiotherapy responses.** *Res Sq* March 20, 2023;rs.3.rs-2663611 CrossRef Medline
53. Choudhury A, Magill ST, Eaton CD, et al. **Meningioma DNA methylation groups identify biological drivers and therapeutic vulnerabilities.** *Nat Genet* 2022;54:649–59 CrossRef Medline

Sex-Specific Patterns of Cerebral Atrophy and Enlarged Perivascular Spaces in Patients with Cerebral Amyloid Angiopathy and Dementia

J. Pinho, F.C. Almeida, J.M. Araújo, Á. Machado, A.S. Costa, F. Silva, A. Francisco, M. Quintas-Neves, C. Ferreira, J.P. Soares-Fernandes, and T.G. Oliveira



ABSTRACT

BACKGROUND AND PURPOSE: Cerebral amyloid angiopathy is characterized by amyloid β deposition in leptomeningeal and superficial cortical vessels. Cognitive impairment is common and may occur independent of concomitant Alzheimer disease neuropathology. It is still unknown which neuroimaging findings are associated with dementia in cerebral amyloid angiopathy and whether they are modulated by sex. This study compared MR imaging markers in patients with cerebral amyloid angiopathy with dementia or mild cognitive impairment or who are cognitively unimpaired and explored sex-specific differences.

MATERIALS AND METHODS: We studied 58 patients with cerebral amyloid angiopathy selected from the cerebrovascular and memory outpatient clinics. Clinical characteristics were collected from clinical records. Cerebral amyloid angiopathy was diagnosed on MR imaging on the basis of the Boston criteria. Visual rating scores for atrophy and other imaging features were independently assessed by 2 senior neuroradiologists.

RESULTS: Medial temporal lobe atrophy was higher for those with cerebral amyloid angiopathy with dementia versus those cognitively unimpaired ($P = .015$), but not for those with mild cognitive impairment. This effect was mainly driven by higher atrophy in men with dementia, compared with women with and without dementia ($P = .034$, $P = .012$; respectively) and with men without dementia ($P = .012$). Enlarged perivascular spaces in the centrum semiovale were more frequent in women with dementia versus men with and without dementia ($P = .021$, $P = .011$; respectively) and women without dementia ($P = .011$).

CONCLUSIONS: Medial temporal lobe atrophy was more prominent in men with dementia, whereas women showed a higher number of enlarged perivascular spaces in the centrum semiovale. Overall, this finding suggests differential pathophysiologic mechanisms with sex-specific neuroimaging patterns in cerebral amyloid angiopathy.

ABBREVIATIONS: $A\beta$ = amyloid β ; AD = Alzheimer disease; ARWMC = age-related white matter changes; CAA = cerebral amyloid angiopathy; cSS = cortical superficial siderosis; EPVS = enlarged perivascular spaces; IQR = interquartile range; MCI = mild cognitive impairment; MTA = medial temporal lobe atrophy

Cerebral amyloid angiopathy (CAA) is pathologically characterized by amyloid β ($A\beta$) deposition in the walls of leptomeningeal and cortical small vessels.¹ Clinically, it is a major cause of intracerebral hemorrhage, and it may present not only as other acute neurologic manifestations, such as transient focal

neurologic episodes, but also with slowly progressive cognitive impairment.² In vivo diagnosis has been made possible by the Boston diagnostic criteria, which require the presence of multiple lobar microbleeds, multiple major lobar hemorrhages, and a single hemorrhage accompanied by cortical superficial siderosis (cSS), with other causes having been excluded.² The recently proposed version 2 of the Boston criteria for diagnosis of CAA additionally included the presence of nonhemorrhagic markers such as a high burden of enlarged perivascular spaces (EPVS) in the centrum semiovale and a multispot pattern of white matter hyperintensities.³

Received January 23, 2023; accepted after revision May 7.

From the Department of Neurology (J.P., A.S.C.), University Hospital RWTH Aachen, Aachen, Germany; Life and Health Sciences Research Institute (F.C.A., M.Q.-N., T.G.O.), School of Medicine, and Algoritmi Center (F.S., A.F.), University of Minho, Braga, Portugal; Life and Health Sciences Research Institute/3Bs (F.C.A., M.Q.-N., T.G.O.), Portuguese Government Associate Laboratory, Braga/Guimarães, Portugal; Department of Neuroradiology (F.C.A.), Centro Hospitalar Universitário do Porto, Porto, Portugal; Departments of Neurology (J.M.A., Á.M., C.F.) and Neuroradiology (M.Q.-N., J.P.S.-F., T.G.O.), Hospital de Braga, Braga, Portugal; and JARA Institute Molecular Neuroscience and Neuroimaging (A.S.C.), Forschungszentrum Jülich and RWTH Aachen University, Aachen, Germany.

The research of A.S. Costa is supported by a START Grant (I18/20) from the Faculty of Medicine of the RWTH Aachen University. No other specific allocated funding is reported.

Please address correspondence to Tiago Gil Oliveira, MD, Life and Health Sciences Research Institute, School of Medicine, University of Minho, Campus Gualtar, 4710-057 Braga, Portugal; e-mail: tiago@med.uminho.pt; @TGO_lab

Indicates article with online supplemental data.

<http://dx.doi.org/10.3174/ajnr.A7900>

Structural MR imaging studies in CAA demonstrate an intermediate pattern of atrophy between cognitively healthy and the one seen in Alzheimer's disease (AD).^{4,5} Additionally, AD is frequently associated with CAA, with more than 80% of patients with AD on postmortem examination showing at least some degree of CAA pathology.⁶ Furthermore, studies evaluating the effect of CAA on cognition have suggested that it might play an independent role in cognitive impairment, potentially with a pattern of cognitive deficits distinct from that found in typical AD,⁷⁻¹¹ even though this connection is still under study.¹² However, the relationship between cognitive impairment in patients with CAA and brain atrophy has not been studied in detail. Moreover, while sex-specific differences have been found in AD, few studies have explored their effect in CAA.¹³

Another imaging marker of increasing interest in CAA is the observation of EPVS visible on MR imaging. EPVS in the centrum semiovale have been associated with increased cortical vascular $A\beta$ in the overlying cortex^{14,15} and indirect measures of CAA severity, such as cortical microbleeds and cSS.¹⁶⁻¹⁸ Altogether, these findings suggest that impaired perivascular drainage of $A\beta$ might be associated with a higher frequency of EPVS in the centrum semiovale. However, whether these imaging findings are associated with cognitive impairment in CAA and whether they might be differentially modulated by sex have not been studied.

Our goal was to study brain MR imaging features in CAA, such as cerebral atrophy and the frequency of EPVS, and their relationship with the severity of cognitive impairment and sex in patients with CAA.

MATERIALS AND METHODS

Statement of Ethics

The study was approved by the Ethics for Health Commission of Hospital de Braga.

Patient Clinical and Imaging Data

This was a retrospective study of adult patients with possible or probable CAA according to the modified Boston criteria,³ diagnosed in the Department of Neurology of Hospital de Braga during a 4-year period. Patients with a diagnosis of CAA were selected after an analysis of all individual records of patients attending the cerebrovascular outpatient clinic and the memory outpatient clinic during the study period. All patients underwent 1.5T brain MR imaging (including T1-, T2-, and T2*-weighted images and T2 FLAIR). MR imaging acquisition protocol was constant throughout the study period. Demographic and clinical variables were collected from the digital clinical records. Patients were followed in the neurology outpatient clinic as part of the routine clinical care. Diagnosis of mild cognitive impairment (MCI) and dementia according to local and international guidelines^{19,20} was based on clinical evaluation and available clinical records from the neurology outpatient clinic. MCI was defined as the presence of cognitive symptoms expressed by the patient or next-of-kin, with objective impairment in at least 1 domain of cognitive function and absence of impairment on social or occupational functioning.¹⁹ Dementia was defined as the presence of cognitive impairment severe enough to interfere with the activities of daily living.

Imaging Score Assessments

MR images were independently reviewed by 2 experienced neuro-radiologists, blinded to clinical information, for the classification of the following: the presence of cSS (focal = restricted to 3 sulci, disseminated = involving >3 sulci) on axial T2* acquisitions; age-related white matter changes (ARWMC) using axial T2 FLAIR acquisitions at the level of basal ganglia (0 = no lesions; 1 = 1 focal lesion [≥ 5 mm]; 2 ≥ 1 focal lesion; 3 = confluent lesions) and centrum semiovale (0 = no lesions; 1 = focal lesions; 2 = beginning confluence of lesions; 3 = diffuse involvement of the entire region with or without U-fiber involvement);²¹ and the semiquantitative scale measuring the burden of EPVS using axial T2 acquisitions in the basal ganglia and centrum semiovale (0 = none; 1 = 1-10; 2 = 11-20; 3 = 21-40; 4 ≥ 40).²² Brain regional atrophy was assessed using a group of validated MR imaging visual rating scales on the following regions: anterior cingulate (graded from 0 to 3), orbito-frontal (graded from 0 to 3), anterior temporal (graded from 0 to 4), fronto-insular (graded from 0 to 3), medial temporal (graded from 0 to 4), and posterior regions (graded from 0 to 3).²³ For each brain region scale, the average of both hemispheres was calculated, and an average of both classifiers was used. Brain regions affected by intracerebral hemorrhage or encephalomalacia from a previous hemorrhage were excluded from assessment. Relative levels were computed as a percentage of maximum possible atrophy for each regional scale. Reference images for each rating scale were provided to the classifiers on the basis of Harper et al,²³ to aid the rating process. Interobserver agreement was calculated using the intraclass correlation coefficient for single measures with the 95% CI (Online Supplemental Data). Disagreements of >1 in each rating score were reviewed by the 2 raters, and a consensus was reached.

Statistical Analysis

Demographic and clinical characteristics of patients with CAA with normal cognition, MCI, and dementia were compared using a 1-way ANOVA with a Tukey honestly significant difference correction for multiple comparisons, the χ^2 test, and the Fisher exact test, as appropriate. Visual rating scores were compared among cognition status groups using pair-wise Wilcoxon tests with Bonferroni correction for multiple comparisons. For analyses based on dementia status, patients with normal cognition and MCI were merged to constitute a group without dementia, and patients with dementia remained as the dementia group. Demographic and clinical comparisons were performed using a Welch *t* test or Wilcoxon tests, as appropriate. Regional brain atrophy scores were compared between sex and dementia groups using pair-wise Wilcoxon tests with a Bonferroni correction for multiple comparisons. ARWMC in the basal ganglia and centrum semiovale correlations with regional brain volumes were performed using the Spearman correlation. Regional brain volumes in the group positive for cSS were compared with those in the group negative for cSS using the Wilcoxon test. For the multivariable linear regression using medial temporal lobe atrophy (MTA) as the dependent variable, age was coded as a continuous variable, and sex and the presence of cSS and dementia, as categorical variables, constituting the independent variables, with a dementia \times sex interaction. Contrast testing was then performed for group-of-interest comparison, and *P* values were corrected with the Bonferroni method for multiple comparisons. For comparison

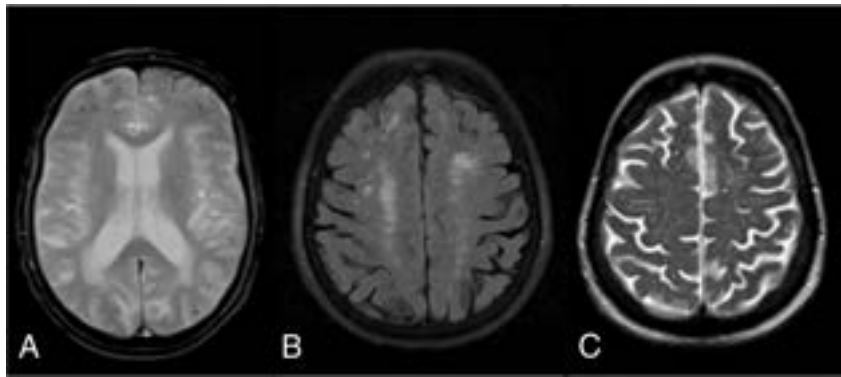


FIG 1. Brain MR imaging pathologic features of CAA pathology. A, Axial T2* image from a 76-year-old male patient shows left frontal cortical siderosis and multiple foci of microhemorrhages of the predominant frontal location bilaterally. B, Axial T2 FLAIR image from a 73-year-old woman shows centrum semiovale white matter T2-hyperintense lesions attributed to chronic small-vessel ischemia. C, Axial T2 image from a 78-year-old female patient shows EPVS in the centrum semiovale.

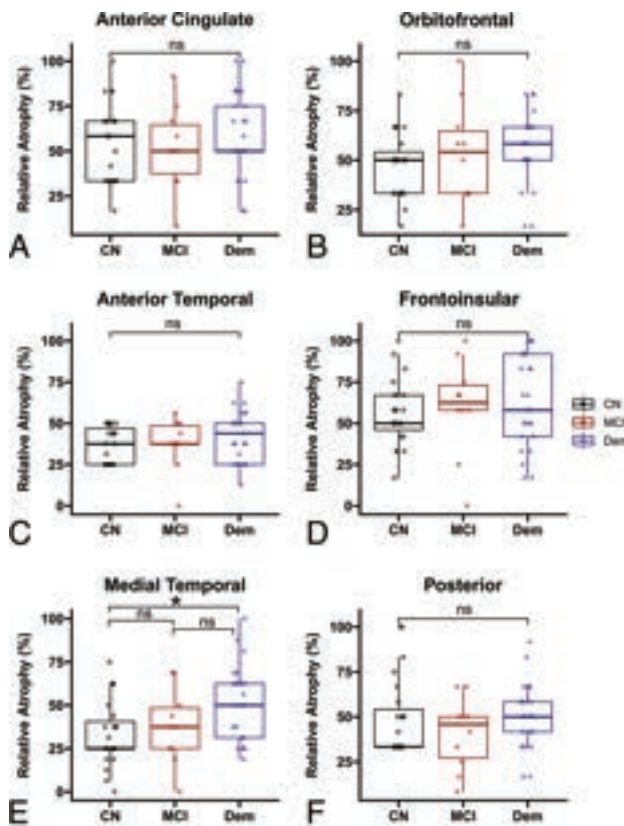


FIG 2. Regional brain atrophy as measured by the visual rating score compared across cognition levels: normal, MCI, dementia. The regions evaluated are the anterior cingulate (A), orbitofrontal (B), anterior temporal (C), frontoinsular (D), medial temporal (E), and posterior (F). Statistical significance is considered at P values $< .05$ (asterisk). CN indicates cognitively unimpaired; Dem, dementia; ns, not significant.

of scores of EPVS among groups, we used pair-wise Wilcoxon tests with a Bonferroni correction for multiple comparisons. All statistical analyses were conducted using RStudio, Version 1.4.1103 (<http://rstudio.org/download/desktop>).

RESULTS

Our study population consisted of 58 patients, with a mean age of 71.6 (SD, 9.8) years, and 50% were men. Most of the patients were

selected from the cerebrovascular outpatient clinic ($n = 48$, 83%), and the remainder were selected from the memory clinic ($n = 10$, 17%). All cases were confirmed to show characteristic CAA findings on brain MR imaging (Fig 1). Most patients presented with vascular risk factors: Hypertension was present in 78%; dyslipidemia, in 59%; and diabetes mellitus, in 22% of patients. Among our study population, 23 patients (40%) presented with normal cognition, 10 presented with MCI (17%), and 25 presented with dementia (43%). Baseline characteristics of the study population according to the presence of normal cognition, MCI, or dementia are presented in the Online Supplemental Data. The group with dementia was older than the group with normal cognition ($P = .004$).

Regarding visual rating scores for each brain region, increased MTA was found in patients with dementia compared with patients with normal cognition ($P = .015$; normal cognition: median = 25; interquartile range [IQR] = 15.65; dementia: median = 50; IQR = 31.2; Fig 2). There were no significant pair-wise differences across groups in the other brain regions.

Mediators of MTA

We analyzed the relationship between MTA and other variables such as sex, age, the presence of cSS, and the Fazekas score. Characteristics of patients with and without dementia and by sex are shown in the Online Supplemental Data.

We found more severe MTA in male patients with dementia compared with female patients with dementia ($P = .034$; female dementia: median = 50.0; IQR = 34.4; male dementia: median = 62.5; IQR = 25.1) and compared with men without dementia ($P = .012$; men with no dementia: median = 31.3; IQR = 21.9) and women without dementia ($P = .012$; women with no dementia: median = 31.3; IQR = 12.5; Fig 3).

There were no significant differences

in other brain regions. More severe MTA was observed in patients with cSS ($P = .017$; cSS: median = 46.9; IQR = 35.9; no cSS: median = 25.0; IQR = 21.8; Fig 4A). We also observed more severe atrophy of the posterior and anterior cingulate regions in patients with cSS (Online Supplemental Data). More severe MTA was also associated with increased white matter hyperintense lesions in both the basal ganglia ($\rho = 0.59$, $P < .001$) and the periventricular white matter ($\rho = 0.47$,

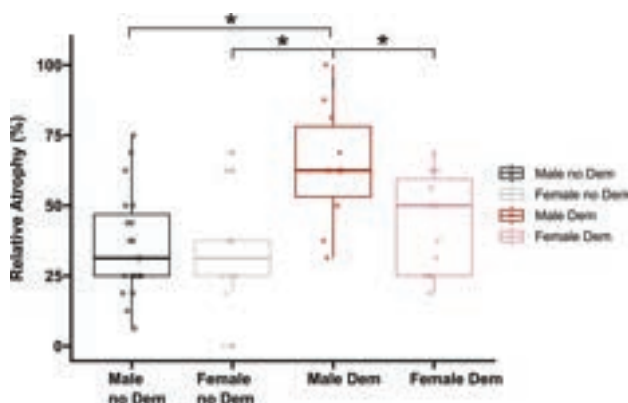


FIG 3. MTA as measured by the visual rating scale across dementia groups and sex: Male no Dem; Female no Dem; Male Dem; Female Dem. Statistical significance is considered at P values $< .05$. Dem indicates dementia.

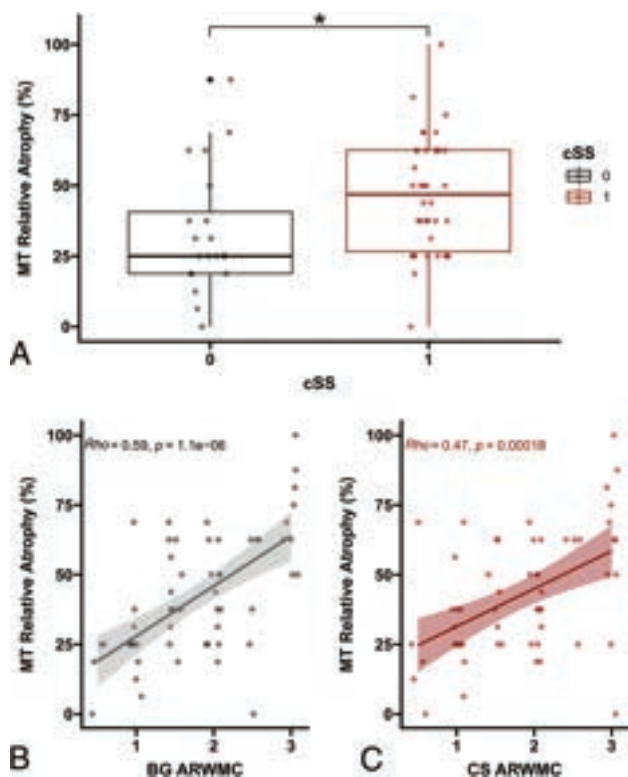


FIG 4. Determinants of MTA in CAA. A, MTA as measured by visual rating across the presence (1) or absence (0) of cSS. B, Spearman correlation analysis of MTA with basal ganglia age-related white matter changes (BG ARWMC). C, Spearman correlation analysis of MTA with centrum semiovale age-related white matter changes (CS ARWMC). Statistical significance is considered at P values $< .05$ (asterisk). MT indicates medial temporal lobe.

$P < .001$; Fig 4B, -C). We found this same pattern of association for all brain regions (Online Supplemental Data).

To confirm the sex-specific results, we conducted a multivariable linear regression model with age, sex, and the presence of cSS and dementia as independent variables, including a dementia \times sex interaction, and MTA as the dependent variable (Online Supplemental Data). Increasing age was associated with increased MTA ($P < .010$), and contrast tests (Online Supplemental Data) revealed that male patients with dementia

have significantly greater atrophy compared with female patients with dementia ($P = .025$) and compared with male patients without dementia ($P = .011$).

Frequency of EPVS

We assessed whether the frequency of EPVS was different according to the cognitive status of the patient. We found that the burden of EPVS is increased in the centrum semiovale but not in the basal ganglia in patients with dementia versus those with normal cognition ($P = .023$; normal cognition: median = 2.0; IQR = 1.75; dementia: median = 3.0; IQR = 1.5; Fig 5A, -B). When we divided the groups according to sex and the presence of dementia, we found that women with dementia showed a higher burden of EPVS in the centrum semiovale compared with men with dementia ($P = .021$; female dementia: median = 3.5; IQR = 1.0; male dementia: median = 2.0; IQR = 1.4) and with women without dementia ($P = .011$; women without dementia: median = 1.25; IQR = 1.5) and men without dementia ($P = .011$; men without dementia: median = 2.5; IQR = 2.0; Fig 5C).

DISCUSSION

Our results indicate a sex-specific pattern of cerebral atrophy and EPVS in patients with CAA and dementia. More severe MTA was associated with dementia in male patients with CAA but not in women, whereas a higher frequency of EPVS in the centrum semiovale was associated with dementia in female patients but not in male patients.

AD and CAA are frequently associated and share common pathophysiological pathways.^{1,24} Accordingly, decreased hippocampal volume, a known feature of AD, is also found to a lesser degree in sporadic CAA,⁵ and MTA has been implicated as a predictor of incidental dementia in patients with CAA.²⁵ We

found that the medial temporal lobe is the only brain region evaluated in our study to be correlated with dementia (Fig 2), in line with these previous observations.

Sex-specific differences have also been reported, with increased severity of CAA pathology found in male patients with AD, independent of age and AD neuropathologic severity.¹³ Our results indicate that male patients with dementia have more severe MTA than women with dementia, even after correction for major confounders such as age and the presence of cSS (Fig 3 and Online

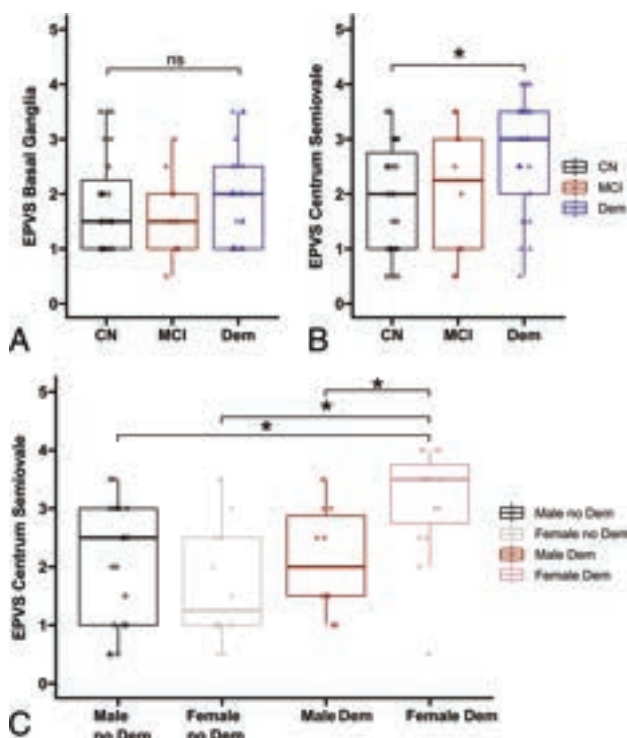


FIG 5. EPVS across cognition groups. A, Basal ganglia EPVS. B, Centrum semiovale EPVS. C, Centrum semiovale EPVS across dementia by sex groups. Statistical significance is considered at P values $< .05$ (asterisk). CN indicates cognitively unimpaired; Dem, dementia; ns, not significant.

Supplemental Data), suggesting that, in CAA, sex might play a differential role in neurodegeneration in this brain region.

The mechanisms underlying brain atrophy in patients with CAA are not fully understood. It is thought, however, that the consequences of the amyloidotic small-vessel disease, such as cortical microinfarcts, white matter lesions, and ischemic demyelination are important contributors to cortical thinning in CAA.²⁴ Concomitant AD pathology is likely an additional contributor to brain atrophy in some patients with CAA, but how often and to what extent remain unclear.¹ Most interesting, the increased severity of CAA in male patients with AD has been interpreted as a sign of higher susceptibility to vascular damage.¹³ Accordingly, this sex-related small-vessel disease susceptibility might explain why men with dementia have higher atrophy than women with dementia, whereas the putative contribution from parenchymal amyloid might add to increased atrophy relative to men without dementia. Recently, men with sporadic CAA were shown to present with an earlier onset of disease and a more hemorrhagic phenotype compared with women, supporting the hypothesis of increased vascular burden in these patients.²⁶ The fact that dementia in women was not significantly associated with more severe MTA compared with women without dementia might suggest that, at least partially, different factors in the pathophysiology of the disease may play a role.

We have found that the burden of EPVS in the centrum semiovale but not in the basal ganglia is higher in patients with dementia (Fig 5). This is in line with the general dichotomy of basal ganglia EPVS being associated with small-vessel disease arteriosclerosis, and the centrum semiovale EPVS with CAA.²⁷

Remarkably, we found a higher burden of EPVS in the centrum semiovale in female patients with dementia (Fig 5), suggesting a possible dementia mechanism in this sex group. Indeed, the presence of these enlarged spaces has been associated with vascular $A\beta$ deposition,^{14,15} which is in accordance with the hypothesis that centrum semiovale EPVS are associated with impaired perivascular drainage of $A\beta$. Our results provide further evidence in support of this hypothesis. However, centrum semiovale EPVS in AD are associated with cognitive impairment independent of amyloid burden.²⁸ The mechanisms behind this association thus remain to be established. Furthermore, sex differences in the burden of perivascular spaces have not been found in other CAA cohorts,^{26,29} but these studies have not examined the joint effect of sex and dementia. Future work is needed to assess the mediation of sex and cognitive status on the prevalence of neuroimaging findings in CAA.

Even though our results support previous observations from the literature, there are relevant limitations in this study that should be considered. The small sample size limits generalization and the possibility of controlling for other confounders. Absent systematic detailed neuropsychological data for our cohort are also a relevant limitation, which precludes further analyses related to the clinical significance of regional atrophy or atrophy patterns. Additionally, the lack of neuropathologic data does not allow the verification of the etiology of dementia and the opportunity to assess the contribution of parenchymal and vascular pathology to cerebral atrophy. Despite these limitations, our findings are aligned with previous literature and suggest sex-differential mechanisms of dementia in patients with CAA. Future studies should address neuropathologically confirmed cases or alternatively use biologic biomarkers such as blood or CSF markers or PET data.

Finally, we used structured semiquantitative visual assessments for each of the neuroimaging metrics, which have less spatial and numeric granularity than automated quantitative techniques. While the latter are in the process of entering clinical practice, visual semiquantitative scores are easy to implement and ready to use by neuroradiologists. Visual rating scores for atrophy assessment have been consistently shown to correlate with automated volume quantification across different studies.^{23,30-32} This finding suggests that, overall, visual rating scales have regional specificity and are sensitive to volume variations, even though at a lower resolution and detail. Future studies using regional volume quantification are needed to study atrophy patterns in patients with CAA and dementia and their modulation by sex. While still in development, new techniques of perivascular space segmentation have opened

up the possibility of including numerous metrics, encompassing volume, dimensions, and shape, to study their function.³³ Given the importance of this marker in CAA, future work contemplating these approaches may reveal new insights into the role of perivascular spaces. Regarding microbleeds, new methods are currently in development,³⁴ and regarding white matter hyperintensities, there is now a variety of segmentation packages available for use.^{35,36} Future work implementing quantitative techniques is needed to confirm these results and potentially explore new associations with more detailed analysis of these neuroimaging findings.

CONCLUSIONS

Dementia in CAA appears to be associated with more marked MTA in men, whereas in women, a higher burden of EPVS in the centrum semiovale was observed. Overall, this finding suggests that there may be differential pathophysiologic mechanisms with sex-specific neuroimaging patterns in dementia in CAA, motivating further confirmatory studies in larger, independent cohorts.

Disclosure forms provided by the authors are available with the full text and PDF of this article at www.ajnr.org.

REFERENCES

- Greenberg SM, Bacsikai BJ, Hernandez-Guillamon M, et al. **Cerebral amyloid angiopathy and Alzheimer disease: one peptide, two pathways.** *Nat Rev Neurol* 2020;16:30–42 CrossRef Medline
- Greenberg SM, Charidimou A. **Diagnosis of cerebral amyloid angiopathy: evolution of the Boston criteria.** *Stroke* 2018;49:491–97 CrossRef Medline
- Charidimou A, Boulouis G, Frosch MP, et al. **The Boston criteria version 2.0 for cerebral amyloid angiopathy: a multicentre, retrospective, MRI-neuropathology diagnostic accuracy study.** *Lancet Neurol* 2022;21:714–25 CrossRef Medline
- Subotic A, McCreary CR, Saad F, et al. **Cortical thickness and its association with clinical cognitive and neuroimaging markers in cerebral amyloid angiopathy.** *J Alzheimers Dis* 2021;81:1663–71 CrossRef Medline
- Fotiadis P, van Rooden S, van der Grond J, et al; Alzheimer's Disease Neuroimaging Initiative. **Cortical atrophy in patients with cerebral amyloid angiopathy: a case-control study.** *Lancet Neurol* 2016;15:811–19 CrossRef Medline
- Attems J, Jellinger KA, Lintner F. **Alzheimer's disease pathology influences severity and topographical distribution of cerebral amyloid angiopathy.** *Acta Neuropathol* 2005;110:222–31 CrossRef Medline
- Pfeifer LA, White LR, Ross GW, et al. **Cerebral amyloid angiopathy and cognitive function: the HAAS autopsy study.** *Neurology* 2002;58:1629–34 CrossRef Medline
- Boyle PA, Yu L, Nag S, et al. **Cerebral amyloid angiopathy and cognitive outcomes in community-based older persons.** *Neurology* 2015;85:1930–36 CrossRef Medline
- Xiong L, Davidsdottir S, Reijmer YD, et al. **Cognitive profile and its association with neuroimaging markers of non-demented cerebral amyloid angiopathy patients in a stroke unit.** *J Alzheimers Dis* 2016;52:171–78 CrossRef Medline
- Moulin S, Labreuche J, Bombois S, et al. **Dementia risk after spontaneous intracerebral haemorrhage: a prospective cohort study.** *Lancet Neurol* 2016;15:820–29 CrossRef Medline
- Case NF, Charlton A, Zwiars A, et al. **Cerebral amyloid angiopathy is associated with executive dysfunction and mild cognitive impairment.** *Stroke* 2016;47:2010–16 CrossRef Medline
- Costa AS, Pinho J, Kucöikienė D, et al. **Cerebral amyloid angiopathy in amyloid-positive patients from a memory clinic cohort.** *J Alzheimers Dis* 2021;79:1661–72 CrossRef Medline
- Shinohara M, Murray ME, Frank RD, et al. **Impact of sex and APOE4 on cerebral amyloid angiopathy in Alzheimer's disease.** *Acta Neuropathol* 2016;132:225–34 CrossRef Medline
- Perosa V, Oltmer J, Munting LP, et al. **Perivascular space dilation is associated with vascular amyloid- β accumulation in the overlying cortex.** *Acta Neuropathol* 2022;143:331–48 CrossRef Medline
- Tsai HH, Pasi M, Tsai LK, et al. **Centrum semiovale perivascular space and amyloid deposition in spontaneous intracerebral hemorrhage.** *Stroke* 2021;52:2356–62 CrossRef Medline
- Bouvy WH, van Veluw SJ, Kuijf HJ, et al; Utrecht Vascular Cognitive Impairment (VCI) Study Group. **Microbleeds colocalize with enlarged juxtacortical perivascular spaces in amnesic mild cognitive impairment and early Alzheimer's disease: A 7 Tesla MRI study.** *J Cereb Blood Flow Metab* 2020;40:739–46 CrossRef Medline
- Charidimou A, Boulouis G, Pasi M, et al. **MRI-visible perivascular spaces in cerebral amyloid angiopathy and hypertensive arteriopathy.** *Neurology* 2017;88:1157–64 CrossRef Medline
- Charidimou A, Meegahage R, Fox Z, et al. **Enlarged perivascular spaces as a marker of underlying arteriopathy in intracerebral haemorrhage: a multicentre MRI cohort study.** *J Neurol Neurosurg Psychiatry* 2013;84:624–29 CrossRef Medline
- Albert MS, DeKosky ST, Dickson D, et al. **The diagnosis of mild cognitive impairment due to Alzheimer's disease: recommendations from the National Institute on Aging-Alzheimer's Association workgroups on diagnostic guidelines for Alzheimer's disease.** *Alzheimers Dement* 2011;7:270–79 CrossRef Medline
- Morris JC, Edland S, Clark C, et al. **The consortium to establish a registry for Alzheimer's disease (CERAD), Part IV: rates of cognitive change in the longitudinal assessment of probable Alzheimer's disease.** *Neurology* 1993;43:2457–65 CrossRef Medline
- Wahlund LO, Barkhof F, Fazekas F, et al. **A new rating scale for age-related white matter changes applicable to MRI and CT.** *Stroke* 2001;32:1318–22 CrossRef Medline
- Potter GM, Chappell FM, Morris Z, et al. **Cerebral perivascular spaces visible on magnetic resonance imaging: development of a qualitative rating scale and its observer reliability.** *Cerebrovasc Dis* 2015;39:224–31 CrossRef Medline
- Harper L, Fumagalli GG, Barkhof F, et al. **MRI visual rating scales in the diagnosis of dementia: evaluation in 184 post-mortem confirmed cases.** *Brain* 2016;139:1211–25 CrossRef Medline
- Brenowitz WD, Nelson PT, Besser LM, et al. **Cerebral amyloid angiopathy and its co-occurrence with Alzheimer's disease and other cerebrovascular neuropathologic changes.** *Neurobiol Aging* 2015;36:2702–08 CrossRef Medline
- Xiong L, Boulouis G, Charidimou A, et al. **Dementia incidence and predictors in cerebral amyloid angiopathy patients without intracerebral hemorrhage.** *J Cereb Blood Flow Metab* 2018;38:241–49 CrossRef Medline
- Koemans EA, Castello JP, Rasing I, et al. **Sex differences in onset and progression of cerebral amyloid angiopathy.** *Stroke* 2023;54:306–14 CrossRef Medline
- Gouveia-Freitas K, Bastos-Leite AJ. **Perivascular spaces and brain waste clearance systems: relevance for neurodegenerative and cerebrovascular pathology.** *Neuroradiology* 2021;63:1581–97 CrossRef Medline
- Jeong SH, Cha J, Park M, et al. **Association of enlarged perivascular spaces with amyloid burden and cognitive decline in Alzheimer disease continuum.** *Neurology* 2022 Aug 19. [Epub ahead of print] CrossRef Medline
- Charidimou A, Jäger RH, Peeters A, et al. **White matter perivascular spaces are related to cortical superficial siderosis in cerebral amyloid angiopathy.** *Stroke* 2014;45:2930–35 CrossRef Medline
- Ingala S, van Maurik IS, Altomare D, et al. **Clinical applicability of quantitative atrophy measures on MRI in patients suspected of Alzheimer's disease.** *Eur Radiol* 2022;32:7789–99 CrossRef Medline
- Wahlund LO, Julin P, Johansson SE, et al. **Visual rating and volumetry of the medial temporal lobe on magnetic resonance imaging in**

- dementia: a comparative study.** *J Neurol Neurosurg Psychiatry* 2000;69:630–35 CrossRef Medline
32. Ferreira D, Cavallin L, Granberg T, et al; AddNeuroMed Consortium and for the Alzheimer's Disease Neuroimaging Initiative. **Quantitative validation of a visual rating scale for frontal atrophy: associations with clinical status, APOE e4, CSF biomarkers and cognition.** *Eur Radiol* 2016;26:2597–610 CrossRef Medline
33. Barisano G, Lynch KM, Sibilia F, et al. **Imaging perivascular space structure and function using brain MRI.** *Neuroimage* 2022;257:119329 CrossRef Medline
34. Chesebro AG, Amarante E, Lao PJ, et al. **Automated detection of cerebral microbleeds on T2*-weighted MRI.** *Sci Rep* 2021;11:4004 CrossRef Medline
35. Schmidt P, Gaser C, Arsic M, et al. **An automated tool for detection of FLAIR-hyperintense white-matter lesions in multiple sclerosis.** *Neuroimage* 2012;59:3774–83 CrossRef Medline
36. Griffanti L, Zamboni G, Khan A, et al. **BIANCA (Brain Intensity AbNormality Classification Algorithm): a new tool for automated segmentation of white matter hyperintensities.** *Neuroimage* 2016;141:191–205 CrossRef Medline

MR Imaging Findings in a Large Population of Autoimmune Encephalitis

S. Gillon, M. Chan, J. Chen, E.L. Guterman, X. Wu, C.M. Glastonbury, and Y. Li



ABSTRACT

BACKGROUND AND PURPOSE: Autoimmune encephalitis is a rare condition in which autoantibodies attack neuronal tissue, causing neuropsychiatric disturbances. This study sought to evaluate MR imaging findings associated with subtypes and categories of autoimmune encephalitis.

MATERIALS AND METHODS: Cases of autoimmune encephalitis with specific autoantibodies were identified from the medical record (2009–2019). Cases were excluded if no MR imaging of the brain was available, antibodies were associated with demyelinating disease, or >1 concurrent antibody was present. Demographics, CSF profile, antibody subtype and group (group 1 intracellular antigen or group 2 extracellular antigen), and MR imaging features at symptom onset were reviewed. Imaging and clinical features were compared across antibody groups using χ^2 and Wilcoxon rank-sum tests.

RESULTS: Eighty-five cases of autoimmune encephalitis constituting 16 distinct antibodies were reviewed. The most common antibodies were anti-*N*-methyl-D-aspartate ($n = 41$), anti-glutamic acid decarboxylase ($n = 7$), and anti-voltage-gated potassium channel ($n = 6$). Eighteen of 85 (21%) were group 1; and 67/85 (79%) were group 2. The median time between MR imaging and antibody diagnosis was 14 days (interquartile range, 4–26 days). MR imaging had normal findings in 33/85 (39%), and 20/33 (61%) patients with normal MRIs had anti-*N*-methyl-D-aspartate receptor antibodies. Signal abnormality was most common in the limbic system (28/85, 33%); 1/68 (1.5%) had susceptibility artifacts. Brainstem and cerebellar involvement were more common in group 1, while leptomeningeal enhancement was more common in group 2.

CONCLUSIONS: Sixty-one percent of patients with autoimmune encephalitis had abnormal brain MR imaging findings at symptom onset, most commonly involving the limbic system. Susceptibility artifact is rare and makes autoimmune encephalitis less likely as a diagnosis. Brainstem and cerebellar involvement were more common in group 1, while leptomeningeal enhancement was more common in group 2.

ABBREVIATIONS: AIE = autoimmune encephalitis; anti-Gq1b = anti-ganglioside Q1b; anti-LGII = anti-leucine-rich glioma inactivated 1; CASPR2 = contactin-associated protein-like 2; GABA = gamma-aminobutyric acid; GAD = glutamic acid decarboxylase; GFAP = glial fibrillary acidic protein; NMDA = *N*-methyl-D-aspartate; PD-1 = programmed cell death protein 1; VGCC = voltage gated calcium channel; VGKC = voltage-gated potassium channel

Autoimmune encephalitis (AIE) is an increasingly recognized cause of acute or subacute altered mental status and neurologic disturbance associated with antibodies against neuronal antigens.¹ Such antibodies may develop independently or in response to malignancies such as small-cell lung cancer and ovarian teratomas, which may be occult at the time of

presentation.² The clinical diagnosis of AIE can be challenging because the initial presentation can mimic other neurologic problems or primary psychiatric disorders.^{2,3} MR imaging of the brain plays an important role in excluding other neurologic diagnoses and in suggesting the possibility of AIE.^{4,5} Common MR imaging findings in AIE include limbic encephalitis, though findings may vary by antibody subtype, with some antibodies showing a predilection for the deep gray nuclei, brainstem, or cerebellum.^{1,6} Prior studies of AIE have also shown that more than half of all cases may have normal MR imaging findings at presentation.⁷

Antibodies associated with AIE have been classified into 2 groups: antibodies with intracellular neuronal antigens (group 1) and antibodies with extracellular neuronal antigens (group 2) (Table 1). AIE associated with group 1 antibodies is more often associated with an underlying malignancy, has an overall poorer

Received July 24, 2022; accepted after revision May 24, 2023.

From the School of Medicine (S.G., J.C.), Department of Neurology (E.L.G.), and Department of Radiology and Biomedical Imaging (X.W., C.M.G., Y.L.), University of California San Francisco, San Francisco, California; and Department of Radiology (M.C.), University of Toronto, Toronto, Ontario, Canada.

Please address correspondence to Yi Li, MD, Department of Radiology and Biomedical Imaging, University of California, San Francisco, 505 Parnassus Ave, M-391, San Francisco, CA 94143-0628; e-mail: yi.li@ucsf.edu

Indicates article with online supplemental data.

<http://dx.doi.org/10.3174/ajnr.A7907>

Table 1: Classification of autoantibodies in this cohort into group 1 (intracellular antigens) versus group 2 (extracellular antigens) autoimmune encephalitis

Group 1 Antibodies	Group 2 Antibodies
Anti-CV2	Anti-AMPA α
Anti-GAD	Anti-CASPR2
Anti-Hu	Anti-DPPX
Anti-Ma2/Ta	Anti-GABA A
Anti-Yo	Anti-GABA B
	Anti-GFAP
	Anti-GQ1b
	Anti-LGI1
	Anti-NMDA
	Anti-PD1
	Anti-VGCC
	Anti-VGKC

Note:—AMPA α indicates α -amino-3-hydroxy-5-methyl-4-isoxazolepropionic acid receptor.

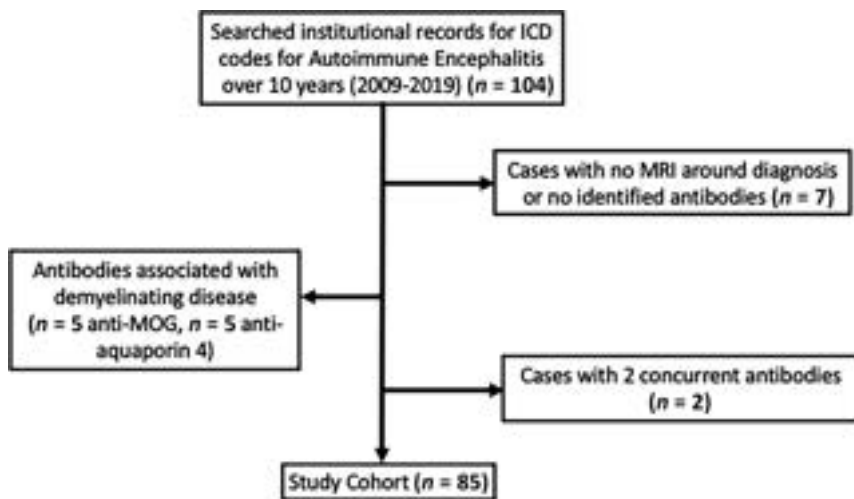


FIG 1. Flowchart of patient inclusion and exclusion criteria for the study. MOG indicates myelin oligodendrocyte; NMO, neuromyelitis optica.

prognosis, and is relatively less responsive to treatment. In contrast, AIE associated with group 2 antibodies has a better prognosis, and antibody titers more closely correlate with the severity of symptoms and response to treatment.^{2,8}

Timely diagnosis of AIE is important because earlier treatment is more likely to reverse symptoms.⁹ Although there are many reports in the literature detailing the imaging appearance of specific individual autoantibodies,^{1,8-25} there are currently very few scientific articles investigating the distribution of imaging features associated with different antibodies in a large population of AIE,^{7,26-28} allowing the development of a framework with which to evaluate this category of diseases.¹ In this study, we analyzed the brain MR imaging of 85 patients from our institution diagnosed with AIE, with imaging performed around the time of diagnosis. We hypothesize there are specific MR imaging findings more commonly associated with certain antineuronal antibodies and antibody groups.

MATERIALS AND METHODS

This retrospective, single-institution, cross-sectional study was Health Insurance Portability and Accountability Act-compliant

and approved by the institutional review board of our institution (University of California San Francisco). All eligible participants were identified by searching the medical record for Internal Classification of Disease (ICD9 and ICD10) codes for AIE between 2009 and 2019. Inclusion criteria were the following (Fig 1): 1) diagnosis of AIE between 2009 and 2019; 2) specific laboratory-confirmed autoantibodies from CSF and/or blood that were thought to be contributory to the patient's neurologic abnormality, on the basis of review of clinical notes; and 3) MR imaging of the brain obtained during the immediate work-up of the laboratory-confirmed AIE diagnosis. Patients with a diagnosis of autoimmune demyelinating disease, such as anti-aquaporin-4 antibody-mediated neuromyelitis optica and anti-myelin oligodendrocyte-associated disease, were excluded from this study because these entities constitute a different class of disease.

The medical record was searched for demographic characteristics including sex and age and clinical/laboratory data including CSF cell count, CSF protein level, the presence of underlying malignancy, pre-existing or newly diagnosed at symptom onset, and the specific laboratory-confirmed autoantibody. The medical record was evaluated for the presence of potential confounding clinical factors, such as clinical seizures at the time of MR imaging and the initiation of steroid therapy before MR imaging.

MR imaging of the brain associated with the work-up and subsequent laboratory diagnosis was independently scored by 2 blinded neuroradiologists with 5 and 7 years of experience, and discrepancies were resolved by consensus. The magnetic field strength and available sequences by MR imaging were catalogued. MR imaging findings were classified as normal or abnormal. Studies with abnormal findings were scored for the presence of structural or signal abnormality in the following predefined locations, selected on the basis of their association with AIE in prior literature: limbic, extralimbic cortex, deep gray nuclei (including hypothalamus), deep white matter, periventricular white matter, subcortical white matter, brainstem, cerebellum, and cervicomedullary junction.^{1,10} Additionally, studies were scored on the basis of whether they demonstrated abnormality on DWI or SWI or enhancement in the following distributions: white matter, perivenular, leptomeningeal (including cranial nerve enhancement). Expected age-appropriate imaging findings, such as age-appropriate parenchymal volume loss or nonspecific T2 FLAIR hyperintensity in the white matter within expected limits for age, were not categorized as abnormalities for this study.

Statistical Analysis

Statistical analysis was conducted using STATA, Version 16 (StataCorp).²⁹ We examined the distribution of patient characteristics among those with group 1 and 2 antibodies using χ^2

Table 2: Demographic and clinical features of 85 patients with laboratory-proved autoimmune encephalitis, stratified by antibody group

	All (n = 85)	Group 1 (n = 18)	Group 2 (n = 67)	P Value
Age (median) (IQR)	36 (24–62)	49.5 (29–64)	32 (22–61)	.11
Male sex	25/85 (29%)	4/18 (22%)	21/67 (31%)	.45
CSF leukocytosis	57/85 (67%)	11/18 (61%)	46/67 (69%)	.69
CSF elevated protein	33/85 (39%)	11/18 (61%)	22/67 (33%)	.06
Diagnosis of malignancy	15/85 (18%)	6/18 (33%)	9/67 (13%)	.05
Diagnosis of teratoma/hamartoma	10/85 (12%)	2/18 (11%)	8/67 (12%)	.95

Note:—IQR indicates interquartile range.

and Wilcoxon rank-sum tests. We further examined the distribution of imaging findings between group 1 and 2 antibodies using the χ^2 test. A *P* value < .05 was defined as a statistically significant result.

RESULTS

Clinical and Demographic Findings

Of 104 patients with antibody-proved AIE between 2009 and 2019, seven were excluded due to the lack of MR imaging from the time of diagnosis, 10 were excluded for the diagnosis of autoimmune demyelinating disease (5 cases of neuromyelitis optica and 5 cases of myelin oligodendrocyte glycoprotein associated disease), and 2 were excluded for the concurrent detection of 2 autoantibodies, precluding evaluation for the causative antibody (Fig 1). Eighty-five patients diagnosed with AIE had an MR imaging of the brain performed a median of 14 days (interquartile range, 4–26 days) before the laboratory-confirmed diagnosis of AIE.

In this cohort, the median age at presentation was 36 years (interquartile range, 24–62 years, Table 2), and most patients were women (71%). Regarding the CSF cell count, 57 (67%) patients had CSF leukocytosis and 33 (39%) patients had elevated protein. There was a trend toward elevated CSF protein more frequently seen in those with group 1 antibodies compared with group 2 (61% versus 33%, *P* = .06). Fifteen patients (18%) had a malignancy discovered around the time of their AIE diagnosis, and 10 (12%) had nonmalignant tumors such as hamartomas and teratomas. Only 2 patients with malignancy had pre-existing malignancy known before symptom onset. The rate of malignant tumor was significantly higher in group 1 than in group 2 (33% versus 13%, *P* < .05, Table 2), though there was no significant difference in the rates of teratomas and hamartomas between the two groups. Thirty-five patients (41%) had clinical or electroencephalography seizures around the time of MR imaging. Nine patients (11%) had been treated with steroids, and 3 patients (4%) with IV immunoglobulin up to 1 month before imaging.

Specific Autoimmune Antibodies

In 85 patients, 16 distinct types of AIE antibodies were found (Online Supplemental Data). The most common antibodies were anti-*N*-methyl-D-aspartate (NMDA) receptor antibodies (*n* = 41), anti-glutamic acid decarboxylase (GAD) antibodies (*n* = 7), and anti-voltage-gated potassium channel (VGKC) antibodies (*n* = 6). Eighteen of 85 (21%) were in group 1, and 67/85 (79%) were in group 2 antibodies.

MR Imaging Findings by AIE Group

Of the 85 brain MR images evaluated in this study, 30/85 (35%) were performed at 3T and 55/85 (65%) were performed at 1.5T. Eighty-four of 85 (99%) studies included DWI, 85/85 (100%) included T1-weighted imaging, 85/85 (100%) included T2 FLAIR imaging, 68/85 (80%) included SWI in the form of either SWI/iron sensitive imaging/gradient recalled-echo/multiplanar

gradient-recalled, and 80/85 (94%) included T1-postcontrast imaging. The frequency of imaging findings by AIE group and for all specific antibody subtypes is shown in the Online Supplemental Data.

There were significant differences between group 1 and group 2 AIE with respect to the percentage with signal abnormality in the brainstem and cerebellum (Online Supplemental Data). Brainstem signal abnormality was more common in group 1 AIE, seen in anti-Hu, anti-Ma2/Ta, and anti-CV2 (Online Supplemental Data). Among group 2 AIE, brainstem signal abnormality was seen with anti-gial fibrillary acidic protein (GFAP) and anti-voltage gated calcium channel (VGCC) but was less common compared with group 1. Cerebellar signal abnormality was also significantly more common in group 1 AIE, seen in anti-Hu, anti-Yo, anti-CV2, and anti-GAD (Online Supplemental Data). Among group 2 AIE, cerebellar signal abnormality was seen in anti-NMDA, anti-GFAP, anti-VGCC, anti-programmed cell death protein 1 (PD-1), and anti-ganglioside Q1b (GQ1B), but it was less common compared with group 1.

Antibody Subtype Based on MR Imaging Findings

MR imaging findings were abnormal in 52/85 (61%) patients. The most common areas of signal abnormality in the overall cohort were limbic (28/85, 33%), extralimbic cortex (18/85, 21%), and periventricular white matter (17/85, 20%, Online Supplemental Data). Ten cases (12%) had reduced diffusion, which was not significantly more common in either group 1 or group 2 (1/18, 6% versus 9/67, 13%, *P* = .36). Only 1/68 (1.5%) had susceptibility artifacts, which were in a case of anti-NMDA encephalitis.

Normal MR Imaging Findings. Thirty-three of 85 (39%) patients with AIE had normal findings on MR imaging of the brain. Patients with anti-NMDA encephalitis constituted those with the most normal MR imaging findings (20/33, 61%). Other patients with normal MR imaging had laboratory-confirmed anti-Hu, anti-Yo, anti-GAD, anti-NMDA, anti- α -amino-3-hydroxy-5-methyl-4-isoxazolepropionic acid receptor (AMPA), anti-VGCC, anti-DPPX, anti-GQ1B, anti-VGKC, anti-leucine-rich glioma inactivated 1 (LGI1) and anti-contactin-associated protein-like 2 (CASPR2).

Limbic Signal Abnormality. Limbic signal abnormality was present in 28/85 (33%) patients and seen in anti-Hu, anti-Ma2/Ta, anti-CV2, anti-GAD, anti-NMDA, anti-gamma-aminobutyric acid (GABA)-B, anti-GFAP, anti-VGKC, and anti-CASPR2 (Online Supplemental Data).

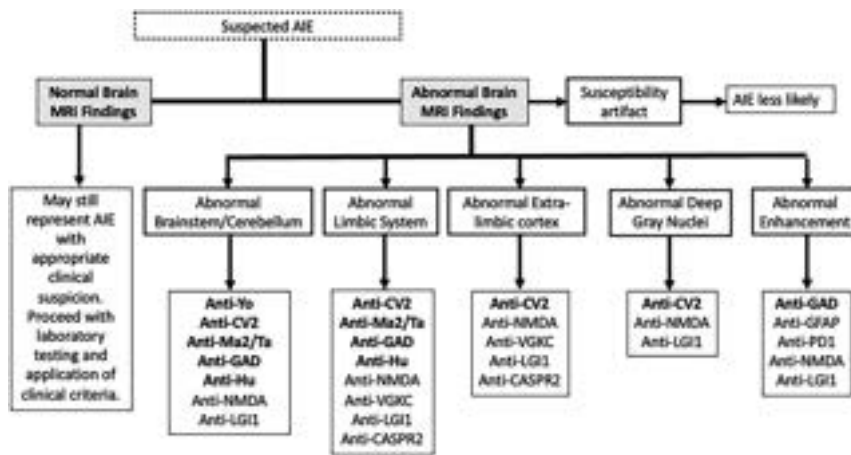


FIG 2. Proposed imaging stratification algorithm for patients with suspected AIE. Boldface anti-bodies belong to the group 1 classification.

Deep Gray Signal Abnormality. Deep gray signal abnormality was present in 10/85 (12%) patients and seen in anti-Ma2/Ta, anti-CV2, anti-GAD, anti-NMDA, and anti-LGI1 encephalitis (Online Supplemental Data).

Deep White Matter Signal Abnormality. Eleven of 85 (13%) patients had deep white matter signal abnormality, including those with anti-Hu, anti-CV2, anti-GAD, anti-NMDA, anti-GFAP, and anti-VGCC (Online Supplemental Data).

Subcortical White Matter Signal Abnormality. Sixteen of 85 (19%) patients demonstrated subcortical white matter signal abnormality, including patients with anti-Hu, anti-Yo, anti-NMDA, anti-GABA-B, anti-GFAP, anti-VGCC, and anti-VGKC (Online Supplemental Data).

Periventricular White Matter Signal Abnormality. Seventeen of 85 (20%) patients demonstrated periventricular white matter signal abnormality, including patients with anti-CV2, anti-GAD, anti-NMDA, anti-GFAP, anti-VGCC, and anti-VGKC (Online Supplemental Data).

Extralimbic Cortex. Eighteen of 85 (21%) patients demonstrated extralimbic cortical signal abnormality, including patients with anti-CV2, anti-GAD, anti-NMDA, anti-GABA-A, anti-GFAP, anti-VGCC, anti-VGKC, anti-LGI1, and anti-CASPR2 (Online Supplemental Data).

Brainstem. Five of 85 (6%) patients demonstrated brainstem signal abnormality, including patients with anti-Hu, anti-Ma2/Ta, anti-CV2, anti-GFAP, and anti-VGCC encephalitis (Online Supplemental Data). Brainstem signal abnormality was more commonly seen in group 1 AIE (Online Supplemental Data).

Cerebellum. Ten of 85 (12%) patients demonstrated cerebellar signal abnormality or volume loss, including patients with anti-Hu, anti-Yo, anti-CV2, anti-GAD, anti-NMDA, anti-GFAP, anti-VGCC, anti-PD-1, and anti-GQ1B encephalitis (Online

Supplemental Data). Cerebellar abnormality was more common with group 1 than group 2 AIE (Online Supplemental Data).

White Matter Enhancement. Three of 80 (4%) patients demonstrated white matter enhancement, including patients with anti-GFAP and anti-PD-1 encephalitis (Online Supplemental Data). For anti-PD-1 encephalitis, the white matter enhancement was cerebellar in location.

Deep Gray Enhancement. One of 80 (1%) patients demonstrated deep gray enhancement seen in a patient with anti-LGI1 encephalitis (Online Supplemental Data).

Perivascular Enhancement. Four of 80 (5%) patients demonstrated perivascular enhancement, including patients with anti-GAD, anti-NMDA, and anti-GFAP (Online Supplemental Data).

Leptomeningeal/Cranial Nerve Enhancement. Two of 80 (2.5%) patients demonstrated leptomeningeal enhancement, both of whom had anti-GQ1B encephalitis. One demonstrated cranial nerve enhancement, and the other demonstrated enhancement along the cerebellar folia in regions of abnormal cerebellar signal (Online Supplemental Data).

DISCUSSION

In our retrospective study of consecutive patients from our institution diagnosed with laboratory-confirmed AIE, we found MR imaging abnormalities present in approximately two-thirds of patients at the time of symptom onset, and limbic signal abnormality was the most common, seen in 33% of patients. Although there were many overlapping features among the specific autoantibody subtypes, group 1 antibodies more commonly involved the brainstem and cerebellum, while group 2 more commonly demonstrated leptomeningeal enhancement. Certain imaging findings were seen more commonly with specific antibody subtypes. Our findings support an imaging framework for suggesting AIE by imaging and potentially specific AIE subtypes based on MR imaging findings (Fig 2).^{26,28,30}

The results of our imaging analysis reinforce the findings of many smaller studies and case reports on specific autoantibodies.^{4,7,9,10,13,18,20,21,24-27,31} The anti-NMDA receptor antibody was the most common antibody in our cohort, similar to findings in other cohort studies.^{19,27,38} Only 1 patient in the cohort demonstrated susceptibility artifacts suggestive of hemorrhage, and this was in a patient with anti-NMDA receptor encephalitis, who developed AIE after herpes simplex virus encephalitis. This finding reinforces prior studies and case reports on AIE, which have not described susceptibility artifacts as an imaging feature of AIE; thus, the presence of susceptibility typically makes AIE a less likely diagnosis.^{16,32}

In our study, 39% of patients had normal MR imaging findings despite antibody-proved AIE. Normal MR imaging findings

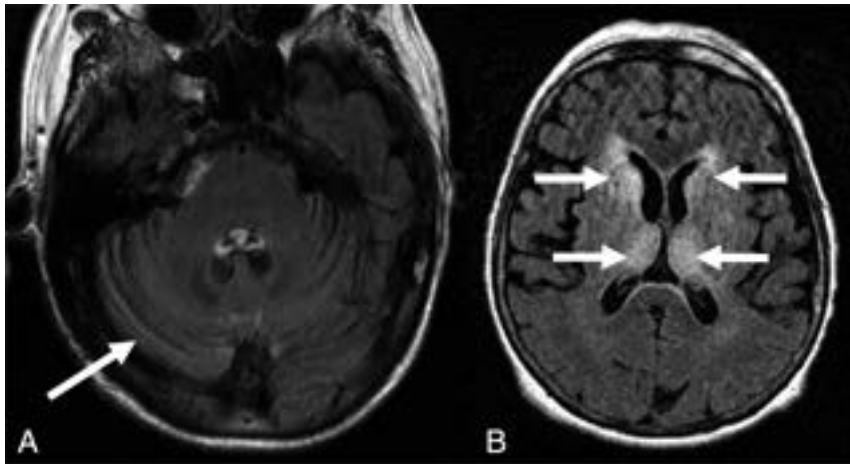


FIG 3. Imaging findings in examples of group 1 antibody AIE. A, A 65-year-old woman with a history of ovarian cancer who developed emesis, ataxia, and gait instability. Axial FLAIR images demonstrate enlarged cerebellar folia (*large white arrow*), compatible with volume loss. Subsequent work-up revealed anti-Yo encephalitis. B, A 44-year-old woman with 9 months of progressive ophthalmoplegia, amnesia, mild hemiparesis, and vertigo. Axial FLAIR imaging demonstrates deep gray and periventricular white matter hyperintensity (*white arrows*). The patient was subsequently diagnosed with anti-CV2 encephalitis.

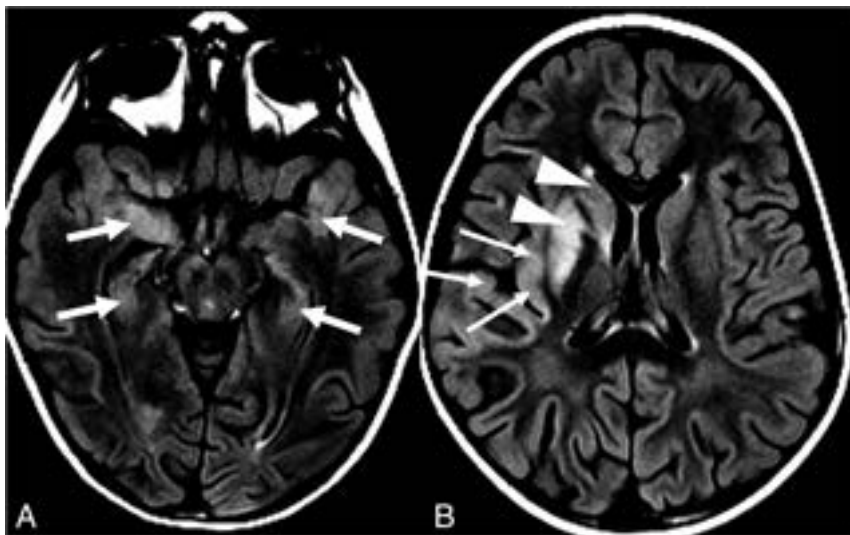


FIG 4. A 22-year-old man with no major medical history presented with subacute, progressive, altered mental status and psychiatric symptoms including paranoia and visual and auditory hallucinations. He subsequently developed memory loss and aphasia and was ultimately diagnosed with anti-NMDA receptor encephalitis. Axial FLAIR images of the patient at 2 different levels are shown. A, At the level of the temporal horns, there is FLAIR hyperintensity and swelling of bilateral hippocampi and medial temporal lobes (*white arrows*). B, At the level of the lateral ventricular bodies, there is FLAIR hyperintensity and swelling of the right insular and superior temporal cortices (*thin white arrows*), as well as the right caudate head and putamen (*white arrowhead*).

were seen in several AIE subtypes, most commonly anti-NMDA encephalitis. Prior studies have demonstrated that a subset of patients with AIE will have normal MR imaging findings despite clinically-apparent neuropsychiatric disturbances.² In 1 prior study, 40% of patients with NMDA receptor encephalitis had normal MR imaging findings, similar to the results in our study.¹⁹ A separate study analyzing 77 patients with a diverse subset of antibodies found that 63% of patients presented with normal or nonspecific MR imaging findings at symptom onset.⁷

abnormalities with T2 hyperintensities primarily in the mesial temporal lobes with occasional involvement of the brainstem and thalami.^{13,37}

Patients in our cohort with anti-GFAP astrocytopathy demonstrated periventricular and deep white matter signal abnormality, with perivenular enhancement in the deep white matter (Fig 5), consistent with previous review articles and case reports.^{4,11,25} Patients with anti-GQ1b antibody-associated AIE (Fig 6) were the only ones in our cohort to demonstrate leptomeningeal and

Notably, brain MR imaging findings may initially be normal, and MR imaging changes can develop subsequently, thus demonstrating the importance of follow-up imaging in patients with a suspected diagnosis of AIE.⁵ Additional imaging modalities such as PET/CT and additional imaging sequences such as arterial spin-labeling perfusion may be helpful adjuncts in the work-up of those patients with AIE and otherwise normal MR imaging findings.³³⁻³⁵ Most important, normal MR imaging findings do not exclude AIE as a diagnosis in the context of appropriate clinical suspicion, and appropriate laboratory work-up should ensue.

On a group level, our study found a higher percentage of brainstem and cerebellar involvement in group 1 AIE. Although the evaluation of individual subtypes of AIE was challenging due to the small number of patients with some subtypes, a few general trends could be appreciated. Multiple subtypes demonstrated limbic involvement, some of which, including anti-Ma2/Ta, anti-GAD, and anti-Hu also involved the brainstem or cerebellum. Anti-CV2 (Fig 3) and anti-LGI1 involved the limbic system, extralimbic cortex, and deep gray nuclei. Some cases of anti-NMDA involved all of the following: limbic, extralimbic cortex, deep gray nuclei, and brainstem/cerebellum (Fig 4). Multiple prior case reports and smaller studies support the conclusions of our study that these subtypes cause limbic encephalitis, often with additional involvement.^{2,6,9,12,23,26,36}

Patients with anti-Yo antibody-associated AIE in our cohort had cerebellar signal abnormality and volume loss (Fig 3), which has been described in prior articles describing anti-Yo antibodies as a cause of paraneoplastic cerebellar degeneration.^{21,24} Previous reports of anti-Ma2/Ta describe brain

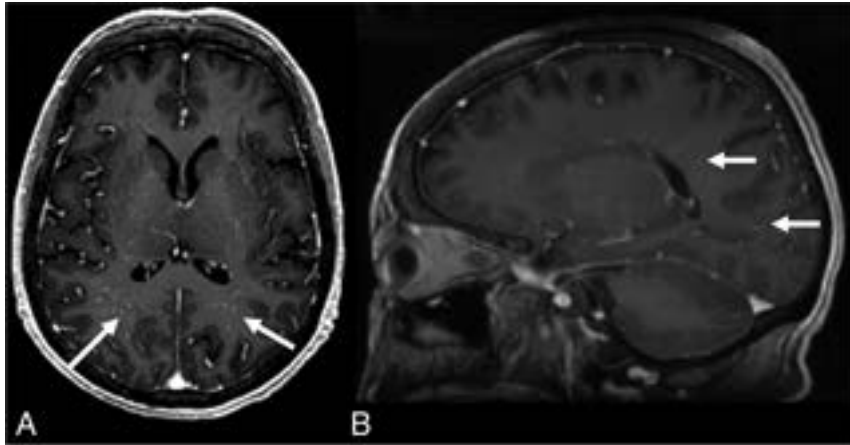


FIG 5. A 43-year-old woman with progressive, altered mental status and right-leg and buttock paresthesia. Subsequent testing revealed anti-GFAP encephalitis. Axial (A) and sagittal (B) post-contrast T1-weighted imaging demonstrates linear perivenular enhancement (white arrows) radiating into the periventricular white matter.

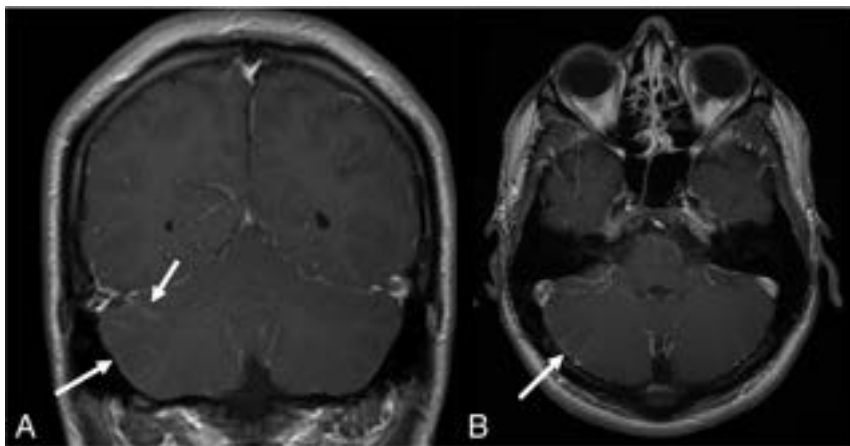


FIG 6. A 20-year-old man with a several-day history of headache and new-onset diplopia with a subsequent work-up revealing anti-GQ1b encephalitis. Axial (A) and coronal (B) post-contrast T1-weighted imaging demonstrates leptomeningeal enhancement of the right cerebellar hemisphere (white arrows).

cranial nerve enhancement, consistent with previous descriptions in the literature.²⁰ Because anti-GQ1b is thought to cause Miller Fisher syndrome, a variant of Guillain-Barre syndrome affecting cranial nerves, this imaging feature corresponds to clinical symptoms.¹⁵ In a study analyzing 15 patients with anti-GQ1b antibodies, 14 of 16 MR imaging examinations demonstrated at least 1 cranial nerve abnormality.²⁰

In keeping with prior studies,^{26,28,30} most patients with AIE in our study were women (71%) and young (median age, 36 years). There was a significantly higher rate of associated malignancy with group 1 antibodies, in line with the findings in prior literature.^{2,38} Patients with group 1 antibodies demonstrated elevated CSF protein compared with group 2. A prior study investigating CSF findings in AIE found similar results, with 53% of patients with group 1 antibodies demonstrating elevated CSF protein versus 37% of those with group 2 antibodies.³⁹ The predominant theory for this phenomenon is that CSF protein generally increases with age, and because patients with group 1 antibodies

typically are older, the increased incidence of elevated CSF protein could be correlated to increased age.^{30,39}

To our knowledge, this study represents the largest scientific imaging evaluation of a consecutive cohort of patients with laboratory-proved AIE. While prior literature has been published on individual AIE subtypes, few articles have studied AIE as a whole and provided a framework for approaching the diagnosis by imaging. However, our study does have several limitations. While we studied many cases of AIE in aggregate, there were few individual cases of rare antibody subtypes. Our study lacked an age-matched control group, but age-related changes were intentionally not scored in our imaging review. Because the cohort dates back to 2008, many older MR images were obtained with 2D sequences at 1.5T; however, these studies are of diagnostic quality and remain consistent with image quality in current clinical practice. Not all patients had SWI or postcontrast imaging performed around the time of diagnosis, limiting the detection of abnormalities on those sequences. Additionally, approximately 15% of patients had received prophylactic steroid or IV immunoglobulin therapy before imaging, which may decrease the severity of the findings seen on MR imaging. Because 41% of patients in this study had seizures around the time of imaging, it is possible that some imaging findings may represent the manifestation of concurrent seizures, particularly cortical- and deep gray-reduced diffusion; however, no patients had imaging abnormalities confined only to these regions; thus, we believe that most abnormalities are attributable to the underlying AIE in these cases. Finally, because we studied only the initial MR images obtained around the time of symptom onset and not subsequent follow-up imaging, we did not study the evolution of these imaging findings and whether patients with initial normal MR imaging findings subsequently developed abnormalities. Future longitudinal, multicenter studies are needed to increase the follow-up time and sample size to generate more specific conclusions in this population.

CONCLUSIONS

In this single-institution study of 85 consecutive patients with the confirmed diagnosis of AIE, approximately two-thirds had abnormal findings on brain MR imaging, with limbic signal abnormality the most common abnormal imaging finding.

Susceptibility artifacts are rarely seen in AIE (only noted in 1 patient in our study); thus, their presence makes AIE less likely. While we documented certain imaging features to be more frequent in certain subtypes of AIE, in many cases, imaging findings at symptom onset were normal but were still useful to rule out alternative causes of the patient's neurologic presentation. Early identification of neuroimaging features of AIE will lead to earlier diagnosis, treatment, and potentially improved clinical outcomes.

Disclosure forms provided by the authors are available with the full text and PDF of this article at www.ajnr.org.

REFERENCES

- Ball C, Fiscaro R, Morris L, et al. **Brain on fire: an imaging-based review of autoimmune encephalitis.** *Clin Imaging* 2022;84:1–30 CrossRef Medline
- Kelley BP, Patel SC, Marin HL, et al. **Autoimmune encephalitis: pathophysiology and imaging review of an overlooked diagnosis.** *AJNR Am J Neuroradiol* 2017;38:1070–78 CrossRef Medline
- Glaser CA, Gilliam S, Schnurr D, et al; California Encephalitis Project, 1998–2000. **In search of encephalitis etiologies: diagnostic challenges in the California Encephalitis Project, 1998–2000.** *Clin Infect Dis* 2003;36:731–42 CrossRef Medline
- Theroux LM, Goodkin HP, Heinan KC, et al. **Extreme delta brush and distinctive imaging in a pediatric patient with autoimmune GFAP astrocytopathy.** *Mult Scler Relat Disord* 2018;26:121–23 CrossRef Medline
- Abboud H, Probasco JC, Irani S, et al; Autoimmune Encephalitis Alliance Clinicians Network. **Autoimmune encephalitis: proposed best practice recommendations for diagnosis and acute management.** *J Neurol Neurosurg Psychiatry* 2021;92:757–68 CrossRef Medline
- Budhram A, Leung A, Nicolle MW, et al. **Diagnosing autoimmune limbic encephalitis.** *CMAJ* 2019;191:E529–34 CrossRef Medline
- Saraya AW, Worachotsueptrakun K, Vutipongsatorn K, et al. **Differences and diversity of autoimmune encephalitis in 77 cases from a single tertiary care center.** *BMC Neurol* 2019;19:273 CrossRef Medline
- Si Z, Wang A, Liu J, et al. **Typical clinical and imaging manifestations of encephalitis with anti- γ -aminobutyric acid B receptor antibodies: clinical experience and a literature review.** *Neurol Sci* 2019;40:769–77 CrossRef Medline
- Kotsenas AL, Watson RE, Pittock SJ, et al. **MRI findings in autoimmune voltage-gated potassium channel complex encephalitis with seizures: one potential etiology for mesial temporal sclerosis.** *AJNR Am J Neuroradiol* 2014;35:84–89 CrossRef Medline
- Wu H, Yu H, Joseph J, et al. **Neuroimaging and CSF findings in patients with autoimmune encephalitis: a report of eight cases in a single academic center.** *Neurol Int* 2022;14:176–85 CrossRef Medline
- Lin J, Lu L, Li J. **Typical linear radial periventricular enhancement in a patient with glial fibrillary acidic protein (GFAP) astrocytopathy.** *Neurol Sci* 2022;43:2895–97 CrossRef Medline
- Zouras S, Stephens JW, Abburu SR, et al. **Anti-LGI1 encephalitis causing faciobrachial dystonic seizures.** *BMJ Case Rep* 2017;2017:bcr-2017-221089 CrossRef Medline
- Vogrig A, Joubert B, Maureille A, et al. **Motor neuron involvement in anti-Ma2-associated paraneoplastic neurological syndrome.** *J Neurol* 2019;266:398–410 CrossRef Medline
- Compta Y, Iranzo A, Santamaria J, et al. **REM sleep behavior disorder and narcoleptic features in anti-Ma2-associated encephalitis.** *Sleep* 2007;30:767–69 CrossRef Medline
- Saul RF. **Neuro-ophthalmology and the anti-GQ1b antibody syndromes.** *Curr Neurol Neurosci Rep* 2009; 379–83 CrossRef Medline
- Bacchi S, Franke K, Wewegama D, et al. **Magnetic resonance imaging and positron emission tomography in anti-NMDA receptor encephalitis: a systematic review.** *J Clin Neurosci* 2018;52:54–59 CrossRef Medline
- Ha J, Na BS, Ahn JH, et al. **Anti-CV2/CRMP5 paraneoplastic chorea effectively managed with intravenous amantadine.** *Tremor Other Hyperkinet Mov (N Y)* 2019;9 CrossRef Medline
- Wu X, Wang H, Xu G, et al. **Anti-CV2 autoimmune encephalitis with Parkinson-like symptoms and bilateral leukoencephalopathy: a case report.** *Front Neurol* 2019;10:1064 CrossRef Medline
- Gomez-Figueroa E, Garcia-Estrada C, Paredes-Aragon E, et al. **Brain MRI volumetric changes in the follow-up of patients with anti-NMDAR encephalitis.** *Clin Neurol Neurosurg* 2021;209:106908 CrossRef Medline
- Lee B, Lee JH, Lim YM, et al. **High-resolution MR imaging of cranial neuropathy in patients with anti-GQ1b antibody syndrome.** *J Neurol Sci* 2021;423:117380 CrossRef Medline
- Renard D, Taieb G, Briere C, et al. **Mild encephalitis/encephalopathy with a reversible splenial, white matter, putaminal, and thalamic lesions following anti-Yo rhombencephalitis.** *Acta Neurol Belg* 2012;112:405–07 CrossRef Medline
- Li W, Wu S, Meng Q, et al. **Clinical characteristics and short-term prognosis of LGI1 antibody encephalitis: a retrospective case study.** *BMC Neurol* 2018;18:1–8 CrossRef Medline
- Neo S, Yeo T, Chen Z, et al. **Acute radiological features facilitate diagnosis and prognosis of anti-N-methyl-D-aspartate receptor (NMDAR) and anti-voltage-gated potassium channel (VGKC) encephalitis in adults.** *J Neurol Sci* 2020;419:117216 CrossRef Medline
- Endres D, Perlov E, Stich O, et al. **Case report: low-titre anti-Yo reactivity in a female patient with psychotic syndrome and frontoparieto-cerebellar atrophy.** *BMC Psychiatry* 2015;15:112 CrossRef Medline
- Fang B, McKeon A, Hinson SR, et al. **Autoimmune glial fibrillary acidic protein astrocytopathy: a novel meningoencephalomyelitis.** *JAMA Neurol* 2016;73:1297–307 CrossRef Medline
- Swayne A, Warren N, Prain K, et al. **An Australian state-based cohort study of autoimmune encephalitis cases detailing clinical presentation, investigation results, and response to therapy.** *Front Neurol* 2021;12:607773 CrossRef Medline
- Gu Y, Zhong M, He L, et al. **Epidemiology of antibody-positive autoimmune encephalitis in Southwest China: a multicenter study.** *Front Immunol* 2019;10:2611 CrossRef Medline
- Wang Y, Miao A, Shi Y, et al. **Influencing electroclinical features and prognostic factors in patients with anti-NMDAR encephalitis: a cohort follow-up study in Chinese patients.** *Sci Rep* 2020;10:10753 CrossRef Medline
- Stata Statistical Software: Release 16. 2019. <https://www.stata.com/stata-news/news35-1/updates-to-stata16/>. Accessed May 5, 2022
- Zrzavy T, Höftberger R, Wimmer I, et al. **Longitudinal CSF findings in autoimmune encephalitis: a monocentric cohort study.** *Front Immunol* 2021;12:646940 CrossRef Medline
- Shao X, Fan S, Luo H, et al. **Brain magnetic resonance imaging characteristics of anti-leucine-rich glioma-inactivated 1 encephalitis and their clinical relevance: a single-center study in China.** *Front Neurol* 2021;11:618109 CrossRef Medline
- Vallabhaneni D, Naveed MA, Mangla R, et al. **Perfusion imaging in autoimmune encephalitis.** *Case Rep Radiol* 2018;2018:3538645 CrossRef Medline
- Bordonne M, Chawki MB, Doyen M, et al. **Brain 18F-FDG PET for the diagnosis of autoimmune encephalitis: a systematic review and a meta-analysis.** *Eur J Nucl Med Mol Imaging* 2021;48:3847–58 CrossRef Medline
- Yedavalli VS, Hamam O, Bahouth M, et al. **Arterial spin labeling imaging characteristics of anti-leucine-rich glioma-inactivated 1 encephalitis: a qualitative and quantitative analysis.** *Front Neurol* 2022;13:850029 CrossRef Medline

35. Probasco JC, Solnes L, Nalluri A, et al. **Abnormal brain metabolism on FDG-PET/CT is a common early finding in autoimmune encephalitis.** *Neurol Neuroimmunol Neuroinflamm* 2017;4:e352 CrossRef Medline
36. Heine J, Prüss H, Bartsch T, et al. **Imaging of autoimmune encephalitis: relevance for clinical practice and hippocampal function.** *Neuroscience* 2015;309:68–83 CrossRef Medline
37. Dalmau J, Rosenfeld MR. **Autoimmune encephalitis update.** *Neuro Oncol* 2014;16:771–78 CrossRef Medline
38. Rees JH. **Paraneoplastic syndromes: when to suspect, how to confirm, and how to manage.** *J Neurol Neurosurg Psychiatry*.2004;75 (Suppl 2):ii43–50 CrossRef Medline
39. Hébert J, Gros P, Lapointe S, et al. **Searching for autoimmune encephalitis: beware of normal CSF.** *J Neuroimmunol* 2020;345:577285 CrossRef Medline

Early Detection of Underlying Cavernomas in Patients with Spontaneous Acute Intracerebral Hematomas

A. Bani-Sadr,¹ O.F. Eker,² T.-H. Cho,³ R. Ameli,⁴ M. Berhouma,⁵ M. Cappucci,⁶ L. Derex,⁷ L. Mechtouff,⁸ D. Meyronet,⁹ N. Nighoghossian,¹⁰ Y. Berthezène, and M. Hermier¹¹



ABSTRACT

BACKGROUND AND PURPOSE: Early identification of the etiology of spontaneous acute intracerebral hemorrhage is essential for appropriate management. This study aimed to develop an imaging model to identify cavernoma-related hematomas.

MATERIALS AND METHODS: Patients 1–55 years of age with acute (≤ 7 days) spontaneous intracerebral hemorrhage were included. Two neuroradiologists reviewed CT and MR imaging data and assessed the characteristics of hematomas, including their shape (spherical/ovoid or not), their regular or irregular margins, and associated abnormalities including extraleSIONAL hemorrhage and peripheral rim enhancement. Imaging findings were correlated with etiology. The study population was randomly split to provide a training sample (50%) and a validation sample (50%). From the training sample, univariate and multivariate logistic regression was performed to identify factors predictive of cavernomas, and a decision tree was built. Its performance was assessed using the validation sample.

RESULTS: Four hundred seventy-eight patients were included, of whom 85 had hemorrhagic cavernomas. In multivariate analysis, cavernoma-related hematomas were associated with spherical/ovoid shape ($P < .001$), regular margins ($P = .009$), absence of extraleSIONAL hemorrhage ($P = .01$), and absence of peripheral rim enhancement ($P = .002$). These criteria were included in the decision tree model. The validation sample ($n = 239$) had the following performance: diagnostic accuracy of 96.1% (95% CI, 92.2%–98.4%), sensitivity of 97.95% (95% CI, 95.8%–98.9%), specificity of 89.5% (95% CI, 75.2%–97.0%), positive predictive value of 97.7% (95% CI, 94.3%–99.1%), and negative predictive value of 94.4% (95% CI, 81.0%–98.5%).

CONCLUSIONS: An imaging model including ovoid/spherical shape, regular margins, absence of extraleSIONAL hemorrhage, and absence of peripheral rim enhancement accurately identifies cavernoma-related acute spontaneous cerebral hematomas in young patients.

ABBREVIATION: DVA = developmental venous anomaly

Acute spontaneous intracerebral hematomas are frequent and remain a major cause of morbidity and mortality.¹ The

prognosis and treatment depend on the underlying cause of bleeding. In older patients, primary hemorrhages, due to hypertension or amyloid angiopathy, are the most frequent. The probability of finding a secondary cause, such as vascular malformations, is increased in younger patients.

An etiologic work-up based on imaging is advocated in all patients younger than 55 years of age.^{2,3} In patients presenting with acute spontaneous intracerebral hemorrhage, the shape of the hematoma on imaging performed in the acute phase is correlated with prognosis: Irregular margins may predict hematoma expansion⁴ and have been associated with death and major disability.⁵ In some instances, the shape of the hematoma may also suggest the underlying pathology. Lobar intracerebral hemorrhage with finger-like projections is suggestive of amyloid angiopathy.⁶ Some imaging features, including mixed-aged blood, mulberry-like clusters, and a developmental venous anomaly (DVA) in the vicinity of the hematoma, may suggest an underlying cavernoma. A spherical or ovoid hematoma has sometimes been reported in hemorrhagic

Received January 24, 2023; accepted after revision May 29.

From the Department of Neuroradiology (A.B.-S., O.F.E., R.A., M.C., Y.B., M.H.), Stroke Department (T.-H.C., L.D., L.M., N.N.), Skull Base Surgery Unit (M.B.), Department of Neurosurgery B, and Institute of Pathology East, Neuropathology (D.M.), East Group Hospital, Hospices Civils de Lyon, Bron, France; Creatis Laboratory (A.B.-S., O.F.E., Y.B.), National Center for Scientific Research Unit Mixte de Recherche 5220, Institut National de la Santé et de la Recherche Médicale U 5220, Claude Bernard Lyon I University, Villeurbanne, France; CarMeN Laboratory (T.-H.C., L.M., N.N.), Institut National de la Santé et de la Recherche Médicale U1060, Claude Bernard Lyon I University, Bron, France; Research on Healthcare Performance (L.D.), Institut National de la Santé et de la Recherche Médicale U 1290, Claude Bernard Lyon I University, Domaine Rockefeller, Lyon, France.

A. Bani-Sadr and O.F. Eker contributed equally and are co-first authors.

Please address correspondence to Alexandre Bani-Sadr, MD, Department of Neuroradiology, East Group Hospital, Hospices Civils de Lyon, 59 Boulevard Pinel, 69500 Bron, France; e-mail: apbanisadr@gmail.com



Indicates article with online supplemental data.

<http://dx.doi.org/10.3174/ajnr.A7914>

cerebral cavernomas.^{7,8} However, this characteristic is not mentioned in the widely used MR imaging classification of cavernomas described by Zabramski et al,⁹ and recent reviews on the imaging of acute spontaneous cerebral hemorrhages did not report it as a critical finding.^{10,11} Consequently, the predictive value of a spherical or ovoid hematoma in diagnosing underlying cerebral cavernoma is as yet unknown.

We aimed to assess the radiologic characteristics of hemorrhagic cerebral cavernomas compared with other etiologies in a large series of patients 55 years of age or younger presenting with acute spontaneous intracerebral hematomas. We built and evaluated a radiologic model to predict an underlying cavernoma in case of acute spontaneous intracerebral hematoma.

MATERIALS AND METHODS

We performed a retrospective study in a tertiary hospital (Pierre Wertheimer Hospital, Hospices de Lyon).

Data Availability Statement

Further anonymized data can be provided to qualified investigators on request to the corresponding author.

Ethics Statement

The local ethics committee approved the study and waived the need for informed consent.

Inclusion Criteria

On the basis of our radiology database, we retrieved patients with a diagnosis of symptomatic spontaneous acute cerebral hemorrhage during a 12-year period (January 2010 to December 2021). We included patients 1 year of age and older and 55 years and younger presenting with a first episode of acute-to-early subacute (≤ 7 days) intracerebral hematoma either on CT or MR imaging. Admission imaging had to be available on the PACS to allow multiplanar assessment.

Exclusion Criteria

Patients presenting with intracerebral hematomas lacking imaging data or having poor image quality and no definite or probable etiology after work-up or with traumatic lesions, known brain tumors, hematomas following either IV thrombolytic therapy, interventional neuroradiology, or neurosurgery were excluded. Patients with hematomas of >7 days and intracerebral hematomas with a largest diameter of <10 mm were also excluded.

Etiologies of the Hematoma

The final etiologic diagnosis was determined by consensus between stroke neurologists and neuroradiologists after reviewing all available etiologic work-ups. Etiologic diagnoses were classified as follows: cerebral aneurysm, arteriovenous shunt (ie, AVM, AVF, AVM draining into a DVA), cerebral cavernoma, cerebral vein thrombosis (ie, direct visualization of thrombi in the cerebral venous system on either contrast-enhanced CT or MR imaging or cerebral angiography), hypertension, probable amyloid angiopathy, spontaneous hemorrhagic transformation of ischemic stroke, reversible vasoconstriction syndrome, posterior reversible encephalopathy syndrome, pseudoaneurysm in the setting of infective endocarditis, other vasculopathies (ie, Moyamoya,

vasculitis), neoplasms with acute hemorrhagic presentation, and toxic or coagulation disorders.

For cavernomas, diagnosis was made on the basis of either histopathology^{12,13} or follow-up.¹⁴ Mixed vascular lesions with both cavernous components and capillary telangiectasia at histopathology were classified as cavernomas. Follow-up-based diagnoses were established by consensus after review of the medical files and required a cerebral angiography with negative findings and at least 12 months of follow-up with a favorable clinical course and a typical imaging course of cavernoma as previously described.^{9,14}

Data Collection

Two senior neuroradiologists (A.B.-S., M.H.) reviewed neuroimaging examinations (CT scanner, 1.5T or 3T MR imaging scanners) at the acute (ie, ≤ 7 days) phase. After undergoing a training period of 100 cases, blinded to clinical data and final diagnosis, they reviewed, independently, imaging data of all patients, and discrepancies were settled by consensus.

They classified hematoma shape as being "spherical/ovoid" or not (Fig 1) and as having regular or irregular margins according to the following definition: regular, no angular aspect at any part of the hematoma border; irregular, ≥ 1 angular aspect protruding from any part of the hematoma (Fig 2). Hematomas with lobulated margins without any angular aspect were considered regular (Fig 2). Hematoma location was classified as supratentorial lobar, supratentorial deep, brainstem, cerebellar, or multifocal.

Associated anomalies, including extralesional hemorrhage (ie, intraventricular, subarachnoid, subdural), peripheral rim enhancement, evidence of blood-breakdown products of varying stages, DVA, arteriovenous shunt, and aneurysm, were assessed after analysis of all available imaging data. Radiologic signs of small-vessel disease were also evaluated (microbleeds on T2* and white matter disease with a total Fazekas score of ≥ 2 using FLAIR or CT when MR imaging was not available¹⁵).

Whenever possible, hematoma shape and margins were evaluated on T2*-weighted MR imaging performed in the acute phase, and on T1 and T2 FLAIR sequences when susceptibility artifacts obscured the margins. Plain CT was used when MR imaging data were not available. Volumes were obtained by measuring hematoma diameters and calculated using the ABC/2 score.¹⁶

In case of multiple acute hematomas, the analysis focused on the largest one.

Baseline demographic and clinical characteristics, including medications, patient history, and Glasgow Coma Scale score were collected from the medical records, blinded to imaging data.

Statistical Analysis

Data are presented as counts (percentages) for binary variables and medians (interquartile range) for continuous variables because none were assumed to have normal distributions. Interrater agreement for radiologic characteristics was assessed using the Cohen κ coefficient. Descriptive statistics were performed using parametric or nonparametric tests as appropriate. The study population was randomly split into 2 parts to provide a training sample (50%) and a validation sample (50%). Using the training sample, we performed univariate logistic regression to evaluate putative predictive

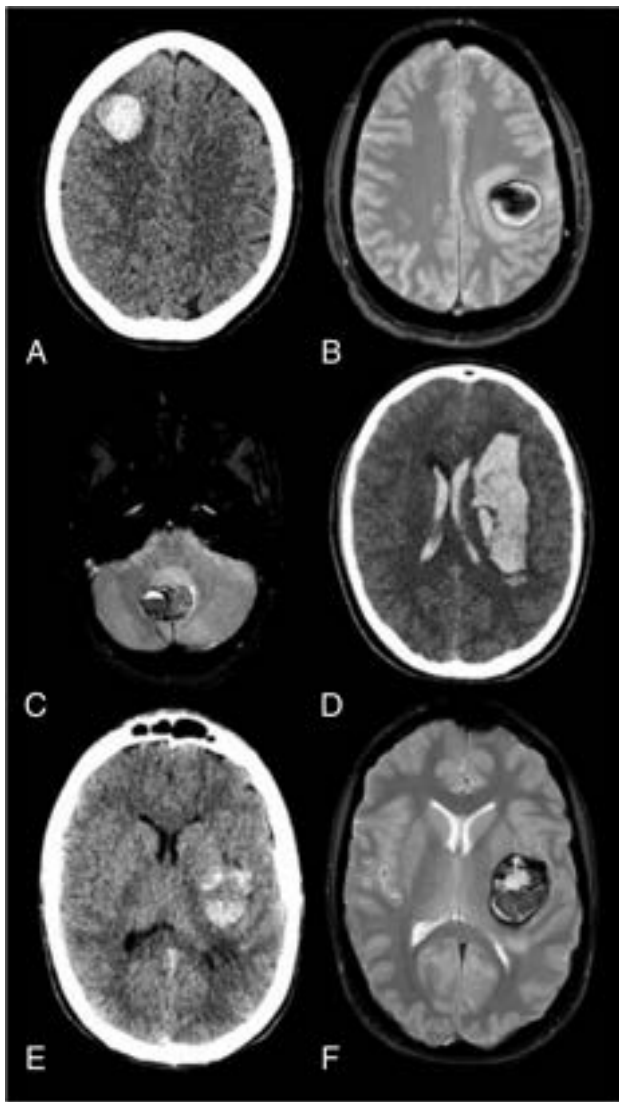


FIG 1. Assessment of hematoma shape. A, Spherical, acute lobar hematoma on plain CT of a patient with a pathologically proved hemorrhagic cerebral cavernoma. B, Spherical lobar hematoma on T2*-weighted imaging in a patient with pathologically proved hemorrhagic cerebral cavernoma. C, Ovoid cerebellar hematoma on T2*-weighted imaging of a patient with pathologically proved hemorrhagic cavernoma. D, Plain CT obtained at admission in a patient with an angiographically proved cerebral AVM. The elongated shape of the hematoma did not fulfill the criteria spherical or ovoid. Its margins were considered irregular because angular aspects were present. It was associated with intraventricular hemorrhage. E and F, Hemorrhagic cerebral cavernoma. Both plain CT (D) and T2* MR images (E) were available to assess the hematoma shape. The hematoma shape was classified as spherical/ovoid on the basis of MR imaging.

factors of underlying cavernomas. A multivariable model was subsequently built using a forward selection with a *P* value threshold of .05. A decision tree including these variables was constructed using a recursive partitioning method (package *rpart*;¹⁷ <https://www.rdocumentation.org/packages/rpart/versions/4.1.19>). Briefly, this method recursively assesses all possible splits to provide the optimal combination to distinguish hemorrhagic cavernomas from other causes of hematoma. In addition, it is not affected by

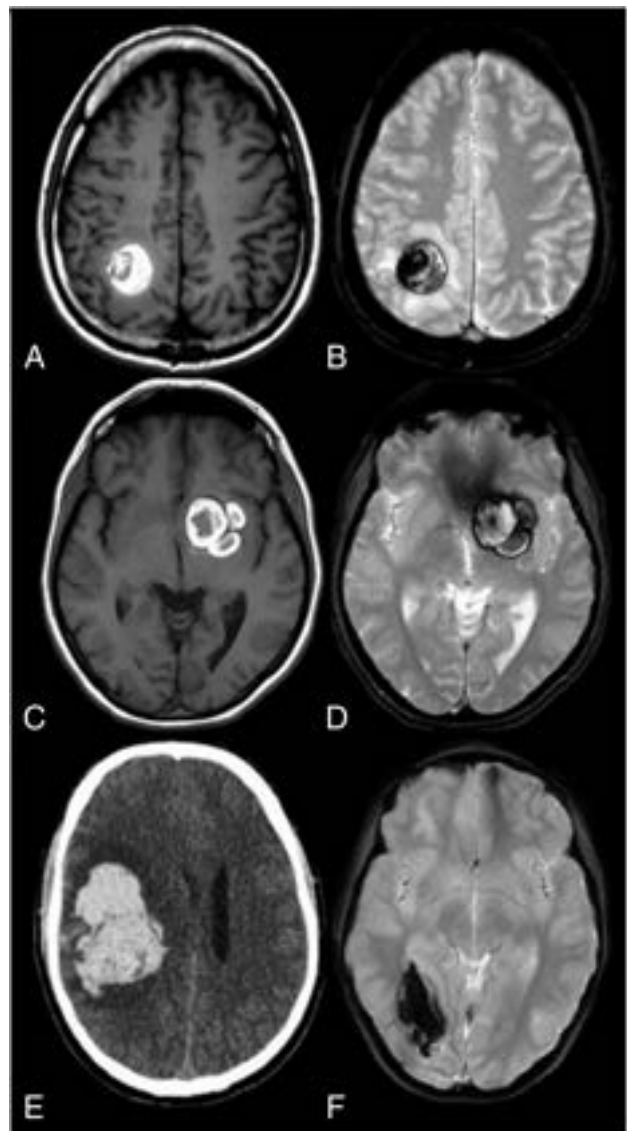


FIG 2. Assessment of hematoma margins. A and B, T1- and T2*-weighted MR imaging shows a hematoma with regular margins in a patient with pathologically proved hemorrhagic cavernoma in the setting of familial cavernomatosis. C and D, T1 and T2*-weighted MR imaging shows a hematoma in a patient with a pathologically proved cerebral cavernoma. The lesion was multiloculated with bumpy borders. The margins were classified as regular because no angular aspect was present in any part of the lesion. Hematoma with irregular margins presenting with angular aspects on plain CT (E) and T2*-weighted MR imaging (F) in 2 patients with arteriovenous shunts proved by cerebral angiography.

multicollinearity effects and correlation among variables. Using the validation sample, we assessed the performance (accuracy, sensitivity, specificity, negative and positive predictive values) of this decision tree by means of a 10-fold cross-validation. The performance of the model was assessed in the whole validation population and among the validation population in patients 18 years of age or younger.

A 2-sided *P* value < .05 was considered statistically significant. All statistical analyses were performed with the R statistical and computing software, Version 3.2.1 (<http://www.r-project.org/>).

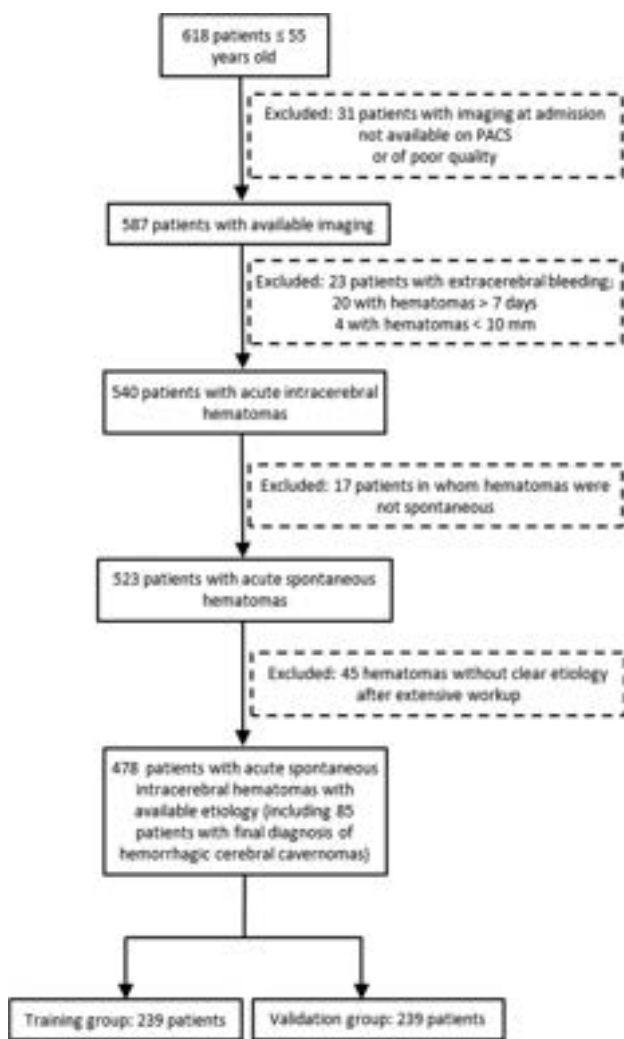


FIG 3. Flowchart of study population.

RESULTS

Descriptive Analysis of the Population

During the study period, we identified 618 patients with a suggestion of acute spontaneous intracerebral hematoma based on imaging reports. One hundred forty subjects were excluded from the study: Thirty-one had unavailable or poor-quality imaging, 23 had purely extracerebral hemorrhages, 20 had hematomas of >7 days, 4 had infracentric hematomas, 45 had no definite etiology at work-up, and in 17, the hematoma was not spontaneous (trauma, surgery, IV thrombolysis). Finally, 478 patients met the inclusion and exclusion criteria. The patient flowchart is shown in Fig 3.

The median age of the study population was 41 years (interquartile range, 26.0–49.0 years), and 259 (54.2%) were men. The Online Supplemental Data detail the number of subjects included for each hematoma etiology and the imaging modalities available for each.

Among them, 85 patients (17.8%) had hemorrhagic cavernomas. The diagnosis of cavernoma was histologically proved in 55 patients, and the remaining 30 patients had at least 12 months of clinical and MR imaging follow-up. Among patients with cavernomas, 27 (31.8%) underwent DSA in the acute phase despite negative findings on noninvasive angiography.

Interrater agreement was good for all radiologic characteristics with a κ coefficient ranging from 0.77 to 0.96. Descriptive clinical and radiologic characteristics of the study population are presented in the Online Supplemental Data. The following characteristics of intracerebral hematomas were associated with cavernomas: spherical or ovoid shape, regular margins, evidence of blood products of varying ages within the lesion, absence of extralesional hemorrhage, absence of peripheral rim enhancement, presence of a DVA near the hematoma, smaller hematoma volume, and no evidence of microbleed or white matter disease. Spherical or ovoid hematomas were significantly smaller (median volume, 6.6 mL; interquartile range, 2.3–12.3 mL, versus 21.6 mL; interquartile range, 9.0–43.1 mL; $P < .001$). Among patients with familial multiple cavernous malformation syndrome ($n = 8$), radiologic characteristics did not significantly differ (all $P \geq .32$) from those of sporadic cavernomas.

Generalized Logistic Regressions

Generalized logistic regressions were performed using the training sample ($n = 239$). At multivariate analysis, the following criteria were significantly associated with cavernomatous etiology: a spherical or ovoid shape, regular margins, absence of extralesional hemorrhage, and absence of peripheral rim enhancement. These parameters were included in the decision tree.

The Table summarizes crude and adjusted ORs of incorporated parameters.

Performance of the Decision Tree Model

When we applied it to the validation sample, the decision tree had the following performance: a diagnostic accuracy of 96.1%, 95% CI, 92.2%–98.4%; a sensitivity of 98.0%, 95% CI, 95.8%–98.9%; a specificity 89.5%, 95% CI, 75.2%–97.0%; a positive predictive value of 97.7%, 95% CI, 94.3%–99.1%; and a negative predictive value of 94.4%, 95% CI, 81.0%–98.5%.

Figure 4 illustrates the decision tree applied to the validation sample.

Among the 71 patients 18 years of age or younger, including 16 with hemorrhagic cavernomas, the decision tree had the following diagnostic performance on the validation sample: a diagnostic accuracy of 96.7% (95% CI, 83.3%–99.9%); a sensitivity of 90.0% (95% CI, 55.5%–99.8%); a specificity 100% (95% CI, 83.9%–100%); a positive predictive value of 100% (95% CI, 66.4%–100%); and a negative predictive value of 95.5% (95% CI, 83.3%–99.9%).

DISCUSSION

Recognizing the underlying etiology of acute spontaneous intracerebral hematomas may be challenging. Cerebral cavernomas are one of the most frequent causes of spontaneous intraparenchymal hematomas in children and young adults.^{18,19} Our study based on a large sample size showed that acute hematomas due to cerebral cavernomas were associated with radiologic characteristics, including a spherical or ovoid shape, regular margins, absence of extralesional hemorrhage, and absence of peripheral rim enhancement. Using these characteristics, we built an accurate radiologic predictive model of hemorrhagic cerebral cavernomas.

Barras et al²⁰ proposed a definition of irregular hematomas, which demonstrated a usefulness in predicting early hematoma

expansion and poor outcome in patients with hemorrhagic stroke.^{4,5,20} The definition we used in the present study differed somewhat from theirs. We assessed hematoma regularity on the whole hematoma (any section, any multiplanar reconstruction plane) rather than specifically on the largest hematoma axial section; and hematomas with any angular aspect arising from their surface were considered here as irregular.

Pathogenetic Hypothesis

We hypothesized that the spherical or ovoid shape and regular margins of hemorrhagic cerebral cavernomas may be due to the presence of a peripheral capsule or pseudocapsule. This capsule, which has often been reported previously,^{21,22} may prevent the extent of bleeding and may contribute to the low incidence of extralesional hemorrhages. According to Abe et al,²² the hematomas arising from cerebral cavernomas often present with a thick capsule, consisting of hyalinized walls and numerous capillaries, and resemble the capsules of chronic subdural hematomas. Although the pathogenesis of the hematoma capsules is not well-understood, it is regarded as the source of intralesional hemorrhage rather than a secondary change after hemorrhage. Most cavernous malformation hemorrhages are not overt and are contained within the margins of the lesion capsule, contrasting with hematomas due to the rupture of other cerebral vascular malformations.^{23,24} However, a peripheral capsule is not always found at the pathologic analysis of hemorrhagic cerebral cavernomas.²⁵ Bleeding within a cavernoma is

believed to occur at low pressure at the capillary level.²⁶ Such low pressure may contribute to explaining why hematomas due to cerebral cavernomas are usually less devastating than those occurring at high pressure, and they typically tend to displace rather than lacerate the surrounding parenchyma.²⁷ In the present study, hematoma volume was lower in patients with cavernomas, and the clinical status assessed by the Glasgow Coma Scale was better than in those with other etiologies of bleeding.

The differential diagnosis of a spherical or ovoid hemorrhagic lesion with regular margins mainly includes hemorrhagic neoplasms. In agreement with previous reports, we found that the absence of peripheral rim enhancement following contrast injection was a useful finding to distinguish cerebral cavernomas from hemorrhagic tumors.^{28,29} Rare cases of “encapsulated intracerebral hematomas” with a spherical shape and regular margins have been reported. Most were chronic, sometimes with peripheral rim enhancement following contrast injection, and were due to cavernomas or following radiosurgery for AVMs or, rarely, aggressive brain tumors.³⁰ In our study, patients with chronic lesions and those with a previous history of cerebral radiation therapy were excluded.

Clinical Implications

Accurate early identification of the etiology of acute spontaneous intracerebral hematomas has several implications. It has a prognostic interest because the morbidity and mortality of cerebral bleeding due to cavernomas are considered lower than in the general setting,³¹ with a 1-month case fatality rate after intracerebral hemorrhage of 2.0%.³² The risk of early hematoma expansion may be lower than in other causes of bleeding. Because cavernomas are angiographically occult malformations, their

Univariate and multivariate logistic regression for the diagnosis of hemorrhagic cavernomas

	Crude OR (95% CI)	P Value	Adjusted OR (95% CI)	P Value
Spherical/ovoid	36.60 (15.89–110.20)	<.001	6.11 (2.64–15.08)	<.001
Regular margins	34.81 (14.99–103.90)	<.001	3.38 (1.44–8.61)	.009
Extralesional hemorrhage	0.06 (0.02–0.15)	<.001	0.39 (0.18–0.76)	.01
Peripheral rim enhancement	0.18 (0.03–0.53)	.009	0.29 (0.13–0.59)	.002

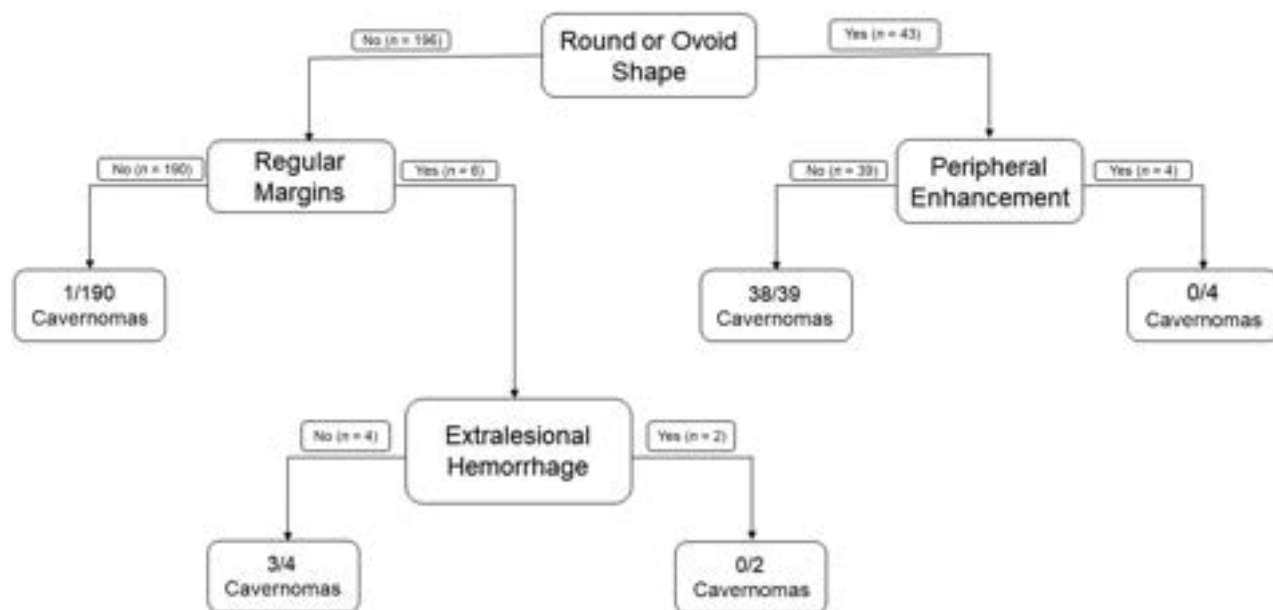


FIG 4. Decision tree model applied to the validation sample.

early recognition may avoid the risks of futile invasive cerebral angiography. Conventional angiography is not recommended in the evaluation of cerebral cavernomas, unless a differential diagnosis of arteriovenous malformation is being considered.³³ Early recognition of symptomatic hemorrhagic cerebral cavernomas may be useful in the accurate enrollment of patients in future trials testing drugs to prevent iterative bleeding.³⁴

Limitations of the Study

This study has limitations. Because our series originates from a third-referral single center with neurosurgical and interventional neuroradiology facilities, our findings may not be representative of the general population. Referral bias could have resulted in a disproportionately high number of patients with vascular malformations. Because we included patients 55 years of age or younger, our model may, therefore, not be appropriate in older patients. The criterion standard for the diagnosis of hemorrhagic cerebral cavernomas remains histopathology, and in our study, the diagnosis was based on such analyses in 55 of 85 patients; in 30 patients, the diagnosis was established by follow-up.

The diagnostic accuracy of our predictive model was not improved when adding other parameters associated with hemorrhagic cavernomas (ie, evidence of blood products of varying ages within the lesion, presence of a DVA close to the hematoma, smaller hematoma volume, and no evidence of microbleeds or white matter disease). However, this issue might be due to the size of our study population. Indeed, the discovery of a DVA next to a hematoma should suggest a cavernoma as the etiology of the hemorrhage, and a DVA may increase the risk of bleeding from cavernomas.³⁵ The presence of acute hemorrhage might have obscured mixed-aged blood and DVAs in some cases. Moreover, we observed that hematomas due to cavernomas were smaller than in other etiologies, but we could not demonstrate a causal relationship between hematoma size and shape. Finally, we performed an internal validation but not an external validation. A large-scale, multicenter, prospective, external validation of our model is necessary.

CONCLUSIONS

Spontaneous acute intracerebral hemorrhage with spherical or ovoid shape, regular margins, absence of extralesional hemorrhage, and absence of peripheral rim enhancement is highly suggestive of an underlying cerebral cavernoma in patients 55 years of age or younger. A decision tree including these parameters seems to have excellent performance and requires further validation because it may have major implications and prognostic interest in clinical practice.

Disclosure forms provided by the authors are available with the full text and PDF of this article at www.ajnr.org.

REFERENCES

1. Gross BA, Jankowitz BT, Friedlander RM. **Cerebral intraparenchymal hemorrhage: a review.** *JAMA* 2019;321:1295–303 CrossRef Medline
2. Kamel H, Navi BB, Hemphill JC 3rd. **A rule to identify patients who require magnetic resonance imaging after intracerebral hemorrhage.** *Neurocrit Care* 2013;18:59–63 CrossRef Medline
3. Salmela MB, Mortazavi S, Jagadeesan BD, et al; Expert Panel on Neurologic Imaging. **ACR Appropriateness Criteria Cerebrovascular Disease.** *J Am Coll Radiol* 2017;14:S34–61 CrossRef Medline
4. Morotti A, Boulouis G, Dowlatshahi D, et al; International NCCT ICH Study Group. **Standards for detecting, interpreting, and reporting noncontrast computed tomographic markers of intracerebral hemorrhage expansion.** *Ann Neurol* 2019;86:480–92 CrossRef Medline
5. Delcourt C, Zhang S, Arima H, et al; INTERACT2 Investigators. **Significance of hematoma shape and density in intracerebral hemorrhage: the Intensive Blood Pressure Reduction in Acute Intracerebral Hemorrhage Trial study.** *Stroke* 2016;47:1227–32 CrossRef Medline
6. Rodrigues MA, Samarasekera N, Lerpiniere C, et al. **The Edinburgh CT and genetic diagnostic criteria for lobar intracerebral haemorrhage associated with cerebral amyloid angiopathy: model development and diagnostic test accuracy study.** *Lancet Neurol* 2018;17:232–40 CrossRef Medline
7. Mottolese C, Hermier M, Stan H, et al. **Central nervous system cavernomas in the pediatric age group.** *Neurosurg Rev* 2001;24:55–71; discussion 72–73 CrossRef Medline
8. Kurihara N, Suzuki H, Kato Y, et al. **Hemorrhage owing to cerebral cavernous malformation: imaging, clinical, and histopathological considerations.** *Jpn J Radiol* 2020;38:613–21 CrossRef Medline
9. Zabramski JM, Wascher TM, Spetzler RF, et al. **The natural history of familial cavernous malformations: results of an ongoing study.** *J Neurosurg* 1994;80:422–32 CrossRef Medline
10. Kranz PG, Malinzak MD, Amrhein TJ. **Approach to imaging in patients with spontaneous intracranial hemorrhage.** *Neuroimaging Clin N Am* 2018;28:353–74 CrossRef Medline
11. Rindler RS, Allen JW, Barrow JW, et al. **Neuroimaging of intracerebral hemorrhage.** *Neurosurgery* 2020;86:E414–23 CrossRef Medline
12. Tomlinson FH, Houser OW, Scheithauer BW, et al. **Angiographically occult vascular malformations: a correlative study of features on magnetic resonance imaging and histological examination.** *Neurosurgery* 1994;34:792–99; discussion 799–800 CrossRef Medline
13. Frischer JM, Pipp I, Stavrou I, et al. **Cerebral cavernous malformations: congruency of histopathological features with the current clinical definition.** *J Neurol Neurosurg Psychiatry* 2008;79:783–88 CrossRef Medline
14. Flemming KD, Kumar S, Lanzino G, et al. **Baseline and evolutionary radiologic features in sporadic, hemorrhagic brain cavernous malformations.** *AJNR Am J Neuroradiol* 2019;40:967–72 CrossRef Medline
15. Fazekas F, Barkhof F, Wahlund LO, et al. **CT and MRI rating of white matter lesions.** *Cerebrovasc Dis* 2002;13(Suppl 2):31–36 CrossRef Medline
16. Webb AJ, Ullman NL, Morgan TC, et al; MISTIE and CLEAR Investigators. **Accuracy of the ABC/2 score for intracerebral hemorrhage: systematic review and analysis of MISTIE, CLEAR-IVH, and CLEAR III.** *Stroke* 2015;46:2470–76 CrossRef Medline
17. Breiman L, Friedman JH, Olshen RA, et al. *Classification and Regression Trees.* Routledge; 2017
18. Boulouis G, Blauwblomme T, Hak JF, et al. **Nontraumatic pediatric intracerebral hemorrhage.** *Stroke* 2019;50:3654–61 CrossRef Medline
19. Goldstein HE, Solomon RA. **Epidemiology of cavernous malformations.** *Handb Clin Neurol* 2017;143:241–47 CrossRef Medline
20. Barras CD, Tress BM, Christensen S, et al; Recombinant Activated Factor VII Intracerebral Hemorrhage Trial Investigators. **Density and shape as CT predictors of intracerebral hemorrhage growth.** *Stroke* 2009;40:1325–31 CrossRef Medline
21. Zabramski JM, Henn JS, Coons S. **Pathology of cerebral vascular malformations.** *Neurosurg Clin N Am* 1999;10:395–410 CrossRef Medline
22. Abe M, Fukudome K, Sugita Y, et al. **Thrombus and encapsulated hematoma in cerebral cavernous malformations.** *Acta Neuropathol* 2005;109:503–09 CrossRef Medline
23. Cordonnier C, Al-Shahi Salman R, Bhattacharya JJ, et al; SIVMS Collaborators. **Differences between intracranial vascular malformation types in the characteristics of their presenting haemorrhages: prospective, population-based study.** *J Neurol Neurosurg Psychiatry* 2008;79:47–51 CrossRef Medline

24. Ellis JA, Barrow DL. **Supratentorial cavernous malformations.** *Handb Clin Neurol* 2017;143:283–89 CrossRef Medline
25. Steiger HJ, Markwalder TM, Reulen HJ. **Clinicopathological relations of cerebral cavernous angiomas: observations in eleven cases.** *Neurosurgery* 1987;21:879–84 CrossRef Medline
26. Little JR, Awad IA, Jones SC, et al. **Vascular pressures and cortical blood flow in cavernous angioma of the brain.** *J Neurosurg* 1990;73:555–59 CrossRef Medline
27. Flemming KD, Lanzino G. **Cerebral cavernous malformation: what a practicing clinician should know.** *Mayo Clin Proc* 2020;95:2005–20 CrossRef Medline
28. Sze G, Krol G, Olsen WL, et al. **Hemorrhagic neoplasms: MR mimics of occult vascular malformations.** *AJR Am J Roentgenol* 1987;149:1223–30 CrossRef Medline
29. Kumar S, Brinjikji W, Lanzino G, et al. **Distinguishing mimics from true hemorrhagic cavernous malformations.** *J Clin Neurosci* 2020;74:11–17 CrossRef Medline
30. Nishiyama A, Toi H, Takai H, et al. **Chronic encapsulated intracerebral hematoma: three case reports and a literature review.** *Surg Neurol Int* 2014;5:88 CrossRef Medline
31. Taslimi S, Modabbernia A, Amin-Hanjani S, et al. **Natural history of cavernous malformation: systematic review and meta-analysis of 25 studies.** *Neurology* 2016;86:1984–91 CrossRef Medline
32. Horne MA, Flemming KD, Su IC, et al; Cerebral Cavernous Malformations Individual Patient Data Meta-analysis Collaborators. **Clinical course of untreated cerebral cavernous malformations: a meta-analysis of individual patient data.** *Lancet Neurol* 2016;15:166–73 CrossRef Medline
33. Akers A, Al-Shahi Salman R, Awad AI, et al. **Synopsis of guidelines for the clinical management of cerebral cavernous malformations: consensus recommendations based on systematic literature review by the Angioma Alliance Scientific Advisory Board Clinical Experts Panel.** *Neurosurgery* 2017;80:665–80 CrossRef Medline
34. Awad IA, Polster SP. **Cavernous angiomas: deconstructing a neurosurgical disease.** *J Neurosurg* 2019;131:1–13 CrossRef Medline
35. Idiculla PS, Gurala D, Philipose J, et al. **Cerebral cavernous malformations, developmental venous anomaly, and its coexistence: a review.** *Eur Neurol* 2020;83:360–68 CrossRef Medline

Perifocal Edema in Patients with Meningioma is Associated with Impaired Whole-Brain Connectivity as Detected by Resting-State fMRI

V.M. Stoecklein, S. Wunderlich, B. Papazov, N. Thon, M. Schmutzer, R. Schinner, H. Zimmermann, T. Liebig, J. Ricke, H. Liu, J.-C. Tonn, C. Schichor, and S. Stoecklein



ABSTRACT

BACKGROUND AND PURPOSE: Meningiomas are intracranial tumors that usually carry a benign prognosis. Some meningiomas cause perifocal edema. Resting-state fMRI can be used to assess whole-brain functional connectivity, which can serve as a marker for disease severity. Here, we investigated whether the presence of perifocal edema in preoperative patients with meningiomas leads to impaired functional connectivity and if these changes are associated with cognitive function.

MATERIALS AND METHODS: Patients with suspected meningiomas were prospectively included, and resting-state fMRI scans were obtained. Impairment of functional connectivity was quantified on a whole-brain level using our recently published resting-state fMRI-based marker, called the dysconnectivity index. Using uni- and multivariate regression models, we investigated the association of the dysconnectivity index with edema and tumor volume as well as cognitive test scores.

RESULTS: Twenty-nine patients were included. In a multivariate regression analysis, there was a highly significant association of dysconnectivity index values and edema volume in the total sample and in a subsample of 14 patients with edema, when accounting for potential confounders like age and temporal SNR. There was no statistically significant association with tumor volume. Better neurocognitive performance was strongly associated with lower dysconnectivity index values.

CONCLUSIONS: Resting-state fMRI showed a significant association between impaired functional connectivity and perifocal edema, but not tumor volume, in patients with meningiomas. We demonstrated that better neurocognitive function was associated with less impairment of functional connectivity. This result shows that our resting-state fMRI marker indicates a detrimental influence of peritumoral brain edema on global functional connectivity in patients with meningiomas.

ABBREVIATIONS: DCI = dysconnectivity index; GLM = generalized linear models; MOCA = Montreal Cognitive Assessment; PTBE = peritumoral brain edema; rsfMRI = resting-state fMRI; tSNR = temporal SNR

Meningioma is the most common intracranial tumor in adults with a reported annual incidence rate of 8.81 per 100,000 inhabitants in the United States.¹ The clinical course of patients with meningiomas is usually benign, with long progression-free

survival after surgical resection. Most meningiomas are extra-axial tumors, even though some grade 2 meningiomas invade the surrounding brain tissue² and some authors even suggest that in rare cases, meningiomas can be purely intraparenchymal.³ Even in the absence of brain invasion, healthy brain tissue can be affected by the tumor, illustrated by some meningiomas causing formation of peritumoral brain edema. This suggests that the presence of these tumors, even though extra-axially located, leads to interaction between the tumor and the surrounding brain parenchyma. A number of factors by which meningiomas influence the healthy brain and cause the formation of peritumoral brain edema (PTBE) have been discussed in recent years, including the secretion of vascular endothelial growth factor A, matrix metalloproteinases, and interleukin-6.⁴ Taken together, there is ample evidence to support an intricate interaction between meningiomas and healthy brain in some cases. This notion is reinforced by the finding that neuropsychological deficits are common in patients with meningiomas. Numerous studies have demonstrated that complex neurocognitive

Received November 3, 2022; accepted after revision May 28, 2023.

From the Department of Neurosurgery (V.M.S., N.T., M.S., J.-C.T., C.S.), German Cancer Consortium (V.M.S., N.T., J.-C.T., C.S.), Department of Radiology (S.W., B.P., R.S., J.R., S.S.), and Department of Neuroradiology (H.Z., T.L.), Ludwig-Maximilians-University Munich, Munich, Germany; Department of Radiology (H.L.), Athinoula A. Martinos Center for Biomedical Imaging, Massachusetts General Hospital/Haard Medical School, Boston, Massachusetts; and Department of Neuroscience (H.L.), Medical University of South Carolina, Charleston, South Carolina.

C. Schichor and S. Stoecklein contributed equally to this work.

This work was supported by a grant from Deutsche Krebshilfe (Consortium "Aggressive Meningiomas") to V.M.S. and C.S.

Please address correspondence to Veit Stoecklein, MD, Department of Neurosurgery, Ludwig-Maximilians-University, Marchioninistr 15, 81377 Munich, Germany; e-mail: veit.stoecklein@med.uni-muenchen.de; @StoeckleinVeit

Indicates article with online supplemental data.

<http://dx.doi.org/10.3174/ajnr.A7915>

functions like attention, memory, or executive functioning are impaired in patients with meningiomas, indicating that the presence of a meningioma may disturb the complex neuronal networks that are the physiologic basis of these functions.^{5,6}

Recently, functional connectivity measured by resting-state functional MR imaging (rsfMRI) has been suggested as a marker of disease severity in a cohort of patients with gliomas by our group.⁷ RsfMRI exploits the physiologic fluctuations of oxygenated blood in the brain, which reflects neuronal activity, to assess the functional architecture of the human brain.^{8,9} The entirety of functional connections in the brain is often referred to as the functional connectome. In our aforementioned study,⁷ it could be demonstrated that patients with more aggressive gliomas exhibited more impairment of functional connectivity. This outcome established the concept that the individual disease burden of patients with brain tumors can be captured by assessing the impairment of functional connectivity caused by the tumor, using rsfMRI. To this end, we developed an imaging tool that quantifies and visualizes impairment of whole-brain functional connectivity in the individual patient, called the dysconnectivity index (DCI).⁷ Quantification was based on the deviation of each individual connectivity profile from the distribution of connectivity profiles of a healthy reference group.

In the present study, we intended to extend this concept to patients with suspected meningiomas. Here, it was our goal to assess whether meningiomas affect functional connectivity and whether functional connectivity is influenced by factors like tumor size and the presence of perifocal edema.

MATERIALS AND METHODS

Study Design

Patients with a suspected meningioma on initial contrast-enhanced MR imaging were prospectively included from January 2017 to March 2021. Patients presented with outside MR imaging scans to the skull base clinic at Ludwig-Maximilians-University Hospital. Exclusion criteria were younger than 18 years of age, previous cranial surgery or radiation therapy, and any contraindications to MR imaging such as non-MR imaging–safe metal implants. Patients underwent rsfMRI scanning before craniotomy and resection of the tumors. A histopathologic diagnosis was made according to the criteria set forth in the 2016 version of the World Health Organization grading system.¹⁰ Patients underwent neuropsychological testing on the day of the MR imaging procedure using the Montreal Cognitive Assessment (MOCA) test.¹¹ In 2 patients, the MOCA could not be performed because the test was not available in the respective patient's native language. The study was approved by the local institutional review board and was performed in accordance with the Declaration of Helsinki. Written informed consent was obtained from all study participants.

Scanning Procedure of rsfMRI

RsfMRI was performed as described previously.⁷ Briefly, acquisition of the MR imaging data on a 3T scanner (Magnetom Skyra; Siemens) included two 6-minute runs with a total scanning time of 12 minutes. Structural MR images were acquired with a sagittal 3D T1WI sequence (radiofrequency pulses and MPRAGE). For

details of the MR imaging protocol, please refer to the Online Supplemental Data.

Preprocessing

For all scans, the quality control criteria of the mean section-based temporal signal-to-noise ratio (tSNR) > 100 and mean relative motion < 0.5 mm were fulfilled.¹² Structural MR imaging data were processed using the FreeSurfer software package, Version 6.0 (<http://surfer.nmr.mgh.harvard.edu>). For further information please refer to the Online Supplemental Data. Preprocessing of the rsfMRI data sets was performed using FMRIprep, Version 20.2.2 (<https://fmripred.org/en/stable/>) based on Neuroimaging in Python (Nipype <https://nipype.readthedocs.io/en/latest/index.html>).¹³ The first 5 functional images were deleted. The remaining frames were standardized and smoothed with a 6.0-mm full width at half maximum Gaussian kernel. MCFLIRT (FSL, Version 5.0.9; <https://fsl.fmrib.ox.ac.uk/fsl/fslwiki/MCFLIRT>)¹⁴ was performed for the subsequent head motion correction using ICA-AROMA (<https://github.com/maartenmennes/ICA-AROMA>).¹⁵ Last, nuisance regression, filtering, and detrending were performed.¹⁵ Nuisance regression included regression of the global signal, CSF, and white matter signal. Filtering comprised high and low band pass filtering, applying cutoff values of 0.01 and 0.08, respectively. For each subject, a correlation matrix of the 3352 voxels for the left hemisphere and 3316 voxels for the right hemisphere was calculated and normalized using *z* scores.

Calculation of the DCI

The DCI was calculated analogous to methods previously described by Stoecklein et al.⁷ Also, see the Online Supplemental Data. Briefly, connections that diverge beyond a certain threshold from the distribution of the respective connection in the reference group were counted as “dysconnected.” The individual patient's dysconnectivity count was then summarized in each hemisphere and normalized to the number of voxels in the respective hemisphere, resulting in the DCI. For each patient, the dysconnectivity count of each voxel was assigned to the respective voxel. The resulting map was smoothed using a Gaussian kernel (full width half maximum = 2 mm) and projected onto each individual patient's anatomic space.

Shrinking of the Tumor Area

Meningiomas are almost exclusively extra-axial tumors; therefore, that the tumor is embedded in the functional architecture of the brain in a relevant manner is not to be expected. Consequently, we tried to avoid distortion of the functional connectome by minimizing the nonfunctional tumor area in our data set. The Advanced Normalization Tools software package (ANTs <http://stnava.github.io/ANTs/>) registration is a software tool that uses a mathematic method for performing deformable image registration.¹⁶ The algorithm optimizes a deformation field that maps points from one image to the corresponding points in another image, specifically the anatomic atlas being used. When no lesion map is provided to the algorithm, the lesional area is automatically warped and shrunk, resulting in a smaller but potentially imprecisely registered lesion area.

Patient characteristics

Parameter	No PTBE	PTBE	Significance
Age (mean ± SEM) (yr)	53 ± 2.6	66 ± 2.9	$P = .0014$
Sex	2 Male, 13 female	5 Male, 9 female	$P = .21$
Tumor volume (mean ± SEM) (cm ³)	15.0 ± 3.7	35.5 ± 8.2	$P = .0124$
Tumor location			
Frontal	6	6	$P = .97$
Temporal	5	4	
Parietal	3	0	
Occipital	1	1	
Multiple lobes	0	3	

Note.—SEM indicates standard error of the mean.

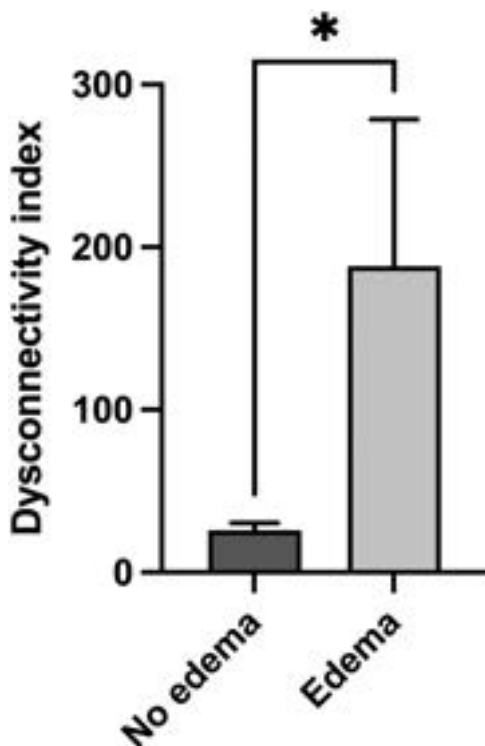


FIG 1. Comparison of the DCI in patients without and with PTBE. The left column shows the mean (SD) in patients without PTBE ($n = 15$) compared with the mean (SD) in patients with PTBE (right column, $n = 14$) ($*P = .04$, Mann-Whitney test).

Volumetry

Tumor and edema volume was determined using the Brainlab Elements software package (Brainlab). Tumor volume was semimanually segmented by a board-certified radiologist (S.S.) and a board-certified neurosurgeon (V.M.S.) on the basis of contrast-enhanced T1WIs. Similarly, edema volume was determined by semimanual segmentation of T2WIs. Tumor location was assessed as frontal, temporal, parietal, occipital, or multiple (meaning that the tumor affects >1 lobe).

Statistical Analysis

Generalized linear models (GLMs) were used to conduct univariate and multivariate correlation analyses. Group comparisons were calculated using the Mann-Whitney test. P values $\leq .05$ were considered significant.

RESULTS

Patient Characteristics

Twenty-nine patients were prospectively enrolled (mean age, 58.2 [SD, 12.3] years; 22 women). The mean age was higher in patients with PTBE ($P = .0014$). For details see the Table.

Tumor and Edema Characteristics

Twenty-six patients were diagnosed with World Health Organization grade 1 tumors; 3 patients, with grade 2 tumors.

The diagnosis of a grade 2 meningioma was made on the basis of elevated mitotic counts in 2 cases and on brain infiltration alone in 1 case. Mean tumor volume for all patients was 24.9 cm³ (range, 2.2–113 cm³). Fifteen patients had no perifocal edema. In patients who had PTBE ($n = 14$), the mean edema volume was 50.0 cm³ (range, 3.5–118 cm³). Two of 3 patients with grade 2 tumors had PTBE. In these patients, edema and tumor volume were not significantly correlated ($r = -0.1101$, $P = .4903$). Tumor volume was higher in patients with PTBE compared with patients without PTBE ($P = .0124$, see the Table for details).

Impaired Functional Connectivity Is Strongly Correlated with Edema Volume

The univariate GLM revealed a highly significant association of edema volume and impaired functional connectivity, as indicated by the DCI ($P = .0002$). In multivariate GLM analyses adding the potential confounders age, sex, and tSNR, none of these parameters showed a significant association with the DCI ($P = .3920$, $P = .2583$, $P = .3559$, respectively), while the association between edema volume and the DCI remained significant ($P = .0023$, $P = .0002$, $P = .0011$, respectively). Thus, this analysis showed that age did not have a significant influence on the association of PTBE and impaired functional connectivity even though patients with PTBE were older than patients without PTBE. Furthermore, a group comparison between patients without and with PTBE revealed a significantly higher DCI in the group with PTBE ($P = .04$, Fig 1).

When restricting the analysis to 14 patients with PTBE, we could grossly replicate our results: Univariate analysis revealed a significant association of edema volume and the DCI ($P = .0301$). In multivariate GLM analyses adding age and tSNR, neither of these parameters showed a significant association with the DCI ($P = .2702$ and $P = .1718$, respectively), while the association between edema volume and the DCI remained significant ($P = .0486$ and $P = .0487$, respectively). Only when adding the potential confounder sex did the association between edema volume and the DCI fail to reach significance ($P = .0594$), while sex itself also did not show a significant association with the DCI ($P = .4545$). The analysis was furthermore repeated without the patients with grade 2 tumors ($n = 26$). A significant association of PTBE and the DCI could still be demonstrated ($P = .0002$).

Abnormal Functional Connectivity Is Not Correlated with Tumor Volume

Tumor volume was not significantly associated with the DCI, neither in a univariate analysis ($P = .2345$) nor in the multivariate

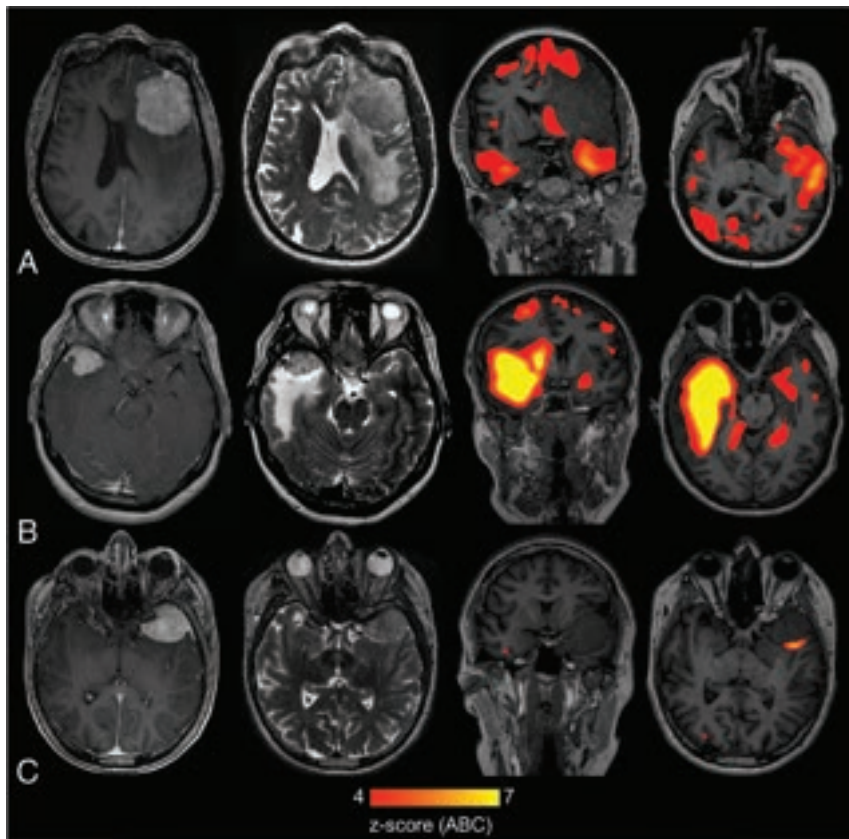


FIG 2. Individual connectome maps in patients with meningiomas. *A*, Connectome map of a patient with a large meningioma (contrast-enhanced TIWI, *first image from the left*) with extensive PTBE (T2WI, *second image from the left*). Connectome analysis shows extensive impairment of functional connectivity in widespread brain regions in both hemispheres (*third and fourth images from the left*). *B*, Connectome map of a patient with a small meningioma (contrast-enhanced TIWI, *first image from the left*), which still causes extensive PTBE (T2WI, *second image from the left*). Connectome analysis shows extensively impaired connectivity in the whole brain with a focus on regions with PTBE (*third and fourth images from the left*). *C*, Connectome map of a patient with a large meningioma (contrast-enhanced TIWI, *first image from the left*) without PTBE (T2WI, *second image from the left*). Connectome analysis shows minimal disturbance of functional connectivity adjacent to the tumor (*third and fourth images from the left*).

GLM adding age, sex, and tSNR ($P = .7771$, $P = .2094$, $P = .6843$, respectively), even though patients with PTBE were found to have larger tumors. Furthermore, multivariate analyses did not reveal a significant association of tumor volume and tumor location with the DCI ($P = .4846$ and $P = .9228$, respectively), while the association between edema volume and the DCI remained significant ($P = .0005$ and $P = .0023$, respectively) when adding these parameters to the model. Analogously, in 14 patients with PTBE, when we added tumor volume to the model, the association between edema volume and the DCI remained significant ($P = .0309$), while no association between tumor volume and the DCI could be detected ($P = .4623$).

Association of Abnormal Functional Connectivity and Cognitive Performance

Most interesting, we found a significant negative association between abnormal connectivity and the MOCA test results ($P = .0023$), which stayed significant even after controlling for age, sex, and tSNR ($P = .0223$, $P = .0010$, $P = .0112$, respectively), indicating

that a higher DCI is associated with impaired neuropsychological performance. Along these lines, the MOCA showed a significant negative correlation with PTBE ($r = -0.5572$, $P = .0025$).

Individual Connectome Maps

Figure 2 shows representative examples of individual connectome maps in patients with meningiomas. Figure 2A displays the connectome map of a patient with a large tumor with extensive PTBE. Here, widespread abnormal connectivity in both hemispheres is demonstrated. Figure 2B depicts the connectome map of a patient with a small meningioma that still causes extensive PTBE. Widespread abnormal connectivity in both hemisphere is also demonstrated. Figure 2C, on the other hand, shows the connectome map of a patient with a large meningioma without PTBE. Here, only very limited abnormal connectivity adjacent to the tumor is observed.

DISCUSSION

We present a prospective study of patients with newly diagnosed meningiomas. We found that there is a positive association between edema volume and impairment of functional connectivity. We did not find, however, an association between tumor volume and abnormal functional connectivity. We also did not find substantially abnormal functional connectivity in patients without peritumoral edema, irrespective of tumor size. Taken together, it appears that substantial interaction between meningioma and healthy brain parenchyma indicated by peritumoral edema is necessary for disturbances in connectivity to occur. A possible functional significance for this finding in patients with meningiomas is suggested because abnormal functional connectivity was associated with worse neuropsychological performance as indicated by the MOCA test scores.

These findings could open new avenues of research and possibly lay the foundation for new treatment rationales in patients with meningiomas. We found that the presence of PTBE in patients with meningiomas caused damage to global functional connectivity. This finding might indicate that the biochemical interaction between surrounding healthy brain and tumor, which leads to edema formation, also has functional implications for the whole brain. Taken together this gives rise to the question of how this observed effect of damaged functional connectivity in the whole brain of patients with substantial peritumoral edema is mediated. Exactly how PTBE in patients with meningiomas arises is still a matter of intense debate. Many possible causes for edema formation have been discussed in

the past; eg, dysfunction of the glymphatic system of the brain has recently been implicated in edema formation.¹⁷

It is becoming clearer, however, that increased proinflammatory cytokines play an important role in the formation of perifocal edema. Interleukin-6, which has a prominent role in the regulation of inflammatory processes,¹⁸ has been described as a relevant factor in the development of PTBE. It was found that the expression of interleukin-6 was 7-fold higher in tumor cells from meningiomas with perifocal edema.¹⁹ Furthermore, a number of other cytokines such as chemokine 12 and transforming growth factor β are being produced in the tumor microenvironment.⁴ This finding goes to show that meningiomas with PTBE might trigger immunological activity of the host. It is possible that this immunologic activity, in turn, could have a proinflammatory effect in the whole brain.

This change in the inflammatory status of the brain could lead to altered brain function. There is ample evidence to support systemic inflammation altering functional connectivity in the brain. It could be shown, for example, that the infusion of low doses of lipopolysaccharide, which triggers systemic inflammation with a subsequent increase of systemic interleukin-6, led to major changes in functional connectivity as determined by rsfMRI.²⁰ Furthermore, a recent study that investigated the link between systemic inflammation and depression found that functional connectivity was altered in patients with depression, depending on systemic inflammation.²¹ It appears obvious from these studies that there is an effect of systemic inflammation on brain function that is reflected in altered functional connectivity. A similar effect might occur in our patient cohort because of the local proinflammatory milieu caused by the tumor. This could constitute a pathophysiologic link between PTBE and damaged whole-brain functional connectivity.

Additionally, edema is likely to interfere with local blood circulation and thus with the blood oxygen level–dependent signal per se, possibly accounting for a fraction of the effect that we have observed. Our data suggest that edema affects functional connectivity on a more global level. This suggestion can be substantiated by the fact that disruption of functional connectivity was also observed in the nonlesional hemisphere, as seen in Figs 2A, -B. If there was only a local effect of blood oxygen level–dependent signal distortion, one would expect that disruption of functional connectivity would be limited to the lesional hemisphere.

The observation that whole-brain functional connectivity is altered in patients with meningiomas with substantial PTBE leads to the question of whether this finding has importance for neurocognitive function in these patients. It has been shown in a previous study that the presence of PTBE is associated with worse postoperative cognitive function in patients with meningiomas.²² This finding indicates that PTBE has detrimental effects on neurocognition, even though this study was limited by the small sample size with no preoperative data available. An additional study looking at patients with meningiomas preoperatively, however, also found that PTBE has a detrimental effect on neurocognition when patients with and without edema were compared.²³ In summary, there is evidence in the literature that PTBE leads to cognitive impairment that goes beyond what would be expected from mass effect alone. These results support the findings of our study,^{22,23} in which impaired global functional connectivity was associated

with PTBE in patients with meningiomas. Furthermore, impaired functional connectivity was associated, in our study, with decreased neurocognitive performance. We did not, however, find a correlation between tumor size and impaired functional connectivity. This result implies that even very small meningiomas that cause the formation of substantial PTBE also cause impaired functional connectivity with ensuing detrimental effects on neurocognition.

Taken together, our findings suggest that the abnormal functional connectivity associated with PTBE observed in our study could have pathophysiologic significance for the development of neurocognitive impairment in patients with meningiomas. Further prospective studies to test whether functional connectivity improves after resection and consecutive regression of PTBE and whether this improvement is associated with better neurocognitive function seem warranted and have been currently launched at our department.

Limitations

A potential limitation of our study is that our method for measuring functional connectivity in patients with intracranial tumors was originally developed for application in patients with intra-axial tumors. To compensate for this shortcoming, we developed a method to computationally remove the tumors from the imaging space and compute abnormal functional connectivity only in the nontumoral areas of the brain. It cannot be fully excluded that this automated “shrinking” of tumors is a potential cause of errors, eg, by removing nontumoral areas from the imaging space and thus underestimating the degree of damage to functional connectivity. Furthermore, age, sex, tumor volume, and functional data quality (assessed by tSNR) constitute potential confounders. However, in multivariate analyses including these potential confounders, PTBE remained a significant factor for an elevated DCI. Furthermore, we failed to observe a statistically significant association between tumor size as well as age and impairment of functional connectivity, even though patients in the PTBE group were older and had larger tumor volume (Table). Our data thus support the notion that the presence of edema alone, irrespective of tumor size and patient age, is an indicator of pathophysiologic processes, which have an impact on functional connectivity. As a note of caution, we would like to point out that dysconnectivity is calculated in gray matter only but might partially spill into white matter areas in individual dysconnectivity maps due to resolution and smoothing effects.

CONCLUSIONS

We present a prospective study in a cohort of patients with meningiomas with and without perifocal edema. We found that functional connectivity is more impaired in patients with edema, independent of tumor size and other potentially confounding factors. We were also able to demonstrate that less impairment of functional connectivity was associated with better neuropsychological performance. This finding indicates a possible role for our rsfMRI marker as an indicator of pathophysiologic processes with an impact on cognition in patients with meningiomas.

Disclosure forms provided by the authors are available with the full text and PDF of this article at www.ajnr.org.

REFERENCES

1. Ostrom QT, Patil N, Cioffi G, et al. **CBTRUS Statistical Report: Primary Brain and Other Central Nervous System Tumors Diagnosed in the United States in 2013-2017.** *Neuro Oncol* 2020;22:iv1-96 CrossRef Medline
2. von Spreckelsen N, Kessler C, Brokinkel B, et al. **Molecular neuropathology of brain-invasive meningiomas.** *Brain Pathol* 2022;32:e13048 Medline
3. Ohba S, Abe M, Hasegawa M, et al. **Intraparenchymal meningioma: clinical, radiologic, and histologic review.** *World Neurosurg* 2016;92:23-30 CrossRef Medline
4. Berhouma M, Jacquesson T, Jouanneau E, et al. **Pathogenesis of peri-tumoral edema in intracranial meningiomas.** *Neurosurg Rev* 2019;42:59-71 CrossRef Medline
5. Meskal I, Gehring K, Rutten GJ, et al. **Cognitive functioning in meningioma patients: a systematic review.** *J Neurooncol* 2016;128:195-205 CrossRef Medline
6. Tucha O, Smely C, Preier M, et al. **Preoperative and postoperative cognitive functioning in patients with frontal meningiomas.** *J Neurosurg* 2003;98:21-31 CrossRef Medline
7. Stoecklein VM, Stoecklein S, Galie F, et al. **Resting-state fMRI detects alterations in whole brain connectivity related to tumor biology in glioma patients.** *Neuro Oncol* 2020;22:1388-98 CrossRef Medline
8. Smith SM, Fox PT, Miller KL, et al. **Correspondence of the brain's functional architecture during activation and rest.** *Proc Natl Acad Sci U S A* 2009;106:13040-45 CrossRef Medline
9. Biswal B, Yetkin FZ, Haughton VM, et al. **Functional connectivity in the motor cortex of resting human brain using echo-planar MRI.** *Magn Reson Med* 1995;34:537-41 CrossRef Medline
10. Louis DN, Perry A, Reifenberger G, et al. **The 2016 World Health Organization Classification of Tumors of the Central Nervous System: a summary.** *Acta Neuropathol* 2016;131:803-20 CrossRef Medline
11. Nasreddine ZS, Phillips NA, Bedirian V, et al. **The Montreal Cognitive Assessment, MoCA: a brief screening tool for mild cognitive impairment.** *J Am Geriatr Soc* 2005;53:695-99 CrossRef Medline
12. Van Dijk KR, Sabuncu MR, Buckner RL. **The influence of head motion on intrinsic functional connectivity MRI.** *Neuroimage* 2012;59:431-38 CrossRef Medline
13. Esteban O, Markiewicz CJ, Blair RW, et al. **fMRIPrep: a robust pre-processing pipeline for functional MRI.** *Nat Methods* 2019;16:111-16 CrossRef Medline
14. Jenkinson M, Bannister P, Brady M, et al. **Improved optimization for the robust and accurate linear registration and motion correction of brain images.** *Neuroimage* 2002;17:825-41 CrossRef Medline
15. Pruim RH, Mennes M, van Rooij D, et al. **ICA-AROMA: a robust ICA-based strategy for removing motion artifacts from fMRI data.** *Neuroimage* 2015;112:267-77 CrossRef Medline
16. Avants BB, Epstein CL, Grossman M, et al. **Symmetric diffeomorphic image registration with cross-correlation: evaluating automated labeling of elderly and neurodegenerative brain.** *Med Image Anal* 2008;12:26-41 CrossRef Medline
17. Toh CH, Siow TY, Castillo M. **Peritumoral brain edema in metastases may be related to glymphatic dysfunction.** *Front Oncol* 2021;11:725354 CrossRef Medline
18. Kang SJ, Narazaki M, Metwally H, et al. **Historical overview of the interleukin-6 family cytokine.** *J Exp Med* 2020;217:e21090347 CrossRef Medline
19. Park KJ, Kang SH, Chae YS, et al. **Influence of interleukin-6 on the development of peritumoral brain edema in meningiomas.** *J Neurosurg* 2010;112:73-80 CrossRef Medline
20. Labrenz F, Wrede K, Forsting M, et al. **Alterations in functional connectivity of resting state networks during experimental endotoxemia: an exploratory study in healthy men.** *Brain Behav Immun* 2016;54:17-26 CrossRef Medline
21. Kitzbichler MG, Aruldass AR, Barker GJ, et al; Neuroimmunology of Mood Disorders and Alzheimer's Disease (NIMA) Consortium. **Peripheral inflammation is associated with micro-structural and functional connectivity changes in depression-related brain networks.** *Mol Psychiatry* 2021;26:7346-54 CrossRef Medline
22. van Nieuwenhuizen D, Slot KM, Klein M, et al. **The association between preoperative edema and postoperative cognitive functioning and health-related quality of life in WHO grade I meningioma patients.** *Acta Neurochir (Wien)* 2019;161:579-88 CrossRef Medline
23. Liouta E, Koutsarnakis C, Liakos F, et al. **Effects of intracranial meningioma location, size, and surgery on neurocognitive functions: a 3-year prospective study.** *J Neurosurg* 2016;124:1578-84 CrossRef Medline

Exploratory Multisite MR Spectroscopic Imaging Shows White Matter Neuroaxonal Loss Associated with Complications of Type 1 Diabetes in Children

L.Y. Cai, C. Tanase, A.W. Anderson, N.J. Patel, C.A. Lee, R.S. Jones, L.M. LeSturgeon, A. Mahon, I. Taki, J. Juvera, S. Pruthi, K. Gwal, A. Ozturk, H. Kang, A. Rewers, M.J. Rewers, G.T. Alonso, N. Glaser, S. Ghetti, S.S. Jaser, B.A. Landman, and L.C. Jordan



ABSTRACT

BACKGROUND AND PURPOSE: Type 1 diabetes affects over 200,000 children in the United States and is associated with an increased risk of cognitive dysfunction. Prior single-site, single-voxel MRS case reports and studies have identified associations between reduced NAA/Cr, a marker of neuroaxonal loss, and type 1 diabetes. However, NAA/Cr differences among children with various disease complications or across different brain tissues remain unclear. To better understand this phenomenon and the role of MRS in characterizing it, we conducted a multisite pilot study.

MATERIALS AND METHODS: In 25 children, 6–14 years of age, with type 1 diabetes across 3 sites, we acquired T1WI and axial 2D MRSI along with phantom studies to calibrate scanner effects. We quantified tissue-weighted NAA/Cr in WM and deep GM and modeled them against study covariates.

RESULTS: We found that MRSI differentiated WM and deep GM by NAA/Cr on the individual level. On the population level, we found significant negative associations of WM NAA/Cr with chronic hyperglycemia quantified by hemoglobin A1c ($P < .005$) and a history of diabetic ketoacidosis at disease onset ($P < .05$). We found a statistical interaction ($P < .05$) between A1c and ketoacidosis, suggesting that neuroaxonal loss from ketoacidosis may outweigh that from poor glucose control. These associations were not present in deep GM.

CONCLUSIONS: Our pilot study suggests that MRSI differentiates GM and WM by NAA/Cr in this population, disease complications may lead to neuroaxonal loss in WM in children, and deeper investigation is warranted to further untangle how diabetic ketoacidosis and chronic hyperglycemia affect brain health and cognition in type 1 diabetes.

ABBREVIATIONS: DKA = diabetic ketoacidosis; HbA1c = hemoglobin A1c; MRSI = magnetic resonance spectroscopic imaging; T1D = type 1 diabetes

Type 1 diabetes (T1D) affects almost 1.7 million individuals, including >200,000 children and adolescents in the United States.¹ With time, children with T1D may experience declines in cognitive functions such as memory, attention, and problem solving.² These deficits, in turn, may impair subsequent T1D management, leading to further worsening of glycemic control

and additional T1D complications.² Thus, the public health implications of understanding and preventing cognitive decline in this population are considerable.³

Prior neuroimaging studies have uncovered structural brain changes in T1D populations. Poor glycemic control has been negatively correlated with GM and WM growth in children with T1D.^{4,5} Furthermore, hippocampal changes have been found in children with dysglycemia, some of which were hypothesized to reflect a response to injury, such as disruption of normal pruning.^{6,7} T1D and hyperglycemia have also been negatively associated with localized DTI microstructural measures of brain health.⁸

Received February 18, 2023; accepted after revision May 3.

From the Department of Biomedical Engineering (L.Y.C., A.W.A., B.A.L.), Vanderbilt University Institute of Imaging Science (A.W.A., B.A.L.), and Department of Electrical and Computer Engineering (B.A.L.), Vanderbilt University, Nashville, Tennessee; Departments of Psychiatry and Behavioral Sciences (C.T.) and Psychology (A.M., S.G.), University of California, Davis, Davis, California; Departments of Radiology and Radiological Sciences (A.W.A., S.P., B.A.L.), Pediatrics (N.J.P., R.S.J., S.S.J., L.C.J.), Neurology (C.A.L., L.C.J.), Medicine (L.M.L.), and Biostatistics (H.K.), Vanderbilt University Medical Center, Nashville, Tennessee; Department of Pediatrics (I.T., A.R., M.J.R.), Barbara Davis Center (G.T.A.), and Department of Psychiatry (J.J.), University of Colorado Anschutz Medical Campus, Aurora, Colorado; and Departments of Radiology (K.G., A.O.) and Pediatrics (N.G.), University of California Davis Health, University of California Davis School of Medicine, Sacramento, California.

This work was conducted, in part, by using the resources of the Advanced Computing Center for Research and Education at Vanderbilt University, Nashville, Tennessee and was supported by the National Institutes of Health (under award numbers 1U34DK123895-01, U34DK123894-01, and T32GM007347) and by the National Science Foundation under award number 2040462.

The content is solely the responsibility of the authors and does not necessarily represent the official views of the National Institutes of Health or the National Science Foundation.

Please address correspondence to Leon Y. Cai, Medical-Image Analysis and Statistical Interpretation Lab, 400 24th Ave S, FGH 369, Vanderbilt University, Nashville, TN 37212; e-mail: leon.y.cai@vanderbilt.edu; @LeonCai

Indicates open access to non-subscribers at www.ajnr.org

Indicates article with online supplemental data.

<http://dx.doi.org/10.3174/ajnr.A7895>

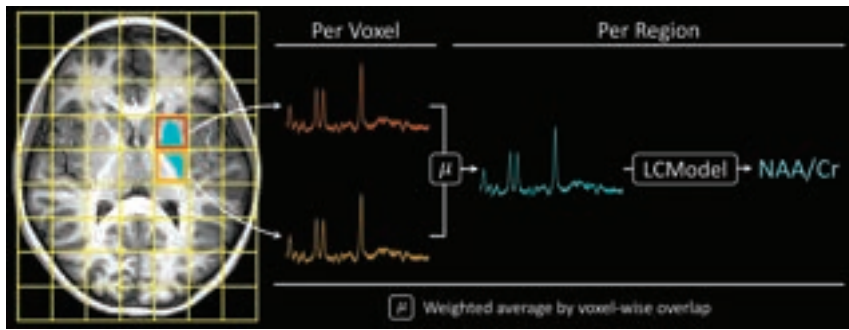


FIG 1. Illustrated MRSI workflow. After acquiring 2D MRSI and an associated T1WI-based segmentation, one spectrum for each region was generated by combining the spectra for all overlapping voxels in a weighted average based on overlap contribution (Equation). The regionally-weighted spectra were subsequently fit using LCMoel to compute metabolite peaks, resulting in one metabolite ratio computed per participant per region. Of note, the pictured MRSI grid is provided only for illustrative purposes and does not represent collected data.

Prior studies have also identified similar regional changes in brain function. Differences in activation across the cingulum, hypothalamus, cortex, deep GM nuclei, and other regions have been observed with regard to changes in working memory and visual and motor processes as well as T1D severity.⁹⁻¹² Taken together, these studies suggest that not meeting glycemic targets in T1D may be associated with regional changes in brain structure and function but do not directly assess neuronal health or neurochemistry. Thus, the mechanism underlying these changes remains unclear.

Changes to neurochemistry can be measured using MRS. Specifically, the ratio of NAA to Cr (NAA/Cr) is thought to reflect neuronal density and health, with decreasing NAA/Cr values reflecting a decline in normal metabolic functioning and neuronal loss. Prior MRS studies suggest that T1D and/or episodes of diabetic ketoacidosis (DKA) may contribute to reduced NAA/Cr.¹³⁻¹⁵ Additionally, associations between reduced NAA/Cr in the frontal regions and reduced cognitive performance have been detected in typically developing children.¹⁶ However, these studies have largely been limited to case reports or single-site, single-voxel studies, and studies have yet to investigate differences across children with various T1D complications or be integrated with regions or tissues defined on structural MR imaging to explore differences localized to different parts of the brain.^{13-15,17}

Thus, to further understand the effects of T1D on the brain and the role of MRS and MR imaging in characterizing them across different tissue regions, we conducted a multisite pilot study using tissue-weighted 2D magnetic resonance spectroscopic imaging (MRSI) in hopes of motivating larger neuroimaging studies of this population. We hypothesized that children with T1D and increased exposure to hyperglycemia, indicated by higher hemoglobin A1c (HbA1c), would exhibit lower NAA/Cr compared with children with T1D with less exposure to hyperglycemia. Furthermore, we hypothesized that a history of DKA may contribute to these differences and explored whether this finding may be localized to certain tissues or regions across the brain.

MATERIALS AND METHODS

Study Cohort and Imaging Acquisitions

We imaged 25 children 6–14 years of age with T1D with no contraindications to MR imaging or other major medical conditions

across 3 sites: A, B, and C. We acquired 3D T1WI and 2D chemical shift MRSI. At site A, all images were acquired on a 3T Achieva scanner (Philips Healthcare); at site B, on a 3T Tim Trio scanner (Siemens); and at site C, on a 3T Magnetom Skyra scanner (Siemens). We also recorded each participant's sex, age at imaging, duration of T1D (defined as time between diagnosis and imaging), whether they presented in DKA at diagnosis, HbA1c assessed once within 3 months of imaging, and race. All HbA1c measurements were obtained with point-of-care tests conducted at regular diabetes clinic visits except for 1 participant at site A whose HbA1c value was obtained with venipuncture.

T1WI was acquired at 1.0-mm isotropic resolution with TE/TR = 2.9/6310 ms at site A and 3.5/2500 ms at sites B and C. MRSI was acquired with 2D point-resolved spectroscopy sequences in an axial slice at the level of the basal ganglia with suppression bands placed around the skull. Images at site A were acquired with 20 × 24 voxels with TE/TR = 144/2000 ms at 9.58 × 9.58 × 15 mm resolution. Images at sites B and C were acquired with 16 × 16 voxels with TE/TR = 135/1690 ms at 12.5 × 12.5 × 10 mm resolution. The full MRSI parameters are available in the Online Supplemental Data.

Written informed consent and assent was provided by guardians and participants, respectively. This study was approved by the Institutional Review Boards at all sites.

Computing Regionally Weighted Metabolite Ratios

Overall, we used the following: 1) regional segmentations of different tissues derived from T1WI, 2) removed voxels with lipid interference, 3) computed regionally weighted spectra for each participant, and 4) computed metabolite ratios per participant per region.

First, T1WI was segmented using the spatially localized atlas network tiles framework followed by a manual review for quality to obtain a segmentation of the brain, the WM, and 6 deep GM nuclei: right and left caudate, basal ganglia (globus pallidus and putamen), and thalami (Online Supplemental Data).¹⁸

Second, we excluded MRSI voxels in the brain with large signal interference from lipids. For each participant, we computed the real spectrum for each MRSI voxel within the brain and fit it between 1.8 and 0.2 ppm with a line of best fit. We then computed the root mean square error between the spectrum and the line for each voxel and identified and excluded outliers as those voxels with errors 1.5 times the interquartile range above the 75th or below the 25th percentile.¹⁹

Third, using the T1WI segmentations and 2D MRSI slabs, we computed regionally weighted spectra for each participant using a weighted average approach (Fig 1). Any given region defined on T1WI overlapped a number of MRSI voxels, indicating that the spectrum for that region was a combination of signals from the overlapping MRSI voxels. Thus, for a region, r , we computed

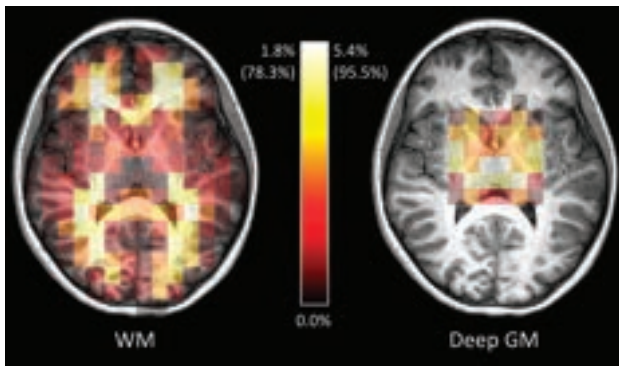


FIG 2. Maps of weights used to compute weighted average spectra for WM and deep GM in a representative participant. Each voxel is colored to represent its percent contribution to the tissue-weighted spectra as well as the corresponding voxel-wise volume fraction in parentheses.

the spectrum of that region, s_r , by taking a weighted average of the signals from the overlapping MRSI voxels, s^i , as shown in the Equation, where v_r is the total volume of region r overlapping the MRSI slab and v_r^i is the volume of region r overlapping the i th MRSI voxel.

$$s_r = \sum_i \frac{v_r^i}{v_r} s^i.$$

We focused on WM and deep GM regions and visualized the percentage contribution of each MRSI voxel to the resultant spectrum of these tissues as well as the analogous tissue volume fractions in a representative participant (Fig 2). The tissue volume fraction for MRSI voxel i was computed as v_r^i/v_r , where v^i is the volume of MRSI voxel i itself. Cortical GM was not analyzed to avoid artifacts from suppression bands placed around the skull.

Fourth, the weighted average spectra for each region for each participant in the time domain were passed into LCModel (<http://s-provencher.com/lcmodel.shtml>) basis-fitting software to compute metabolite ratios (Fig 1 and Online Supplemental Data).²⁰ TE-specific 3T basis sets provided by LCModel were used to compute the NAA/Cr from the spectra for each region. Notably, the NAA peaks used for ratio computation were themselves computed from the sum of the NAA and *N*-acetyl aspartylglutamate peaks fit with LCModel. Similarly, the Cr peaks were computed from the sum of the Cr and phosphocreatine peaks. This decision was made in line with recommendations from LCModel because it is difficult to separate NAA from *N*-acetyl aspartylglutamate and Cr from phosphocreatine at 3T. Furthermore, the ratios were filtered on the basis of the %SD metric of the constituent peaks computed by LCModel before analysis. Briefly, %SD is a contrast-to-noise metric representing the Cramér-Rao lower bounds of estimated SDs of the peak fits. All peaks with a %SD of >20% and any associated ratios were removed from consideration, in line with recommendations from LCModel that the %SD threshold be no greater than 20%.

Calibrating Metabolite Ratios among Sites

As detailed in the Online Supplemental Data, we calibrated site-wise differences in TE/TR and observed scanner differences to compare NAA/Cr across sites, in line with prior work noting the

need for multisite MRS harmonization, especially with scanners from multiple vendors (Online Supplemental Data).²¹⁻²³ Briefly, a Braino MRS phantom (GE Healthcare) was scanned at each site using the same site-specific protocols. We identified the NAA and Cr peaks in the center voxels of the phantom within the VOI with LCModel. We computed the ratio of the median NAA to median Cr values to obtain a site-specific correction factor. For each site, the NAA/Cr ratios computed from participant imaging were subsequently divided by the site's correction factor to normalize among sites.

Associations of NAA/Cr with Complications of T1D

To investigate tissue-weighted associations of NAA/Cr with T1D complications on the population level, we regressed the calibrated ratios in the WM and deep GM against study demographics in a forward model selection process, evaluating the Akaike Information Criterion, adjusted coefficients of determination (R^2), effect sizes, and *P* values. Specifically, we investigated the relationship of chronic hyperglycemia, DKA, and their interaction with NAA/Cr and subsequently added additional covariates to identify the presence of other effects. Race was omitted due to sample-size limitations. All models included an intercept term that is not presented.

RESULTS

Study Cohort and Regionally Weighted Spectra

The demographics of our study cohort stratified by site are reported in Table 1. The sites were reasonably balanced overall, given this small pilot study, but some differences existed by site, particularly the duration of T1D and DKA at onset. To account for these differences, we calibrated site-wise differences and used statistical models that included these covariates.

The resultant spectra for the WM and deep GM as well as the deep GM split into 6 nuclei are shown via means and 95% confidence intervals across participants (Fig 3). All deep GM spectra have little-to-no lipid interference after voxel exclusion, though the WM spectra have some. This finding is logical because WM extends closer to pericranial fat than deep GM structures do. However, this interference in WM does not qualitatively impact the NAA peaks (2.0 ppm). We also observed that the NAA and Cr (3.0 ppm) peaks demonstrate consistent morphology across participants. We counted the median number of excluded voxels per MRSI image to be 5, indicating roughly <5% excluded voxels per participant. Last, the median number of voxels used in WM ranged from 120 to 130, and in deep GM as a whole, it ranged from 30 to 40. Overall, these spectra were found acceptable for further NAA/Cr analysis.

Tissue-Weighted Differences in Metabolite Ratios

To investigate NAA/Cr differences by tissue, we plotted the ratios across participants in the WM, 6 deep GM nuclei, and deep GM as a whole (Fig 4A). We investigated regional differences with pair-wise Wilcoxon signed-rank tests after false discovery rate multiple comparison correction and without calibration because the comparisons were matched within participants and not pooled across sites.

NAA/Cr in the WM was significantly higher than in deep GM generally ($P < .005$) and in the caudate and basal ganglia specifically ($P < .005$ bilaterally) (Fig 4B). We also found differences between the WM and right thalamus ($P < .05$) (Fig 4B). This difference was not recapitulated on the left, but significant differences were not found between the left and right thalamus (Fig 4C). Additionally, left-right symmetric differences were present in deep GM nuclei, with increasing NAA/Cr from the caudate to the basal ganglia ($P < .05$ on the right and $P = .082$ on the left) to the thalamus ($P < .005$ bilaterally) (Fig 4D). These results suggest that our methodology identified tissue-weighted differences in NAA/Cr matched within each participant on the individual level and that these differences are largely left-right symmetric.

Associations of NAA/Cr with Complications of T1D

The forward model selection results are reported in Table 2. In the WM, we identified a statistically significant negative association between HbA1c and NAA/Cr, suggesting that elevated HbA1c is associated with decreased NAA/Cr. We also found large changes in the HbA1c and DKA effects with the addition of an interaction term between HbA1c and DKA status: Both effect sizes increased dramatically, the DKA effect became significant, and the interaction term nearly cancelled out the HbA1c effect. Additionally, these glycemic effects alone resulted in the model

with the lowest Akaike Information Criterion and highest adjusted R^2 . The addition of the age, sex, and duration covariates did not improve the Akaike Information Criterion or noticeably change identified effects, suggesting that these additional covariates did not capture meaningful variance otherwise. In deep GM, no analogous associations in NAA/Cr or drops in the Akaike Information Criterion were identified as more terms were added. Similar findings were observed in a secondary sensitivity analysis with an expanded model selection process incorporating all combinations of variables.

We visualized the WM model with the lowest Akaike Information Criterion in Fig 5. The negative HbA1c effect identified is visually present when considering all sites both together and separately. We also observed the DKA and interaction effects, recognizing small sample sizes and potential confounding by site. For instance, the participants from site C had higher NAA/Cr values, but none had DKA at onset, whereas the participants from site B had lower NAA/Cr values but most had DKA at onset. At site A, where 50% of participants had DKA at onset, no qualitatively appreciable difference in NAA/Cr with DKA was found. These qualitative findings were supported quantitatively when a fixed site effect was added to the models in a secondary sensitivity analysis. The relationship of the glycemic effects to each other remained but were reduced in magnitude

and lost significance, as expected. Additionally, in secondary analyses considering the sites separately, similar trends were observed albeit without statistical significance due to further reduced sample sizes, also as expected.

Taken together, these results suggest that T1D effects in NAA/Cr were measurable across sites but potentially at a magnitude smaller than the site effects. Specifically, NAA/Cr in WM decreased both with increasing HbA1c and with DKA, consistent with neuroaxonal loss.

Table 1: Cohort demographics by site

	Site A	Site B	Site C	Overall
Sample size (No.)	10	11	4	25
Age (yr) (mean)	10.6 (SD, 1.1)	10.5 (SD, 2.7)	8.5 (SD, 1.3)	10.2 (SD, 2.0)
Sex, female (No.)	7 (70%)	5 (45%)	3 (75%)	15 (60%)
Duration (yr) (mean)	2.6 (SD, 2.3)	4.6 (SD, 3.3)	0.3 (SD, 0.1)	3.1 (SD, 3.0)
HbA1c (%) (mean)	9.5 (SD, 3.2)	8.5 (SD, 1.9)	6.2 (SD, 0.9)	8.5 (SD, 2.6)
DKA at onset (No.)	5 (50%)	9 (82%)	0 (0%)	14 (56%)
Race (No)				
White	7 (70%)	8 (73%)	4 (100%)	19 (76%)
Black/African American	2 (20%)	1 (9%)	0 (0%)	3 (12%)
Multiracial (black/white)	0 (0%)	1 (9%)	0 (0%)	1 (4%)
Other	1 (10%)	1 (9%)	0 (0%)	2 (8%)

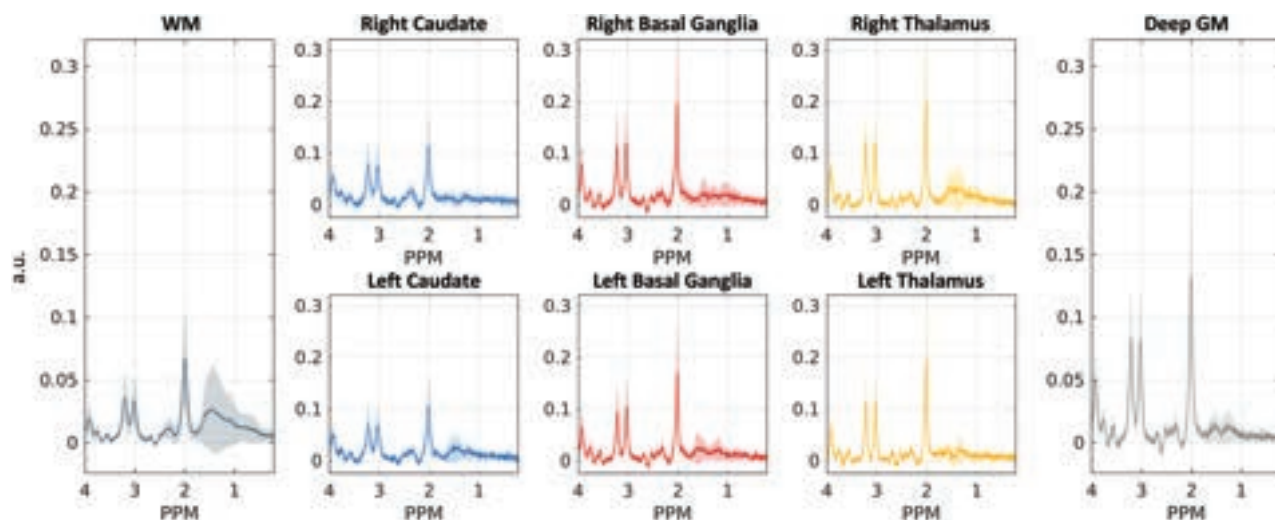


FIG 3. Mean regionally weighted spectra with 95% confidence intervals across participants from 0.2 to 4.0 ppm. Spectra were extracted for each region for each participant from LCMoDel and plotted after baseline subtraction. a.u. indicates arbitrary units.

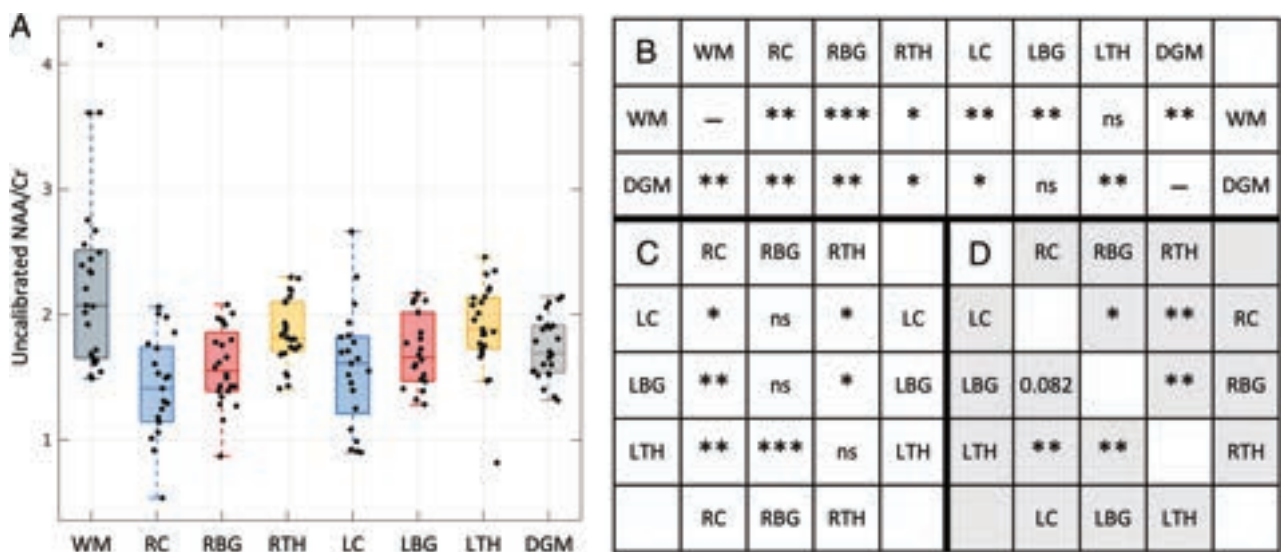


FIG 4. Differences in NAA/Cr in T1D by region. *A*, The uncalibrated NAA/Cr ratios from the regionally weighted spectra are shown across participants. *B*, *P* values of statistical comparisons between WM and deep GM as a whole and the individual deep nuclei. *C*, *P* values of contralateral comparisons in deep GM nuclei. *D*, *P* values of ipsilateral comparisons in deep GM nuclei. Statistical significance between regions was determined with pair-wise Wilcoxon signed-rank tests after false discovery rate correction (en dash indicates not tested; ns, not significant; single asterisk, $P < .05$; double asterisks, $P < .005$; triple asterisks, $P < .0005$). RC indicates right caudate; RBG, right basal ganglia; RTH, right thalamus; LC, left caudate; LBG, left basal ganglia; LTH, left thalamus; DGM, deep GM.

Table 2: Effect sizes, Akaike Information Criterion, and adjusted R^2 for forward model selection of NAA/Cr in WM and deep GM with T1D covariates

Tissue	HbA1c	DKA	HbA1c x DKA	Age	Sex	Duration	Akaike	aR ²
WM	-0.086 ^a	—	—	—	—	—	17.581	0.291
	-0.080 ^b	-0.095	—	—	—	—	19.083	0.273
	-0.171 ^{a,c}	-1.142 ^{b,c}	0.130 ^{b,c}	—	—	—	15.373 ^c	0.394 ^c
	-0.169 ^a	-1.156 ^b	0.131 ^b	-0.009	—	—	17.298	0.365
	-0.187 ^a	-1.209 ^b	0.141 ^b	-0.001	0.175	—	17.086	0.389
Deep GM	-0.187 ^a	-1.267 ^b	0.144 ^b	-0.005	0.189	0.012	18.799	0.362
	-0.016 ^c	—	—	—	—	—	-29.356 ^c	0.061 ^c
	-0.018	0.034	—	—	—	—	-27.785	0.034
	-0.027	-0.065	0.012	—	—	—	-26.087	-0.001
	-0.029	-0.043	0.010	0.011	—	—	-24.800	-0.023
	-0.027	-0.035	0.009	0.010	-0.018	—	-22.922	-0.075
	-0.028	-0.086	0.011	0.007	-0.005	0.011	-22.194	-0.079

Note:—The en dash indicates that term was not included in model; aR², adjusted R².

^a $P < .005$.

^b $P < .05$.

^c Model with lowest Akaike Information Criterion.

However, the HbA1c effect was reduced in the presence of DKA, suggesting that reductions in NAA/Cr due to DKA may outweigh those due to increased HbA1c.

DISCUSSION

MRSI Image Processing in Children with T1D

We found 2D MRSI to be an effective tool for identifying localized tissue-weighted NAA/Cr differences in children with T1D across multiple sites. On an individual level, we identified higher NAA/Cr in the WM than in deep GM, consistent with prior studies in healthy adults.²⁴ On the population level, we found negative associations with complications of T1D in WM, specifically reduced NAA/Cr with chronic hyperglycemia and DKA, as discussed in following sections.

In children with T1D, MRS has been used as single-voxel spectroscopy in single-site case reports.¹³⁻¹⁶ Single-voxel spectroscopy has the benefit of allowing investigators to place a voxel in tissue as desired to measure metabolite ratios in a single location in the brain with higher signal-to-noise ratios.²⁵ However, this approach makes it difficult to resolve tissue or region differences in metabolite ratios across the brain with a single acquisition or to retroactively analyze other locations that were not prospectively defined.²⁵ We demonstrate that 2D MRSI, even with a lower signal-to-noise ratio than single-voxel spectroscopy, when combined with weighted signal averaging, overcomes these limitations in pediatric T1D samples at multiple sites. This suggests that future, large-scale, multisite MRSI studies that are better equipped to sample diverse participants from this population can benefit from 2D imaging.

As it stands, there is no widely accepted methodology for identifying region-specific metabolite ratios from 2D MRSI, largely due to 3 key challenges. The first is accounting for partial volume effects among different brain tissues. The second is accounting for magnetic field inhomogeneities, eddy currents, and other nonlinearities that may exist across large structures or spatial dependencies like those due to chemical shift displacement. The third is accounting for noise that can exist in every single step of MRSI analysis, including signal acquisition, frequency transformation, spectral baseline modeling, basis fitting, and peak computation. Existing techniques using linear regression or

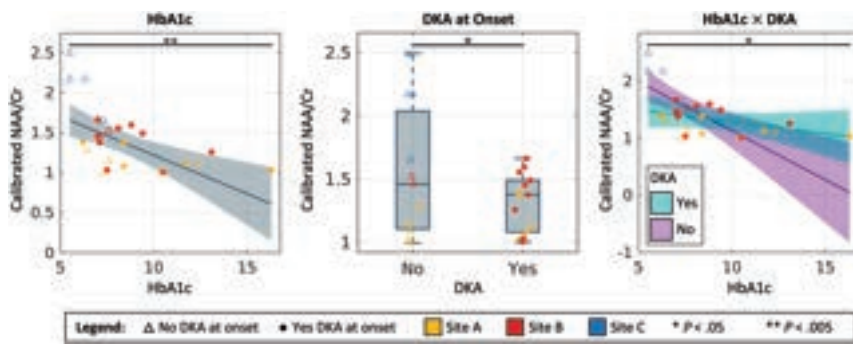


FIG 5. Associations of NAA/Cr in WM with T1D complications. The calibrated NAA/Cr ratios in WM are shown plotted against HbA1c, DKA status, and their interaction. Data points are colored by site with the symbol denoting the participant's DKA status.

source separation methods have primarily focused on overcoming partial volume effects.^{24,26,27} However, we note that these techniques are performed later in the MRSI workflow and risk compounding and propagating noise, yielding measurements with reduced meaning. Thus, we propose first performing the weighted averaging operation in the signal domain without explicit partial volume modeling to exchange increased tissue specificity for reduced noise artifacts. Accordingly, we emphasize that the results reported here are “weighted” by tissue as opposed to being absolutely “specific” to tissue. We note that this design choice was made in large part due to considerations for noisy and variable data that may arise from multisite studies. Furthermore, we note that no approach has yet successfully modeled spatial inhomogeneities, dependencies, and nonlinearities. Thus, in the future, we hope for sequences with higher signal-to-noise ratios and to extend this idea of regional mapping in the signal domain with posterior matrix inversions to better incorporate partial volume effects and to add direct consideration of spatial nonlinearities, extending emerging methodologies.^{24,26,27}

When computing metabolite ratios with LCModel, we leveraged “default” 3T basis sets provided by LCModel instead of computing “custom,” scanner-specific sets using pulse sequences and envelope parameters.^{28,29} This design choice was made for the following reasons: 1) to simplify both the present and future studies across multiple sites where MRSI pulse sequences and envelope parameters may not be readily available or reliably queried from scanners (as was the case for sites B and C presently); 2) because custom basis sets leveraging techniques like density operator simulation or the Versatile Simulation, Pulses, and Analysis (VeSPA; <https://www.opensourceimaging.org/project/vespa-versatile-simulation-pulses-analysis/>) toolkit primarily impact multiplet signals, whereas NAA and Cr are largely singlet;²⁸⁻³⁰ and 3) because initial attempts using these custom sets did not dramatically affect results.

We used data from multiple sites acquired with different TE/TRs to maximize the sample size available for analysis. Thus, this approach required empiric calibration for site-wise effects via phantom studies for this pilot study. However, scanner calibration is an open problem, and many other calibration options exist. Careful consideration of site-wise effects should be used in future studies, including the use of matched TE/TR acquisitions and scanner hardware when possible.

WM NAA/Cr and Chronic Hyperglycemia

We found a negative association between WM NAA/Cr and hyperglycemia, as measured by HbA1c, that was not present in the deep

GM. HbA1c is an average measure of chronic glucose control in the 3 months preceding the measurement.³¹ Thus, we interpret this negative association as evidence that prolonged hyperglycemia is associated with neuroaxonal loss in WM diffusely in children with T1D. This finding builds on prior DTI studies in this population that have suggested a relationship between hyperglycemia and WM biomarkers and represents a novel exploration of diffuse WM neurochemistry, as opposed to focal investigations performed in prior single-voxel MRS studies.^{8,13-16}

While small sample sizes can produce underpowered or overfit models,

we are reassured that this effect was significant throughout the forward model selection process and was not suppressed by additional covariates. Furthermore, we found that the best model identified through model selection explained roughly 40% of the variance in the data, indicating high explainability in a noisy system with a small sample size. Thus, we hope these small-scale, exploratory results serve as evidence to motivate larger multisite studies to elaborate on these findings. Notably, larger-scale studies should further investigate the clinical implications of these findings and their associations with cognitive outcomes. Additionally, given that HbA1c is an average measurement of blood sugar across time, future studies could clarify which aspects of glycemic variability are most impactful, including time spent in the target glucose range, daily excursions, pre- and postprandial levels, and the number of hyper- or hypoglycemic episodes.³² Inclusion of continuous glucose monitoring data may allow these effects to be characterized.

We note the absence of an age effect in our results. Prior MRS studies have established age effects in NAA and Cr at low TEs (around 30 ms) in children.³³ However, different TEs, such as the long TEs used presently (>100 ms), affect different peaks differently, and changing NAA and changing Cr do not equate to changing NAA/Cr, especially in a small sample. Thus, to balance the need for modeling age against the differences between metabolite- and ratio-based analyses as well as the uncertainties of MRS at different TEs, we included age as a variable during model selection as opposed to explicitly acquiring a control group for age in this pilot study.

WM NAA/Cr and DKA

We found throughout the model selection process that participants with DKA at disease onset had a decreased WM NAA/Cr, similar to the HbA1c effect, and that the HbA1c effect was muted in the presence of DKA. However, we found that these effects were only revealed when considered jointly with and in the context of HbA1c via inclusion of an interaction term between the two. DKA is a well-known complication of T1D, marked by an acute elevation of blood sugar to dangerous levels coupled with the onset of acidosis due to the development of ketones, potential cerebral edema, and other metabolic changes.³⁴ Thus, these associations suggest that WM neuroaxonal integrity may be diffusely affected by episodes of DKA in a manner that outweighs chronic changes from prolonged hyperglycemia.

As mentioned previously, the primary limitation to this interpretation is the potential confounding by site. Differences in DKA frequency by site as well as site effects that may be larger in magnitude than glycemic effects make it difficult to untangle the two. Another limitation is that patients with frequent episodes of DKA may also have higher HbA1c levels.³⁵ Moreover, due to the multifactorial nature of DKA, it is unclear which of its aspects may be contributing to these findings. Furthermore, we investigated the presence of DKA at the onset of T1D, but due to sample size limitations, we were not able to account for DKA severity or subsequent episodes.

In short, we recognize that neurophysiologic changes in T1D are multifactorial and did not account for all possible variables in this pilot study. We note that this limitation is common in other neuroimaging studies examining brain structure and function in T1D, including those with larger sample sizes.³⁶ One large-scale study in which the number of DKA episodes, severity of DKA, hyperglycemia, hypoglycemia, and duration of T1D were simultaneously accounted for only considered behavioral outcomes without neuroimaging.³⁷ Despite our small sample size, however, we found significant effects that were not suppressed, even as additional covariates were added. Thus, these small-scale associations support that larger studies of WM health in T1D should do the following: 1) consider interactions between acute T1D complications, like DKA, and chronic glucose control, and 2) take into account balanced DKA groups per site and rigorous harmonization of different acquisition and scanner effects, as mentioned previously.

Last, we note that both the DKA and HbA1c effects were seen only in the WM and not in GM. This finding is consistent with other studies that have found reductions in WM volume in children 6 months after DKA and reductions in WM structural integrity.³⁸⁻⁴⁰ Thus, we would expect NAA/Cr to be reduced in WM related to neuroaxonal loss. Other studies have also found reductions in GM volume in individuals with T1D, and it has been posited that patients with long-standing T1D may have partial neuronal loss or dysfunction related to their disease.^{41,42} Our findings may indicate that cerebral WM is more vulnerable to glycemic injury, and we suspect that a reduction in GM NAA/Cr would also be seen if our participants had long-standing T1D. Alternatively, the absence of effects in GM may simply be related to the small sample size in this pilot study.

CONCLUSIONS

Our pilot study represents a step toward understanding the neurophysiology underlying brain changes in T1D, elucidating its relationship to complications of T1D, and characterizing how MRSI and MR imaging may be integrated to monitor brain health. For instance, studies have shown alterations in cerebral WM structure and reduced WM volume in children with T1D using structural and diffusion tensor imaging and that these WM changes are associated with reduced neurocognitive scores.⁴³⁻⁴⁵ Thus, there are clear clinical ramifications for this work, and using MRSI adds to our understanding of potential mechanisms of injury. Furthermore, neuroimaging is not currently part of the monitoring algorithm for individuals with T1D. However, assessment for subtle neurologic injury with MR imaging of the brain

is recommended at least once in childhood and once in adulthood in a different chronic illness in which WM injury may lead to changes in clinical care.⁴⁶ One can thus envision how assessing neuroaxonal loss or dysfunction might be clinically relevant for T1D.

We present a novel exploration of tissue-weighted MRSI in children with T1D and a first attempt to untangle the effects of DKA and chronic hyperglycemia on neuronal integrity in different tissues across the brain in this population. We found that MRSI differentially identified NAA/Cr in T1D by tissue and complications of T1D were associated with markers of neuroaxonal loss in WM. Our study has 3 key limitations: 1) reduced tissue-specificity and spatial homogeneity in exchange for tissue-weighting with improved signal-to-noise, 2) reduced power due to limited sample sizes, and 3) large site effects. However, the notable public health implications for this population and our preliminary findings motivate the need for higher signal-to-noise 2D MRSI sequences and innovative analysis methods that explicitly consider partial volume effects and spatial nonlinearities. Moreover, these new methods should be leveraged in large-scale, harmonized multisite MRSI and MR imaging studies to better understand and monitor changes in brain neurochemistry and neurocognition in children with T1D.

Disclosure forms provided by the authors are available with the full text and PDF of this article at www.ajnr.org.

REFERENCES

- Centers for Disease Control and Prevention. **National Diabetes Statistics Report: Estimates of Diabetes and Its Burden in the United States.** 2020. <https://www.cdc.gov/diabetes/data/statistics-report/index.html>. Accessed September 10, 2020
- Cato A, Hershey T. **Cognition and type 1 diabetes in children and adolescents.** *Diabetes Spectr* 2016;29:197–202 CrossRef Medline
- Jaser SS, Jordan LC. **Brain health in children with type 1 diabetes: risk and protective factors.** *Curr Diab Rep* 2021;21:12 CrossRef Medline
- Mauras N, Mazaika P, Buckingham B, et al; Diabetes Research in Children Network (DirecNet). **Longitudinal assessment of neuroanatomical and cognitive differences in young children with type 1 diabetes: association with hyperglycemia.** *Diabetes* 2015;64:1770–79 CrossRef Medline
- Mazaika PK, Weinzimer SA, Mauras N, et al; Diabetes Research in Children Network (DirecNet). **Variations in brain volume and growth in young children with type 1 diabetes.** *Diabetes* 2016;65:476–85 CrossRef Medline
- Hershey T, Perantie DC, Wu J, et al. **Hippocampal volumes in youth with type 1 diabetes.** *Diabetes* 2010;59:236–41 CrossRef Medline
- Foland-Ross LC, Reiss AL, Mazaika PK, et al; the Diabetes Research in Children Network (DirecNet). **Longitudinal assessment of hippocampus structure in children with type 1 diabetes.** *Pediatr Diabetes* 2018;19:1116–23 CrossRef Medline
- Antenor-Dorsey JA, Shimony JS, Hershey T. **Diffusion tensor imaging of the brain in type 1 diabetes.** *Eur Med J Diabetes* 2014;2:42–47 CrossRef
- Foland-Ross LC, Tong G, Mauras N, et al; Diabetes Research in Children Network (DirecNet). **Brain function differences in children with type 1 diabetes: a functional MRI study of working memory.** *Diabetes* 2020;69:1770–78 CrossRef Medline
- Musen G, Simonson DC, Bolo NR, et al. **Regional brain activation during hypoglycemia in type 1 diabetes.** *J Clin Endocrinol Metab* 2008;93:1450–57 CrossRef Medline

11. Šuput Omladić J, Slana Ozimicó A, Vovk A, et al. **Acute hyperglycemia and spatial working memory in adolescents with type 1 diabetes.** *Diabetes Care* 2020;43:1941–44 CrossRef Medline
12. Gallardo-Moreno GB, González-Garrido AA, Gudayol-Ferré E, et al. **Type 1 diabetes modifies brain activation in young patients while performing visuospatial working memory tasks.** *J Diabetes Res* 2015;2015:703512 CrossRef Medline
13. Wootton-Gorges SL, Buonocore MH, Kuppermann N, et al. **Cerebral proton magnetic resonance spectroscopy in children with diabetic ketoacidosis.** *AJNR Am J Neuroradiol* 2007;28:895–99 Medline
14. Wootton-Gorges SL, Buonocore MH, Caltagirone RA, et al. **Progressive decrease in N-acetylaspartate/creatine ratio in a teenager with type 1 diabetes and repeated episodes of ketoacidosis without clinically apparent cerebral edema: evidence for permanent brain injury.** *AJNR Am J Neuroradiol* 2010;31:780–81 CrossRef Medline
15. Sarac K, Akinci A, Alkan A, et al. **Brain metabolite changes on proton magnetic resonance spectroscopy in children with poorly controlled type 1 diabetes mellitus.** *Neuroradiology* 2005;47:562–65 CrossRef Medline
16. Ozturk A, Degaonkar M, Matson MA, et al. **Proton MR spectroscopy correlates of frontal lobe function in healthy children.** *AJNR Am J Neuroradiol* 2009;30:1308–14 CrossRef Medline
17. Mangia S, Kumar AF, Moheet AA, et al. **Neurochemical profile of patients with type 1 diabetes measured by 1H-MRS at 4 T.** *J Cereb Blood Flow Metab* 2013;33:754–59 CrossRef Medline
18. Huo Y, Xu Z, Xiong Y, et al. **3D whole brain segmentation using spatially localized atlas network tiles.** *Neuroimage* 2019;194:105–19 CrossRef Medline
19. Walfish S. **A review of statistical outlier methods.** *Pharmaceutical Technology* 2006;30:82–86
20. Provencher SW. **Estimation of metabolite concentrations from localized in vivo proton NMR spectra.** *Magn Reson Med* 1993;30:672–79 CrossRef Medline
21. Cai LY, Tanase C, Anderson AW, et al. **Multimodal neuroimaging in pediatric type 1 diabetes: a pilot multisite feasibility study of acquisition quality, motion, and variability.** In: Išgum I, Colliot O, eds. *Medical Imaging 2022: Image Processing*. Vol 12032. SPIE; 2022:135 CrossRef
22. Povazōan M, Mikkelsen M, Berrington A, et al. **Comparison of multivendor single-voxel MR spectroscopy data acquired in healthy brain at 26 sites.** *Radiology* 2020;295:171–80 CrossRef Medline
23. Graf C, MacMillan EL, Fu E, et al. **Intra- and inter-site reproducibility of human brain single-voxel proton MRS at 3 T.** *NMR Biomed* 2019;32:1–10 CrossRef Medline
24. Tal A, Kirov II, Grossman RI, et al. **The role of gray and white matter segmentation in quantitative proton MR spectroscopic imaging.** *NMR Biomed* 2012;25:1392–400 CrossRef Medline
25. Maudsley AA, Andronesi OC, Barker PB, et al. **Advanced magnetic resonance spectroscopic neuroimaging: experts' consensus recommendations.** *NMR Biomed* 2021;34:e4309 CrossRef Medline
26. Goryawala MZ, Sheriff S, Stoyanova R, et al. **Spectral decomposition for resolving partial volume effects in MRS.** *Magn Reson Med* 2018;79:2886–95 CrossRef Medline
27. Hetherington HP, Pan JW, Mason GF, et al. **Quantitative 1H spectroscopic imaging of human brain at 4.1 T using image segmentation.** *Magn Reson Med* 1996;36:21–29 CrossRef Medline
28. Lally PJ, Montaldo P, Oliveira V, et al; MARBLE Consortium. **Magnetic resonance spectroscopy assessment of brain injury after moderate hypothermia in neonatal encephalopathy: a prospective multicentre cohort study.** *Lancet Neurol* 2019;18:35–45 CrossRef Medline
29. Choi C, Ganji SK, DeBerardinis RJ, et al. **2-Hydroxyglutarate detection by magnetic resonance spectroscopy in IDH-mutated patients with gliomas.** *Nat Med* 2012;18:624–29 CrossRef Medline
30. Soher BJ, Semanchuk P, Todd D, et al. **VeSPA: Integrated applications for RF pulse design, spectral simulation and MRS data analysis.** *Mag Reson Med* 2023 May 15. [Epub ahead of print] CrossRef Medline
31. American Diabetes Association. **Glycemic targets: standards of medical care in diabetes—2021.** *Diabetes Care* 2021;44(Suppl 1):S73–84 CrossRef Medline
32. Lundholm MD, Emanuele MA, Ashraf A, et al. **Applications and pitfalls of hemoglobin A1C and alternative methods of glycemic monitoring.** *J Diabetes Complications* 2020;34:107585 CrossRef Medline
33. Holmes MJ, Robertson FC, Little F, et al. **Longitudinal increases of brain metabolite levels in 5-10 year old children.** *PLoS One* 2017;12:e0180973 CrossRef Medline
34. American Diabetes Association. **Diabetes care in the hospital: standards of medical care in diabetes-2021.** *Diabetes Care* 2021;44(Suppl 1):S211–20 CrossRef Medline
35. Ryan CM, van Duinkerken E, Rosano C. **Neurocognitive consequences of diabetes.** *Am Psychol* 2016;71:563–76 CrossRef Medline
36. Aye T, Mazaika PK, Mauras N, et al; Diabetes Research in Children Network (DirecNet) Study Group. **Impact of early diabetic ketoacidosis on the developing brain.** *Diabetes Care* 2019;42:443–49 CrossRef Medline
37. Ghetti S, Kuppermann N, Rewers A, et al; Pediatric Emergency Care Applied Research Network (PECARN) DKA FLUID Study Group. **Cognitive function following diabetic ketoacidosis in children with new-onset or previously diagnosed type 1 diabetes.** *Diabetes Care* 2020;43:2768–75 CrossRef Medline
38. Cameron FJ, Scratch SE, Nadebaum C, et al; DKA Brain Injury Study Group. **Neurological consequences of diabetic ketoacidosis at initial presentation of type 1 diabetes in a prospective cohort study of children.** *Diabetes Care* 2014;37:1554–62 CrossRef Medline
39. Antenor-Dorsey JA, Meyer E, Rutlin J, et al. **White matter microstructural integrity in youth with type 1 diabetes.** *Diabetes* 2013;62:581–89 CrossRef Medline
40. Fox LA, Hershey T, Mauras N, et al; Diabetes Research in Children Network (DirecNet). **Persistence of abnormalities in white matter in children with type 1 diabetes.** *Diabetologia* 2018;61:1538–47 CrossRef Medline
41. Seaquist ER. **The impact of diabetes on cerebral structure and function.** *Psychosom Med* 2015;77:616–21 CrossRef Medline
42. Stanton-yonge N, Sampedro F, Méndez J, et al. **Structural gray and white matter differences in patients with type 1 diabetes and impaired awareness of hypoglycemia.** *J Clin Endocrinol Metab* 2021;106:450–58 CrossRef Medline
43. Aye T, Barnea-Goraly N, Ambler C, et al. **White matter structural differences in young children with type 1 diabetes: a diffusion tensor imaging study.** *Diabetes Care* 2012;35:2167–73 CrossRef Medline
44. Mauras N, Buckingham B, White NH, et al; Diabetes Research in Children Network (DirecNet). **Impact of type 1 diabetes in the developing brain in children: a longitudinal study.** *Diabetes Care* 2021;44:983–92 CrossRef Medline
45. Toprak H, Yetis H, Alkan A, et al. **Relationships of DTI findings with neurocognitive dysfunction in children with type 1 diabetes mellitus.** *Br J Radiol* 2016;89:20150680–15 CrossRef Medline
46. DeBaun MR, Jordan LC, King AA, et al. **American Society of Hematology 2020 guidelines for sickle cell disease: prevention, diagnosis, and treatment of cerebrovascular disease in children and adults.** *Blood Adv* 2020;4:1554–88 CrossRef Medline

Association of Lower Age and Cardiorespiratory Events during Intra-Arterial Chemotherapy for Retinoblastoma: A Prospective Observational Study

M.F. Lima, L.F. Teixeira, S.B.d.M. Teruya, C.R.P.D. Macedo, V.M.d.S. Pinto, T.A. Terra, and J.R.F. Fonseca

ABSTRACT

BACKGROUND AND PURPOSE: Retinoblastoma is the most common primary intraocular tumor in childhood. Intra-arterial chemotherapy is becoming the standard of care for both first-line and rescue therapy, thus improving survival rates and decreasing the adverse effects of retinoblastoma treatment. Cardiorespiratory adverse events during general anesthesia for intra-arterial chemotherapy, including decreased lung compliance and bradycardia, have been described, but data regarding associated factors are still lacking. We aimed to assess the characteristics of patients and procedures associated with cardiorespiratory events during intra-arterial chemotherapy.

MATERIALS AND METHODS: We performed a prospective monocenter observational study in children diagnosed with retinoblastoma undergoing intra-arterial chemotherapy under general anesthesia. The occurrence of cardiorespiratory events was registered. We also assessed clinical and procedural characteristics potentially associated with these events.

RESULTS: A cardiorespiratory event was observed in 22 (12.5%) procedures, predominantly a decrease in tidal volume observed in 16 (9%) procedures. The median age was lower in the procedures with a cardiorespiratory event (20.43 [SD, 11.76] months versus 30.11 [SD, 24.17] months) ($P < .05$). Other variables such as bilateral disease or a previous intra-arterial chemotherapy treatment were not associated with the occurrence of a cardiorespiratory event.

CONCLUSIONS: In children undergoing intra-arterial chemotherapy for retinoblastoma treatment, cardiorespiratory events were observed in 12.5% of procedures. Lower age was associated with this complication. Although predominantly mild, these events should have prompt diagnosis and treatment to prevent further deterioration and worse outcomes.

ABBREVIATIONS: EtCO₂ = end-tidal CO₂; IAC = intra-arterial chemotherapy; MAC = minimum alveolar concentration; SpO₂ = saturation of peripheral oxygen

Retinoblastoma is the most common primary intraocular tumor in childhood, occurring mostly in children younger than 2 years of age. If diagnosed early, the survival rate reaches near 100% in high-income countries.¹ During the past decades, retinoblastoma treatment has markedly advanced with a paradigm change from external beam radiation and systemic chemotherapy to more selective local therapies, increasing cure rates and decreasing adverse effects.²

Ophthalmic artery chemosurgery—also known as superselective ophthalmic artery chemotherapy—is a type of intra-arterial

chemotherapy (IAC) and represents one of the treatment modalities for first-line or rescue therapy.³ It involves the insertion of a microcatheter into the ophthalmic artery to deliver chemotherapy directly to the affected eye. Chemotherapy is delivered in high doses directly to the tumor, resulting in less systemic adverse effects and higher eye-salvage rates, becoming the standard of care in many centers.⁴

IAC is usually performed with the patient under general anesthesia, and adverse reactions involving the cardiac and respiratory systems have been consistently demonstrated.⁵⁻¹⁰ Those cardiorespiratory events are probably secondary to an autonomic reflex whose mechanism remains to be elucidated. A broad spectrum of clinical manifestations can be observed such as an abrupt decrease in lung compliance, bradycardia, and cardiac arrest, thus posing specific challenges for anesthesiologists. Early detection and prompt treatment are of utmost importance in preventing further deterioration.¹⁰

Although some groups have reported these adverse cardiorespiratory reactions, associated factors remain to be demonstrated. We designed this study to describe our experience and assess the characteristics of patients and procedures associated with these cardiorespiratory events recorded during IAC.

Received January 18, 2023; accepted after revision May 3.

From the Instituto de Oncologia Pediátrica (C.R.P.D.M., L.F.T., S.B.d.M.T.), Grupo de Apoio ao Adolescente e à Criança com Câncer, Departamento de Diagnóstico por Imagem (J.R.F.F.), Departamento de Oftalmologia (L.F.T.), Disciplina de Anestesiologia (M.F.L., T.A.T., V.M.d.S.P.), Dor e Medicina Intensiva, and Instituto da Criança (S.B.d.M.T.), Faculdade de Medicina, Universidade de São Paulo, São Paulo, Brazil.

Please address correspondence to Mariana F. Lima, MD, Disciplina de Anestesiologia, Dor e Medicina Intensiva, Universidade Federal de São Paulo, Rua Napoleão de Barros, 715-5° Andar-Hospital São Paulo, Vila Clementino, CEP: 04024-002. São Paulo, SP, Brazil; e-mail: mariana.lima@unifesp.br

 Indicates article with online supplemental data.

<http://dx.doi.org/10.3174/ajnr.A7896>

MATERIALS AND METHODS

This prospective, observational, monocenter study was conducted in a pediatric cancer center from March 2020 to December 2021. This center is a reference hospital for retinoblastoma treatment. This study was approved by the local research board (EXT 008/2019) and the local Ethics Committee (CAAE. 28598120.5.00005505) and registered at ClinicalTrials.gov (NCT04451304). Informed consent was obtained from the parents or guardians and children when appropriate. We enrolled consecutive children who underwent IAC for retinoblastoma under general anesthesia.

IAC was performed in children with retinoblastoma as first-line therapy or rescue therapy after local treatment or systemic chemotherapy. The choice of IAC drugs was based on disease severity and included combinations of melphalan, topotecan, and carboplatin.

Anesthesia

IAC was performed with the patient under general anesthesia in an operating room with angiography. Induction was accomplished with IV propofol or inhaled sevoflurane, and all patients had their tracheas intubated with an appropriate tube size. Other anesthetics choice, including a muscle relaxant, was at the discretion of the attending anesthesiologist. Maintenance was accomplished with oxygen 50%, air, and sevoflurane 1.0–1.5 minimum alveolar concentration (MAC) adjusted for age. Atropine was not prophylactically administered. Mechanical ventilation was set in a pressure-control mode to a volume of 8–10 mL/kg with positive end-expiratory pressure of 5 cm H₂O. The respiratory rate was adjusted to achieve an end-tidal CO₂ (EtCO₂) of 35 mm Hg.

The electrocardiogram, peripheral oxygen saturation, EtCO₂, and sevoflurane were continuously monitored. Noninvasive blood pressure was measured at 3-minute intervals.

Procedure

IAC was performed by a single experienced interventional neuroradiologist. With the patient under general anesthesia, an ultrasound-guided puncture of the common femoral artery was performed, and a 3F pediatric arterial sheath was introduced into the arterial lumen. A flow microcatheter of 1.2 or 1.5F with a microguide of 0.07 or 0.08 inch (Balt, Montmorency, France) was guided into the ICA under fluoroscopy and then to the ostium of the ophthalmic artery. As per protocol, the microcatheter was navigated into the ophthalmic artery. In case of a difficult approach to the ophthalmic artery ostium, the microcatheter was retrieved under roadmaps. After we ensured the correct microcatheter tip position with fluoroscopic confirmation by injecting iodine contrast media, chemotherapy was infused slowly. Systemic IV heparinization with an initial heparin bolus of 75 IU/kg was performed. When infusion was complete, the microcatheter and the arterial introducer were removed, and local hemostasis was achieved by manual compression for 5 minutes at the puncture site, followed by a pressure bandage for 4 hours. The patient remained in rest for 4–6 hours with the lower limbs in extension and was discharged from the hospital after this period.

Variables Collected

We collected demographic data and previous therapeutic interventions for retinoblastoma, including previous IAC, and data regarding anesthesia techniques and drugs. Data related to IAC

were also registered such as catheter size and chemotherapy drugs. We collected vital signs and respiratory parameters at the following moments: immediately before femoral puncture, immediately after internal carotid catheterization, and during the cardiorespiratory event if observed.

Cardiorespiratory events were defined as any unexpected cardiac or respiratory event requiring treatment during IAC. We assessed the presence of decreased lung compliance (characterized by an abrupt decrease in tidal volume); hypoxia (a decrease in saturation of peripheral oxygen [SpO₂] of >10% from baseline or decrease in SpO₂ of <90%); slow-rising nonplateauing capnography; hypotension (a decrease in systolic blood pressure of >20%); bradycardia (a decrease in heart rate of >20%); and cardiac arrest. Events occurring during anesthesia induction or emergence were not considered. If >1 event occurred concomitantly, all of them were registered. In the cases in which cardiorespiratory events were observed, we registered the time and the treatment to alleviate the symptoms.

Statistical Analysis

On the basis on the literature^{5–10} and a previous retrospective pilot study with 100 cases at our institution, the expected percentage of cardiorespiratory events in this population was set at 10%. Considering the number of patients required for a logistic regression analysis with a minimum of 2 covariates in the model, we estimated that 200 patients were required to obtain 20 adverse cardiorespiratory events.

For descriptive purposes, categorical variables were presented through relative and absolute frequencies. According to their distributions, continuous variables were described as means and SDs or median and interquartile ranges. Normality was evaluated through skewness, kurtosis, and graphical methods.

Children with and without cardiorespiratory events were compared using the Pearson χ^2 test, the Fisher exact test, the Welch 2-sample *t* test, or the Wilcoxon rank-sum test, as appropriate. To identify independent predictors of the cardiorespiratory event, we performed a multivariable analysis using logistic regression based on prior knowledge and the results of univariate analysis. The following variables were considered a priori for inclusion in the multivariable models: age, previous procedures, catheter size, bilaterality, and procedural duration. The catheter size was strongly correlated with age, so the catheter size (considered a confounder) was excluded from the multivariable model. The results were expressed as ORs with 95% CIs.

Patients older than 84 months of age could be considered outliers (*n* = 9), so we repeated the analyses excluding them. The results were similar to those with the full sample, which was maintained as the primary analysis.

All analyses were 2-sided, and the final *P* values < .05 were considered significant. All analyses were performed in SPSS statistical software (Version 26.0; IBM) or R statistical and computing software (<http://www.r-project.org/>).

RESULTS

We included 175 treatment sessions (11 bilateral) in 71 children during the study period. In 96 (55%) procedures, the children were female. Overall, the mean age was 29 (SD, 23.21) months. In 22

Table 1: Clinical and demographic characteristics

Characteristic	Overall (n = 175) ^a	No Cardiorespiratory Event (n = 153) ^a	Cardiorespiratory Event (n = 22) ^a	P Value ^b
Female sex	96 (55%)	82 (54%)	14 (64%)	.376
Age (m)	28.93 (23.21)	30.11 (24.17)	20.43 (11.76)	.004
Weight (kg)	13.00 (10.00–15.65)	13.00 (9.90–16.00)	11.30 (10.00–14.50)	.228
Bronchial hyperreactivity	19 (11%)	19 (12%)	0 (0%)	.136
Rhinitis	1 (1%)	1 (1%)	0 (0%)	>.999
Previous bronchiolitis	5 (3%)	5 (3%)	0 (0%)	>.999
Upper respiratory tract infections <15 days	8 (5%)	8 (5%)	0 (0%)	.598
Parental smoking	9 (5%)	7 (5%)	2 (9%)	.315
No clinical history	137 (78%)	117 (76%)	20 (91%)	.169

^a Data are No. (%), mean (SD), median (25th–75th percentiles).

^b Determined by the Pearson χ^2 test; Welch 2-sample t test; Fisher exact test; Wilcoxon rank-sum test.

procedures, we observed a cardiorespiratory event, and they occurred in children significantly younger (20.43 [SD, 11.76] months) than those without this complication (30.11 [SD, 24.17] months) ($P < .05$). This significant difference was not observed in the variable weight (Table 1). Figure 1 demonstrates the predicted risk of a cardiorespiratory event based on age. For a previous respiratory history or symptoms such as upper respiratory tract infection in the past 15 days, we did not find a difference between patients with or without cardiorespiratory events (Table 1).

In 23 (15%) procedures, children were premedicated to alleviate anxiety. The drug was predominantly midazolam. In 151 procedures (88%), children received sevoflurane inhalational induction combined with a propofol bolus and a fentanyl bolus. The total fentanyl mean dose was 3.6 (SD, 3.3) mcg/kg. A single dose of muscle relaxant was administered to facilitate intubation in 83 (48%) procedures. Anesthesia maintenance was achieved with sevoflurane 1.0–1.5 MAC. The mean IAC duration was 80 minutes (interquartile range, 70.00–95.00 minutes), while the mean anesthesia duration was 130.00 minutes (interquartile range, 115.00–150.00 minutes), with no difference observed between patients with or without cardiorespiratory events (Online Supplemental Data).

The most frequent cardiorespiratory event was a decrease in tidal volume, observed in 16 (9%) procedures. This event was primarily treated by improving ventilation with manual or mechanical increases in inspiratory pressure as well as discontinuing the catheterization maneuver. Other cardiorespiratory events and interventions are described in Table 2. Hemodynamic complications such as hypotension or bradycardia were less common. In addition, none of the procedures were interrupted and postponed due to these complications.

Baseline vital signs, measured just before femoral puncture, were similar among patients with or without cardiorespiratory events. Vital signs, EtCO₂, and tidal volume variations before and during the cardiorespiratory event are presented in Fig 2.

Cardiorespiratory events occurred predominantly during internal carotid artery catheterization—primarily in the supraclavicular and cavernous segments—in 14/22 (64%) procedures, followed by ophthalmic artery catheterization in 3/22 (14%) and chemotherapy administration in 4/22 (18%) procedures.

In this study, the median number of previous procedures for IAC was 2.00 (interquartile range, 0.00–3.00). Having undergone a previous IAC did not differ between patients with a cardiorespiratory event (19, 86%) and without this complication (106, 72%). Among the patients with a cardiorespiratory event, 3/22 had never undergone an IAC.

The logistic regression model showed an association between lower age and the cardiorespiratory event, though it was not statistically significant. IAC duration, bilateral procedure, and previous IAC were not predictive variables in this model (Table 3).

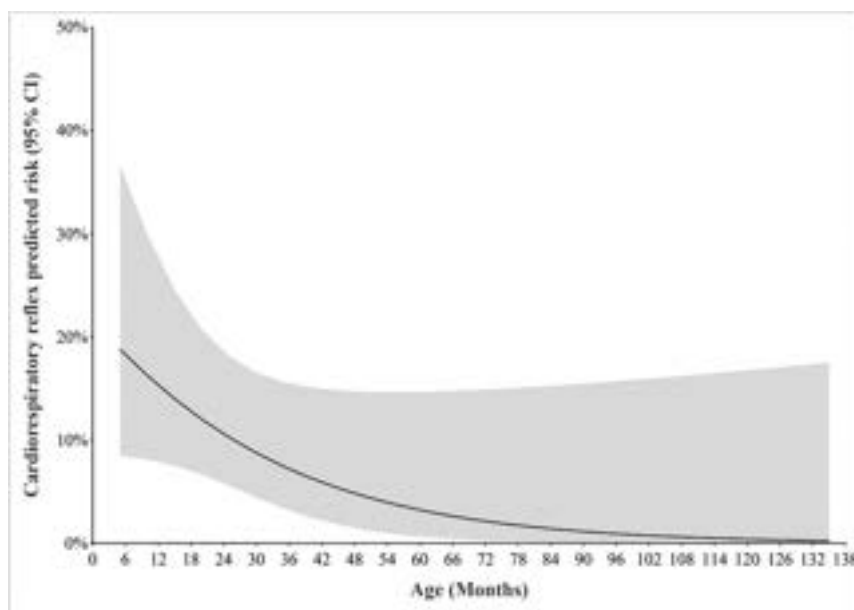


FIG 1. Predicted risk of a cardiorespiratory event based on age.

DISCUSSION

In this study, a cardiorespiratory event was observed in 12.5% of procedures in children with retinoblastoma undergoing IAC. These complications were primarily mild and had a rapid resolution. The median age was lower in the patients with a cardiorespiratory event. Other variables such as bilateral disease

or a previous IAC treatment were not associated with the occurrence of a cardiorespiratory event.

Severe cardiorespiratory events during IAC were demonstrated in 2011 when Gobin et al¹⁰ described reflex bronchospasm during artery catheterization. Lately, some authors have reported an incidence of 10%–25% of severe cardiorespiratory events.^{5,7,8,10} In this study, all procedures were performed by a single experienced interventional neuroradiologist who has performed >1500 IAC procedures in children with retinoblastoma. We believe this long learning curve may have contributed to our incidence in the lower range (12.5%), particularly if mechanoreceptors

Table 2: Adverse cardiorespiratory events and treatment during intra-arterial chemotherapy

Events and Treatment	
Characteristic (n = 175) ^a	
Uneventful	153 (87%)
Reduced tidal volume (>10% from baseline)	16 (9%)
SpO ₂ drop (>10% or below 90% even if transient)	7 (4%)
Change in the capnography curve to an ascending pattern	3 (2%)
Hypotension	5 (3%)
Bradycardia	2 (1%)
Cardiorespiratory arrest	0 (0%)
Treatment (n = 22) ^a	
Manual ventilation	13 (59%)
Increased inspiratory pressure	8 (36%)
Increase in FiO ₂	12 (55%)
Crystalloid bolus	5 (23%)
Atropine	0 (0%)
Epinephrine	4 (18%)
Propofol bolus	2 (9%)
Increased sevoflurane	0 (0%)
Interruption of the procedure	1 (5%)
Neuromuscular blocker administration	0 (0%)
Spontaneous resolution	2 (9%)

Note:—FiO₂ indicates fraction of inspired oxygen.

^aData are No.

play a role in triggering cardiorespiratory events. In our center, anesthesiologists are also trained and experienced in this specific procedure. Therefore, the team can diagnose such complications early, preventing further deterioration.¹⁰

We found an association between younger age and cardiorespiratory events, which was different from the results in other studies.⁸ The older median age of our population (29 versus 20 months) may have led to this finding. Considering that this complication is probably an autonomic reflex response, such as the trigeminal-cardiac and oculo-respiratory reflexes, a higher resting vagal tone in young children may justify this finding. The lack of association between weight and a cardiorespiratory event reinforces the role of autonomic immaturity in the occurrence of this complication.

Some authors have proposed a sensitization of the reflex arc mechanism because patients present with this complication only in the second or subsequent procedures.⁵ In our study, this complication occurred in 3 of the 22 patients who had never undergone this treatment before. This finding is in line with findings in a previous case series.¹¹

In common with Philips et al⁵ and Gobin et al,¹⁰ cardiorespiratory events occurred predominantly during carotid, at the supraclavicular and cavernous segments, and ophthalmic catheterization. We did not observe an association between the type of event (respiratory or cardiovascular) and the catheter site at the moment it was detected.

The protective role of a high anesthetic depth on the occurrence of autonomic reflexes is well-established.^{12,13} However, Nghe et al⁸ observed a high incidence (20%) of serious cardiorespiratory events during IAC, despite deep anesthesia. Unfortunately, we did not assess the depth of anesthesia in this study, though patients received standardized sevoflurane maintenance with 1.0–1.5 MAC adjusted for age.

The cardiorespiratory events were predominantly an abrupt decrease in lung compliance followed by a mild decrease in the SpO₂ treated with manual positive pressure with resolution in seconds or a few minutes. None of the IACs were interrupted and postponed after a severe cardiorespiratory event, different from the situation in other case series.^{5,8}

This study confirms earlier findings that may help to predict cardiorespiratory events during IAC, such as the most probable moment (carotid and ophthalmic catheterization). Therefore, anesthesiologists can be aware and ready to treat this potentially life-threatening condition. The lower age in patients who developed this event and a trend toward an association between lower age and the event also help to identify patients at risk.

Some limitations of this study are inherent to its observational nature, so we cannot assume the associated factor as causative. Additionally, we believe anesthesia management may affect the incidence of cardiorespiratory events, and the lack of anesthesia standardization in our study may hamper its reproducibility. A clinical trial testing the effect of a

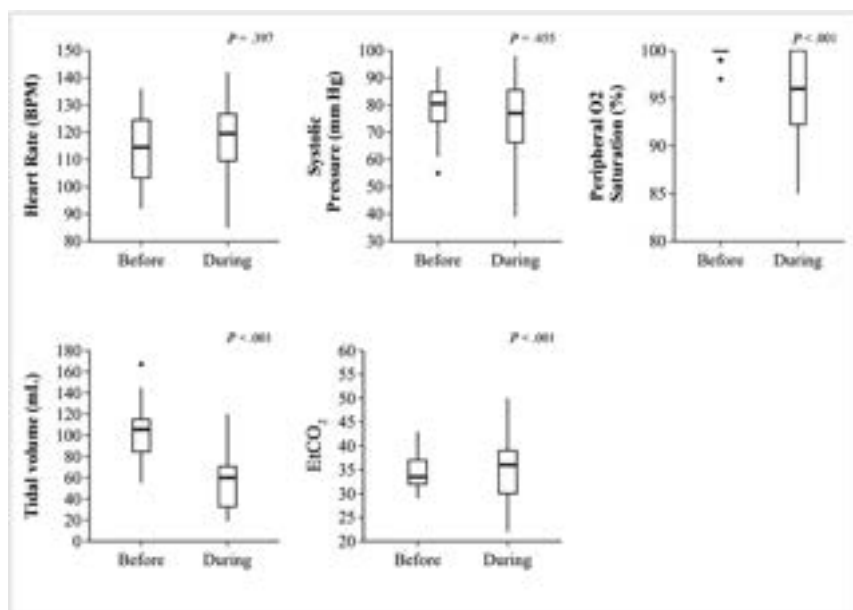


FIG 2. Vital signs and respiratory parameters measured before (immediately before femoral puncture) and during the cardiorespiratory event. BPM indicates beats per minute.

Table 3: Logistic regression model assessing age, IAC duration, bilateral procedure, and previous IAC as risk factors for cardiorespiratory events

Characteristic	OR	95% CI	P Value
Age (mo)	0.96	0.92–1.00	.079
IAC duration	1.00	0.98–1.02	.825
Bilateral IAC	0.63	0.03–3.85	.672
Previous IAC	2.69	0.84–12.1	.133

neuromuscular blockade on the incidence of cardiorespiratory events would also provide further elucidation about cause-effect mechanisms.

CONCLUSIONS

In children undergoing IAC for retinoblastoma treatment, cardiorespiratory events were observed in 12.5% of procedures. Lower ages were associated with this complication occurrence. Although predominantly mild and with a rapid resolution, these events should have prompt diagnosis and treatment to prevent further deterioration and worse outcomes.

Disclosure forms provided by the authors are available with the full text and PDF of this article at www.ajnr.org.

REFERENCES

1. Fabian ID, Abdallah E, Abdullahi SU, et al; Global Retinoblastoma Study Group. **Global retinoblastoma presentation and analysis by national income level.** *JAMA Oncol* 2020;6:685–95 CrossRef Medline
2. Schaiquevich P, Francis JH, Cancela MB, et al. **Treatment of retinoblastoma: what is the latest and what is the future.** *Front Oncol* 2022;12:822330 CrossRef Medline
3. PDQ Pediatric Treatment Editorial Board. **Retinoblastoma Treatment (PDQ®): Health Professional Version.** April 11, 2023. In: *PDQ Cancer*

Information Summaries. Bethesda (MD): National Cancer Institute (US); 2002 Medline

4. Silvera VM, Guerin JB, Brinjikji W, et al. **Retinoblastoma: what the neuroradiologist needs to know.** *AJNR Am J Neuroradiol* 2021;42:618–26 CrossRef Medline
5. Phillips TJ, McGuirk SP, Chahal HK, et al. **Autonomic cardio-respiratory reflex reactions and superselective ophthalmic arterial chemotherapy for retinoblastoma.** *Paediatr Anaesth* 2013;23:940–45 CrossRef Medline
6. Harris EA, Gaynor B. **Trigemino-cardiac reflex after direct infusion of chemotherapy into the ophthalmic artery for retinoblastoma.** *Journal of Clinical & Experimental Ophthalmology* 2014;05:365 CrossRef
7. Kato MA, Green N, O'Connell K, et al. **A retrospective analysis of severe intraoperative respiratory compliance changes during ophthalmic arterial chemosurgery for retinoblastoma.** *Paediatr Anaesth* 2015;25:595–602 CrossRef Medline
8. Nghe MC, Godier A, Shaffii A, et al. **Prospective analysis of serious cardiorespiratory events in children during ophthalmic artery chemotherapy for retinoblastoma under a deep standardized anesthesia.** *Paediatr Anaesth* 2018;28:120–26 CrossRef Medline
9. Scharoun JH, Han JH, Gobin YP. **Anesthesia for ophthalmic artery chemosurgery.** *Anesthesiology* 2017;126:165–72 CrossRef Medline
10. Gobin YP, Dunkel IJ, Marr BP, et al. **Intra-arterial chemotherapy for the management of retinoblastoma: four-year experience.** *Arch Ophthalmol* 2011;129:732–37 CrossRef Medline
11. Harris EA. **Letter to the Editor regarding 'Autonomic cardio-respiratory reflex reactions and superselective ophthalmic arterial chemotherapy for retinoblastoma' by Phillips, McGuirk, Chahal.** *Paediatr Anaesth* 2014;24:229–30 CrossRef Medline
12. Yi C, Jee D. **Influence of the anaesthetic depth on the inhibition of the oculocardiac reflex during sevoflurane anaesthesia for paediatric strabismus surgery.** *Br J Anaesth* 2008;101:234–38 CrossRef Medline
13. Meuwly C, Chowdhury T, Sandu N, et al. **Anesthetic influence on occurrence and treatment of the trigemino-cardiac reflex: a systematic literature review.** *Medicine (Baltimore)* 2015;94:e807 CrossRef Medline

Correlation between Multiparametric MR Imaging and Molecular Genetics in Pontine Pediatric High-Grade Glioma

V. Rameh, S. Vajapeyam, A. Ziaei, P. Kao, W.B. London, S.J. Baker, J. Chiang, J. Lucas, C.L. Tinkle, K.D. Wright, and T.Y. Poussaint



ABSTRACT

BACKGROUND AND PURPOSE: Molecular profiling is a crucial feature in the “integrated diagnosis” of CNS tumors. We aimed to determine whether radiomics could distinguish molecular types of pontine pediatric high-grade gliomas that have similar/overlapping phenotypes on conventional anatomic MR images.

MATERIALS AND METHODS: Baseline MR images from children with pontine pediatric high-grade gliomas were analyzed. Retrospective imaging studies included standard precontrast and postcontrast sequences and DTI. Imaging analyses included median, mean, mode, skewness, and kurtosis of the ADC histogram of the tumor volume based on T2 FLAIR and enhancement at baseline. Histone H3 mutations were identified through immunohistochemistry and/or Sanger or next-generation DNA sequencing. The log-rank test identified imaging factors prognostic of survival from the time of diagnosis. Wilcoxon rank-sum and Fisher exact tests compared imaging predictors among groups.

RESULTS: Eighty-three patients had pretreatment MR imaging and evaluable tissue sampling. The median age was 6 years (range, 0.7–17 years); 50 tumors had a K27M mutation in *H3-3A*, and 11, in *H3C2/3*. Seven tumors had histone H3 K27 alteration, but the specific gene was unknown. Fifteen were H3 wild-type. Overall survival was significantly higher in *H3C2/3*- compared with *H3-3A*-mutant tumors ($P = .003$) and in wild-type tumors compared with any histone mutation ($P = .001$). Lower overall survival was observed in patients with enhancing tumors ($P = .02$) compared with those without enhancement. *H3C2/3*-mutant tumors showed higher mean, median, and mode ADC_{total} values ($P < .001$) and ADC_{enhancement} ($P < .004$), with lower ADC_{total} skewness and kurtosis ($P < .003$) relative to *H3-3A*-mutant tumors.

CONCLUSIONS: ADC histogram parameters are correlated with histone H3 mutation status in pontine pediatric high-grade glioma.

ABBREVIATIONS: DIPG = diffuse intrinsic pontine glioma; DMG = diffuse midline glioma; HGG = high-grade glioma; *IDH* = isocitrate dehydrogenase; OS = overall survival; PG = postgadolinium; pHGG = pediatric-type high-grade glioma

Diffuse intrinsic pontine glioma (DIPG) is defined as an expansile T1-hypointense, T2-hyperintense nonenhancing pontine tumor involving at least 50% of the ventral pons and engulfing the basilar artery.^{1–3} These tumors were reclassified in

the 2021 World Health Organization classification of CNS tumors, emphasizing that molecular features are as essential as histology in diagnosing pontine tumors.^{3,4} Numerous molecular changes of clinicopathologic utility were incorporated, and the designation of a subset of tumors formerly called DIPG as H3 K27–altered diffuse midline glioma highlights the importance of this mutation in defining a disease entity.^{2,3}

Pontine H3 K27–altered diffuse midline glioma (DMG) is an aggressive pediatric-type high-grade glioma (pHGG) with a median age at diagnosis of 6–7 years and a poor prognosis, with <10% overall survival (OS) of >2 years.^{5–7} The diagnosis has historically been based on clinical and MR imaging characteristics.¹ Surgery was not considered an option due to the location and infiltrative nature of the tumor, and biopsy was uncommonly performed after weighing risks and benefits.⁸

Recently, feasible and safe biopsies and postmortem examinations have led to a greater understanding of the unique genetic profiles of these tumors and the consequent identification of new

Received March 9, 2023; accepted after revision May 22.

From the Department of Radiology (V.R., S.V., A.Z., T.Y.P.), Boston Children's Hospital, Harvard Medical School, Boston, Massachusetts; Department of Pediatric Oncology (P.K., W.B.L., K.D.W.), Dana-Farber Cancer Institute, Harvard Medical School, Boston, Massachusetts; and Departments of Developmental Neurobiology (S.J.B.), Pathology (J.C.), and Radiation Oncology (J.L., C.L.T.), St. Jude Children's Research Hospital, Memphis, Tennessee.

This work was supported, in part, by the American Lebanese Syrian Associated Charities and the National Cancer Institute grant P30 CA021765 (St. Jude Cancer Center support grant) and P01 CA096832.

Please address correspondence to Tina Young Poussaint, MD, Department of Radiology, Boston Children's Hospital, 300 Longwood Ave, Boston, MA 02115; e-mail: tinayoung.poussaint@childrens.harvard.edu; @TYPoussaintMD; @vanessaramerh

Indicates open access to non-subscribers at www.ajnr.org

Indicates article with online supplemental data.

<http://dx.doi.org/10.3174/ajnr.A7910>

potential therapeutic targets.⁹⁻¹¹ Specifically, the somatic mutations of histone H3 genes (*H3-3A* and *H3C2/3*), leading to their protein products H3.3 and H3.1, respectively, and the substitution of a lysine for methionine have been identified. Up to 90% of pontine high-grade gliomas (HGGs) have an H3 mutation, with ~65% in *H3-3A* and ~25% in *H3C2/3*. Approximately 10% of pontine HGGs lack an H3 mutation.^{5,10,12-14} Advances in “liquid biopsy,” namely the ability to detect these mutations in circulating tumor DNA or CSF tumor DNA, may enable noninvasive testing of molecular profiling in DMG and longitudinal monitoring when the patient is on therapy.^{15,16}

Prior investigators identified certain MR imaging features associated with worse prognosis in pontine HGGs, such as shorter survival in patients with lower mean ADC histogram values, a lower Cho/Cr ratio on MRS, and the presence of the H3 K27 alteration.¹⁷⁻¹⁹

It is now increasingly understood that different genomic alterations in histone H3 isoforms result in tumors with variable behavior and clinical prognosis, including differences between *H3C2/3*- and *H3-3A*-mutant tumors.²⁰⁻²²

To date, few studies have elucidated these differences using radiogenomic methods. This emerging technique uses primarily pretreatment baseline multiparametric MR imaging features and correlates them with pathologic and molecular data obtained from a specific tissue biopsy site.^{12,18,23-26} Furthermore, a more recently described, multimodel approach proposed the use of MR imaging radiomics and clinical data to predict at least 1 of 3 important mutations (*H3.1*, *ACVRI*, and *TP53*) in pontine pHGGs. This efficient model can be used with the absence of data on biopsy and/or genetic results.²⁷

In this study, we correlated different baseline MR imaging features and OS in pontine pHGG subtypes with molecular parameters using ADC histogram analyses in a large cohort of children newly diagnosed with pontine HGG who underwent tissue sampling.

MATERIALS AND METHODS

Subjects

This was a retrospective study approved by the institutional review board and performed in accordance with the Declaration of Helsinki. All consecutive patients who were clinically diagnosed with DIPG or pontine DMG at the time of presentation at St. Jude Children’s Research Hospital between 2002 and 2019 and had postmortem or biopsy data and baseline MR images were included. Each patient underwent histologic tumor evaluation at postmortem examination following unsuccessful therapy and/or stereotactic biopsy before initiation of treatment, with the choice of biopsy site left to the neurosurgeon’s discretion.

Immunohistochemistry or next-generation DNA sequencing or both were used to identify histone H3 mutations, as previously described.²⁸ We defined 4 H3 mutation groups: 1) *H3-3A* K27-mutant; 2) *H3C2/H3C3* K27-mutant; 3) H3 K27-mutant, specific genes were unknown; and 4) H3 wild-type. The latter may include pHGG (DMG, H3 K27-altered, subtype H3 wild-type with *EZH1P* overexpression, and pHGG, H3 wild-type and isocitrate dehydrogenase [*IDH*] wild-type) or adult-type diffuse glioma (astrocytoma, *IDH* mutant and glioblastoma, *IDH* wild-type).³ Overall survival was measured for all patients, calculated as the length of time from diagnosis to death and/or the last follow-up.

Imaging Analysis

Baseline MR imaging of the brain was used for analysis as previously described.²⁴ MR imaging examinations were performed primarily (94%) on Siemens MR imaging scanners and the remaining on GE Healthcare scanners. Scanner details are provided in the Online Supplemental Data. The protocol included sagittal T1, axial T2, precontrast axial T2 FLAIR, axial DTI, and postgadolinium (PG) 3D T1.

Volumetric analysis of the tumor was obtained by generating 3D ROIs on a Vitrea workstation (Canon Medical) using Vital 3D Medical Imaging software (Access Radiology) on the anatomic sequences. This procedure was performed on the T2 FLAIR imaging by delineating the abnormal T2-hyperintense signal seen in the pons. When T2 FLAIR was unavailable, this parameter was estimated using a 2D T2 TSE sequence. The volume of enhancing tumor was assessed on the PG 3D T1 sequence.

ADC maps from the DTI data were generated on the scanner in most cases and off-line using OsiriX (Pixmeo SARL) when scanner-generated ADC maps were not available. To generate the ADC histogram, we registered ADC maps to the anatomic sequence of interest (T2 FLAIR or T2 and PG T1) using tools from the FSL library (<http://www.fmrib.ox.ac.uk/fsl>),²⁹ previously described by Poussaint et al.¹⁷ In summary, $b = 0$ (and subsequently the ADC map) was transformed into the space of the anatomic sequences, and 3D ROIs were created using the thresholding feature in Fiji (<http://fiji.sc>),³⁰ an Open Source (<https://opensource.org/>) distribution of Java modules along with ImageJ software (National Institutes of Health). Values from every pixel in the tumor volume from the ADC map were then extracted, and histograms were generated. Within each tumor, values of the mean, SD, median, mode, skewness, and kurtosis of the ADC histogram for the total tumor volume (referred to as ADC_total) and the enhancing tumor volume (referred to as ADC_enhancement) were used for statistical analysis. The choice of these ADC histogram metrics was based on previous studies.^{14,19}

Statistical Analysis

Clinical and demographic variables were summarized using descriptive statistics. Continuous measures were summarized using medians and ranges. Categorical measures were summarized using frequencies and proportions. Kaplan-Meier curves of OS were generated, and point estimates of OS \pm standard error were presented at 6, 12, and 18 months. The histone H3 mutation groups were tested for association with OS using a log-rank test. Continuous variables (mean ADC_total, median ADC_total, mode of ADC_total, mean ADC_enhancement, and median ADC_enhancement) were dichotomized on the median value and tested for association with OS using a log-rank test. The Wilcoxon rank-sum test was used to compare continuous imaging predictors between categorical end points of the histone mutation groups. The Fisher exact test was used to compare categorical imaging predictors (presence/absence of tumor volume enhancement versus molecular subgroup). Two-sided P values $\leq .05$ were considered statistically significant. Given the hypothesis-generating nature of these analyses, no adjustment for multiple hypothesis testing was performed. R statistical and computing

Table 1: Baseline characteristics of patients with pontine pHGG (n = 83)

Patient Characteristic	No. (%) or Median (Range)
Sex	
Male	43 (52)
Female	40 (48)
Race	
White	60 (72)
Black	19 (23)
Other	4 (5)
Age at registration (yr)	6 (0.7–17)
Histone mutation status	
H3-3A	50 (60)
H3C2/3	11 (13)
Wild-type	15 (18)
H3 K27–altered, specific gene unknown	7 (8)
Presence of enhancement	
Yes	54
No	25
Unknown	4
Median follow-up time of surviving patients (mo)	10.3 (2.3–76.2)

software Version 3.5.0 (<http://www.r-project.org>) and SAS Version 9.4 (SAS Institute) were used for statistical analyses.

RESULTS

Patient Population Characteristics

There were 305 consecutively treated children with suspected pontine pHGG. Eighty-three patients met the eligibility criteria with MR imaging features of pontine pHGG on pretreatment MR imaging and evaluable tissue sampling. Of the 83 patients in the study, biopsy samples were obtained from 26 patients, and postmortem material, from 50 patients for genetic testing. Of these, 73 patients had evaluable DTI data at baseline (Online Supplemental Data) and were included for all ADC histogram analyses. In addition, 29 of 73 patients were treated during the study time period (September 2002 to December 2009).

The median age and follow-up time were 6 years (range, 0.7–17 years) and 10.3 months (range, 2.3–76.2 months), respectively.

The cohort consisted of 43 (52%) male and 40 (48%) female patients, of whom 23 (28%) were nonwhite. H3 K27–altered tumors were categorized as follows in Table 1: H3-3A ($n = 50$; 60%), H3C2/3 ($n = 11$; 13%), H3-mutant specific gene unknown ($n = 7$; 8%), and wild-type ($n = 15$; 18%).

Histone Mutation, Overall Survival, and ADC Histogram Metrics

The mean OS at 12 months for all patients was 37% [SD, 5.5%] (Online Supplemental Data).

Children with H3C2/3-mutant tumors ($n = 11$) had significantly higher OS compared with those with H3-3A mutation ($n = 50$) (73% [SD, 13.4%] versus 17 [SD, 5.6%] at 1 year, respectively; $P = .003$) (Online Supplemental Data and Fig 1A). Those patients with H3 wild-type HGG tumors ($n = 15$) had significantly higher OS compared with H3C2/3- and H3-3A-mutant tumors (63% [SD, 13.3%] versus 32% [SD, 5.8%] at 1 year, respectively; $P = .001$) (Online Supplemental Data and Fig 1B).

The OS was significantly lower in patients with enhancing tumors compared with patients whose tumors showed no enhancement (29% [SD, 6.5%] versus 56% [SD, 10%] at 1 year, respectively; $P = .02$) (Online Supplemental Data).

However, there was no statistical association between histone H3 mutation groups and the presence of enhancement: $P = .2$ for the association of enhancement and histone mutations (H3-3A versus H3C2/3) and $P = .7$ for the association of enhancement with any histone mutation versus wild-type.

When we compared group median values, the H3-3A-mutant group ($n = 46$) demonstrated lower values of mean ADC_{total} ($P < .001$), median ADC_{total} ($P < .001$), mode ADC_{total} ($P < .001$), mean (PG) ADC_{enhancement} ($P = .004$), median (PG) ADC_{enhancement} ($P = .003$), and mode (PG) ADC_{enhancement} ($P = .002$) compared with the H3C2/3-mutant group ($n = 9$) (Table 2 and Fig 2A). Skewness ADC_{total} ($P = .003$) and kurtosis ADC_{total} ($P = .002$) were significantly higher in H3-3A- versus H3C2/3-mutant tumors (Table 2 and Fig 2B).

There was no significant difference in ADC histogram metrics between H3 wild-type ($n = 12$) and mutant tumors ($n = 61$), even though the survival of patients with wild-type tumors was significantly longer (Table 3).

Histone Mutation and Tumor Volume

The total tumor volume varied among mutation groups; however, these differences did not meet statistical significance ($P = .2$ and 0.8, respectively) (Tables 2 and 3). No significant differences in the volume of tumor enhancement were identified between the various mutational profiles (H3-3A versus H3C2/3 ($P = .6$) and any histone H3 mutation versus wild-type ($P = .4$) (Tables 2 and 3).

DISCUSSION

Advances in genomic and epigenetic analyses have led to an improved understanding of the clinical and biologic behavior of pontine HGGs.¹³ The discovery of histone H3 mutations in 70%–84% of pontine pHGGs was an important turning point in our understanding of this tumor.^{10,31–33} Clinoradiologic and prognostic criteria were then refined with histone H3 genotyping because mutations in the H3-3A- and H3C2/3 genes correlate with different phenotypical and biologic behaviors and differences in OS.^{20,25} Prior work by Jaimes et al²⁴ demonstrated differences in ADC histogram parameters and enhancement among various histone mutations of pontine HGG. This radiogenomic tool offers a framework for differentiating these alterations non-invasively and, most important, identifying those that have a worse overall survival. In this study, we examined whether radiomics could distinguish among molecular subtypes of pontine pHGG with similar/overlapping phenotypes on conventional anatomic MR images and with ADC histogram parameters.^{17,18,24} ADC values in this study were all derived from DTI data rather than routine clinical DWIs.

Correlations among ADC values, tumor cellularity, and response to treatment in low-grade and high-grade pediatric brain tumors have been previously studied.^{34–36} The ADC histogram is a valuable tool for describing diffusion characteristics in the total tumor volume on T2 FLAIR and postcontrast T1-weighted images.

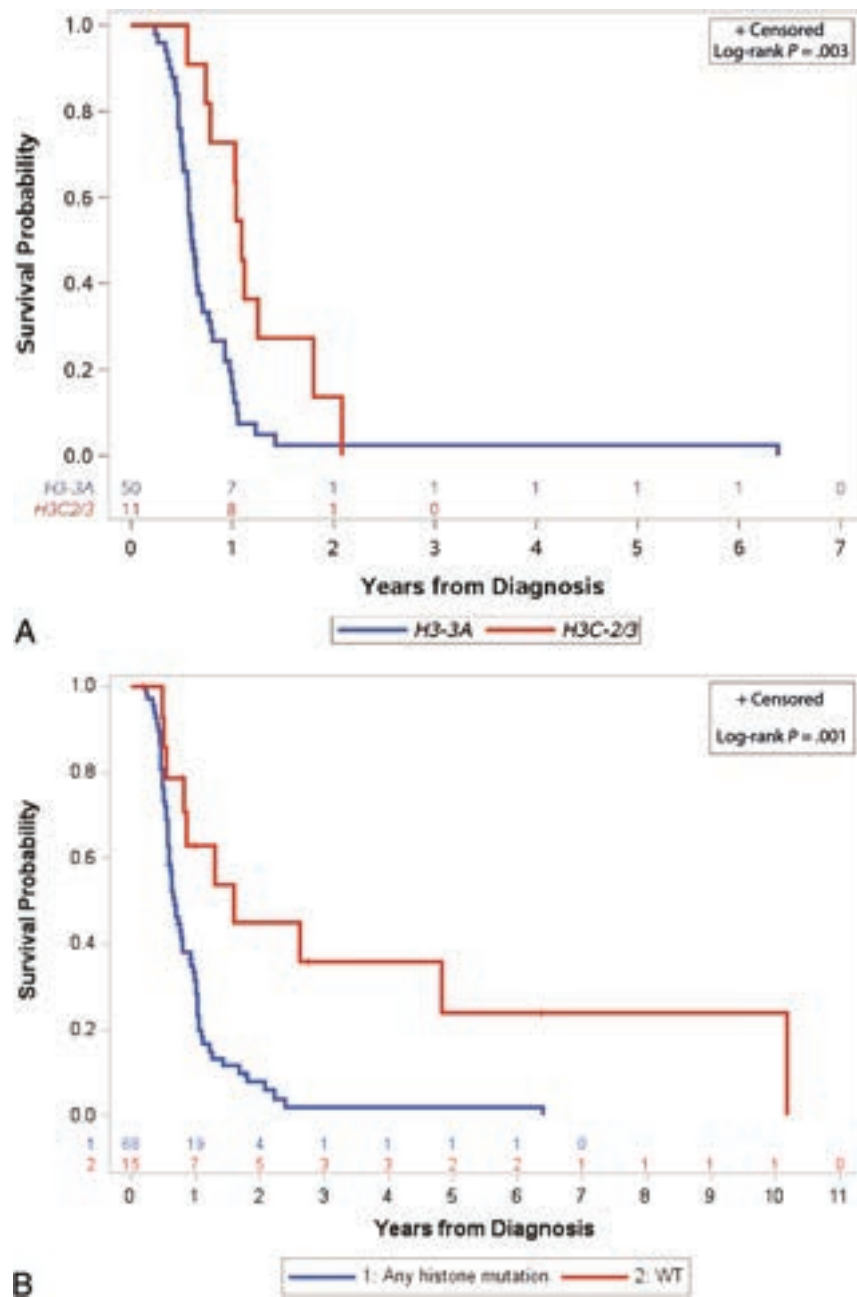


FIG 1. Differences in OS between variant histone profiles. A, Kaplan-Meier curves of a patient's OS by histone H3 mutation: *H3-3A* ($n = 50$) versus *H3C2/3* ($n = 11$). B, Kaplan-Meier curves of OS for patients with tumors with histone H3 mutation (*H3-3A*, *H3C2/3*, and H3-mutant, specific gene unknown) ($n = 68$) versus H3 wild-type ($n = 15$) tumors.

Key ADC histogram metrics found to correlate with survival, treatment response, and mutational status are the mean, SD, median, mode, skewness, and kurtosis of the ADC histogram for the total tumor volume and the enhancing tumor volume.^{17,24} This study focuses on those ADC metrics in our statistical analyses to limit the number of comparisons, thereby increasing statistical power. Poussaint et al¹⁷ previously studied the correlation between ADC histogram metrics and progression-free survival in patients with pontine HGGs. Although tumor molecular characteristics were not studied in the aforementioned work, the authors found 2 peak histogram distributions (unimodal and bimodal), with the unimodal peak increased skewness likely due to increasing cellularity.

Poussaint et al also reported that the mean ADC was lower in children with shorter survival. Chen et al³⁷ found a negative correlation between fractional anisotropy and survival, and although the correlation between ADC histograms and tumor profiles was not studied, one may extrapolate that lower ADC values correlated with more aggressive tumor behavior.

Castel et al²⁰ reported that MR imaging features correlated histologically with extensive extracellular edema, present primarily within *H3C2/3*- compared with *H3-3A*-mutant tumors. ADC values were lower in *H3-3A*-mutant tumors, concurring with this work. This may be attributed to the differences in the oncogenic mechanisms of these alterations. Jaimes et al²⁴ suggested that

Table 2: Association of measures of continuous imaging features with variant histone H3–altered tumors

Imaging Metric	H3-3A		H3C2/3		P Value ^a
	No.	Median (Range)	No.	Median (Range)	
ADC total ($\times 10^{-6}$ mm ² /s)					
Mean	46	1227.51 (538.06–1710.88)	9	1586.56 (1224.37–1797.58)	.001
Median	46	1185 (532–1755)	9	1654 (1215–1842)	.001
Mode	46	1168.14 (450.92–1902.53)	9	1703.88 (1263.52–1961.24)	.001
Skewness	38	0.91 (–0.49–2.16)	9	–0.20 (–0.89–0.88)	.003
Kurtosis	38	1.57 (–0.60–9.71)	9	0.40 (–0.78–1.79)	.002
ADC_enhancement ($\times 10^{-6}$ mm ² /s)					
Mean	33	1138.81 (689.44–1509.96)	7	1390.54 (1033.58–1898.26)	.004
Median	33	1085 (667–1532)	7	1364 (995–1890)	.003
Mode	33	1012.56 (577.86–1617.56)	7	1393.38 (966.31–1746.86)	.002
Skewness	31	1.27 (–0.56–2.82)	7	0.52 (–0.71–2.61)	.1
Kurtosis	31	2.08 (–0.94–13.03)	7	0.85 (–0.84–9.09)	.3
FLAIR/T2/T1 PG volume ($\times 10^3$ mm ³)					
FLAIR/T2	44	35.75 (7.97–77.53)	10	41.10 (22.84–77.57)	.2
Enhancing	32	1.90 (0.07–14.10)	9	5.04 (0.04–8.25)	.6

^a Wilcoxon rank-sum test.

increased cellularity was the reason for the increased kurtosis and skewness in *H3-3A*-mutant tumors compared with *H3C2/3*-mutant tumors.

Calmon et al¹² also reported that *H3C2/3*-mutant tumors had higher ADC values than *H3-3A*-mutant tumors in 27 patients who underwent pretreatment MR imaging and biopsy for their pontine pHGGs. They also hypothesized that *H3C2/3*-mutant tumors demonstrated increased extracellular edema due to ion channel gene downregulation.¹² A higher positive nuclear density was noted relative to *H3C2/3*-mutant tumors, which they postulated may be secondary to interstitial edema differences. However, they did not perform quantitative analysis of the edema, and their study focused on only the biopsied sample of the tumor and not the total tumor volume. Furthermore, the *H3C2/3*- and *H3-3A*-mutant tumors showed associated histologic differences, with the former containing mesenchymal glioblastoma subtypes and astroglial cells and the latter containing proneural glioblastoma multiforme and oligodendrocytic signatures.²⁰

Our analysis of ADC histogram metrics in *H3-3A*-mutant pontine pHGGs demonstrates significantly lower mean and median ADC values of total tumor volume with higher skewness and kurtosis than the *H3C2/3*-mutant tumors, concurring with the findings of Jaimes et al.²⁴ Our study reports no significant difference between ADC histogram metrics of wild-type and H3 K27–mutant profiles, consistent with the study published by Jaimes et al and Castel et al.³⁸ This result is likely related to the similar biologic phenotype of these 2 profiles with the loss of H3 K27 trimethylation. In addition, the heterogeneous nature of these tumors may also be a valid contributor. Pertinent to this study, Aboian et al^{18,26} previously found no statistically significant association between the MR imaging characteristics of pontine wild-type or H3 K27–altered HGGs, specifically edema, enhancement, necrosis, and the infiltrative nature of the tumors.

Piccardo et al²² found a statistical correlation between MR imaging parameters such as DWI, spectroscopy, and perfusion in pontine HGGs. Significantly lower ROI ADC values were found in H3 K27–altered tumors compared with H3 wild-type.

Their sample size was small and included HGGs in all locations, not just the pons. Furthermore, all the H3 K27–altered tumors included in their 22-patient cohort were *H3-3A*-mutant.

As mentioned previously and similar to the results published by Khuong-Quang et al,³² we found that children with H3 wild-type HGGs have significantly higher OS compared with those with *H3-3A*- and *H3C2/3*-mutant tumors. We also found that children with *H3C2/3*-mutant tumors had significantly higher OS than those with an *H3-3A* mutation. This finding is concordant with the work of Castel et al,²⁰ which demonstrated that OS differs significantly between histone H3 alterations. *H3C2/3*-mutant tumors have an overall better prognosis because they tend to metastasize less frequently and may respond better to radiation therapy.

Similar results were reported in the studies by Calmon et al¹² and Jaimes et al,²⁴ who studied 27 and 50 patients with DIPGs, respectively. Additionally, patients with *H3C2/3*-mutant tumors tended to present at a younger age, approximately 2 years younger than patients with *H3-3A*-mutant tumors.¹²

In our cohort, enhancement was associated with a significantly worse OS, confirming previous studies.^{17,24} However, the total tumor volume seen on T2 FLAIR or volume of enhancement was not significantly associated with OS. Similar to findings of Jaimes et al²⁴ and Calmon et al,¹² differences in enhancing volumes were higher, though not significantly, in *H3C2/3*- compared with *H3-3A*-mutant tumors, with the latter carrying a worse prognosis. This finding is likely multifactorial and may be explained by higher microvascular density and perhaps increased vascular/contrast leakage in *H3C2/3*, though also not statistically significant, and may not adequately reflect the internal milieu in these tumors.¹²

Our study has several limitations. All of the tumors in our cohort are pontine pHGGs, and future work will have to include HGGs in other locations. While our sample size is the largest to date to study associations of ADC histogram metrics with histone H3 gene alterations in pontine HGGs, these results should be validated in larger, prospective studies, given the breakdown in histone-altered tumor subsets. Second, we

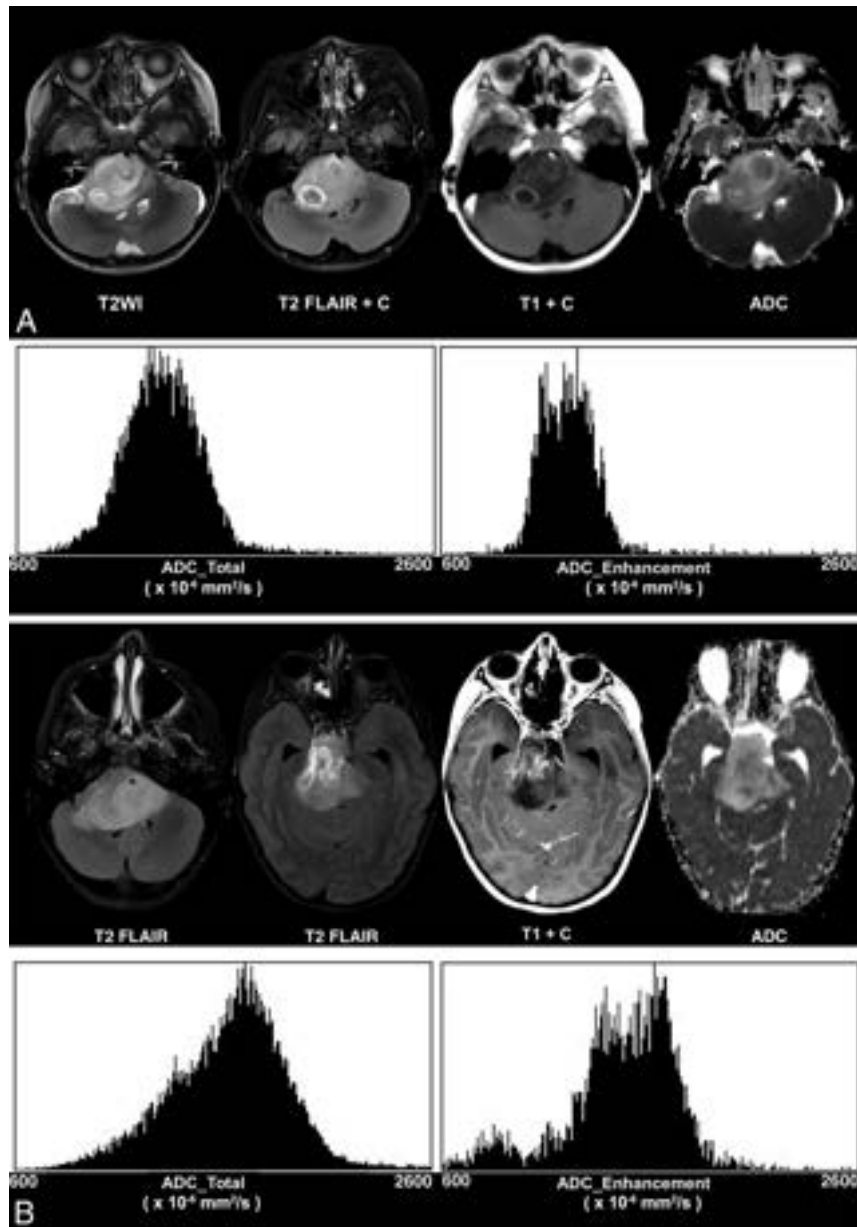


FIG 2. Differences in ADC histogram parameters among histone H3 K27–altered tumors. *H3-3A*-mutant tumor (A) shows lower ADC_{total} mode ($1252.531 \times 10^{-6} \text{ mm}^2/\text{s}$), higher ADC_{total} skewness (0.673), and higher ADC_{total} kurtosis (2.721) relative to *H3C2/3*-altered tumor (B) (ADC_{total} mode: $1703.875 \times 10^{-6} \text{ mm}^2/\text{s}$; ADC_{total} skewness: -0.231 ; and ADC_{total} kurtosis: 0.399). *H3-3A*-mutated tumor (A) shows lower mean (PG) ADC_{enhancement} ($1216.092 \times 10^{-6} \text{ mm}^2/\text{s}$), median (PG) ADC_{enhancement} ($1206 \times 10^{-6} \text{ mm}^2/\text{s}$), and mode (PG) ADC_{enhancement} ($1103.723 \times 10^{-6} \text{ mm}^2/\text{s}$), relative to *H3C2/3*-mutated tumor (B): mean (PG) ADC_{enhancement} ($1461.677 \times 10^{-6} \text{ mm}^2/\text{s}$), median (PG) ADC_{enhancement} ($1500 \times 10^{-6} \text{ mm}^2/\text{s}$), and mode (PG) ADC_{enhancement} ($1665.322 \times 10^{-6} \text{ mm}^2/\text{s}$). A, A 3-year-old girl with *H3-3A*-mutant diffuse midline glioma and OS = 217 days. B, An 8-year-old girl with *H3C2/3*-mutant diffuse midline glioma and OS = 761 days.

did not perform a direct correlation to the histologic data or include advanced imaging techniques such as perfusion in our multiparametric MR imaging analysis. Third, we did not test for *EZH1P* overexpression and *IDH1/2* mutations in our tumor samples and did not perform DNA methylation profiling for tumor subtyping; therefore, we cannot distinguish different tumor subtypes in our H3 wild-type category. Finally, the studies in this retrospective analysis were performed during 18 years and on multiple scanners at the same institution. ADC values have been found to be fairly consistent across scanner types and strengths in both in vivo³⁹ and in phantom studies,⁴⁰ and the

ADC values found in this study are consistent with those in the literature.^{17,24} However, the possible variability of ADC values derived from DTI data from multiple scanners may still be a limitation of this study.

Future work may incorporate machine learning algorithms on large data sets to expand our knowledge of the biologic features of these tumors. Wagner et al⁴¹ found radiomics features on standard MR imaging that were associated with progression-free survival in pediatric diffuse pontine glioma not based on mutational status. Future applications could incorporate mutational analyses in a larger data set.

Table 3: Association of measures of continuous imaging features with variant histone H3–altered versus H3 wild-type tumors

Imaging Metric	Any Histone Mutation		Wild-Type		P Value ^a
	No.	Median (Range)	No.	Median (Range)	
ADC total ($\times 10^{-6}$ mm ² /s)					
Mean	61	1302.42 (538.06–1797.58)	12	1350.77 (922.96–1729.62)	.98
Median	61	1245 (532–1842)	12	1345 (917–1781)	.97
Mode	61	1250.51 (450.92–1961.24)	12	1305.29 (863.39–1805.47)	.9
Skewness	52	0.68 (–0.89–3.11)	11	0.98 (–0.30–2.57)	.3
Kurtosis	52	1.4 (–0.78–15.62)	11	2.82 (–0.78–10.77)	.1
ADC_enhancement ($\times 10^{-6}$ mm ² /s)					
Mean	45	1152.88 (689.44–1898.26)	6	1199.86 (956.62–1723.18)	.7
Median	45	1142.00 (667–1890)	6	1187.00 (807–1762)	.7
Mode	45	1062.49 (577.86–1746.86)	6	1175.10 (719.70–1805.78)	.6
Skewness	43	0.86 (–0.85–4.73)	6	0.67 (–0.14–1.86)	.7
Kurtosis	43	1.69 (–0.94–29.06)	6	1.35 (0.098–12.45)	.9
FLAIR/T2/T1 PG volume ($\times 10^3$ mm ³)					
FLAIR/T2	60	35.13 (7.97–77.57)	13	32.77 (10.13–79.62)	.8
Enhancing	46	1.96 (0.04–14.10)	8	1.95 (0.01–4.71)	.4

^a Wilcoxon rank-sum test.

CONCLUSIONS

MR imaging features, including ADC histogram metrics, are different across *H3C2/3-*, *H3-3A*-mutant, and H3 wild-type pontine HGGs. Future advances in noninvasive imaging approaches will seek to improve our understanding of the biology and physiology of these aggressive tumors and will help prognosticate survival.

ACKNOWLEDGMENTS

This work is in memory of our wonderful friend and colleague Zoltan Patay, MD, PhD, who contributed to this work and was dedicated to improving the health of children everywhere.

Disclosure forms provided by the authors are available with the full text and PDF of this article at www.ajnr.org.

REFERENCES

- Barkovich AJ, Krischer J, Kun LE, et al. **Brain stem gliomas: a classification system based on magnetic resonance imaging.** *Pediatr Neurosurg* 1990;16:73–83 CrossRef Medline
- Louis DN, Perry A, Reifenberger G, et al. **The 2016 World Health Organization Classification of Tumors of the Central Nervous System: a summary.** *Acta Neuropathol* 2016;131:803–20 CrossRef Medline
- Louis DN, Perry A, Wesseling P, et al. **The 2021 WHO Classification of Tumors of the Central Nervous System: a summary.** *Neuro Oncol* 2021;23:1231–51 CrossRef Medline
- Varlet P, Baker SJ, Ellison DW, et al. **Diffuse midline glioma, H3 K27-altered.** In: WHO Classification of tumors editorial boards. *WHO Classification of Tumours: Central Nervous System Tumours*. 5th ed. IARC Press; 2021:69–73
- Hoffman LM, Veldhuijzen van Zanten SE, Colditz N, et al. **Clinical, radiologic, pathologic, and molecular characteristics of long-term survivors of diffuse intrinsic pontine glioma (DIPG): a collaborative report from the International and European Society for Pediatric Oncology DIPG Registries.** *J Clin Oncol* 2018;36:1963–72 CrossRef Medline
- Ostrom QT, Patil N, Cioffi G, et al. **CBTRUS Statistical Report: Primary Brain and Other Central Nervous System Tumors Diagnosed in the United States in 2013–2017.** *Neuro Oncol* 2020;22:iv1–96 CrossRef Medline
- Leach JL, Roebker J, Schafer A, et al. **MR imaging features of diffuse intrinsic pontine glioma and relationship to overall survival:**

- report from the International DIPG Registry.** *Neuro Oncol* 2020;22:1647–57 CrossRef Medline
- Albright AL, Packer RJ, Zimmerman R, et al. **Magnetic resonance scans should replace biopsies for the diagnosis of diffuse brain stem gliomas: a report from the Children’s Cancer Group.** *Neurosurgery* 1993;33:1026–29; discussion 1029–30 CrossRef Medline
 - Puget S, Beccaria K, Blauwblomme T, et al. **Biopsy in a series of 130 pediatric diffuse intrinsic pontine gliomas.** *Childs Nerv Syst* 2015;31:1773–80 CrossRef Medline
 - Wu G, Diaz AK, Paugh BS, et al. **The genomic landscape of diffuse intrinsic pontine glioma and pediatric non-brainstem high-grade glioma.** *Nat Genet* 2014;46:444–50 CrossRef Medline
 - Gupta N, Goumnerova LC, Manley P, et al. **Prospective feasibility and safety assessment of surgical biopsy for patients with newly diagnosed diffuse intrinsic pontine glioma.** *Neuro Oncol* 2018;20:1547–55 CrossRef Medline
 - Calmon R, Dangouloff-Ros V, Varlet P, et al. **Radiogenomics of diffuse intrinsic pontine gliomas (DIPGs): correlation of histological and biological characteristics with multimodal MRI features.** *Eur Radiol* 2021;31:8913–24 CrossRef Medline
 - Mackay A, Burford A, Carvalho D, et al. **Integrated molecular meta-analysis of 1,000 pediatric high-grade and diffuse intrinsic pontine glioma.** *Cancer Cell* 2017;32:520–537.e5 CrossRef Medline
 - Kfoury-Beaumont N, Prakasam R, Pondugula S, et al. **The H3K27M mutation alters stem cell growth, epigenetic regulation, and differentiation potential.** *BMC Biol* 2022;20:124 CrossRef Medline
 - Lu VM, Power EA, Zhang L, et al. **Liquid biopsy for diffuse intrinsic pontine glioma: an update.** *J Neurosurg Pediatr* 2019 Sep 6. [Epub ahead of print] CrossRef Medline
 - Azad TD, Jin MC, Bernhardt LJ, et al. **Liquid biopsy for pediatric diffuse midline glioma: a review of circulating tumor DNA and cerebrospinal fluid tumor DNA.** *Neurosurg Focus* 2020;48:E9 CrossRef Medline
 - Poussaint TY, Vajapeyam S, Ricci KI, et al. **Apparent diffusion coefficient histogram metrics correlate with survival in diffuse intrinsic pontine glioma: a report from the Pediatric Brain Tumor Consortium.** *Neuro Oncol* 2016;18:725–34 CrossRef Medline
 - Aboian MS, Tong E, Solomon DA, et al. **Diffusion characteristics of pediatric diffuse midline gliomas with histone H3-K27M mutation using apparent diffusion coefficient histogram analysis.** *AJNR Am J Neuroradiol* 2019;40:1804–10 CrossRef Medline
 - Zhang P, Duan Y, Gu G, et al. **Clinical, pathological, and radiological features of 80 pediatric diffuse intrinsic pontine gliomas: a single-institute study.** *Front Oncol* 2023;13:1007393 CrossRef Medline
 - Castel D, Philippe C, Calmon R, et al. **Histone H3F3A and HIST1H3B K27M mutations define two subgroups of diffuse intrinsic pontine**

- gliomas with different prognosis and phenotypes. *Acta Neuropathol* 2015;130:815–27 CrossRef Medline
21. Castel D, Grill J, Debily MA. **Histone H3 genotyping refines clinicoradiological diagnostic and prognostic criteria in DIPG.** *Acta Neuropathol* 2016;131:795–96 CrossRef Medline
 22. Piccardo A, Tortora D, Mascelli S, et al. **Advanced MR imaging and ¹⁸F-DOPA PET characteristics of H3K27M-mutant and wild-type pediatric diffuse midline gliomas.** *Eur J Nucl Med Mol Imaging* 2019;46:1685–94 CrossRef Medline
 23. Lapin DH, Tsoli M, Ziegler DS. **Genomic insights into diffuse intrinsic pontine glioma.** *Front Oncol* 2017;7:57 CrossRef Medline
 24. Jaimes C, Vajapeyam S, Brown D, et al. **MR imaging correlates for molecular and mutational analyses in children with diffuse intrinsic pontine glioma.** *AJNR Am J Neuroradiol* 2020;41:874–81 CrossRef Medline
 25. Giagnacovo M, Antonelli M, Biassoni V, et al. **Retrospective analysis on the consistency of MRI features with histological and molecular markers in diffuse intrinsic pontine glioma (DIPG).** *Childs Nerv Syst* 2020;36:697–704 CrossRef Medline
 26. Aboian MS, Solomon DA, Felton E, et al. **Imaging characteristics of pediatric diffuse midline gliomas with histone H3 K27M mutation.** *AJNR Am J Neuroradiol* 2017;38:795–800 CrossRef Medline
 27. Khalid F, Goya-Outi J, Escobar T, et al. **Multimodal MRI radiomic models to predict genomic mutations in diffuse intrinsic pontine glioma with missing imaging modalities.** *Front Med (Lausanne)* 2023;10:1071447 CrossRef Medline
 28. Chiang J, Diaz AK, Makepeace L, et al. **Clinical, imaging, and molecular analysis of pediatric pontine tumors lacking characteristic imaging features of DIPG.** *Acta Neuropathol Commun* 2020;8:57 CrossRef Medline
 29. Jenkinson M, Beckmann CF, Behrens TE, et al. **FSL.** *Neuroimage* 2012;62:782–90 CrossRef Medline
 30. Schindelin J, Arganda-Carreras I, Frise E, et al. **Fiji: an open-source platform for biological-image analysis.** *Nat Methods* 2012;9:676–82 CrossRef Medline
 31. Buczkowicz P, Hawkins C. **Pathology, molecular genetics, and epigenetics of diffuse intrinsic pontine glioma.** *Front Oncol* 2015;5:147 CrossRef Medline
 32. Khuong-Quang DA, Buczkowicz P, Rakopoulos P, et al. **K27M mutation in histone H3.3 defines clinically and biologically distinct subgroups of pediatric diffuse intrinsic pontine gliomas.** *Acta Neuropathol* 2012;124:439–47 CrossRef Medline
 33. Wu G, Broniscer A, McEachron TA, et al; St. Jude Children's Research Hospital–Washington University Pediatric Cancer Genome Project. **Somatic histone H3 alterations in pediatric diffuse intrinsic pontine gliomas and non-brainstem glioblastomas.** *Nat Genet* 2012;44:251–53 CrossRef Medline
 34. Koral K, Mathis D, Gimi B, et al. **Common pediatric cerebellar tumors: correlation between cell densities and apparent diffusion coefficient metrics.** *Radiology* 2013;268:532–37 CrossRef Medline
 35. Gauvain KM, McKinstry RC, Mukherjee P, et al. **Evaluating pediatric brain tumor cellularity with diffusion-tensor imaging.** *AJR Am J Roentgenol* 2001;177:449–54 CrossRef Medline
 36. Chenevert TL, Ross BD. **Diffusion imaging for therapy response assessment of brain tumor.** *Neuroimaging Clin N Am* 2009;19:559–71 CrossRef Medline
 37. Chen HJ, Panigrahy A, Dhall G, et al. **Apparent diffusion and fractional anisotropy of diffuse intrinsic brain stem gliomas.** *AJNR Am J Neuroradiol* 2010;31:1879–85 CrossRef Medline
 38. Castel D, Kergrohen T, Tauziède-Espariat A, et al. **Histone H3 wild-type DIPG/DMG overexpressing EZHIP extend the spectrum diffuse midline gliomas with PRC2 inhibition beyond H3-K27M mutation.** *Acta Neuropathol* 2020;139:1109–13 CrossRef Medline
 39. Merhemec Z, Imsirovic B, Bilalovic N, et al. **Apparent diffusion coefficient reproducibility in brain tumors measured on 1.5 and 3 T clinical scanners: a pilot study.** *Eur J Radiol* 2018;108:249–53 CrossRef Medline
 40. Mulkern RV, Ricci KI, Vajapeyam S, et al. **Pediatric brain tumor consortium multisite assessment of apparent diffusion coefficient z-axis variation assessed with an ice-water phantom.** *Acad Radiol* 2015;22:363–69 CrossRef Medline
 41. Wagner MW, Namdar K, Napoleone M, et al. **Radiomic features based on MRI predict progression-free survival in pediatric diffuse midline glioma/diffuse intrinsic pontine glioma.** *Can Assoc Radiol J* 2023;74:119–26 CrossRef Medline

T2-FLAIR Mismatch Sign in Pediatric Low-Grade Glioma

M.W. Wagner, L. Nobre, K. Namdar, F. Khalvati, U. Tabori, C. Hawkins, and B.B. Ertl-Wagner



ABSTRACT

BACKGROUND AND PURPOSE: No qualitative imaging feature currently predicts molecular alterations of pediatric low-grade gliomas with high sensitivity or specificity. The T2-FLAIR mismatch sign predicts *IDH*-mutated 1p19q noncodeleted adult gliomas with high specificity. We aimed to assess the significance of the T2-FLAIR mismatch sign in pediatric low-grade gliomas.

MATERIALS AND METHODS: Pretreatment MR images acquired between January 2001 and August 2018 in pediatric patients with pediatric low-grade gliomas were retrospectively identified. Inclusion criteria were the following: 1) 0–18 years of age, 2) availability of molecular information in histopathologically confirmed cases, and 3) availability of preoperative brain MR imaging with non-motion-degraded T2-weighted and FLAIR sequences. Spinal cord tumors were excluded.

RESULTS: Three hundred forty-nine patients were included (187 boys; mean age, 8.7 [SD, 4.8] years; range, 0.5–17.7 years). *KIAA1549*–*BRAF* proto-oncogene (*BRAF*) fusion and *BRAF* p.V600E mutation were the most common molecular markers ($n = 148$, 42%, and $n = 73$, 20.7%, respectively). The T2-FLAIR mismatch sign was present in 25 patients (7.2%). Of these, 9 were dysembryoplastic neuroepithelial tumors; 8, low-grade astrocytomas; 5, diffuse astrocytomas; 1, a pilocytic astrocytoma; 1, a glioneuronal tumor; and 1, an angiocentric glioma. None of the 25 T2-FLAIR mismatch pediatric low-grade gliomas were *BRAF* p.V600E–mutated. Fourteen of 25 pediatric low-grade gliomas with the T2-FLAIR mismatch sign had rare molecular alterations, while the molecular subtype was unknown for 11 tumors.

CONCLUSIONS: The T2-FLAIR mismatch sign was not observed in the common molecular alterations, *BRAF* p.V600E–mutated and *KIAA1549*–*BRAF* fused pediatric low-grade gliomas, while it was encountered in pediatric low-grade gliomas with rare pediatric molecular alterations.

ABBREVIATIONS: DNET = dysembryoplastic neuroepithelial tumor; pLGG = pediatric low-grade glioma; RAS/MAPK = RAS-mitogen-activated protein kinase; TKDD = tyrosine kinase domain duplication

Pediatric low-grade gliomas (pLGGs) are the most common pediatric brain tumors, accounting for approximately 40%

Received December 16, 2022; accepted after revision May 22, 2023.

From the Division of Neuroradiology (M.W.W., F.K., B.B.E.-W.), Department of Diagnostic Imaging, Department of Neurooncology (L.N., U.T.), and Department of Paediatric Laboratory Medicine (C.H.), Division of Pathology, The Hospital for Sick Children (SickKids), Toronto, Ontario, Canada; Neurosciences & Mental Health Research Program (M.W.W., F.K., B.B.E.-W.), SickKids Research Institute, Toronto, Ontario, Canada; Department of Medical Imaging (M.W.W., K.N., F.K., B.B.E.-W.), Institute of Medical Science (F.K.), Department of Computer Science (K.N., F.K.), and Department of Mechanical and Industrial Engineering (K.N., F.K.), University of Toronto, Toronto, Ontario, Canada; Department of Neuroradiology (M.W.W.), University Hospital Augsburg, Augsburg, Germany; and Vector Institute (F.K.), Toronto, Ontario, Canada.

C. Hawkins was supported by the Canadian Cancer Society (grant No. 702296) and the Canadian Institute of Health Research (grant No. 159805).

Please address correspondence to Matthias W. Wagner, MD, Division of Neuroradiology, Department of Diagnostic Imaging, The Hospital for Sick Children (SickKids), Toronto, ON, Canada; e-mail: m.w.wagner@me.com

Indicates open access to non-subscribers at www.ajnr.org

Indicates article with online supplemental data.

<http://dx.doi.org/10.3174/ajnr.A7916>

of all pediatric brain tumors.^{1,2} They are a heterogeneous group of tumors classified by the World Health Organization as grade 1 or 2.³ Molecular profiling studies have identified genetic events in pLGGs involving the RAS-mitogen-activated protein kinase (RAS/MAPK) pathway.⁴ Most commonly, these are events involving B-Raf proto-oncogene (*BRAF*) or germline neurofibromatosis 1 (*NF1*) alterations.^{5,6} Rarer alterations affect RAS/MAPK signaling, including fibroblast growth factor receptor (*FGFR*)1/2/3, *ROS1*, and non-RAS/MAPK alterations, such as *MYB*, *MYBL1*, *IDH1*, and others.^{1,4} To date, no qualitative imaging features exist predicting any of the pLGG molecular alterations with high sensitivity or specificity.

In 2017, Patel et al⁷ described the T2-FLAIR mismatch sign in a sample of 125 adult lower-grade gliomas to predict *IDH*-mutated 1p19q noncodeleted gliomas with high specificity. It is defined by hyperintense signal on T2-weighted sequences and hypointense signal on FLAIR sequences with a hyperintense peripheral rim. This imaging feature has since gained increasing attention in adult

neuroradiology due to the wide availability of T2-weighted and FLAIR sequences. Currently, there is only anecdotal evidence of the T2-FLAIR mismatch sign in the pediatric population. In 2019, Johnson et al⁸ reported 5 false-positive instances of T2-FLAIR mismatch, 4 of which occurred in children and 3 of which were neoplastic. These included a pilomyxoid astrocytoma, a H3K27M-mutant midline glioma, and a low-grade astrocytoma with an *MYB* rearrangement.⁸ To our knowledge, no prior study has systematically investigated the occurrence of the T2-FLAIR mismatch sign in pLGG.

We therefore aimed to assess the occurrence of the T2-FLAIR mismatch sign in pLGG in a large pediatric institutional cohort.

MATERIALS AND METHODS

Patient Sample

This retrospective study was approved by the local institutional review board (The Hospital for Sick Children, Toronto). Because of the retrospective nature of the study, informed consent was waived by the local research ethics board. All patients were identified from the electronic health record database between January 2001 and August 2018. Patient inclusion criteria were the following: 1) 0–18 years of age, 2) the availability of molecular information in histopathologically confirmed pLGG as defined by Louis et al,⁹ and 3) the availability of preoperative brain MR imaging with non-motion-degraded T2-weighted and FLAIR sequences. Spinal cord tumors were not included in this study.

Molecular Analysis

BRAF fusion status was determined using an nCounter Metabolic Pathways Panel (NanoString Technologies) or fluorescence in situ hybridization, while the *BRAF* p.V600E mutation was determined using immunohistochemistry or droplet digital polymerase chain reaction. Additional alterations were detected by RNA panel sequencing as previously described.⁴ For most patients, molecular analysis was performed with formalin-fixed paraffin-embedded tissue that was obtained at the time of the tissue sampling.

MR Imaging

All patients underwent MR imaging of the brain at 1.5T or 3T across various vendors (Signa, GE Healthcare; Achieva, Philips Healthcare; Magnetom Skyra, Siemens). The standardized sequence protocol at our institution included the following sequences: a sagittal 3D T1-weighted sequence with axial and coronal reformats, an axial DWI, an axial and/or coronal FLAIR sequence, an axial and/or coronal and/or sagittal T2-weighted sequence, an axial SWI or multiplanar gradient recalled acquisition, a gadolinium-based contrast agent-enhanced axial 3D T1-weighted sequence with coronal and sagittal reformats, and a gadolinium-based contrast agent-enhanced axial or coronal T1-weighted spin-echo sequence. All MR imaging data were extracted from the PACS, de-identified for further analyses, and transferred to an off-line workstation.

Analysis of the Study Cohort and Statistical Analysis

Two pediatric neuroradiologists (M.W.W. with 4 years of experience after a pediatric neuroradiology fellowship and B.B.E.-W.

with >15 years of postfellowship experience) reviewed baseline brain MR images of all included patients, blinded to clinical and molecular data. Signal characteristics of brain tumors were reviewed, and the presence of the T2-FLAIR mismatch sign was noted on the basis of the description by Jain et al.¹⁰ Additionally, images were reviewed for the presence of hemosiderin on SWI and multiplanar gradient recalled sequences. Decisions were reached in consensus.

Descriptive statistical analyses were performed using the Statistical Package for the Social Sciences software (SPSS), Version 18 (IBM). For baseline characteristics, continuous data were presented using mean (SD), and categorical data were presented using integers and percentages.

RESULTS

Patient Demographics, Histopathologic Diagnoses, and Molecular Markers

A total of 389 MR images of 389 patients were available for analysis. Of these, 40 MR images were excluded due to a nonavailable FLAIR sequence ($n = 28$), posttherapeutic status ($n = 5$), tumor extending into the cervical cord ($n = 3$), nonavailable molecular information ($n = 2$), a nonavailable T2-weighted sequence ($n = 1$), and motion degradation of the FLAIR sequence ($n = 1$). The inclusion criteria were fulfilled by 349 patients (187 boys, 53.6%). The mean age at the time of diagnosis was 8.7 (SD, 4.8) years (range, 0.5–17.7 years).

The sample consisted of biopsy-proved pilocytic astrocytomas ($n = 151$), low-grade astrocytomas ($n = 66$), gangliogliomas ($n = 43$), dysembryoplastic neuroepithelial tumors (DNETs) ($n = 24$), diffuse astrocytomas ($n = 22$), pilomyxoid astrocytomas ($n = 11$), pleomorphic xanthoastrocytomas ($n = 7$), oligodendrogliomas ($n = 7$), glioneuronal tumors ($n = 5$), angiocentric gliomas ($n = 5$), desmoplastic infantile gliomas ($n = 2$), neurocytomas ($n = 2$), mixed tumor components ($n = 2$), gangliocytoma ($n = 1$), and polymorphous low-grade glioneuronal tumor of the young ($n = 1$). There were no *IDH*-mutant 1p/19q noncodeleted gliomas.

KIAA1549-BRAF fusion was the most common molecular marker ($n = 148$). Less common alterations were *BRAF* p.V600E mutation ($n = 73$), *FGFR1* tyrosine kinase domain duplication (TKDD) ($n = 7$), *NF1* ($n = 11$), *FGFR1-TACC1* fusion ($n = 6$), alterations in *FGFR2* ($n = 6$), *MYB* ($n = 5$), *MYBL1* ($n = 4$), *FGFR1-N546K* ($n = 1$), mutation of *IDH1* ($n = 3$), alteration of *MET* N375S ($n = 2$), *QKI-RAF1* ($n = 2$), *BRAF* V600ins ($n = 2$), *FGFR1* deletion ($n = 1$), *FGFR4* ($n = 1$), *BRAF* D594N and *KRAS* Q61R ($n = 1$), *BRAF-FAM131B* ($n = 1$), *CLCN6-BRAF* ($n = 1$), *FYCO-RAF1* ($n = 1$), fusion of *GOPC-ROS1* ($n = 1$), alterations in *KIT* V825I ($n = 1$), *KRAS*-Q22K ($n = 1$), *MAP2K1* ($n = 1$), *MET* H1112Y ($n = 1$), *MIDI1-NTRK2* ($n = 1$), mutation of *MYB-QKI* ($n = 1$), fusion of *PDGFB-LRP1* ($n = 1$), and alteration of *PDGFRA-K385M* ($n = 1$), *PIK3CA* Q60K ($n = 1$), *RET* D892N ($n = 1$), *SF3B1-NTRK2* ($n = 1$), *TAX1BP1-BRAF* ($n = 1$), *FGFR1*-K654N, T656P ($n = 1$), and *FGFR1*-K646E ($n = 1$). A total of 56 children with pLGG had incomplete test panels. Of those, 50 were negative for *KIAA1549-BRAF* fusion, while no test result was available for 6 tumors. Fifty-three were negative for the *BRAF* p.V600E mutation, while no test result was available for 3

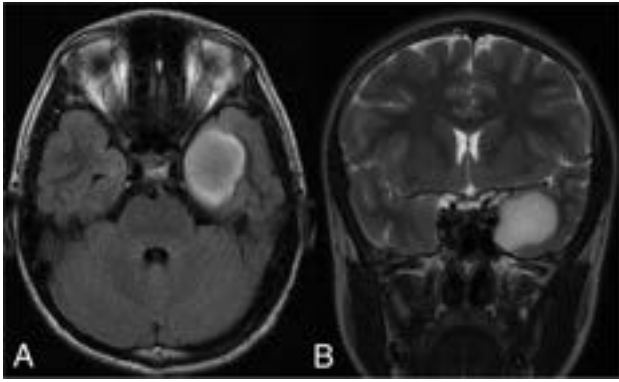


FIG 1. A 13-year-old boy with a left temporal diffuse astrocytoma with an *MYBL1* alteration and T2-FLAIR mismatch sign. A, axial FLAIR and B, coronal T2.

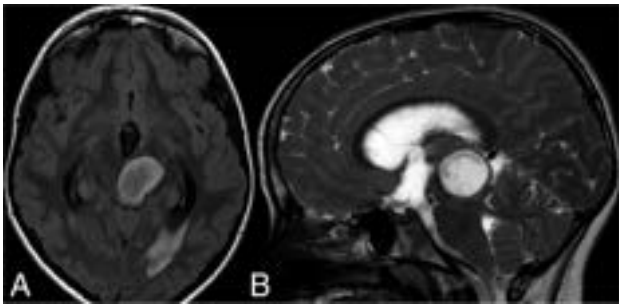


FIG 2. A 10-year-old girl with a midline low-grade astrocytoma with *FGFR1-TACC* fusion and the T2-FLAIR mismatch sign. A, axial FLAIR and B, coronal T2.

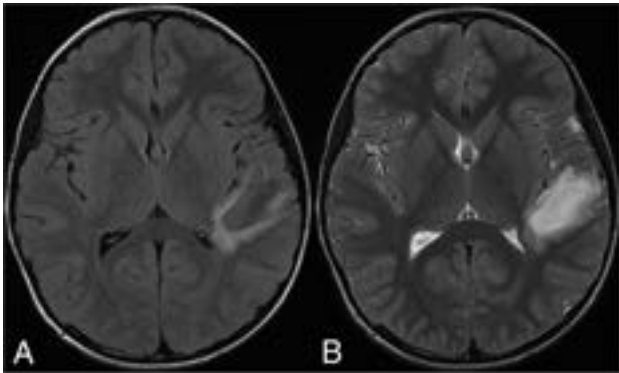


FIG 3. A 9-year-old boy with a left temporal DNET with an *FGFR4* alteration and the T2-FLAIR mismatch sign. A, axial FLAIR and B, sagittal T2.

tumors. Last, 52 were negative for both *FGFR1-N546K* alteration and mutation of *IDH1*, while no test result was available for 4 tumors, respectively.

Analysis of T2-FLAIR Mismatch Sign

The T2-FLAIR mismatch sign was observed in 25 of 349 patients with pLGG (7.2%). Seventeen patients were boys (68%). The mean age was 8.3 (SD, 4.8) years (range, 1–16 years). The T2-FLAIR mismatch sign was encountered in the frontal lobe ($n = 10$), temporal lobe ($n = 7$), parietal lobe ($n = 3$), thalamus ($n = 2$), brainstem ($n = 2$), and intraventricularly ($n = 1$). Of the 25 pLGGs with the T2-FLAIR mismatch sign, 9 were DNETs (36%),

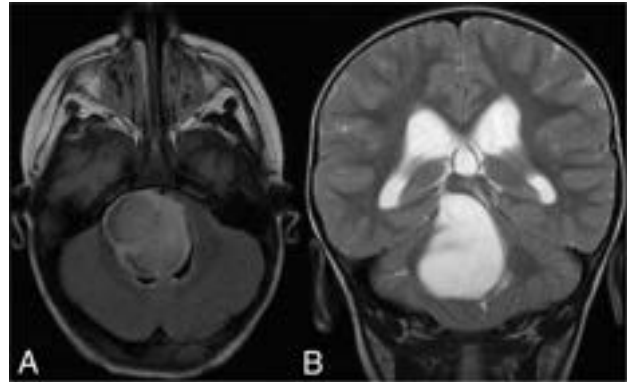


FIG 4. A 2-year-old boy with a brainstem low-grade astrocytoma with *MYB-QKI* fusion and the T2-FLAIR mismatch sign. A, axial FLAIR and B, axial T2.

8 were low-grade astrocytomas (32%), 5 were diffuse astrocytomas (20%), 1 was a pilocytic astrocytoma (4%), 1 was a glioneuronal tumor (4%), and 1 was an angiocentric glioma (4%).

In relation to all patients reviewed, the T2-FLAIR mismatch sign was found in 9 of 24 DNETs (37.5%), 5 of 22 diffuse astrocytomas (22.7%), 1 of 5 glioneuronal tumors (20%), 1 of 5 angiocentric gliomas (20%), 8 of 66 low-grade astrocytomas (12.1%), and 1 of 151 pilocytic astrocytomas (0.7%).

In relation to all patients reviewed, the T2-FLAIR mismatch sign was found in 3 of 4 *MYBL1* pLGGs (75%, Fig 1), 2 of 7 *FGFR1-TKDD* pLGGs (28.6%), 2 of 6 *FGFR1-TACC1* pLGGs (33.3%, Fig 2), 1 of 5 *MYB* pLGGs (20%), 1 of 1 *FGFR4* pLGGs (100%, Fig 3), 1 of 1 *GOPC-ROS1* pLGGs (100%), 1 of 3 *IDH1* pLGGs (33.3%), 1 of 2 *MET N375S* pLGGs (50%), 1 of 1 *MYB-QKI* pLGG (100%, Fig 4), and 1 of 1 *PDGFB-LRP1* pLGG (100%). Among the 11 tumors with incomplete test panels, all were negative for the *BRAF* p.V600E mutation, *FGFR1-N546K* alteration, and a mutation of *IDH1*. Nine of 11 tumors were also negative for *KIAA1549-BRAF* fusion, while no test result was available for 2 tumors.

Notably, no pLGG with the T2-FLAIR mismatch sign was *BRAF* p.V600E–mutated, and at least 23 of 25 tumors with a T2-FLAIR mismatch sign were also negative for *KIAA1549-BRAF* fusion (Online Supplemental Data). The Online Supplemental Data show the distribution of the histopathologic diagnoses of the pLGGs with a T2-FLAIR mismatch sign according to their molecular markers.

No abnormal susceptibility was found in any of the 25 pLGGs with the T2-FLAIR mismatch sign.

DISCUSSION

Using a large institutional cohort, we aimed to assess the occurrence of the T2-FLAIR mismatch sign in pLGGs and its relation to histopathologic and molecular markers. We found the T2-FLAIR mismatch sign to be absent in *KIAA1549-BRAF*–fused and *BRAF* p.V600E–mutated pLGGs. The sign was more commonly noted in rare molecular markers including *MYBL1* pLGG, *FGFR1-TKDD* pLGG, *FGFR1-TACC1* pLGG, *MYB* pLGG, *FGFR4* pLGG, *GOPC-ROS1* pLGG, *IDH1* pLGG, *MET N375S* pLGG, *MYB-QKI* pLGG, and *PDGFB-LRP1* pLGG. Fifty-six tumors had incomplete test panels. However, the most common molecular alterations

(*KIAA1549-BRAF* fusion and *BRAF* p.V600E mutation) in addition to *FGFR1-N546K* alteration and mutation of *IDH1* were excluded in almost all tumors. Of these 56 tumors, 11 (19.6%) demonstrated the T2-FLAIR mismatch sign.

In their recent meta-analysis, Do et al¹¹ systematically reviewed the predictive accuracy of the T2-FLAIR mismatch sign in 1342 adults (age range, 19–82 years) with low-grade gliomas. The sign was found to have a pooled sensitivity of 40% and pooled specificity of 100% for *IDH*-mutant, 1p/19q noncodeleted low-grade gliomas. While the sign has been established in the adult neuroradiology literature, to our knowledge, its significance has never been assessed in a pediatric brain tumor cohort, likely due to greater diversity of histopathology, imaging morphology, and tumor location of pediatric gliomas compared with adult *IDH*-mutant, 1p/19q noncodeleted low-grade gliomas reported by Patel et al.⁷

The mismatch sign is less frequently encountered in the pediatric age group. However, there is anecdotal evidence of a false-positive T2-FLAIR mismatch sign in children. A prior report by Johnson et al⁸ mentioned a false-positive T2-FLAIR mismatch sign in the following: 1) a pilomyxoid astrocytoma in a 2-year-old child, 2) a non-neoplastic lesion (heterotopic gray matter) in a 12-year-old child, 3) a H3K27M-mutant midline glioma in a 14-year-old adolescent, and 4) a low-grade astrocytoma harboring *MYB* rearrangement in an 18-year-old individual. In addition, Kalelioglu et al¹² reported the T2-FLAIR mismatch sign in 1 of 2 pediatric-type diffuse low-grade gliomas with a *MYB/MYBL1* alteration. In our cohort of 352 pLGGs, we found 25 tumors with a T2-FLAIR mismatch (7.1%). This finding raises the question of the significance of the sign in the pediatric population. Unlike Johnson et al, we did not find the sign in pilomyxoid astrocytomas, but we observed the T2-FLAIR mismatch sign in 1 of 5 pLGGs with *MYB* and 3 of 4 pLGGs with a *MYBL1* rearrangement. *MYB* and *MYBL1* serve as transcriptional regulators important for cell proliferation and differentiation.¹ They are hypothesized to reflect a single tumor entity¹³ and represent a distinct group within the pediatric-type diffuse low-grade gliomas in the 2021 WHO Classification of Tumors of the Central Nervous System.³ Furthermore, the T2-FLAIR mismatch sign was present in 2 of 7 *FGFR1-TKDD* pLGGs (28.6%) and 2 of 6 *FGFR1-TACC1* fusion pLGGs (33.3%), which represented 2 diffuse astrocytomas and 2 low-grade astrocytomas histopathologically.

Other rare pLGG subtypes demonstrating the T2-FLAIR mismatch sign included the following molecular markers: *FGFR4* alteration (DNET), *GOPC-ROS1* fusion (pilocytic astrocytoma), *MET* N375S alteration (DNET), *IDH1* mutation, *MYB-QKI* fusion, and *PDGFB-LRP1* fusion (all low-grade astrocytomas). Regarding the commonly encountered histopathologic tumor types in pLGG, only 1 of 151 pilocytic astrocytomas (0.7%), 8 of 66 low-grade astrocytomas (12.1%), and none of 43 gangliogliomas demonstrated the T2-FLAIR mismatch sign. Instead, rarer histopathologies were enriched when encountering the T2-FLAIR mismatch sign, including 9 of 24 DNETs (37.5%), 5 of 22 diffuse astrocytomas (22.7%), 1 of 5 glioneuronal tumors (20%), and 1 of 5 angiocentric gliomas (20%). The rarity of the T2-FLAIR mismatch sign in common histologic tumor and molecular subtypes of pLGG suggests its potential as a diagnostic indicator for uncommon pLGG types.

Prior reports on *IDH*-mutant, 1p/19q noncodeleted low-grade gliomas in adults have demonstrated a strong association between the T2-FLAIR mismatch sign and intratumoral microcystic components.^{7,14–16} This association can likely be attributed to the very long T1- and T2-relaxation times, which are the underlying MR imaging signal characteristics of the mismatched area.¹⁷ Of our 25 pLGGs with T2-FLAIR mismatch, 9 were DNETs, a tumor entity known to demonstrate a microcystic pattern histologically.¹⁸ It is difficult to say whether the microcystic pattern is related to the presence of the sign in other cases of our cohort, including low-grade, diffuse, and pilocytic astrocytomas and glioneuronal and angiocentric gliomas. The answer would require a histopathologic analysis of these cases beyond the scope of this study. While the underlying histopathologic characteristics of the T2-FLAIR mismatch sign in rare pLGG remain to be elucidated, we did not find the T2-FLAIR mismatch in the 2 most common types of molecular alterations of pLGG, *KIAA1549-BRAF* fusion and *BRAF* p.V600E mutation.

Several limitations need to be considered when interpreting the results of our study. First, 2 expert readers subjectively assessed the MR images in consensus, blinded to the molecular marker. Second, there were relatively few pLGGs with rare molecular markers in our sample. Consequently, the significance of the T2-FLAIR mismatch sign in *GOPC-ROS1*, *IDH1*, *MET* N375S, *MYB-QKI*, and *PDGFB-LRP1* requires further clarification. Third, 56 tumors had incomplete test panels. Of these, 11 demonstrated the T2-FLAIR mismatch sign. While it would be interesting to know whether there are rare pLGG molecular subtypes present in this group, we were able to exclude the most common molecular alterations (*KIAA1549-BRAF* fusion and *BRAF* p.V600E mutation) in addition to the *FGFR1-N546K* alteration and the mutation of *IDH1*. Additional molecular analysis in the future may help elucidate the significance of the sign in rare subtypes of pLGG.

CONCLUSIONS

In a large institutional cohort of patients with pLGG, we assessed the occurrence of the T2-FLAIR mismatch sign and its relation to histopathologic and molecular markers. We found that the T2-FLAIR mismatch sign is absent in *KIAA1549-BRAF*-fused and *BRAF* p.V600E-mutated pLGG. The sign was encountered in rare molecular markers of pLGG, including *MYB/MYBL1*, *MYB-QKI*, *FGFR1-TKDD*, *FGFR1-TACC1*, *FGFR4*, *IDH1*, *GOPC-ROS1*, *MET* N375S, and *PDGFB-LRP1*. Due to the rarity of the T2-FLAIR mismatch sign in common histologic tumor types and molecular subtypes of pLGG, it could serve as a diagnostic marker for infrequent pLGG types.

Disclosure forms provided by the authors are available with the full text and PDF of this article at www.ajnr.org.

REFERENCES

1. Ryall S, Tabori U, Hawkins C. Pediatric low-grade glioma in the era of molecular diagnostics. *Acta Neuropathol Commun* 2020;8:30 CrossRef Medline
2. Ostrom QT, Gittleman H, Liao P, et al. CBTRUS Statistical Report: Primary brain and other central nervous system tumors diagnosed

- in the United States in 2010-2014. *Neuro Oncol* 2017;19:v1-88 CrossRef Medline
3. Louis DN, Perry A, Wesseling P, et al. **The 2021 WHO Classification of Tumors of the Central Nervous System: a summary.** *Neuro Oncol* 2021;23:1231-51 CrossRef Medline
 4. Ryall S, Zapotocky M, Fukuoka K, et al. **Integrated molecular and clinical analysis of 1,000 pediatric low-grade gliomas.** *Cancer Cell* 2020;37:569-83.e5 CrossRef Medline
 5. Packer RJ, Pfister S, Bouffet E, et al. **Pediatric low-grade gliomas: implications of the biologic era.** *Neuro Oncol* 2017;19:750-61 CrossRef Medline
 6. AlRayahi J, Zapotocky M, Ramaswamy V, et al. **Pediatric brain tumor genetics: what radiologists need to know.** *Radiographics* 2018;38:2102-22 CrossRef Medline
 7. Patel SH, Poisson LM, Brat DJ, et al. **T2-FLAIR mismatch, an imaging biomarker for IDH and 1p/19q status in lower-grade gliomas: a TCGA/TCIA project.** *Clin Cancer Res* 2017;23:6078-85 CrossRef Medline
 8. Johnson DR, Kaufmann TJ, Patel SH, et al. **There is an exception to every rule-T2-FLAIR mismatch sign in gliomas.** *Neuroradiology* 2019;61:225-27 CrossRef Medline
 9. Louis DN, Perry A, Reifenberger G, et al. **The 2016 World Health Organization Classification of Tumors of the Central Nervous System: a summary.** *Acta Neuropathol* 2016;131:803-20 CrossRef Medline
 10. Jain R, Johnson DR, Patel SH, et al. **“Real world” use of a highly reliable imaging sign: “T2-FLAIR mismatch” for identification of IDH mutant astrocytomas.** *Neuro Oncol* 2020;22:936-43 CrossRef Medline
 11. Do YA, Cho SJ, Choi BS, et al. **Predictive accuracy of T2-FLAIR mismatch sign for the IDH-mutant, 1p/19q noncodeleted low-grade glioma: an updated systematic review and meta-analysis.** *Neurooncol Adv* 2022;4:vdac010 CrossRef Medline
 12. Kalelioglu T, Rama B, Cho BB, et al. **Pediatric-type diffuse low-grade glioma with MYB/MYBL1 alteration: report of 2 cases.** *Neuroradiol J* 2023;36:232-35 CrossRef Medline
 13. Chiang J, Harreld JH, Tinkle CL, et al. **A single-center study of the clinicopathologic correlates of gliomas with a MYB or MYBL1 alteration.** *Acta Neuropathol* 2019;138:1091-92 CrossRef Medline
 14. Tay KL, Tsui A, Phal PM, et al. **MR imaging characteristics of protoplasmic astrocytomas.** *Neuroradiology* 2011;53:405-11 CrossRef Medline
 15. Deguchi S, Oishi T, Mitsuya K, et al. **Clinicopathological analysis of T2-FLAIR mismatch sign in lower-grade gliomas.** *Sci Rep* 2020;10:10113 CrossRef Medline
 16. Fujita Y, Nagashima H, Tanaka K, et al. **The histopathologic and radiologic features of T2-FLAIR mismatch sign in IDH-mutant 1p/19q non-codeleted astrocytomas.** *World Neurosurg* 2021;149:e253-60 CrossRef Medline
 17. Kinoshita M, Uchikoshi M, Sakai M, et al. **T₂-FLAIR mismatch sign is caused by long T₁ and T₂ of IDH-mutant, 1p19q non-codeleted astrocytoma.** *Magn Reson Med Sci* 2021;20:119-23 CrossRef Medline
 18. Suh YL. **Dysembryoplastic neuroepithelial tumors.** *J Pathol Transl Med* 2015;49:438-49 CrossRef Medline

Development of an Ultrasound Scoring System to Describe Brain Maturation in Preterm Infants

A. Stein, E. Sody, N. Bruns, and U. Felderhoff-Müser

ABSTRACT

BACKGROUND AND PURPOSE: Cerebral maturation in preterm infants predominantly occurs postnatally, necessitating the development of objective bedside markers to monitor this process. This study aimed to develop a straightforward objective Ultrasound Score of Brain Development to assess cortical development in preterm infants.

MATERIALS AND METHODS: A total of 344 serial ultrasound examinations from 94 preterm infants born at ≤ 32 weeks of gestation were analyzed to identify brain structures suitable for a scoring system.

RESULTS: Among 11 candidate structures, 3 cerebral landmarks were selected due to their correlation with gestational age: the interopercular opening ($P < .001$), the height of the insular cortex ($P < .001$), and the depth of the cingulate sulcus ($P < .001$). These structures can be easily visualized in a single midcoronal view in the plane through the third ventricle and the foramina of Monro. A score point from 0 to 2 was assigned to each measurement, culminating in a total score ranging from 0 to 6. The Ultrasound Score of Brain Development correlated significantly with gestational age ($P < .001$).

CONCLUSIONS: The proposed Ultrasound Score of Brain Development has the potential for application as an objective indicator of brain maturation in correlation with gestational age, circumventing the need to rely on individual growth trajectories and percentiles for each specific structure.

ABBREVIATIONS: β = regression coefficient; DOL = day or days of life; J = Youden index; PMA = postmenstrual age; ROC = receiver operating characteristic; SD = standard deviation; USBD = Ultrasound Score of Brain Development

Cerebral ultrasound in premature infants is a well-established bedside technique and is suitable for serial noninvasive and cost-effective examinations in clinical routine. Existing prenatal¹⁻⁶ and postnatal ultrasound⁷⁻¹⁴ studies as well as MR imaging studies^{15,16} have described postnatal brain development using growth trajectories of cerebellar diameter, corpus callosum length, and corpus callosum-fastigium length. To distinguish among different postmenstrual ages (PMAs), one should select anatomic structures that either exhibit significant developmental changes apart from growth or only appear at a later PMA. Fetal ultrasound studies^{2,17-19} have established a well-defined temporal sequence of cortical sulcal development. Opercularization with formation of the Sylvian fissure as a 3D process has also been extensively described in prenatal ultrasound studies.^{6,17-21}

Although several of these studies^{7,18,19,22-24} proposed scoring systems, all studies used semiquantitative or pictorial approaches. Van der Knaap et al²³ suggested a scoring system to describe sulcal development from a V-shaped pit to a stage in which the sulcus is deeper than wide in a postnatal MR imaging study in neonates of >30 weeks' PMA. This score was adapted for intrauterine 2D and 3D ultrasound by Pistorius et al¹⁸ and for postnatal MR imaging by Ruoss et al.²² Postnatal standard transfontanelar ultrasound views differ from transabdominal axial prenatal views. Thus, Klebermass-Schrehof et al⁷ used 3D techniques to adapt this score for postnatal ultrasound.

Our goal was to develop a practical and objective scoring system based on 2D assessment of cerebral anatomic structures in standard transfontanelar planes, which can be applied in routine serial postnatal ultrasound examinations to characterize postnatal brain development in accordance with PMA.

MATERIALS AND METHODS

Study Participants

In this retrospective study, 458 preterm infants born $\leq 32 + 0/7$ weeks' PMA at the University Hospital Essen between May 2009

Received January 17, 2023; accepted after revision May 22.

From the Department of Pediatrics I, Neonatology, University Duisburg-Essen, University Hospital Essen, Essen, Germany.

Please address correspondence to Anja Stein, MD, University Duisburg-Essen, University Hospital Essen, Department of Pediatrics I, Neonatology, Hufelandstr. 55, 45147 Essen, Germany; e-mail: anja.stein@uk-essen.de

<http://dx.doi.org/10.3174/ajnr.A7909>

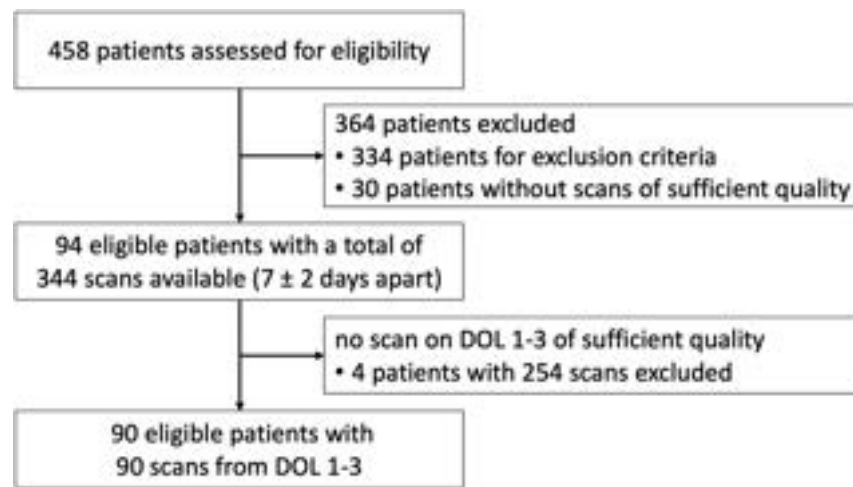


FIG 1. Flowchart of patient recruitment.

Table 1: Patient characteristics

Variable		Patients (n = 94)
Sex (No.)	Male	48
	Female	46
PMA at birth (weeks) ^a	Mean	27.8 (SD, 2.2)
	Range (min–max)	23 + 3/7 to 32 + 0/7
PMA at time of scan (weeks)	Mean	30.9 (SD, 3.4)
	Range (min–max)	23 + 4/7 to 39 + 1/7
Birth weight (g)	Mean	1034 (SD, 349)
	Range (min–max)	340–1810
Birth weight percentile	< 3rd (No.) (%)	3 (3.2%)
	3rd to 10th (No.) (%)	16 (17.0%)
	Mean	25.3 (SD, 2.7)
Head circumference at birth (cm)	Range (min–max)	18.4–31.0
	< 3rd (No.) (%)	2 (2.1%)
Head circumference at birth percentile	3rd to 10th (No.) (%)	21 (22.3%)

Note:—Min indicates minimum; max, maximum.

^aPMA at birth was determined by ultrasound measurement of fetal crown rump length in the first trimester.

and September 2013 were eligible (Fig 1). We excluded 334 infants due to factors potentially influencing brain development, such as intraventricular or intracerebral hemorrhage, cystic periventricular leukomalacia, hydrocephalus, congenital infection, cerebral malformation, chromosomal or syndromal disorder, death during first hospital stay, or transfer to or from another clinic (outborn infants). The quality of archived ultrasound examinations was assessed on the basis of the correct identification of landmarks, symmetry of the required plane, and clear identification of the selected candidate structures. Scans from 30 infants were excluded because >2 of the selected cortical structures in all planes could not be identified and measured. To increase the number of scans and the range of PMAs, we included multiple scans of an individual patient if they were five to nine days apart, resulting in 344 cranial ultrasound examinations of 94 preterm infants (48 male, 46 female; mean birth weight = 1034 [SD, 349] g, range = 340–1810 g) for analysis with a range from 23 + 3/7 weeks at birth to a corrected age of 39 + 1/7 weeks. The total number of ultrasound scans per patient varied from 1 to 8.

The estimated date of delivery was determined by the obstetrician using an ultrasound measurement of crown rump length during first-trimester fetal ultrasound. Gestational age was confirmed

by fetal ultrasound at hospital admission for impending prematurity. There were no cases of unknown or uncertain gestational age in our cohort, but the accuracy of first-trimester dating varied from ± 0.5 to ± 1 weeks.

To exclude the potential influence of the postnatal clinical course on the results, we repeated the analysis by including only 1 scan per patient between the first and third days of life (DOL), which was available for 90 patients. Patient characteristics are summarized in Table 1.

Cranial Ultrasound

All cranial ultrasound examinations were conducted as part of a local routine monitoring protocol for preterm infants of $\leq 32 + 0/7$ weeks PMA during the following timeframes: DOL 1, 3, 5, 7, 14 (± 2 days), 21 (± 2 days), and 28 (± 2 days) and every 14 days (± 2 days) thereafter until 36 + 0/7 weeks' PMA (± 2 days). Additional examinations were performed as clinically indicated. Each examination was conducted by an experienced pediatrician as is standard in Germany, through the anterior fontanelle using a vector 7.5-MHz transducer (Acuson Sequoia 512; Siemens). Archived examinations were retrieved from magneto-optical discs and reopened on the ultrasound machine. A selection of 11 different candidate structures derived from previous studies on cortical development was identified and measured in the archived images in standard midsagittal and midcoronal planes (Fig 2). These planes are well-defined to allow reliable identification of the selected structures. Linear measurements of the height of the insular cortex were compared with measurements along the circumference (2 and 3 in Fig 2). A mean value was used for measurements of the same structure from the left and right hemispheres. Obviously asymmetric coronal images were excluded. The score was not designed to detect asymmetry in development.¹⁸ All measurements were performed by a single observer blinded to the PMA.

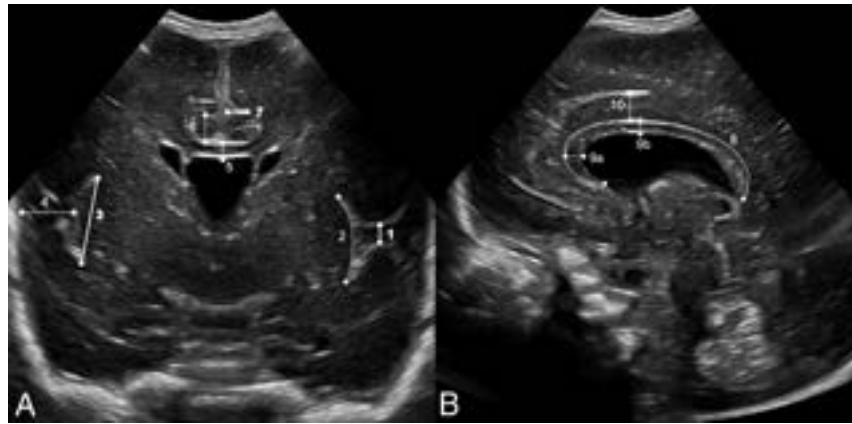


FIG 2. Ultrasound identification of the structures evaluated for the USBD in an infant with a PMA of 26 weeks. *A*, Midcoronal view at the level of the foramina of Monro: interopercular opening* (1), height of the insular cortex—curved measurement (2) and straight measurement* (3), depth of the Sylvian fissure (4), thickness of the corpus callosum (5), height of the cingulate gyrus (6), depth of cingulate sulcus* (7). *B*, Midsagittal view: circumferent length of corpus callosum (8), thickness of corpus callosum (midsagittal) at the genu (9a) and at the body (9b), and height of cingulate gyrus (10). Asterisks indicate structures selected for the USBD (*bold lines, A*).

Table 2: Linear regression analysis of the measured structure and PMA at time of scan

	No.	R	β	P Value
Interopercular opening ^a	343	-0.74	-0.06	<.001
Height of insular cortex, curved measurement	343	0.84	0.09	<.001
Height of insular cortex, straight measurement ^a	343	0.85	0.09	<.001
Depth of Sylvian fissure	341	0.19	0.06	<.001
Thickness of CC (midcoronal)	342	0.26	0.003	<.001
Height of cingulate gyrus (midcoronal)	313	0.72	0.06	<.001
Depth of cingulate sulcus ^a	315	0.83	0.05	<.001
Circumferent length of CC	311	0.68	0.17	<.001
Thickness of CC (midsagittal)				
Genu	335	0.32	0.01	<.001
Body	339	0.18	0.002	<.001
Height of cingulate gyrus (midsagittal)	260	0.44	0.02	<.001
Total USBD (all scans)	312	0.88	0.43	<.001
Total USBD (DOL 1–3)	87	0.76	0.41	<.001

Note:—No. indicates the number of scans in which the structure could be measured; CC, corpus callosum.

^aStructures selected for the USBD.

Statistical Methods

Data analysis and graphic display generation were conducted using SPSS (release 28 for Mac; IBM) and Excel (release 16.53 for Mac; Microsoft). Linear regression of a selected cortical structure measurement with PMA was described by the Pearson correlation coefficient (R), regression coefficient (β), and 95% confidence interval. *P* values < .05 were considered statistically significant. Mean values, SDs, ranges, and interquartile ranges were used as appropriate. Regression curve analyses and receiver operating characteristic (ROC) curves with the Youden index (J) were used to identify and confirm cutoff values for the selected structures contributing to the score.

Development of the Ultrasound Score of Brain Development

The Ultrasound Score of Brain Development (USBBD) aimed to discriminate among different PMAs using the state of cortical development. We sought to separate PMAs in 2-week increments by choosing staggered cutoff points for measurements of the selected structures. Structures were deemed suitable if

measurements demonstrated a clear progression in cortical development with a steep linear regression.

Ethics Approval

The study obtained approval from the local ethics committee of the University Duisburg-Essen (15–6268-BO).

RESULTS

Correlation of the 11 Candidate Structures with PMA

The thickness of the corpus callosum measured in the midcoronal view or at the body in the midsagittal view did not show a significant correlation with PMA when analyzing only scans from

DOL 1–3. All other measurements correlated significantly with PMA (*P* < .001, Table 2), regardless of whether only scans from DOL 1–3 or all available scans were included. The curved and straight measurements of the insular cortex in the midcoronal view correlated equally well.

Development of the USBBD

We selected 3 measurements with the highest correlation coefficients and steep regression curves for the score: the interopercular opening (R = 0.74), the height of the insular cortex (R = 0.85), and the depth of the cingulate sulcus (R = 0.83). These structures are depicted in the midcoronal plane at the level of the foramina of Monro (1, 3, and 7 in Fig 2A), where the insular region develops from a U-shape to a T-shape with closure of the interopercular opening (Fig 3). This plane allows minimal variation in ventral or dorsal displacement of the ultrasound probe, is easily identified, and offers the additional advantage of comparing measurements of the left and right hemispheres in a single view. On the basis of the analysis of the 25th and 75th percentiles (Fig 4) and of ROC curves with the Youden index, cutoff values

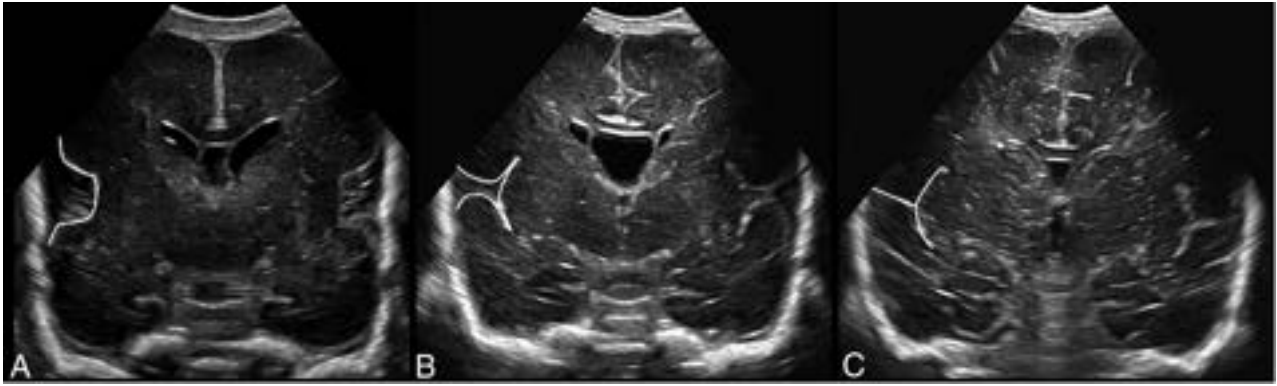


FIG 3. Progression of opercularization with lengthening of insular cortex and closure of interpercular opening in the midcoronal view at different PMAs. A, PMA 22 + 6/7 weeks. B, PMA 30 + 0/7 weeks. C, PMA 34 + 2/7 weeks.

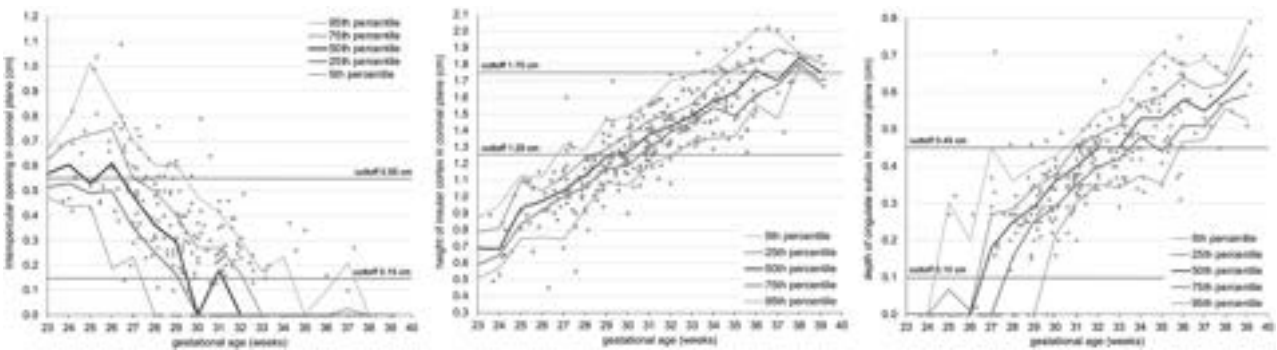


FIG 4. Scatterplot of measurements of selected structures for the USBD and trajectories with 25th and 75th percentiles, regression curves, and selected cutoff values for USBD marked as lines. A, Interpercular opening. B, Height of insular cortex. C, Depth of cingulate sulcus in the midcoronal plane.

for the selected structures at a given PMA were identified. Each individual structure could then be scored from 0 to 2, adding to a total score of 0–6 (Table 3).

Cutoff Points for the Interpercular Opening. One scan could not be evaluated for the interpercular opening due to suboptimal image quality. Only 10 infants were scanned at younger than 25 weeks, with greater variability between measurements. Cutoff points for this age range could not be reliably analyzed using ROC curves. The interpercular opening is the only one of the 3 structures suitable for separation at an early PMA because the cingulate sulcus is not visible yet and the height of the insular cortex is not well-defined due to its U-shape. Seventy percent of the infants at a PMA below 25 weeks had an interpercular opening of ≥ 0.55 cm. A score point of 0 was therefore assigned to infants with an interpercular opening of ≥ 0.55 cm, which applied to 45 of 343 scans.

Complete closure of the Sylvian fissure was defined as an interpercular opening of < 0.15 cm. Complete closure of the Sylvian fissure was achieved at the 25th percentile in scans from 30 weeks' PMA and at the 75th percentile in scans from 33 weeks' PMA. After closure of the Sylvian fissure, this structure can no longer be used to distinguish different PMAs. An interpercular opening of < 0.15 cm identifies infants with a PMA of $> 30 + 6/7$ weeks with a sensitivity of 0.83 and a specificity of 0.76 ($J =$

Table 3: USBD^a

Score Points	0	1	2
Interpercular opening (cm)	≥ 0.55	0.15–0.54	< 0.15
Height of insular cortex (cm)	≤ 1.25	1.26–1.74	≥ 1.75
Depth of cingulate sulcus (cm)	< 0.10	0.11–0.44	≥ 0.45

^a Score points from each structure add to a total score, which can range from a minimum of 0 points to a maximum of 6 points (a higher total score reflects a higher PMA).

0.59). Two score points were assigned to 167 of 343 scans accordingly. A score point of 1 was assigned to the remaining 131 of 343 scans.

Cutoff Points for the Height of the Insular Cortex. Three scans could not be evaluated for the insular cortex due to suboptimal image quality. Growth of the insular cortex to a height > 1.25 cm was achieved at the 25th percentile in scans from 29 weeks' PMA and at the 75th percentile in scans from 31 weeks' PMA. The cutoff value of > 1.25 cm accurately identified infants with a PMA of $> 28 + 6/7$ weeks with a sensitivity of 0.90 and a specificity of 0.84 ($J = 0.74$). In 143 of 341 scans, the height of the insular cortex was ≤ 1.25 cm, and 0 score points were assigned.

Measurements of ≥ 1.75 cm were reached at the 25th percentile in scans from 35 weeks' PMA and at the 75th percentile in scans from 38 weeks' PMA. The cutoff value of ≥ 1.75 cm accurately identified infants with a PMA of $> 34 + 6/7$ weeks with a sensitivity of 0.78 and a specificity of 0.90 ($J = 0.68$). A score

Table 4: PMA mean and range for each USBD score value

Score	No. of Scans with Score Assigned	PMA (Weeks) (mean)	PMA (Weeks) (range)
0	20	25.8 (SD, 1.4)	23 + 4/7 to 29 + 0/7
1	25	26.9 (SD, 1.6)	23 + 5/7 to 29 + 5/7
2	53	28.9 (SD, 1.3)	25 + 0/7 to 32 + 0/7
3	56	30.4 (SD, 1.5)	27 + 0/7 to 35 + 0/7
4	67	32.1 (SD, 1.6)	27 + 1/7 to 36 + 0/7
5	67	34.4 (SD, 1.9)	30 + 2/7 to 39 + 1/7
6	24	36.1 (SD, 1.6)	33 + 2/7 to 39 + 1/7

point of 2 was assigned to 29 of 341 scans accordingly. A score point of 1 was assigned to the remaining 169 of 341 scans.

Cutoff Points for Depth of the Cingulate Sulcus. Twenty-nine scans could not be evaluated for the cingulate sulcus due to insufficient image quality. The first appearance of the cingulate sulcus (defined as a depth >0.10 cm) was at the 25th percentile in scans from 25 weeks' PMA and at the 75th percentile in scans from 28 weeks' PMA. The cutoff value of 0.10 cm accurately identifies infants with a PMA of >25 + 6/7 weeks with a sensitivity of 0.91 and a specificity of 0.89 ($J = 0.80$). A score point of 0 was assigned to 43 of 315 scans. Before the appearance of the cingulate sulcus, it cannot be used to discriminate among different PMAs.

A depth of ≥ 0.45 cm was achieved at the 25th percentile in scans from 31 weeks' PMA and at the 75th percentile in scans from 34 weeks' PMA. The cutoff value of 0.45 cm accurately identifies infants with a PMA above 33 + 6/7 weeks with a sensitivity of 0.89 and a specificity of 0.78 ($J = 0.67$). A score point of 2 was assigned to 110 of 315 scans accordingly. A score point of 1 was assigned to 162 of 315 scans.

In summary, the selected cutoff points should separate infants at approximately 24 and 30 weeks' PMA by the interopercular opening, at 28 and 34 weeks' PMA by the height of the insular cortex, and at 25 and 33 weeks' PMA by the depth of the cingulate sulcus.

Total Score Points in the Final USBD. A total USBD could be calculated in 312 of 344 scans. Table 4 lists means, SDs, and ranges of PMA for each score point of the USBD. To identify the potential impact of postnatally altered brain maturation compared with intrauterine life, we conducted a sensitivity analysis including only scans on DOL 1–3 at a PMA of ≤ 32 weeks at the time of scan. In 90 scans that fulfilled these criteria, no infant scored 5 or 6 and only 6 infants reached a score of 4 (mean PMA = 31.2 [SD, 0.9] weeks; range = 29 + 4/7 to 32 + 1/7 weeks).

Correlation of USBD and PMA. The USBD correlated significantly with PMA ($R = 0.88$, $P < .001$, Fig 5). The USBD increases by 0.43 (95% CI, 0.41–0.46) points per 1 week increase of PMA. Contrariwise, a 1-point increase of the USBD reflects 1.8 weeks or 12.6 days of increase in PMA (95% CI, 1.66–1.87) until the USBD reaches a maximal value of 6 at a mean PMA of 36.1 [SD, 1.6] weeks. In the sensitivity analysis of scans on DOL 1–3, we found a similar correlation ($R = 0.76$, $P < .001$) and an 0.41-point increase of the USBD per 1-week increment of PMA (95% CI, 0.33–0.48). A 1-point increase in the USBD reflects 1.4 weeks or 10 days of increase in PMA (95% CI, 1.17–1.68).

DISCUSSION

This study presents the development of a novel bedside ultrasound scoring system for assessing brain maturation in very preterm infants. Currently, in clinical practice, this result is achieved only through subjective estimation. We identified 3 easily measurable landmark structures in a standard transfontanelar mid-coronal plane, each exhibiting distinct phases of maturation: the interopercular opening, the height of the insular cortex, and the depth of the cingulate sulcus. By combining thresholds for measurements of these 3 structures into a single score, we achieved reliable discrimination of brain maturation with a precision of approximately 2 weeks' PMA per 1-point increase of the score. The developmental stages observed in this study align with the existing literature, though very few ultrasound studies on postnatal cerebral development in preterm infants have focused on sulcal development and opercularization.^{7,24,25}

In our cohort, closure of the Sylvian fissure occurred at a mean PMA of 32.1 (SD, 2.3) weeks, which concurs with the anatomic study by Goldstein et al²⁶ demonstrating closure of the middle operculum at 32–35 weeks and completed development of the Sylvian fissure at a PMA of 32.5 weeks.

We observed the first visibility of the cingulate sulcus at a mean PMA of 26.5 (SD, 1.8) weeks, with the 25th and 75th percentile at 25 and 28 weeks. In prenatal ultrasound studies,^{2,18} the first shallow indentation was found slightly earlier at a mean PMA of 24 weeks, with the 25th and 75th percentiles at 23 and 26 weeks. Our findings are consistent with those of Slagle et al,²⁵ who described the first appearance on postnatal ultrasound at a mean of 26 weeks and an increasing depth in the midcoronal view with gestational age. Ruoss et al²² reported the first visibility of the cingulate sulcus in early postnatal MR imaging at a higher PMA around 28–33 weeks.

Antonio et al²⁷ suggested that assessing the cingulate sulcus and structures on the lateral surface on the brain, particularly opercularization forming the Sylvian fissure, provides reliable indicators of PMA. Our choice of these 3 structures for measurements is further supported by Murphy et al,²⁴ who demonstrated that the sulci with the most distinctive and consistent changes with advancing PMA were the cingulate sulcus in the midsagittal plane and the closure and infolding of the lateral sulcus in the midcoronal plane.

Incorporating these 3 robust measurements into a single score and dividing the score categories into easily memorizable thresholds offer the potential for this score to become a useful bedside tool for assessing the state of brain maturation with reasonable accuracy. The USBD exhibits a linear relationship with PMA from 22 to 36 weeks' PMA. On reaching its maximum value of 6 around 36 weeks PMA, it is no longer suitable for describing further brain development.

The score was developed in infants without acquired or congenital brain anomalies, limiting its routine use in preterm infants with these conditions. Nonetheless, the USBD can be applied for both cross-sectional and longitudinal ultrasound purposes in premature infants, independent of growth trajectories and percentiles for each individual structure. Longitudinal measurements could provide valuable early bedside evidence of delayed cerebral development resulting from postnatal complications during this vulnerable period of rapid brain maturation. This result has already been demonstrated in intrauterine studies of Sylvian fissure and

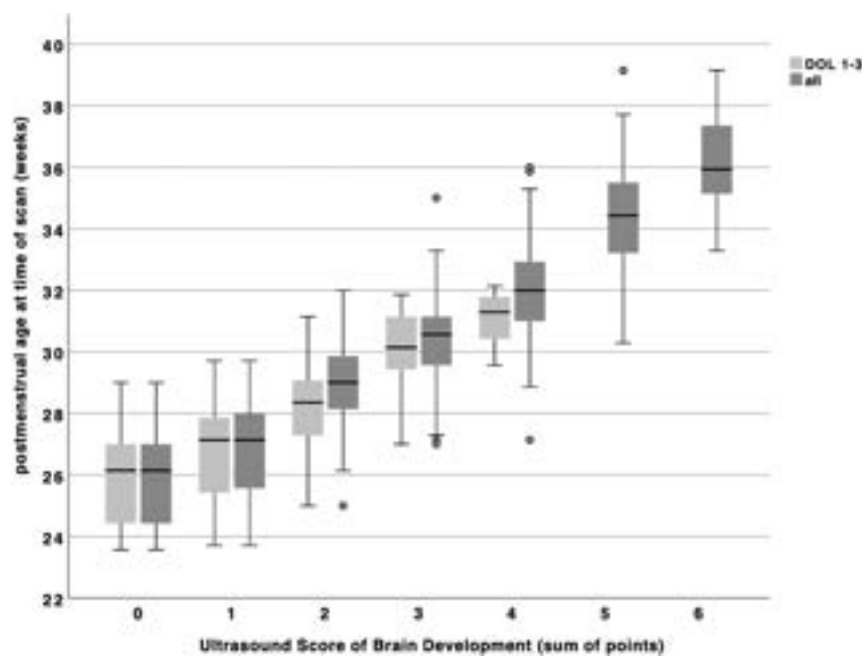


FIG 5. Boxplot of USBD score points by postmenstrual age grouped by day of scan: light gray including only scorable scans from DOL 1–3 ($n = 88$); dark gray including all scorable scans ($n = 312$).

cingulate sulcus development, which are components of the USBD.

A major limitation of our study was its retrospective design, which relied on the quality of archived ultrasound scans. Thirty-two scans had to be excluded from analysis because they were not performed specifically for measuring and symmetric visualization of the selected structures. This exclusion specifically limited the interpretation of the first appearance of the cingulate sulcus and therefore calculation of the USBD. We included only preterm infants born at or below 32 weeks' PMA because they are routinely monitored by a standard ultrasound protocol.

The number of scans at earlier than 25 weeks' PMA was limited and exhibited considerable variability in measurements. To increase the total number of available scans, we included serial scans from infants because the number of suitable patients was limited due to the single-center design. However, the correlation of the 3 selected structures as well as the USBD with PMA remained significant when only scans from DOL 1–3 were analyzed. Inter- and intrarater reproducibility and validity of the proposed scoring system should be determined in future prospective studies. These studies should encompass a more diverse cohort, including a larger number of infants with higher and lower PMAs at birth. Application of the USBD in different cohorts of infants with cerebral injury or other insults with an effect on cerebral development will assess its suitability for early bedside detection of disturbances in brain development.

CONCLUSIONS

This study introduces a novel, pragmatic bedside ultrasound scoring system to assess brain maturation in very preterm infants. By incorporating measurements of 3 easily identifiable landmark structures in a single ultrasound plane, our scoring system achieves reliable discrimination of brain maturation with a

precision of approximately 2 weeks' PMA. The developmental stages observed are consistent with the existing literature. This scoring system has the potential to become a useful bedside tool for accurately assessing brain maturation in preterm infants.

Disclosure forms provided by the authors are available with the full text and PDF of this article at www.ajnr.org.

REFERENCES

- Achiron R, Achiron A. **Development of the human fetal corpus callosum: a high-resolution, cross-sectional sonographic study.** *Ultrasound Obstet Gynecol* 2001;18:343–47 CrossRef Medline
- Cohen-Sacher B, Lerman-Sagie T, Lev D, et al. **Sonographic developmental milestones of the fetal cerebral cortex: a longitudinal study.** *Ultrasound Obstet Gynecol* 2006;27:494–502 CrossRef Medline
- Harreld JH, Bhore R, Chason DP, et al. **Corpus callosum length by gestational age as evaluated by fetal MR imaging.** *AJNR Am J Neuroradiol* 2011;32:490–94 CrossRef Medline
- Cignini P, Padula F, Giorlandino M, et al. **Reference charts for fetal corpus callosum length: a prospective cross-sectional study of 2950 fetuses.** *J Ultrasound Med* 2014;33:1065–78 CrossRef Medline
- Koning IV, Roelants JA, Groenenberg IAL, et al. **New ultrasound measurements to bridge the gap between prenatal and neonatal brain growth assessment.** *AJNR Am J Neuroradiol* 2017;38:1807–13 CrossRef Medline
- Rodriguez-Sibaja MJ, Villar J, Ohuma EO, et al. **Fetal cerebellar growth and Sylvian fissure maturation: international standards from Fetal Growth Longitudinal Study of INTERGROWTH-21st Project.** *Ultrasound Obstet Gynecol* 2021;57:614–23 CrossRef Medline
- Klebermass-Schrehof K, Moerth S, Vergesslich-Rothschild K, et al. **Regional cortical development in very low birth weight infants with normal neurodevelopmental outcome assessed by 3D-ultrasound.** *J Perinatol* 2013;33:533–37 CrossRef Medline
- Klebermass-Schrehof K, Aumuller S, Goeral K, et al. **Biometry of the corpus callosum assessed by 3D ultrasound and its correlation to neurodevelopmental outcome in very low birth weight infants.** *J Perinatol* 2017;37:448–53 CrossRef Medline

9. Benavente-Fernández I, Rodríguez-Zafra E, León-Martínez J, et al. **Normal cerebellar growth by using three-dimensional US in the preterm infant from birth to term-corrected age.** *Radiology* 2018;288:254–61 CrossRef Medline
10. Cuzzilla R, Spittle AJ, Lee KJ, et al. **Postnatal brain growth assessed by sequential cranial ultrasonography in infants born <30 weeks' gestational age.** *AJNR Am J Neuroradiol* 2018;39:1170–76 CrossRef Medline
11. Wu PM, Shih HI, Yu WH, et al. **Corpus callosum and cerebellar vermis size in very preterm infants: relationship to long-term neurodevelopmental outcome.** *Pediatr Neonatol* 2019;60:178–85 CrossRef Medline
12. Huang HC, Chou HC, Tsao PN, et al. **Linear growth of corpus callosum and cerebellar vermis in very-low-birth-weight preterm infants.** *J Formos Med Assoc* 2020;119:1292–98 CrossRef Medline
13. Aisa MC, Barbati A, Gerli S, et al. **Brain 3D-echographic early predictors of neuro-behavioral disorders in infants: a prospective observational study.** *J Matern Fetal Neonatal Med* 2022;35:642–50 CrossRef Medline
14. Arena R, Gallini F, De Rose DU, et al. **Brain Growth Evaluation Assessed with Transfontanellar (B-GREAT) ultrasound: old and new bedside markers to estimate cerebral growth in preterm infants—a pilot study.** *Am J Perinatol* 2022 Jan 4 [Epub ahead of print] CrossRef Medline
15. Teli R, Hay M, Hershey A, et al. **Postnatal microstructural developmental trajectory of corpus callosum subregions and relationship to clinical factors in very preterm infants.** *Sci Rep* 2018;8:7550 CrossRef Medline
16. Thompson DK, Inder TE, Faggian N, et al. **Characterization of the corpus callosum in very preterm and full-term infants utilizing MRI.** *Neuroimage* 2011;55:479–90 CrossRef Medline
17. Husen SC, Koning IV, Go A, et al. **Three-dimensional ultrasound imaging of fetal brain fissures in the growth restricted fetus.** *PLoS One* 2019;14:e0217538 CrossRef Medline
18. Pistorius LR, Stoutenbeek P, Groenendaal F, et al. **Grade and symmetry of normal fetal cortical development: a longitudinal two- and three-dimensional ultrasound study.** *Ultrasound Obstet Gynecol* 2010;36:700–08 CrossRef Medline
19. Quarello E, Stirnemann J, Ville Y, et al. **Assessment of fetal Sylvian fissure operculization between 22 and 32 weeks: a subjective approach.** *Ultrasound Obstet Gynecol* 2008;32:44–49 CrossRef Medline
20. Paules C, Miranda J, Policiano C, et al. **Fetal neurosonography detects differences in cortical development and corpus callosum in late-onset small fetuses.** *Ultrasound Obstet Gynecol* 2021;58:42–47 CrossRef Medline
21. Welling MS, Husen SC, Go A, et al. **Growth trajectories of the human fetal brain in healthy and complicated pregnancies and associations with neurodevelopmental outcome in the early life course.** *Early Hum Dev* 2020;151:105224 CrossRef Medline
22. Ruoss K, Lövblad K, Schroth G, et al. **Brain development (sulci and gyri) as assessed by early postnatal MR imaging in preterm and term newborn infants.** *Neuropediatrics* 2001;32:69–74 CrossRef Medline
23. van der Knaap MS, van Wezel-Meijler G, Barth PG, et al. **Normal gyration and sulcation in preterm and term neonates: appearance on MR images.** *Radiology* 1996;200:389–96 CrossRef Medline
24. Murphy NP, Rennie J, Cooke RW. **Cranial ultrasound assessment of gestational age in low birthweight infants.** *Arch Dis Child* 1989;64:569–72 CrossRef Medline
25. Slagle TA, Oliphant M, Gross SJ. **Cingulate sulcus development in preterm infants.** *Pediatr Res* 1989;26:598–602 CrossRef Medline
26. Goldstein IS, Erickson DJ, Sleeper LA, et al. **The lateral temporal lobe in early human life.** *J Neuropathol Exp Neurol* 2017;76:424–38 CrossRef Medline
27. Antonio GE, Chu WC, Yeung DK, et al. **Imaging of the developing brain.** *Neuroembryol Aging* 2008;5:23–31 CrossRef

Predicting Drug Treatment Outcomes in Childrens with Tuberos Sclerosis Complex–Related Epilepsy: A Clinical Radiomics Study

Z. Hu, D. Jiang, X. Zhao, J. Yang, D. Liang, H. Wang, C. Zhao, and J. Liao



ABSTRACT

BACKGROUND AND PURPOSE: Highly predictive markers of drug treatment outcomes of tuberous sclerosis complex–related epilepsy are a key unmet clinical need. The objective of this study was to identify meaningful clinical and radiomic predictors of outcomes of epilepsy drug treatment in patients with tuberous sclerosis complex.

MATERIALS AND METHODS: A total of 105 children with tuberous sclerosis complex–related epilepsy were enrolled in this retrospective study. The pretreatment baseline predictors that were used to predict drug treatment outcomes included patient demographic and clinical information, gene data, electroencephalogram data, and radiomic features that were extracted from pretreatment MR imaging scans. The Spearman correlation coefficient and least absolute shrinkage and selection operator were calculated to select the most relevant features for the drug treatment outcome to build a comprehensive model with radiomic and clinical features for clinical application.

RESULTS: Four MR imaging–based radiomic features and 5 key clinical features were selected to predict the drug treatment outcome. Good discriminative performances were achieved in testing cohorts (area under the curve = 0.85, accuracy = 80.0%, sensitivity = 0.75, and specificity = 0.83) for the epilepsy drug treatment outcome. The model of radiomic and clinical features resulted in favorable calibration curves in all cohorts.

CONCLUSIONS: Our results suggested that the radiomic and clinical features model may predict the epilepsy drug treatment outcome. Age of onset, infantile spasms, antiseizure medication numbers, epileptiform discharge in left parieto-occipital area of electroencephalography, and gene mutation type are the key clinical factors to predict the epilepsy drug treatment outcome. The texture and first-order statistic features are the most valuable radiomic features for predicting drug treatment outcomes.

ABBREVIATIONS: ASM = antiseizure medication; AUC = area under the receiver operating curve; EEG = electroencephalography; GLCM = gray-level co-occurrence matrix; GLDM = gray-level dependence matrix; GLRLM = gray-level run-length matrix; GLSZM = gray-level size zone matrix; LASSO = least absolute shrinkage and selection operator; TSC = tuberous sclerosis complex

Tuberous sclerosis complex (TSC) is a rare autosomal dominant disorder caused by loss-of-function mutations of the *TSC1* or *TSC2* genes, which can affect multiple organ systems¹

and is frequently associated with tumors of the brain, skin, heart, lungs and kidneys, seizures, and TSC-associated neuropsychiatric disorders, including autism spectrum disorder and cognitive disability.² Epilepsy is the most common and clinically challenging symptom of TSC, affecting approximately 85% of patients,^{3,4} of which nearly two-thirds have the first seizure in the first year of life.^{5,6}

The goal of treatment in TSC is to prevent or control seizures as soon as possible after TSC diagnosis, which will improve cognitive neurodevelopment and enhance the quality of life.³ The

Received July 31, 2022; accepted after revision May 22, 2023.

From the Departments of Neurology (Z.H., X.Z., J.L.) and Radiology (C.Z.), Shenzhen Children's Hospital, Shenzhen, China; Research Centre for Medical AI (D.J., J.Y., D.L.) and Paul C. Lauterbur Research Center for Biomedical Imaging (D.L., H.W.), Shenzhen Institutes of Advanced Technology, Chinese Academy of Sciences, Shenzhen, Guangdong, China; and Shenzhen College of Advanced Technology (D.J., J.Y., D.L.), University of Chinese Academy of Sciences, Shenzhen, Guangdong, China.

Zhanqi Hu, Dian Jiang, and Xia Zhao contributed equally to this study and are co-first authors.

Some of the work was partially supported by the Sanming Project of Medicine in Shenzhen (SZSM201812005), Shenzhen Key Medical Discipline Construction Fund (No.SZXK033), Shenzhen Fund for Guangdong Provincial High-Level Clinical Key Specialties (No.SZGSP012), Pearl River Talent Recruitment Program of Guangdong Province (2019QN01Y986), Shenzhen Science and Technology Program (JCYJ20210324115810030), National Natural Science Foundation of China (61871373, 81729003, and 81901736), and Shenzhen Fundamental Research Program (JCYJ2018 0228175428243).

Please address correspondence to Jianxiang Liao, MD, Department of Neurology, Shenzhen Children's Hospital, 7019, Yitian Rd, Shenzhen 518038, China; e-mail: liaojianxiang@vip.sina.com

Indicates open access to non-subscribers at www.ajnr.org

Indicates article with online supplemental data.

<http://dx.doi.org/10.3174/ajnr.A7911>

classic treatment for epilepsy is antiseizure medication (ASM).⁷ However, >50% of patients with TSC will develop drug-resistant epilepsy,^{8,9} and diagnosing it may take a long time.¹⁰ Therefore, there is an urgent need to investigate the predictive biomarkers for the effectiveness of ASM treatment for patients with epilepsy.

Nervous system manifestations can be observed in almost all cases of TSC, and MR imaging is a technique used routinely to diagnose TSC.¹¹ Cortical tubers are major TSC-related brain manifestations, which show abnormal high or low signals in FLAIR sequences.¹² In addition, FLAIR imaging is widely used to study the epileptogenic zone¹³ and epilepsy mechanism of TSC.¹⁴ Jesmanas et al⁹ reported that MR imaging-defined tuber types were found to be associated with early seizure onset in TSC. In addition, lesion location and type of information features in MR imaging have been shown to be associated with the outcomes of epilepsy drug treatment.¹⁰ However, the features of MR imaging were typically extracted manually, and the description of these features was usually qualitative, subjective, and nonspecific.

Radiomics is an emerging research branch in the field of medical imaging, which aims to extract mineable high-dimensional data from clinical images.^{15,16} Radiomics capture tissue and lesion characteristics, such as heterogeneity, texture, and shape and can be used alone or in combination with demographic, histologic, genomic, or proteomic data to solve clinical problems.¹⁷ Radiomic analyses have been successfully applied to predict the type of tumor-related epilepsy or epilepsy presentation¹⁸⁻²² and treatment outcomes for cancer.²³⁻²⁷ Thus, a noninvasive biomarker based on radiomic analyses that can predict the drug treatment outcome in patients with TSC would be valuable.

In this study, we used FLAIR scans to extract radiomic features including shape, first-order statistics, and textural features that are associated with the drug treatment outcome in patients with TSC. Moreover, we constructed a machine learning model to investigate how accurately we can predict the drug treatment outcome in patients with TSC using radiomic and clinical information.

MATERIALS AND METHODS

Patients

A total of 105 patients with TSC at Shenzhen Children's Hospital between January 2013 and September 2018 were consecutively enrolled in this retrospective study, and informed consent was obtained from all patients before the study. The protocols were approved by the Ethics Committee of Shenzhen Institutes of Advanced Technology, Chinese Academy of Sciences. We included patients who met the following criteria: 1) They had undergone FLAIR MR imaging before ASM treatment, 2) electroencephalography (EEG) was recorded on admission or as an outpatient, 3) they had ASM treatment for at least 1 year, and 4) the ages at MR imaging were younger than 6 months.

Drug treatment outcome was defined according to the Gül Mert et al⁶ and was recorded as controlled or uncontrolled. Patients were considered as controlled if they had not had clinical seizures for at least 1 year. Uncontrolled patients had at least 1 seizure in the past year. Data were randomly split into a training data set ($n = 75$) and an independent test data set ($n = 30$). We

used stratified random sampling to ensure the same class ratios for every set. There was no patient overlap between the training and test sets. The training data set was used to derive clinical and radiomic predictors of epilepsy; then, the classification performance of these predictors was internally validated on the test data set.

Data of 59 routine clinical variables were collected, including patient information, such as sex, age, typical symptoms of TSC, and examination results, as well as *TSC1* and *TSC2* gene test results and EEG features and so forth. This study further used the clinical and MR imaging data of all enrolled cases. The flow chart of the study is illustrated in Fig 1.

Image Acquisition

All MR imaging examinations were performed using a Magnetom Trio 3T scanner (Siemens) with an 8-channel receive-only head coil acquisition. The FLAIR parameters were as follows: TR = 9000 ms, TE = 132 ms, TI = 2600 ms, flip angle = 150°, FOV = 230 × 194 mm², voxel size = 0.7 × 0.7 × 6.0 mm³, and matrix = 320 × 224. The MR imaging data were stored in DICOM format.

Image Processing and Segmentation

In neuroimaging studies, the ROIs are located in the brain tissue. Therefore, we removed the nonbrain tissue in MR imaging using a deep learning model.²⁸

ROIs of the cortical tubers and migration lines were manually drawn by 2 neuroradiologists with >15 years of experience who were blinded to clinical data using open-source software (ITK-SNAP, Version 3.8.0; <http://www.itksnap.org>). ROIs were merged when the difference between the individual ROIs determined by the 2 neuroradiologists was <5%. When there was a >5% difference between these 2 ROIs, the ROI used was determined by a senior neuroradiologist. ROIs of the cortical tubers and migration lines were defined as areas of the MR images that exhibited abnormal hyperintense or hypointense signals. Figure 2 shows some cases of FLAIR images with and without lesions and segmentation in children with TSC. Figure 2A shows the FLAIR images of some children with TSC with lesions, and Fig 2B is the segmentation of Fig 2A. Figure 2C shows the FLAIR images of some children with TSC without lesions.

Radiomic Feature Extraction

Due to differences in equipment parameters such as layer thickness and pixel pitch of MR images, all images were resampled to 1 × 1 × 1 mm³. A publicly available Python package, pyradiomics 3.0.1 (<https://pypi.org/project/pyradiomics/>), was used to extract radiomic features.²⁹ A total of 1132 features consisting of gray-level co-occurrence matrix (GLCM), gray-level run-length matrix (GLRLM), gray-level size zone matrix (GLSZM), gray-level dependence matrix (GLDM), first-order, and shape features were extracted from ROIs on FLAIR.

First-order features described the distribution of voxel intensity within the ROI 3D matrix and the overall information about the cortical tubers. The shape features reflected the volume, surface area, and shape of the cortical tubers. GLCM, GLRLM, GLSZM, and GLDM were collectively referred to as texture

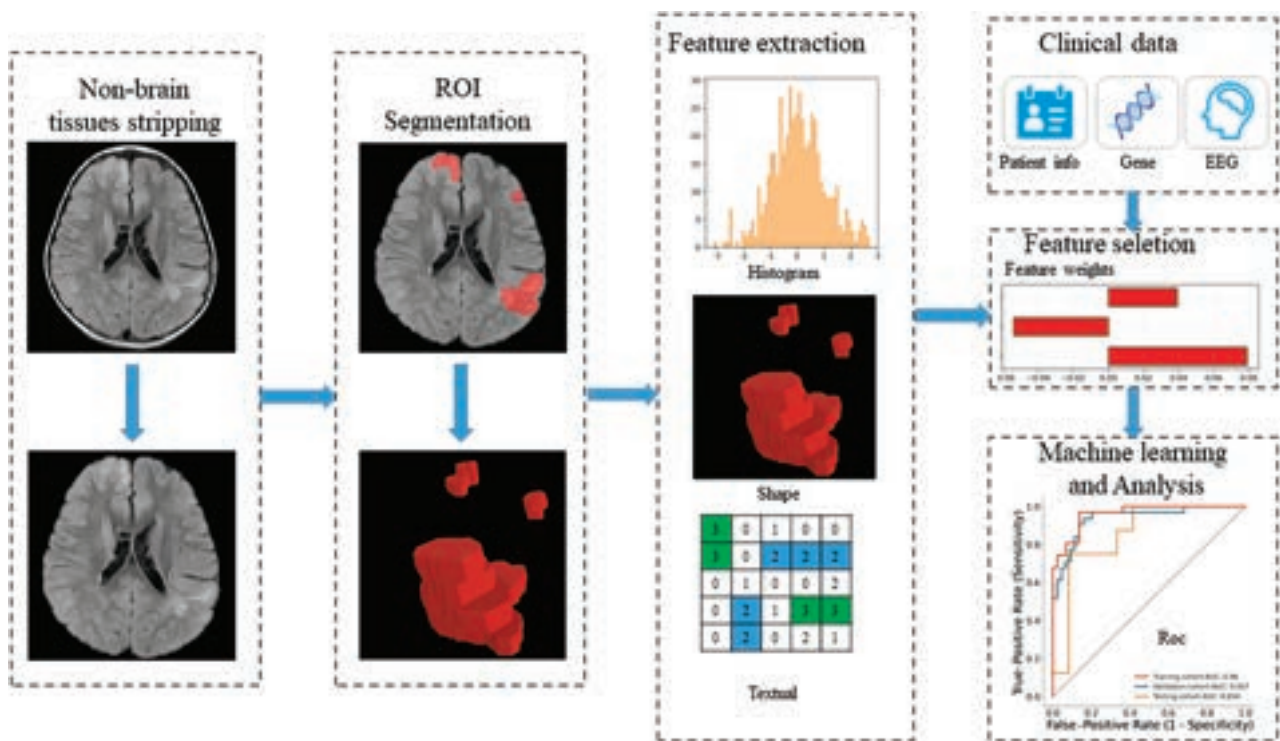


FIG 1. The flowchart of the current study. Patient information, including sex, age, the existence of typical symptoms of TSC, and some examination results. *TSC1* and *TSC2* were gene test results.

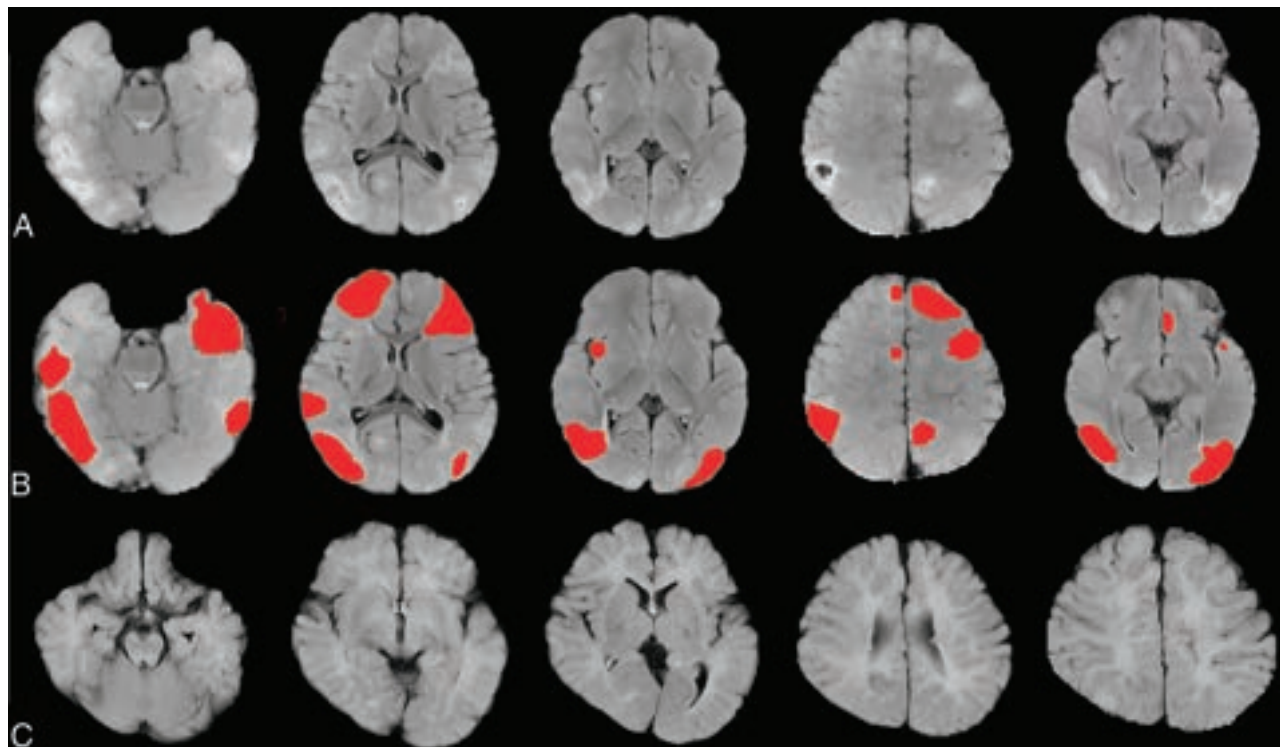


FIG 2. Some cases of FLAIR images with and without lesions and segmentation in children with TSC. A, The FLAIR images of some children with TSC with lesions. B, The segmentation of A. C, The FLAIR image of some children with TSC without lesions. The red color represents the segmentation of lesions.

features. The detailed information and formulas for the detection of the 1132 radiomic features are described in <https://pyradiomics.readthedocs.io/en/latest/>.

Feature Selection

The 1132 radiomic features and 59 routine clinical variables were normalized with *z* score normalization before feature selection.

Table 1: The radiomic and clinical features selected by LASSO regression

Selected Features	P Value of Spearman Correlation ^a	Coefficients of LASSO
Radiomic features		
log-sigma-2-0-mm-3D_gldm_SmallDependenceHighGrayLevelEmphasis	.030	0.026695
wavelet-LLH_glcml_dmn	.036	-0.051160
wavelet-LLL_firstorder_10Percentile	.012	0.023878
wavelet-LLL_firstorder_Mean	.035	0.050790
Clinical features		
Age of onset	<.001	0.117626
Infantile spasms	<.001	-0.147036
Epileptiform discharge in left parieto-occipital area of EEG	<.001	0.098540
ASM numbers	.018	-0.132026
Gene mutation type	.025	-0.047780

First, a bivariate analysis was conducted to screen the radiomic and clinical features. We calculated the *P* values of the Spearman correlation coefficient between each feature and the treatment outcome and identified the features with *P* values < .05. Least absolute shrinkage and selection operator (LASSO) was widely used to compress the coefficients of features and select features to prevent overfitting, so we used a LASSO algorithm to select the key radiomic and clinical features.

Development and Evaluation of an Individualized Prediction Model

On the basis of a cohort of all patients, we used 11 machine learning classifiers, such as support vector machines, random forest, logistic regression, AdaBoost (<https://www.machinelearningplus.com/machine-learning/introduction-to-adaboost>), gradient boosting, and decision tree to build models to predict treatment outcome with clinical information and radiomic features.

Each classifier was trained on the training set using a 10-fold cross-validation procedure and the training process needed to determine the optimal hyperparameters of the classifiers, which were determined by grid search. We selected the best classifier by comparing the performance of classifiers on the validation set. The classifier that achieved the highest area under the receiver operating curve (AUC) score was selected as a candidate solution.

Once trained, the best model was evaluated on the test set. The classification performance of the model was assessed by the receiver operating characteristic curves and AUCs in each cohort. Calibration curves were also plotted to assess the calibration of the radiomic and clinical features.³⁰

Statistical Analysis

In this study, we use frequencies and percentages for categorical variables and median and range for continuous variables. The differences between groups were assessed by an independent samples *t* test, and *P* < .05 was defined as significant. Model training, validation, and testing were implemented with Python (Version 3.8.0).

RESULTS

Demographic and Clinical Data

The main clinical and pathologic characteristics of all 105 patients are listed in the Online Supplemental Data. Of the 105 enrolled patients, 43 (40.9%) were controlled and 62 (59.1%) were

uncontrolled by drug treatment. Age of onset, infantile spasms, gene mutation type, ASM numbers, and epileptiform discharge in the left parieto-occipital area of the EEG were significantly different between the controlled and uncontrolled patients (*P* < .05).

Performance of the Radiomic Signature

Four key radiomic features and 5 clinical features were selected using the Spearman correlation analysis and LASSO regression (Table 1), and the distribution of each radiomic feature in the controlled

and uncontrolled groups is shown in Fig 3A–D. According to the AUC of the validation set that was used to select the best hyperparameters and model, the best classification model is logistic regression (Fig 4). The predictive ability of the model with radiomic and clinical features was shown by the receiver operating characteristic curve (Fig 5A), achieving the best performance of AUC = 0.96, classification accuracy = 90.7%, sensitivity = 0.97, and specificity = 0.86 in the training cohort; AUC = 0.94, classification accuracy = 88.0%, sensitivity = 0.94, and specificity = 0.84 in the validation cohort; and AUC = 0.854, classification accuracy = 80.0%, sensitivity = 0.75, and specificity = 0.83 in the test cohort, respectively. Table 2 shows the test set results on logistic regression models with input of clinical features alone and with input of radiomic and clinical features. Figure 6 shows a performance comparison of clinical features alone and radiomic and clinical features on a logistic regression model in the testing cohorts. The results of the test set with the logistic regression model are shown in Table 2. The model of radiomic and clinical features demonstrated favorable calibration in the training, validation, and testing cohorts (Fig 5B). Figure 5C–E shows the waterfall plots of radiomics and the clinical model to differentiate controlled from uncontrolled patients in the training, validation, and testing cohorts.

DISCUSSION

With the increasing use of drug treatments in epilepsy, a better understanding of patient response to the treatment could help identify the optimal treatment strategy for individual patients.¹⁰ Radiomic approaches, when combined with clinical data, could improve treatment selection. In this study, a prediction model of drug treatment outcome based on radiomic data from MR imaging and clinical data was developed. The results demonstrate that the MR imaging–based radiomic and clinical models could successfully predict the outcome of epilepsy drug treatment among children with TSC.

Reliable prediction of epilepsy drug treatment outcome allows the development of a more targeted treatment, and those patients proved to be drug-resistant should be considered for surgical procedures or other treatment options to increase the curative ratio and reduce mortality.^{31,32} However, determining the epilepsy drug treatment outcome on the basis of its clinical and treatment presentation imposes an apparent lag. Thus, there is a need for a

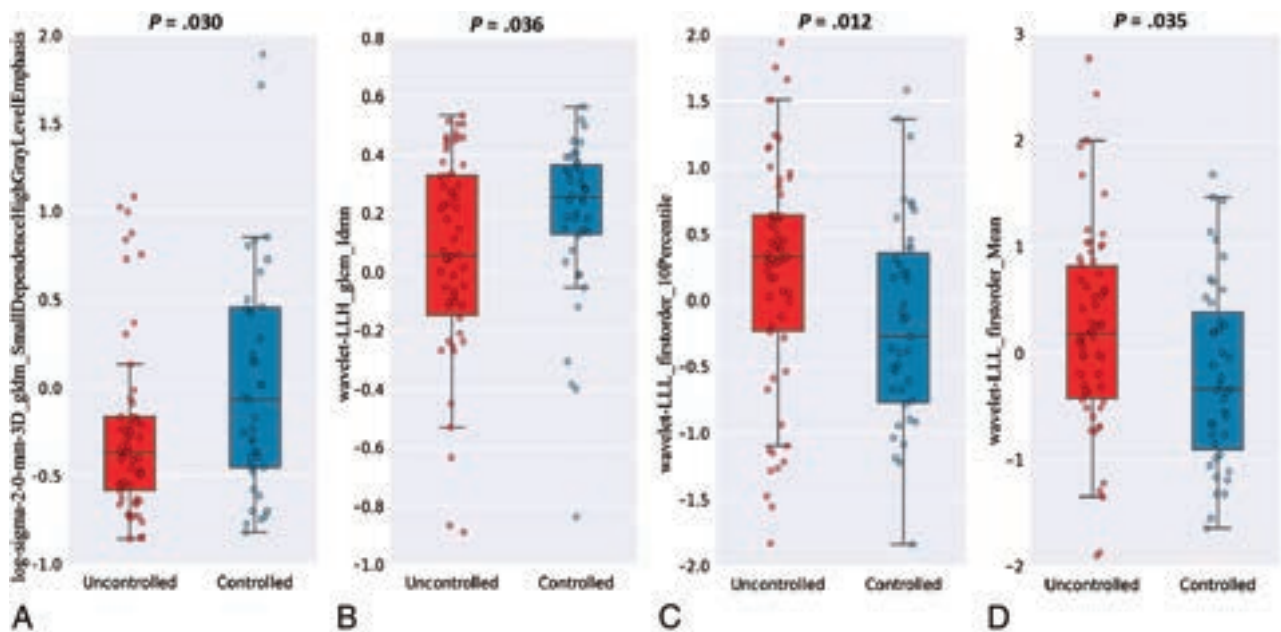


FIG 3. Boxplot of the 4 selected values of radiomic features in controlled and uncontrolled groups. The small *blue and red circles* represent the value of each radiomic feature in the controlled and uncontrolled groups. The *middle line* of the boxplot is the median of the radiomic feature, representing the average level of the radiomic feature. The *upper and lower bounds* of the boxplot are the upper and lower quartiles of the radiomic feature data, respectively. *P* values are the results of the Spearman correlation test.

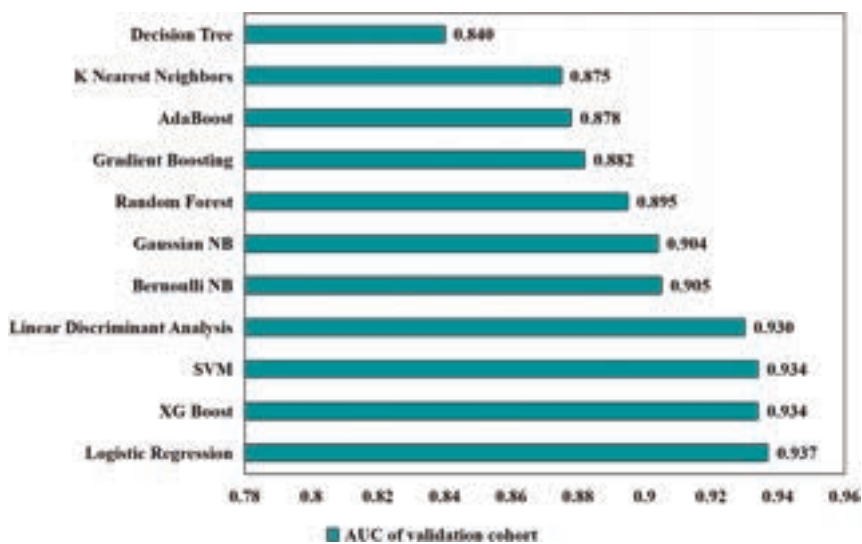


FIG 4. The AUC scores of 11 machine learning models in the validation cohort. According to the AUC of the validation set that was used to select the best hyperparameters and model, the best classification model of radiomic and clinical features is logistic regression. NB indicates Naive Bayes; SVM, support vector machine; XG, eXtreme Gradient.

clinical model capable of predicting epilepsy drug treatment outcome before treatment initiation. In this study, a new model with radiomic and clinical features was developed at baseline to predict the epilepsy drug treatment outcome for patients with TSC, which will provide clinicians with a reliable and noninvasive tool to better select patients for epilepsy drug treatment.

With the rapid development of machine learning and image-processing techniques, a number of studies have developed radiomics-based predictive models for various clinical characteristics, including pathologic grade^{33,34} and treatment and survival

outcomes.^{35,36} The rapid increase of the radiomic application is driven by enriched quantitative image features that clinicians can extract from medical images with high efficiency to guide clinical decision-making.³⁷ Moreover, some researchers have successfully applied radiomic analysis to predict tumor-related epilepsy by combining various quantitative MR imaging features.^{18,20-22} Their works mainly focused on tumor-related epilepsy. However, epilepsy caused by TSC is different. It has distinct clinical manifestations and presentations on MR imaging.¹⁰

To our knowledge, this is the first study to show that radiomics can be used to predict the outcome of epilepsy drug treatment in patients with TSC. Therefore, we tried to demonstrate the associations of these radiomics-based MR imaging features with TSC-related epilepsy drug treatment outcome, and we have achieved a relatively high discrimination accuracy and AUC in all cohorts, which suggest that the radiomic model developed in this study was effective in predicting the outcome of epilepsy drug treatment.

In our study, we selected 4 radiomic features to predict drug treatment outcomes, including log-sigma-2-0-mm-3D_gldm_SmallDependenceHighGrayLevelEmphasis (L_gldm_S), wavelet-LLH_glcM_Idmn (W_glcM_I), wavelet-LLL_firstorder_10Percentile (W_firstorder_10), and wavelet-LLL_firstorder_Mean (W_firstorder_M). L_gldm_S and W_glcM_I are texture features

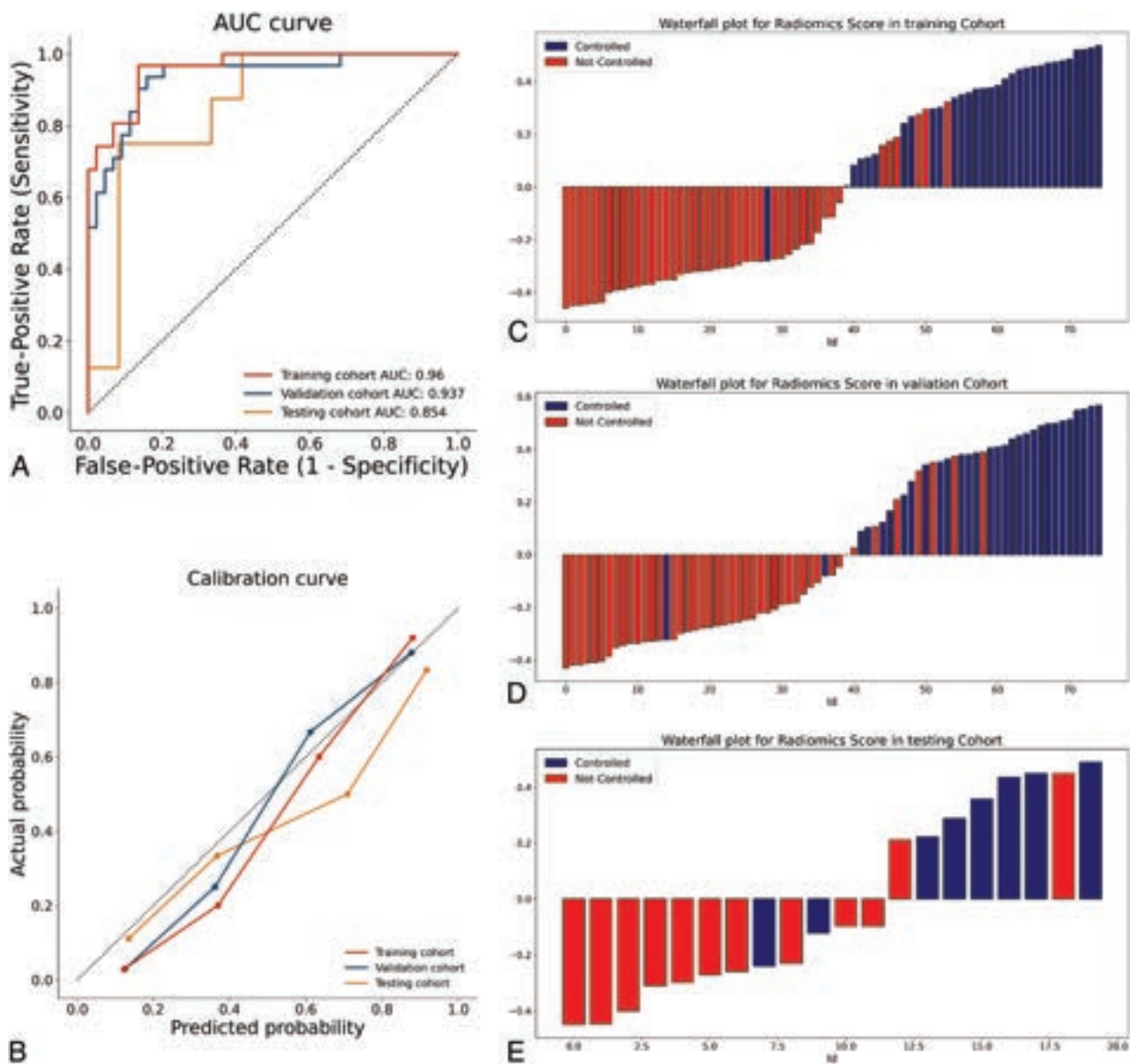


FIG 5. Receiver operating characteristic curve (A), calibration curve (B), and waterfall plots (C–E) of the radiomic and clinical features model in training, cross-validation, and testing cohorts.

Table 2: The results of the logistic regression model in testing cohorts

Input Features	Model	AUC	ACC	SEN	SPE
Clinical features	Logistic regression	0.783	0.767	0.769	0.765
Radiomic and clinical features	Logistic regression	0.854	0.800	0.750	0.830

Note:—ACC indicates accuracy; SEN, sensitivity; SPE, specificity.

that reflect the homogeneity of the tubers. *W_firstorder_10* and *W_firstorder_M* are first-order statistical features that reflect the distribution of signal intensities within the tuber region. Our results imply that the texture features and first-order statistical features are valuable for predicting drug treatment outcomes. Zhao et al³⁸ had reported that the type II lesions (the uneven thickening of the cortex on T2-weighted and FLAIR) were statistically significant between the uncontrolled and controlled groups, similar to findings in our research. MR imaging lesion type features are related to outcomes of epilepsy drug treatment in TSC,^{10,12} which can

indirectly support our present results because the types of lesions are generally classified clinically according to texture structure and the signal intensity of the lesions.

Additionally, our model incorporated both radiomic features and clinical characteristics that are helpful for prediction, such as the age of onset, infantile spasms, ASM numbers, epileptiform discharge in left parieto-occipital area of the EEG, and gene mutation type, making our model more comprehensive and reliable for clinical application. Our study found that about 59.1% of patients with TSC were in the uncontrolled group. It was reported that the drug resistance ratios of TSC-related epilepsy were 59.6%,³⁸ 60%,⁵ and 62%,³⁹ which were similar to those in our study. In addition, about 30 (48.4%) patients in the uncontrolled group had experienced infantile spasms, and 4 (9.3%) patients in the

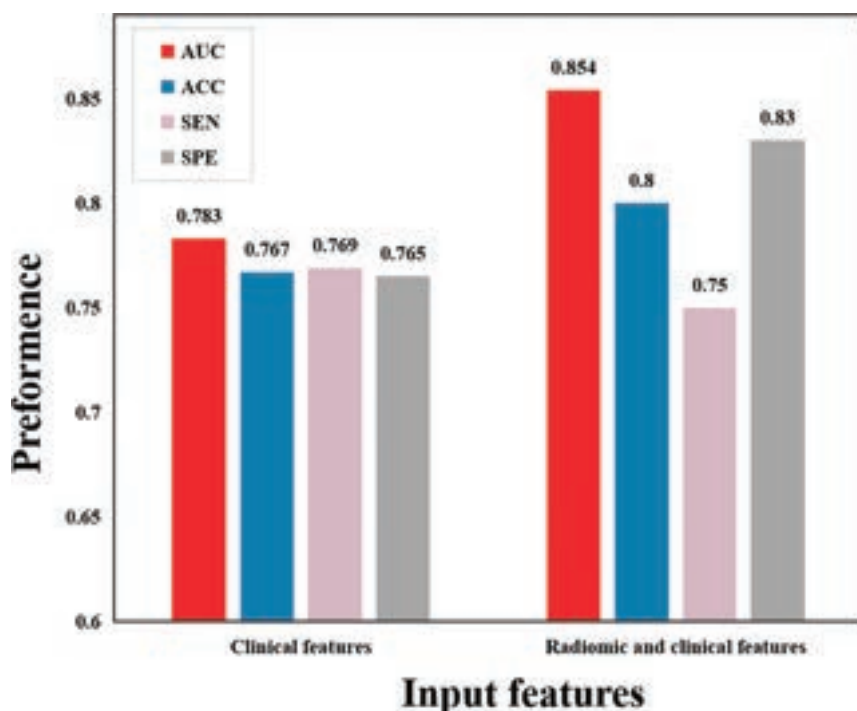


FIG 6. The performance comparison of clinical features alone and radiomic and clinical features on a logistic regression model in testing cohorts. ACC indicates accuracy; SEN, Sensitivity; SPE, specificity.

controlled group had experienced infantile spasms. Previous studies have shown similar results: TSC patients with infantile spasms are more likely to develop drug resistant epilepsy.^{4,40} In our study, the mean age of seizure onset was 10.34 months in the uncontrolled group and 31.17 months in the controlled group. Patients with TSC epilepsy before 1 year of age are more likely to develop resistance than those with onset after 1 year of age,⁴⁰ consistent with our results. Compared with *TSC1* pathogenic mutations, *TSC2* mutations have a more severe clinical phenotype, and the conditions of these patients are usually more difficult to control,^{39,41} consistent with our findings that the proportion of *TSC2* gene mutations was higher in the uncontrolled group.

Our results showed that the severity of EEG discharge in the left parieto-occipital area was correlated with the epilepsy drug treatment outcome, and the EEG discharge in the uncontrolled group was more serious. Previous reports also showed similar results. Some patients with TSC with severe EEG discharges have multifocal EEG discharges related to bilateral asymmetric spike-and-wave complexes. The onset is partial seizures or convulsive seizures, which later develop into drug-resistant epilepsy.^{39,40} In a study of 83 patients with TSC, ASM numbers have been reported as an important risk factor for development of refractory epilepsy in patients with TSC.⁶ In our study, the history of using >3 ASMs is the risk factor that will lead to occurrence of drug-resistant epilepsy.

LASSO is a widely accepted algorithm in feature selection. The 1132 radiomics features extracted in this study may cause overfitting when constructing the model. Therefore, feature dimension reduction and selection were performed to screen the key features that are most closely related to the epilepsy drug

treatment outcome using bivariate analysis and the LASSO algorithm. With features associated with epilepsy drug treatment outcome, we used 11 classic machine learning models for classification and selected the best model on the basis of AUC of cross-validation. Finally, we evaluated the performance of the selected model on the independent test set consisting of unseen data.

Although this study is novel and conducted with advanced methodology, there are several limitations. First, it is a single-center cohort study, and a multi-center cohort study should be further considered to verify the findings of this study. Second, the data set is relatively small because TSC is a rare disease. However, we will collect more data from additional patients with TSC and will use advanced algorithms such as deep learning to make more precise predictions in the future. Finally, our study used only the MR imaging technique, which contains limited information. We will explore the multimodal data such as

CT and PET to construct a more comprehensive radiomic model in future exploration.

CONCLUSIONS

Our study suggests that radiomics could be a noninvasive, efficient, and reliable way to predict patient outcome to drug treatment when combined with clinical data. Furthermore, we identified novel models containing informative clinical covariates and radiomic image features to predict drug treatment outcome. Our results implied that the texture features and first-order statistics features are the most valuable radiomic features for predicting drug treatment outcomes. Age of onset, infantile spasms, ASM numbers, epileptiform discharge in the left parieto-occipital area of EEG, and gene mutation type are the key clinical factors that are most likely to predict the epilepsy drug treatment outcome.

Disclosure forms provided by the authors are available with the full text and PDF of this article at www.ajnr.org.

REFERENCES

- Randle SC. **Tuberous sclerosis complex: a review.** *Pediatr Ann* 2017;46:e166–71 CrossRef Medline
- Henske EP, Józwiak S, Kingswood JC, et al. **Tuberous sclerosis complex.** *Nat Rev Dis Primers* 2016;2:16035 CrossRef Medline
- Curatolo P, Nabbout R, Lagae L, et al. **Management of epilepsy associated with tuberous sclerosis complex: updated clinical recommendations.** *Eur J Paediatr Neurol* 2018;22:738–48 CrossRef Medline
- Słowińska M, Józwiak S, Peron A, et al. **Early diagnosis of tuberous sclerosis complex: a race against time: how to make the diagnosis before seizures?** *Orphanet J Rare Dis* 2018;13:25 CrossRef Medline

5. Fohlen M, Taussig D, Ferrand-Sorbets S, et al. **Refractory epilepsy in preschool children with tuberous sclerosis complex: early surgical treatment and outcome.** *Seizure* 2018;60:71–79 CrossRef Medline
6. Gül Mert G, Altunbaşak Ş, Hergüner Ö, et al. **Factors affecting epilepsy prognosis in patients with tuberous sclerosis.** *Childs Nerv Syst* 2019;35:463–68 CrossRef Medline
7. van der Poest Clement E, Jansen FE, Braun KP, et al. **Update on drug management of refractory epilepsy in tuberous sclerosis complex.** *Paediatr Drugs* 2020;22:73–84 CrossRef Medline
8. Jóźwiak S, Kotulska K, Domańska-Pakiela D, et al. **Antiepileptic treatment before the onset of seizures reduces epilepsy severity and risk of mental retardation in infants with tuberous sclerosis complex.** *Eur J Paediatr Neurol* 2011;15:424–31 CrossRef Medline
9. Jesmanas S, Norvainytė K, Gleiznienė R, et al. **Different MRI-defined tuber types in tuberous sclerosis complex: quantitative evaluation and association with disease manifestations.** *Brain Dev* 2018;40:196–204 CrossRef Medline
10. Yang J, Zhao C, Su S, et al. **Machine learning in epilepsy drug treatment outcome prediction using multi-modality data in children with tuberous sclerosis complex.** In: *Proceedings of the 2020 6th International Conference on Big Data and Information Analytics (BigDIA)*, Shenzhen, China; December 4–6, 2020
11. Russo C, Nastro A, Cicala D, et al. **Neuroimaging in tuberous sclerosis complex.** *Childs Nerv Syst* 2020;36:2497–509 CrossRef Medline
12. Grilli G, Moffa AP, Perfetto F, et al. **Neuroimaging features of tuberous sclerosis complex and Chiari type I malformation: a rare association.** *J Pediatr Neurosci* 2018;13:224–28 CrossRef Medline
13. Hulshof HM, Benova B, Krsek P, et al. **The epileptogenic zone in children with tuberous sclerosis complex is characterized by prominent features of focal cortical dysplasia.** *Epilepsia Open* 2021;6:663–71 CrossRef Medline
14. Stafstrom CE, Staedtke V, Comi AM. **Epilepsy mechanisms in neurocutaneous disorders: tuberous sclerosis complex, neurofibromatosis type 1, and Sturge-Weber syndrome.** *Front Neurol* 2017;8:87 CrossRef Medline
15. Mayerhoefer ME, Materka A, Langs G, et al. **Introduction to radiomics.** *J Nucl Med* 2020;61:488–95 CrossRef Medline
16. Yip SS, Aerts HJ. **Applications and limitations of radiomics.** *Phys Med Biol* 2016;61:R150–66 CrossRef Medline
17. Rizzo S, Botta F, Raimondi S, et al. **Radiomics: the facts and the challenges of image analysis.** *Eur Radiol Exp* 2018;2:36 CrossRef Medline
18. Liu Z, Wang Y, Liu X, et al. **Radiomics analysis allows for precise prediction of epilepsy in patients with low-grade gliomas.** *Neuroimage Clin* 2018;19:271–78 CrossRef Medline
19. Park YW, Choi YS, Kim SE, et al. **Radiomics features of hippocampal regions in magnetic resonance imaging can differentiate medial temporal lobe epilepsy patients from healthy controls.** *Sci Rep* 2020;10:19567 CrossRef Medline
20. Sun K, Liu Z, Li Y, et al. **Radiomics analysis of postoperative epilepsy seizures in low-grade gliomas using preoperative MR images.** *Front Oncol* 2020;10:1096 CrossRef Medline
21. Wang Y, Wei W, Liu Z, et al. **Predicting the type of tumor-related epilepsy in patients with low-grade gliomas: a radiomics study.** *Front Oncol* 2020;10:235 CrossRef Medline
22. Zhang Y, Yan P, Liang F, et al. **Predictors of epilepsy presentation in unruptured brain arteriovenous malformations: a quantitative evaluation of location and radiomics features on T2-weighted imaging.** *World Neurosurg* 2019;125:e1008–15 CrossRef Medline
23. He B, Dong D, She Y, et al. **Predicting response to immunotherapy in advanced non-small-cell lung cancer using tumor mutational burden radiomic biomarker.** *J Immunother Cancer* 2020;8:e000550 CrossRef Medline
24. Khorrami M, Prasanna P, Gupta A, et al. **Changes in CT radiomic features associated with lymphocyte distribution predict overall survival and response to immunotherapy in non-small cell lung cancer.** *Cancer Immunol Res* 2020;8:108–19 CrossRef Medline
25. Sun R, Limkin EJ, Vakalopoulou M, et al. **A radiomics approach to assess tumour-infiltrating CD8 cells and response to anti-PD-1 or anti-PD-L1 immunotherapy: an imaging biomarker, retrospective multicohort study.** *Lancet Oncol* 2018;19:1180–91 CrossRef Medline
26. Trebesch S, Drago SG, Birkbak NJ, et al. **Predicting response to cancer immunotherapy using noninvasive radiomic biomarkers.** *Ann Oncol* 2019;30:998–1004 CrossRef Medline
27. Tunalı I, Gray JE, Qi J, et al. **Novel clinical and radiomic predictors of rapid disease progression phenotypes among lung cancer patients treated with immunotherapy: an early report.** *Lung Cancer* 2019;129:75–79 CrossRef Medline
28. Isensee F, Schell M, Pflueger I, et al. **Automated brain extraction of multisequence MRI using artificial neural networks.** *Hum Brain Mapp* 2019;40:4952–64 CrossRef Medline
29. van Griethuysen JJ, Fedorov A, Parmar C, et al. **Computational radiomics system to decode the radiographic phenotype.** *Cancer Res* 2017;77:e104–07 CrossRef Medline
30. Austin PC, Harrell FE Jr, van Klaveren D. **Graphical calibration curves and the integrated calibration index (ICI) for survival models.** *Stat Med* 2020;39:2714–42 CrossRef Medline
31. Hsieh DT, Jennesson MM, Thiele EA. **Epileptic spasms in tuberous sclerosis complex.** *Epilepsy Res* 2013;106:200–10 CrossRef Medline
32. Liu S, Yu T, Guan Y, et al. **Resective epilepsy surgery in tuberous sclerosis complex: a nationwide multicentre retrospective study from China.** *Brain* 2020;143:570–81 CrossRef Medline
33. Zhang G, Xu L, Zhao L, et al. **CT-based radiomics to predict the pathological grade of bladder cancer.** *Eur Radiol* 2020;30:6749–56 CrossRef Medline
34. Mao B, Zhang L, Ning P, et al. **Preoperative prediction for pathological grade of hepatocellular carcinoma via machine learning-based radiomics.** *Eur Radiol* 2020;30:6924–32 CrossRef Medline
35. Jiang Y, Chen C, Xie J, et al. **Radiomics signature of computed tomography imaging for prediction of survival and chemotherapeutic benefits in gastric cancer.** *EBioMedicine* 2018;36:171–82 CrossRef Medline
36. Staal FC, van der Reijd DJ, Taghavi M, et al. **Radiomics for the prediction of treatment outcome and survival in patients with colorectal cancer: a systematic review.** *Clin Colorectal Cancer* 2021;20:52–71 CrossRef Medline
37. Lambin P, Leijenaar RT, Deist TM, et al. **Radiomics: the bridge between medical imaging and personalized medicine.** *Nat Rev Clin Oncol* 2017;14:749–62 CrossRef Medline
38. Zhao X, Jiang D, Hu Z, et al. **Machine learning and statistic analysis to predict drug treatment outcome in pediatric epilepsy patients with tuberous sclerosis complex.** *Epilepsy Res* 2022;188:107040 CrossRef Medline
39. Jeong A, Nakagawa JA, Wong M. **Predictors of drug-resistant epilepsy in tuberous sclerosis complex.** *J Child Neurol* 2017;32:1092–98 CrossRef Medline
40. Chu-Shore CJ, Major P, Camposano S, et al. **The natural history of epilepsy in tuberous sclerosis complex.** *Epilepsia* 2010;51:1236–41 CrossRef Medline
41. Salussolia CL, Klonowska K, Kwiatkowski DJ, et al. **Genetic etiologies, diagnosis, and treatment of tuberous sclerosis complex.** *Annu Rev Genomics Hum Genet* 2019;20:217–40 CrossRef Medline

Long-Term Imaging Follow-up from the Management of Myelomeningocele Study

E. George, C. MacPherson, S. Pruthi, L. Bilaniuk, J. Fletcher, A. Houtrow, N. Gupta, and O.A. Glenn



ABSTRACT

BACKGROUND AND PURPOSE: Short-term results demonstrate that prenatal repair of a myelomeningocele is associated with a reduction in hydrocephalus and an increased likelihood of the reversal of Chiari II malformations compared with postnatal repair. The purpose of this study was to identify the long-term imaging findings at school age among subjects who underwent pre- versus postnatal repair of a myelomeningocele.

MATERIALS AND METHODS: A subset of subjects enrolled in the Management of Myelomeningocele Study who underwent either prenatal ($n = 66$) or postnatal ($n = 63$) repair of a lumbosacral myelomeningocele and had follow-up brain MR imaging at school age were included. The prevalence of posterior fossa features of Chiari II malformation and supratentorial abnormalities and the change in these findings from fetal to school-age MR imaging were compared between the 2 groups.

RESULTS: Prenatal repair of a myelomeningocele was associated with higher rates of normal location of fourth ventricle and lower rates of hindbrain herniation, cerebellar herniation, tectal beaking, brainstem distortion, and kinking at school age compared with postnatal repair (all $P < .01$). Supratentorial abnormalities, including corpus callosal abnormalities, gyral abnormalities, heterotopia, and hemorrhage, were not significantly different between the 2 groups (all $P > .05$). The rates of resolution of brainstem kinking, tectal beaking, cerebellar and hindbrain herniation, and normalization of fourth ventricle size from fetal to school age MR imaging were higher among the prenatal compared with postnatal surgery group (all, $P < .02$).

CONCLUSIONS: Prenatal repair of a myelomeningocele is associated with persistent improvement in posterior fossa imaging findings of Chiari II malformation at school age compared with postnatal repair.

ABBREVIATIONS: MMC = myelomeningocele; PVNH = periventricular nodular heterotopia

Spinal dysraphism includes a broad spectrum of congenital anomalies with an incidence of ~ 3 per 10,000 live births in the United States.¹⁻³ More than 85% of these are myelomeningoceles

(MMCs), an open neural tube defect that consists of a poorly differentiated neural placode extending into a midline dorsal sac containing CSF.¹⁻³ Almost all fetuses with MMCs have associated Chiari II malformations, characterized by a small posterior fossa and caudal displacement with narrowing and elongation of the fourth ventricle, cerebellum, and brainstem.⁴ It is believed that hindbrain herniation occurs due to leakage of CSF into the sac and amniotic fluid, resulting in chronic CSF hypotension.⁵ The herniation of the posterior fossa contents can further interfere with normal CSF flow (including narrowing and occlusion of the aqueduct) and the development of structures that absorb CSF, resulting in hydrocephalus.⁵ Moreover, MMCs are associated with supratentorial developmental abnormalities, including abnormal corpus callosum, abnormal gyration, and periventricular nodular heterotopia (PVNH).⁶

It is believed that chronic exposure of the poorly developed neural placode and spinal nerves to amniotic fluid results in progressive neuronal loss,⁷ which, in combination with the abnormally formed spinal cord, leads to lower-extremity motor and

Received April 18, 2023; accepted after revision May 23.

From the Departments of Radiology and Biomedical Imaging (E.G., O.A.G.), Neurological Surgery (N.G.), and Pediatrics (N.G.), University of California, San Francisco, San Francisco, California; Biostatistics Center (C.M.), Milken Institute School of Public Health, The George Washington University, Washington, DC; Department of Radiology (S.P.), Monroe Carell Jr. Children's Hospital at Vanderbilt, Nashville, Tennessee; Department of Radiology (L.B.), Children's Hospital of Philadelphia, Philadelphia, Pennsylvania; Department of Psychology (J.F.), University of Houston, Houston, Texas; and Department of Physical Medicine and Rehabilitation (A.H.), University of Pittsburgh, Pittsburgh, Pennsylvania.

This work was supported by the Eunice Kennedy Shriver National Institute of Child Health and Human Development (U01 HD06854: follow-up of the Management of Myelomeningocele Study), funded by the National Institutes of Health. Elizabeth George was supported by the American Society of Neuroradiology Scholar Award.

Please address correspondence to Orit A. Glenn, MD, University of California, San Francisco, 505 Parnassus Ave, San Francisco, CA 94143; e-mail: Orit.Glenn@ucsf.edu

Indicates open access to non-subscribers at www.ajnr.org

Indicates article with online supplemental data.

<http://dx.doi.org/10.3174/ajnr.A7926>

sensory dysfunction and loss of bladder and bowel control. The posterior fossa and supratentorial abnormalities can result in impairment in nonverbal reasoning, attention, language functionality,⁸ and executive function in these children.⁹

Prenatal repair of an MMC was first reported in 1998, and early studies demonstrated reversal of hindbrain herniation and a decreased need for CSF diversion compared with historical controls.^{10,11} The Management of Myelomeningocele Study (MOMS), a randomized controlled trial comparing prenatal with the then-standard postnatal repair of MMCs¹² demonstrated a significant benefit among the prenatal surgery group with a reduced need for CSF diversion at 12 months¹³ and improved motor function at 30 months.¹⁴ Prenatal repair was associated with lower rates of abnormal posterior fossa imaging findings and syringomyelia at 12 months.¹² Additional studies have further confirmed this finding of higher rates of resolution of hindbrain herniation in the prenatal surgery group in the short term.^{15,16} However, the long-term imaging findings of prenatal repair of MMCs are unknown. MOMS2 was designed as a follow-up to MOMS to assess the long-term outcomes of prenatal surgical repair of an MMC when the children were 5–10 years of age. The purpose of this study was to compare the long-term imaging findings and the change in imaging findings from fetal life to school age between children who underwent fetal and postnatal repair of MMCs in MOMS2.

MATERIALS AND METHODS

The MOMS2 study was conducted at the same 3 sites that participated in MOMS (Children's Hospital of Philadelphia, Vanderbilt University, and University of California, San Francisco) and the George Washington University Biostatistics Center served as the data-coordinating center. Institutional review board approval was obtained at each clinical site and the data-coordinating center. Caregivers gave written informed consent, and children gave assent per local institutional review board regulations.

Imaging

The protocol of MOMS has been described previously.¹² Briefly, fetal brain and spine MR imaging performed at 18–26 weeks before intervention were reviewed by an independent committee comprising of 2 pediatric neuroradiologists and a pediatric radiologist. Reviewers were blinded to the assigned surgery group and scored the brain and spine findings, including cerebellar and hindbrain herniation, cerebellar hypoplasia, brainstem kinking, tectal beaking, size of the fourth ventricle, structural abnormalities including those of the corpus callosum, and the presence of a sac overlying the MMC defect.

Study participation for MOMS2 consisted of a single visit when the child was 5–10 years of age at one of the clinical centers or at home if the parent or caregiver declined travel.¹⁷ Children who presented to the clinical center underwent 3T imaging of the brain and spine without sedation or contrast administration. The brain imaging protocol included 3D isotropic T1-weighted MPRAGE, 3D isotropic T2-weighted TSE, and 32-direction DTI. Some patients also had 3D T2 FLAIR imaging and SWI. An independent committee of 3 pediatric neuroradiologists with 9–40 years' experience reviewed the MR images in consensus and were blinded to treatment group, clinical reads, and any prior MR imaging results. Studies were scored on the basis of consensus review and included

Table 1: Demographic variables of the study groups^a

Variable	Prenatal Surgery (n = 66)	Postnatal Surgery (n = 63)	P Value ^b
Age at follow-up (yr)	7.5 (SD, 1.3)	7.3 (SD, 1.2)	.460
Female (No.) (%)	29 (43.9%)	41 (65.1%)	.022
Race (No.) (%)			.334
White	61 (92.4%)	55 (87.3%)	
African American	1 (1.5%)	1 (1.6%)	
Hispanic	2 (3.0%)	5 (7.9%)	
Other	2 (3.0%)	2 (3.2%)	
Gestational age at birth (week)	34.4 (SD, 2.6)	37.5 (SD, 0.8)	<.001
Anatomic lesion level (No.) (%)			.563
Thoracic	2 (3.0%)	1 (1.6%)	
L1–L2	9 (13.6%)	12 (19.1%)	
L3–L4	33 (50.0%)	29 (46.0%)	
L5–S2	22 (33.3%)	21 (33.3%)	
Presence of sac on fetal imaging	48 (72.7%)	54 (87.1%)	.043
Tethered cord release	19 (28.8)	8 (12.7)	.025

^a Values listed are No. (%) or mean (SD).

^b P value for race is white versus all others. P value for lesion level is T1–L2 versus L3–S2.

the location and size of the fourth ventricle (assessed in all planes), tectal beaking (assessed in the sagittal and axial planes), cerebellar hypoplasia (assessed in all planes), brainstem hypoplasia, and brainstem distortion and kinking (assessed in the sagittal plane). Cerebellar herniation was assessed in the sagittal and coronal planes and categorized as mild (at C1), moderate (at C2), or severe (below C2). Hindbrain herniation was assessed in the sagittal plane and categorized on the basis of the location of the cervicomedullary junction as none (above foramen magnum), mild (between foramen magnum and C1), moderate (between C1 and C2), or severe (below C2). Supratentorial features that were assessed included corpus callosum, callosal ridge, hypothalamic adhesion, anterior commissure, presence of abnormal gyration, heterotopia, deep gray nuclei signal, and hemorrhagic and nonhemorrhagic lesions (white matter atrophy). Spine MR imaging was assessed for the presence of syringomyelia and epidermoid cysts. One of the pediatric neuroradiologists involved in the MOMS image review was available to address questions and ensure consistency in scoring. Due to challenges in imaging assessment of a tethered spinal cord after MMC repair, the need for tethered cord release surgery was used as an estimate of the incidence of symptomatic tethered cord.

Statistical Analyses

Categorical variables were compared using the χ^2 test or Fisher exact test, as appropriate. Due to skewed distributions, continuous variables were compared using the Wilcoxon rank-sum test. P values < .05 were considered statistically significant. Statistical analysis used SAS, Version 9.04 (SAS Institute).

RESULTS

Study Population

The mean age at the time of the follow-up visit was 7.5 years in the prenatal and 7.3 years in the postnatal surgery groups (Table 1, P = .46). Most children in both groups were white (92% versus 87%, P = .33), and there was a lower proportion of girls in the prenatal

Table 2: School-age posterior fossa and spine imaging findings in children who underwent prenatal-versus-postnatal surgery

Imaging	Prenatal Surgery n/N (%)	Postnatal Surgery n/N (%)	RR (95% CI)	P Value
Fourth ventricle location				<.001
Normal	19/66 (29)	6/63 (10)		
Low	42/66 (64)	35/63 (56)		
At foramen magnum	3/66 (5)	10/63 (16)		
Below foramen magnum	2/66 (3)	12/63 (19)		
Tectal beaking	53/66 (80)	61/63 (97)	0.83 (0.73–0.94)	.003
Hindbrain herniation				<.001
None	26/66 (39)	8/62 (13)		
Mild	23/66 (35)	12/62 (19)		
Moderate	15/66 (23)	26/62 (40)		
Severe	2/66 (3)	17/62 (27)		
Cerebellar herniation degree				<.001
None	33/66 (50)	8/63 (13)		
Mild	22/66 (33)	21/63 (33)		
Moderate	11/66 (17)	20/63 (32)		
Severe	0	14/63 (22)		
Cerebellar hypoplasia	4/66 (6)	9/63 (14)	0.42 (0.14–1.31)	.12
Brainstem hypoplasia	8/66 (12)	19/63 (30)	0.40 (0.19–0.85)	.01
Brainstem distortion	33/66 (50)	52/63 (83)	0.61 (0.46–0.79)	<.001
Brainstem kinking				<.001
None	53/66 (80)	31/63 (49)		
Mild	11/66 (17)	20/63 (32)		
Moderate	2/66 (3)	11/63 (17)		
Severe	0	1/63 (2)		
Syringomyelia	37/63 (59)	48/59 (81)	0.7 (0.6–0.9)	.007
Epidermoid cyst	7/63 (11)	2/58 (3)	3.2 (0.7–14.9)	.17

Note.—RR indicates relative risk.

surgery group (44% versus 65%, $P = .022$), similar to the MOMS results.¹⁴ The distribution of the MMC lesion level was similar between the 2 groups ($P = .56$). Most of the fetuses in both groups had a sac overlying the defect, with a slightly higher prevalence in the postnatal compared with the prenatal surgery group (87.1% versus 72.7%, $P = .043$).

Imaging Findings at School Age

A higher proportion of children in the prenatal surgery group had a normal location of the fourth ventricle and absence of hindbrain herniation, cerebellar herniation, brainstem distortion, brainstem kinking, brainstem hypoplasia, and tectal beaking compared with the postnatal surgery group at school age (all, $P \leq .01$, Table 2).

Supratentorial malformations such as PVNH, abnormal gyration, and abnormal morphology of the corpus callosum or anterior commissure were not significantly different between treatment groups. The presence of supratentorial abnormalities, including hemorrhage, nonhemorrhagic lesions, abnormal signal of the deep gray nuclei, and diminished parahippocampal gyral volume did not differ between the 2 groups (Online Supplemental Data).

The incidence of syringomyelia was higher in the postnatal compared with prenatal surgery group (81% versus 59%, $P = .007$, Table 2). The prenatal surgery group had a higher rate of tethered cord release surgery (28.8% versus 12.7%, $P = .025$). There was no significant difference between the groups in the incidence of epidermoid cyst on school-age MR imaging ($P = .17$).

Change in Imaging Findings

In the prenatal surgery group, 55% of the children with a small fourth ventricle at baseline fetal MR imaging reverted to normal fourth ventricular size by school age, while only 14% of the children in the postnatal surgery group reverted to a normal-sized fourth ventricle at school age ($P < .001$). There were higher rates of resolution of brainstem kinking, tectal beaking, cerebellar herniation, and hindbrain herniation by school age in the prenatal surgery group compared with the postnatal group (all $P < .05$, Table 3 and Figure). There was new development of syringomyelia by school age in 58% of children who underwent prenatal surgery compared with 78% among those who underwent postnatal surgery ($P = .03$). The change in structural abnormalities (abnormal gyration or PVNH) from fetal MR imaging to school age MR imaging was not significantly different among those who underwent prenatal-versus-postnatal surgery (Table 3).

DISCUSSION

Our study demonstrates that the improvement in structural posterior fossa abnormalities from prenatal compared with postnatal repair of an MMC persists into school age. Early studies of open fetal repair of an MMC demonstrated high rates of resolution of hindbrain herniation in 3–6 weeks following the procedure, with a possibly lower rate of progressive hydrocephalus and an increase in posterior fossa subarachnoid spaces in utero.^{10,18,19} These higher rates of resolution of cerebellar herniation associated with prenatal repair are known to persist in the postnatal period.^{15,16,19} In MOMS, at 12 months of age, the prenatal surgery group demonstrated improved Chiari II–related posterior fossa findings as well as syringomyelia compared with the postnatal surgery group.¹² This is the first study to demonstrate the persistent long-term improvement in Chiari II malformations in school-age children who underwent prenatal compared with postnatal repair of an MMC.

CNS anomalies associated with MMC develop at various gestational ages, with Chiari II malformation being a relatively late manifestation, increasing in prevalence from 31% at 16 weeks to 92% at 16–20 weeks.⁷ In MOMS, the prevalence of severe preoperative hindbrain herniation was not significantly different between the prenatal and postnatal surgery groups.¹⁴ The bony morphology of the posterior fossa is, however, known to change rapidly toward normal after fetal surgery within as early as 1 week postrepair.²⁰ These bony changes continue to improve in the fetal surgery group at 4 weeks postrepair with normalization of the configuration of the posterior fossa, characterized by the clivus-supraocciput angle in the early postnatal period.^{18,21,22} There is,

Table 3: Change in imaging variables from baseline fetal to school age in pre- and postnatal surgery groups

Imaging Variable	Prenatal Surgery	Postnatal Surgery	P Value
Fourth ventricle size	<i>n</i> = 66	<i>n</i> = 63	
Changed from small to normal	36 (55)	9 (14)	<.001
Remained small	28 (42)	51 (81)	
Another pattern	2 (3)	3 (5)	
Tectal beaking	<i>n</i> = 60	<i>n</i> = 54	
Resolved	12 (20)	2 (4)	.008
Not resolved	48 (80)	52 (96)	
Hindbrain herniation	<i>n</i> = 66	<i>n</i> = 62	
Resolved	26 (39)	8 (13)	.001
Remained the same	40 (61)	54 (87)	
Cerebellar herniation	<i>n</i> = 65	<i>n</i> = 62	
Resolved	32 (49)	8 (13)	<.001
Remained the same	32 (49)	53 (85)	
New	1 (2)	1 (2)	
Cerebellar hypoplasia	<i>n</i> = 61	<i>n</i> = 54	
Resolved	44 (72)	33 (61)	.27
Remained the same	17 (28)	20 (37)	
New	0	1 (2)	
Brainstem kinking	<i>n</i> = 38	<i>n</i> = 41	
Resolved	16 (42)	8 (20)	.02
Remained the same	20 (53)	23 (56)	
New	2 (5)	10 (24)	
Structural abnormality (gyral and heterotopia)	<i>n</i> = 64	<i>n</i> = 60	
Resolved	2 (3)	1 (2)	.94
Remained the same	40 (63)	40 (67)	
New	22 (34)	19 (32)	

however, conflicting data on the changes in posterior fossa configuration in the postnatal repair group, with reports of both a lower and relatively normal clivus-supraocciput angle compared with healthy controls.^{21,22} However, the posterior fossa area is known to remain smaller in neonates who underwent prenatal or postnatal repair compared with healthy controls.^{18,22} Although there are differences in imaging timepoints and measurement techniques among these studies, these early changes to the bony posterior fossa configuration could potentially explain the persistent improvement in Chiari II manifestations seen at school age in our study.

Prenatal-versus-postnatal surgery had no significant effect on malformations of the supratentorial brain in childhood. The overall prevalence of malformations such as abnormal gyration and PVNH on fetal imaging were low (3%–8%), similar to findings in prior reports.^{6,18} However, the true prevalence based on childhood imaging is much higher (45%–77%), underscoring

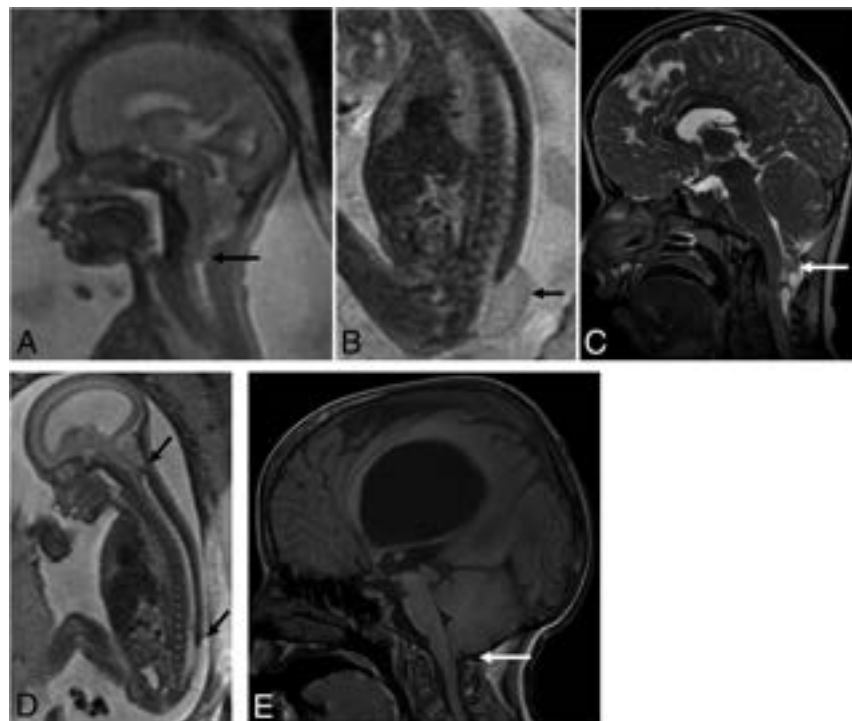


FIGURE. A and B, A 25-week-old fetus with a lumbosacral MMC (arrow) and Chiari II malformation (arrow) with the cerebellum extending to approximately the C3 level. The patient underwent postnatal repair with follow-up MR imaging (C) at 8 years demonstrating persistent brainstem and cerebellar herniation to C2 (white arrow). D, A 21-week 6-day-old fetus with a lower lumbar MMC (arrow) and Chiari II malformation with the cerebellum extending to approximately the C3 level (arrow). E, Status post fetal repair at 22 weeks 5 days with no residual cerebellar or brainstem herniation at 9 years of age (white arrow).

the challenges with prenatal identification of these malformations,²³ particularly in the setting of MMC and Chiari II malformation.¹⁸ The corpus callosum was abnormal in 83%–86% of children, similar to prior reports of 60%–86% on fetal sonography and postnatal MR imaging.^{6,24,25} Supratentorial malformations in MMC are thought to be due to neuroepithelial and ependymal denudation, and these occur at 16 weeks before the development of a Chiari II malformation and hydrocephalus.²⁶ This early and permanent damage to the ependyma could explain the lack of improvement in the incidence of supratentorial malformations despite prenatal MMC repair, which was typically performed at 19–26 weeks in MOMS.¹⁴ However, the effect of the timing of fetal surgery on supratentorial abnormalities remains unknown. Future studies should also assess the effect of prenatal surgery on quantitative structural and connectivity metrics of the supratentorial brain, particularly in the setting of a known lack of improvement in long-term cognitive function with prenatal surgery.¹⁷

It is difficult to directly relate the qualitative evaluations of structural impairments to neurodevelopmental outcomes. Assessment of neurodevelopmental outcomes at school age¹⁷ did not show marked improvement in adaptive behavior and cognitive skills but did report improvement in fine-motor skills in the prenatal surgery group, which is associated with cerebellar function.²⁷ Quantitative assessment of the tectum and its connectivity with the frontal and parietal regions showed stronger attention-orienting and arousal in association with reduced tectal dysmorphology.²⁸ Because prenatal surgery reduces hindbrain herniation and the findings of Chiari II, there may be an indirect effect leading to improved cognitive and motor functions.

Finally, prenatal surgery was associated with a lower incidence of syringomyelia but higher rates of tethered cord release surgery in our cohort. However, spina bifida registry data as well as recent single-institutional data suggest similar rates of tethered cord release surgery of 13%–18% in both prenatal and postnatal surgery cohorts.^{29,30} Our study cohort is slightly older than children in these studies, and the need for tethered cord release is known to increase with age.³¹ Furthermore, practice and indications for detethering can be variable among institutions.³¹

Our study has several limitations. Blood-sensitive sequences were not available in all patients, limiting the assessment of the frequency of hemorrhagic lesions. The presence or absence of a sac overlying the MMC defect and the level and size of the MMC defect may affect the severity and evolution of Chiari II manifestations,^{32–34} which was not adjusted for in our study. However, only a small fraction of cases did not have an overlying sac on fetal imaging. Furthermore, the myelocoele was more prevalent in the prenatal surgery group, which may be underestimating our results on long-term improvement in imaging findings with prenatal surgery because the absence of overlying sac suggests a more severe phenotype.³³ The association of imaging findings with functional outcome was not assessed; however, prenatal repair has been shown to be associated with better mobility and independent functioning at school age.¹⁷ Interpretation of ventricular size is complex in the setting of CSF shunts, shunt revisions, and third ventriculostomy procedures,³⁵ and detailed assessment of ventricular size will be the focus of a future study. In the MOMS2 cohort, all patients in the postnatal surgery group

had hydrocephalus.³⁵ In the prenatal and postnatal surgery groups, ventricular size has been shown to be larger in those with unshunted hydrocephalus compared with those with shunted hydrocephalus and those with no hydrocephalus in the prenatal surgery group.³⁵ Post-MOMS single-institution data and MOMS2 studies also demonstrated fewer shunt placements and shunt revisions in the prenatal compared with the postnatal surgery group both in the short and long term.^{15,17} Finally, quantitative assessments of the bony posterior fossa was not included in this study.

CONCLUSIONS

Our study demonstrates that prenatal repair of an MMC is associated with persistent improvement in posterior fossa imaging findings at school age compared with postnatal repair. This outcome along with long-term neurodevelopmental outcome data provides valuable information for parental counseling for prenatal surgery for MMC.

ACKNOWLEDGMENT

In memory of Elizabeth Thom, PhD, who was instrumental in contributing to this work.

Disclosure forms provided by the authors are available with the full text and PDF of this article at www.ajnr.org.

REFERENCES

1. Agopian AJ, Canfield MA, Olney RS, et al; National Birth Defects Prevention Study. **Spina bifida subtypes and sub-phenotypes by maternal race/ethnicity in the National Birth Defects Prevention Study.** *Am J Med Genet A* 2012;158A:109–15 CrossRef Medline
2. Boulet SL, Yang Q, Mai C, et al; National Birth Defects Prevention Network. **Trends in the postfortification prevalence of spina bifida and anencephaly in the United States.** *Birth Defects Res A Clin Mol Teratol* 2008;82:527–32 CrossRef Medline
3. Parker SE, Mai CT, Canfield MA, et al; National Birth Defects Prevention Network. **Updated national birth prevalence estimates for selected birth defects in the United States, 2004–2006.** *Birth Defects Res A Clin Mol Teratol* 2010;88:1008–16 CrossRef Medline
4. Rossi A, Gandolfo C, Morana G, et al. **Current classification and imaging of congenital spinal abnormalities.** *Semin Roentgenol* 2006;41:250–73 CrossRef Medline
5. McLone DG, Knepper PA. **The cause of Chiari II malformation: a unified theory.** *Pediatr Neurosci* 1989;15:1–12 CrossRef Medline
6. Maurice P, Garel J, Garel C, et al. **New insights in cerebral findings associated with fetal myelomeningocele: a retrospective cohort study in a single tertiary centre.** *BJOG* 2021;128:376–83 CrossRef Medline
7. Ben Miled S, Loeuillet L, Duong Van Huyen JP, et al. **Severe and progressive neuronal loss in myelomeningocele begins before 16 weeks of pregnancy.** *Am J Obstet Gynecol* 2020;223:256 e1–e9 CrossRef Medline
8. Vachha B, Adams R. **Language differences in young children with myelomeningocele and shunted hydrocephalus.** *Pediatr Neurosurg* 2003;39:184–89 CrossRef Medline
9. Foss S, Flanders TM, Heuer GG, et al. **Neurobehavioral outcomes in patients with myelomeningocele.** *Neurosurg Focus* 2019;47:E6 CrossRef Medline
10. Johnson MP, Sutton LN, Rintoul N, et al. **Fetal myelomeningocele repair: short-term clinical outcomes.** *Am J Obstet Gynecol* 2003;189:482–87 CrossRef Medline
11. Tulipan N, Bruner JP, Hernanz-Schulman M, et al. **Effect of intrauterine myelomeningocele repair on central nervous system structure and function.** *Pediatr Neurosurg* 1999;31:183–88 CrossRef Medline

12. Adzick NS, Thom EA, Spong CY, et al; MOMS Investigators. **A randomized trial of prenatal versus postnatal repair of myelomeningocele.** *N Engl J Med* 2011;364:993–1004 CrossRef Medline
13. Tulipan N, Wellons JC 3rd, Thom EA, et al; MOMS Investigators. **Prenatal surgery for myelomeningocele and the need for cerebrospinal fluid shunt placement.** *J Neurosurg Pediatr* 2015;16:613–20 CrossRef Medline
14. Farmer DL, Thom EA, Brock JW 3rd, et al; Management of Myelomeningocele Study Investigators. **The Management of Myelomeningocele Study: full cohort 30-month pediatric outcomes.** *Am J Obstet Gynecol* 2018;218:256.e13 CrossRef Medline
15. Flanders TM, Heuer GG, Madsen PJ, et al. **Detailed analysis of hydrocephalus and hindbrain herniation after prenatal and postnatal myelomeningocele closure: report from a single institution.** *Neurosurgery* 2020;86:637–45 CrossRef Medline
16. Nagaraj UD, Bierbrauer KS, Zhang B, et al. **Hindbrain herniation in Chiari II malformation on fetal and postnatal MRI.** *AJNR Am J Neuroradiol* 2017;38:1031–36 CrossRef Medline
17. Houtrow AJ, Thom EA, Fletcher JM, et al. **Prenatal repair of myelomeningocele and school-age functional outcomes.** *Pediatrics* 2020;145:e2019154 CrossRef Medline
18. Rethmann C, Scheer I, Meuli M, et al. **Evolution of posterior fossa and brain morphology after in utero repair of open neural tube defects assessed by MRI.** *Eur Radiol* 2017;27:4571–80 CrossRef Medline
19. Sutton LN, Adzick NS, Bilaniuk LT, et al. **Improvement in hindbrain herniation demonstrated by serial fetal magnetic resonance imaging following fetal surgery for myelomeningocele.** *JAMA* 1999;282:1826–31 CrossRef Medline
20. Aertsen M, Verduyck J, De Keyser F, et al. **Reliability of MR imaging-based posterior fossa and brainstem measurements in open spinal dysraphism in the era of fetal surgery.** *AJNR Am J Neuroradiol* 2019;40:191–98 CrossRef Medline
21. da Costa MDS, Nicacio JM, Dastoli PA, et al. **Alterations in skull base anatomy in intrauterine and postnatal repaired myelomeningoceles.** *Childs Nerv Syst* 2020;36:2757–63 CrossRef Medline
22. Grant RA, Heuer GG, Carrion GM, et al. **Morphometric analysis of posterior fossa after in utero myelomeningocele repair.** *J Neurosurg Pediatr* 2011;7:362–68 CrossRef Medline
23. Glenn OA, Cuneo AA, Barkovich AJ, et al. **Malformations of cortical development: diagnostic accuracy of fetal MR imaging.** *Radiology* 2012;263:843–55 CrossRef Medline
24. Kunpalin Y, Richter J, Mufti N, et al. **Cranial findings detected by second-trimester ultrasound in fetuses with myelomeningocele: a systematic review.** *BJOG* 2021;128:366–74 CrossRef Medline
25. Morais BA, Solla DJ, Yamaki VN, et al. **Brain abnormalities in myelomeningocele patients.** *Childs Nerv Syst* 2020;36:1507–13 CrossRef Medline
26. de Wit OA, den Dunnen WF, Sollié KM, et al. **Pathogenesis of cerebral malformations in human fetuses with meningocele.** *Cerebrospinal Fluid Res* 2008;5:4 CrossRef Medline
27. Dennis M, Salman MS, Juranek J, et al. **Cerebellar motor function in spina bifida meningocele.** *Cerebellum* 2010;9:484–98 CrossRef Medline
28. Williams VJ, Juranek J, Stuebing K, et al. **Examination of frontal and parietal tectocortical attention pathways in spina bifida meningocele using probabilistic diffusion tractography.** *Brain Connect* 2013;3:512–22 CrossRef Medline
29. Cools MJ, Tang AR, Pruthi S, et al. **A comparison of MRI appearance and surgical detethering rates between intrauterine and postnatal myelomeningocele closures: a single-center pilot matched cohort study.** *Childs Nerv Syst* 2023;39:647–53 CrossRef Medline
30. Worley G, Greenberg RG, Rocque BG, et al. **Neurosurgical procedures for children with myelomeningocele after fetal or postnatal surgery: a comparative effectiveness study.** *Dev Med Child Neurol* 2021;63:1294–1301 CrossRef Medline
31. Dias MS, Wang M, Rizk EB, et al; National Spina Bifida Patient Registry Group. **Tethered spinal cord among individuals with myelomeningocele: an analysis of the National Spina Bifida Patient Registry.** *J Neurosurg Pediatr* 2023;7:1–7 CrossRef Medline
32. Corroenne R, Zhu KH, Johnson E, et al. **Impact of the size of the lesion in prenatal neural tube defect repair on imaging, neurosurgical and motor outcomes: a retrospective cohort study.** *BJOG* 2021;128:392–99 CrossRef Medline
33. Nagaraj UD, Bierbrauer KS, Stevenson CB, et al. **Myelomeningocele versus myelocoele on fetal MR images: are there differences in brain findings?** *AJR Am J Roentgenol* 2018;211:1376–80 CrossRef Medline
34. Fletcher JM, Copeland K, Frederick JA, et al. **Spinal lesion level in spina bifida: a source of neural and cognitive heterogeneity.** *J Neurosurg* 2005;102:268–79 CrossRef Medline
35. Fletcher JM, Houtrow AJ, MacPherson C. **Hydrocephalus and school-age neuropsychological outcomes in the Management of Myelomeningocele prenatal surgery trial: a secondary analysis.** *J Neurosurg Pediatr* 2023 Mar 3. [Epub ahead of print] CrossRef Medline

Validation of a New Semiautomated Segmentation Pipeline Based on the Spinal Cord Toolbox DeepSeg Algorithm to Estimate the Cervical Canal Area

N. Mongay-Ochoa, D. Pareto, M. Alberich, M. Tintore, X. Montalban, À. Rovira, and J. Sastre-Garriga



ABSTRACT

BACKGROUND AND PURPOSE: As in the brain reserve concept, a larger cervical canal area may also protect against disability. In this context, a semiautomated pipeline has been developed to obtain quantitative estimations of the cervical canal area. The aim of the study was to validate the pipeline, to evaluate the consistency of the cervical canal area measurements during a 1-year period, and to compare cervical canal area estimations obtained from brain and cervical MRI acquisitions.

MATERIALS AND METHODS: Eight healthy controls and 18 patients with MS underwent baseline and follow-up 3T brain and cervical spine sagittal 3D MPRAGE. The cervical canal area was measured in all acquisitions, and estimations obtained with the proposed pipeline were compared with manual segmentations performed by 1 evaluator using the Dice similarity coefficient. The cervical canal area estimations obtained on baseline and follow-up T1WI were compared; brain and cervical cord acquisitions were also compared using the individual and average intraclass correlation coefficients.

RESULTS: The agreement between the manual cervical canal area masks and the masks provided by the proposed pipeline was excellent, with a mean Dice similarity coefficient mean of 0.90 (range, 0.73–0.97). The cervical canal area estimations obtained from baseline and follow-up scans showed a good level of concordance (intraclass correlation coefficient = 0.76; 95% CI, 0.44–0.88); estimations obtained from brain and cervical MRIs also had good agreement (intraclass correlation coefficient = 0.77; 95% CI, 0.45–0.90).

CONCLUSIONS: The proposed pipeline is a reliable tool to estimate the cervical canal area. The cervical canal area is a stable measure across time; moreover, when cervical sequences are not available, the cervical canal area could be estimated using brain T1WI.

ABBREVIATIONS: CCaA = cervical canal area; FA = flip angle; GT = ground truth; HC = healthy controls; ICC = intraclass correlation coefficient; LoA = limits of agreement; pwMS = patients with multiple sclerosis; SCT = Spinal Cord Toolbox; SD = standard deviation

In patients with MS, the progression of neurologic disability cannot be explained only by the accumulation of brain white matter lesions.¹ Because neurodegenerative damage of the cervical cord is present in most patients with MS,² recent work has demonstrated the value of cervical cord atrophy as an independent prognostic factor for disability.³

In homology to the brain reserve concept, which implies that individuals with a larger premorbid brain (estimated using total intracranial volume as a proxy of maximal lifetime brain growth) have a lower risk of MS-related cognitive and physical impairment,⁴

a larger cervical canal area (CCaA), which may be taken as a proxy for maximal lifetime spinal cord growth, may also protect against disability.⁵

In this context, a semiautomated pipeline has been developed to obtain quantitative estimations of the CCaA based on brain and cervical 3D T1WI, using the Spinal Cord Toolbox (SCT; <https://www.nitrc.org/projects/sct/>). To validate the reproducibility of the proposed pipeline, we compared CCaA measurements obtained with the SCT with those obtained with the manual ground truth (GT), both in healthy controls (HC) and patients with MS. Then, the performance of the pipeline was evaluated by assessing the CCaA at baseline and 1-year follow-up (scan-rescan test) and evaluating CCaA measurements obtained with brain and cervical T1WI.

MATERIALS AND METHODS

Data Acquisition

An initial set of 10 HC and 21 patients with MS underwent baseline and follow-up brain and cervical spine sagittal 3D MPRAGE. All MRI scans were acquired in a 3T system (Tim Trio; Siemens)

Received November 12, 2022; accepted after revision May 11, 2023.

From the Department of Neurology (N.M.-O., M.T., X.M., J.S.-G.), Multiple Sclerosis Centre of Catalonia, and Section of Neuroradiology (D.P., M.A., À.R.), Department of Radiology, Hospital Universitari Vall d'Hebron, Barcelona, Spain.

Please address correspondence to Deborah Pareto Onghena, PhD, Section of Neuroradiology, Department of Radiology (IDI), Vall d'Hebron, University Hospital, Pg Vall d'Hebron 119-129, 08035 Barcelona, Spain; e-mail: deborah.pareto.idi@gencat.cat

Indicates article with online supplemental data.

<http://dx.doi.org/10.3174/ajnr.A7899>

using the following acquisition parameters: TR = 2300 ms, TE = 2.98 ms, TI = 900 ms, flip angle = 9°, voxel size = 1 × 1 × 1 mm³; brain FOV = 240 × 256 × 176, cervical FOV = 240 × 25 × 128. Additionally, all subjects underwent a brain 2D FLAIR scan (TR = 9000 ms, TE = 93 ms, TI = 2500 ms, flip angle = 120°, voxel size = 0.49 × 0.49 × 3.0 mm³). The positioning protocol was the same across all subjects. The project was approved by the local ethics committee, and subjects signed an informed consent.

Image Processing

The CCaA was measured in all acquisitions using the following in-house pipeline based on the SCT (Version 5.0.1):⁶ First, a segmentation of the cervical cord was obtained with the DeepSeg algorithm. Then, the posterior tip of the C2–C3 intervertebral disc was manually labeled by 2 evaluators (a neurologist with a 7 years' experience and an MRI technician with 11 years' experience). The output from the DeepSeg algorithm, along with these manual intervertebral disc landmarks, was used to normalize the images to the PAM50 atlas,⁷ an unbiased multimodal MRI template of the full spinal cord (C1–L2 vertebral level) and brainstem where several spinal cord structures have been predefined. Previously, a spinal canal template covering from C1 to C5 was created by our research group in the same space as the PAM50 atlas and was added to the predefined structures (PAM50_41; Online Supplemental Data). A spinal canal segmentation mask was created in the same space as the atlas and added to the predefined structures, including the spinal canal template. Then, the images were normalized using the inverse normalization matrix, as proposed by SCT, and finally, the spinal canal mask was transferred from the atlas space to the native space (Fig 1).

Additionally, the total intracranial volume was assessed in all subjects using the T1WI sequences with statistical parametric mapping software (SPM; <http://www.fil.ion.ucl.ac.uk/spm/software/spm12>); the lesion volume was estimated using 2D FLAIR MRI with the Lesion Segmentation Toolbox, included in the SPM software (<https://www.applied-statistics.de/lst.html>).

Statistical Analysis

CCaA was then estimated as the mean cross-sectional area across either 5, 11, or 17 slices centered on the C2–C3 intervertebral disc, representing the 3 groups of comparisons. Anatomically, 5 slices usually cover the C2–C3 cervical disc, 11 slices cover from the lower margin of C2 to the upper margin of C3; and 17 slices cover from the odontoid basis to the midpoint of the posterior arch of C3 (a certain intersubject variability is detected in those limits according to the individual anatomy).

To identify outlier CCaA estimations, we removed all measures with a value beyond 1.5 times the interquartile range.⁸

Then, CCaA estimations in HC and patients with MS were compared by a multivariable regression model adjusted for age and sex; CCaA estimations from baseline and follow-up cervical cord scans and from brain and cervical MRIs were also compared using a paired *t* test.

To assess the reproducibility of the proposed pipeline, we compared the CCaA estimations obtained from the cervical cord and brain T1WI at 2 different time points with the proposed pipeline manual segmentations performed by 1 evaluator, considered the

GT, using the Dice similarity coefficient.⁹ In addition, a second evaluator manually outlined the CCaA to assess the interoperator variability. Additionally, we compared the CCaA mean obtained with the manual GT at baseline for the cervical cord and brain scans using a paired *t* test. The GT, considered the reference value, was measured at the midpoint of C2–C3.

Finally, CCaA estimations obtained on baseline and follow-up cervical cord T1WI were compared; brain and cervical cord acquisitions were also compared using the individual and average intraclass correlation coefficient (ICC)¹⁰ and the Bland-Altman method with their limits of agreement (LoA). Statistical analysis was performed with STATA 16.1 software (StataCorp). Before we performed a *t* test, the normal distribution of different variables was evaluated using the Shapiro-Wilk test, and the homogeneity of variances was determined by the Levene test. To appraise assumptions of linear regression, we checked the normality of residuals using the Shapiro-Wilk test; homoscedasticity was evaluated with the Breusch-Pagan test; independence of observations was determined using the Durbin-Watson test; and collinearity was assessed by the variance inflation factor. The *P* value for significance was set at *P* < .05.

RESULTS

The proposed pipeline failed in only 3 subjects when using 17 slices to obtain the mean CCaA, because the position of the brain scan was too high and did not cover the upper segment of the cervical cord completely.

After we removed 2 HC and 3 patients with MS, the final cohort included CCaA estimations from 8 HC and 18 patients with MS. Clinical and MRI data are shown in the Table. After we evaluated assumptions of linear regression (Shapiro-Wilk test, *P* = .80; Levene test, *P* = .74; Breusch-Pagan test, *P* = .94; Durbin-Watson test, *P* = .84; and variance inflation factor = 1.07), age- and sex-adjusted linear regression models confirmed that there were no significant differences in the CCaA between HC and patients with MS, estimated in both the cervical cord (mean absolute difference = 0.33 mm², β = 0.10, *P* = .54) and brain acquisitions (mean absolute difference = 2.18 mm², β = 0.36, *P* = .14). Consequently, to perform the statistical analysis between different sequences with a larger sample size, we considered HC and patients with MS as a single group (26 subjects).

In the assessment of the reproducibility of the proposed pipeline, the degree of overlap between the CCaA masks generated by the proposed pipeline and the manual GT was excellent with a Dice similarity coefficient mean of 0.90 (range, 0.73–0.97). The distribution across the 4 different acquisitions is shown in Fig 2. Agreement between the 2 evaluators was also excellent, with a Dice similarity coefficient of 0.95 (range, 0.78–1). Furthermore, we did not find significant differences when comparing CCaA estimations obtained with the pipeline and the GT by a *t* test, either at the baseline cervical cord T1WI (mean absolute difference = 9.56 mm², *t* [25] = 1.77, *P* = .09) or brain T1WI (mean absolute difference = 6.35 mm², *t* [25] = 0.82, *P* = .42).

When we compared CCaA estimations obtained from baseline and 1-year follow-up cervical cord MRIs, the highest agreement was obtained with 11 and 17 slices (ICC = 0.76; 95% CI, 0.44–0.88, and ICC = 0.78; 95% CI, 0.56–0.90, respectively).

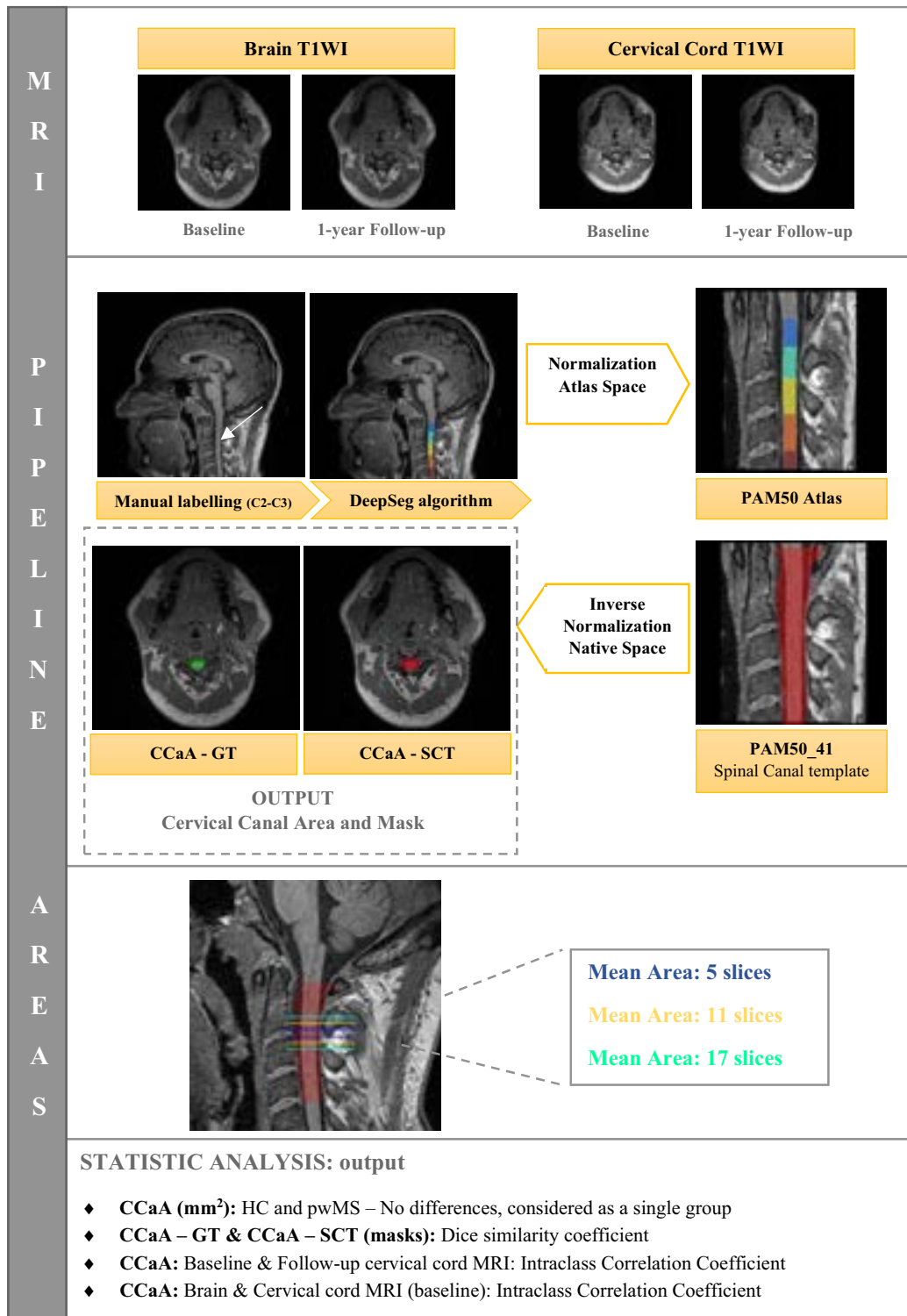


FIG 1. Graphical representation of the proposed pipeline to estimate the cervical canal, including the MRI sequences, a flowchart, the assessment of the mean cervical canal area across the different number of slices, and the statistical analysis performed.

Average ICCs are represented in Fig 3, and they are consistently higher than individual ICCs. Estimations of the CCaA with 17 and 11 slices were also highly similar when using the Bland-Altman method, in contrast to LoA obtained with 5 slices, with a narrower and better-centered LoA (Fig 4, left side). When comparing CCaA estimations obtained from cervical cord T1WI

acquisitions at baseline (mean = 218.37 [SD, 5.02] mm²) and follow-up (mean = 217.09 [SD, 5.62] mm²), we did not find significant differences (mean absolute paired difference = 1.28 mm², $t[25] = 1.22, P = .23$).

CCaA estimations obtained from brain and cervical cord MRIs had a high agreement, independent of the number of slices

Demographic, clinical, and radiologic characteristics of HC and patients with MS

	Patients with MS		P Value ^a
	HC (n = 8)	(n = 18)	
Sex (female) (No.) (%)	5 (62.5%)	11 (61.1%)	.97
Age (mean) (SD) (yr)	30.89 (1.44)	33.84 (1.98)	.36
CCaA (mean) (SD) (mm ²)			
Cervical MRI acquisition	218.15 (4.84)	218.47 (5.23)	.73
Brain MRI acquisition	214.57 (3.97)	216.75 (3.47)	.48
Total intracranial volume (mean) (SD) (mL)	1422.3 (0.10)	1392.9 (0.12)	.55
T2 lesion volume (mean) (SD) (mm ³)	—	2.31 (4.09)	—

Note: —Dash indicates not information available; HC: healthy controls; pwMS, patients with multiple sclerosis; SD, standard deviation.

^a Values correspond to univariate comparisons using parametric and non-parametric tests, as convenience.

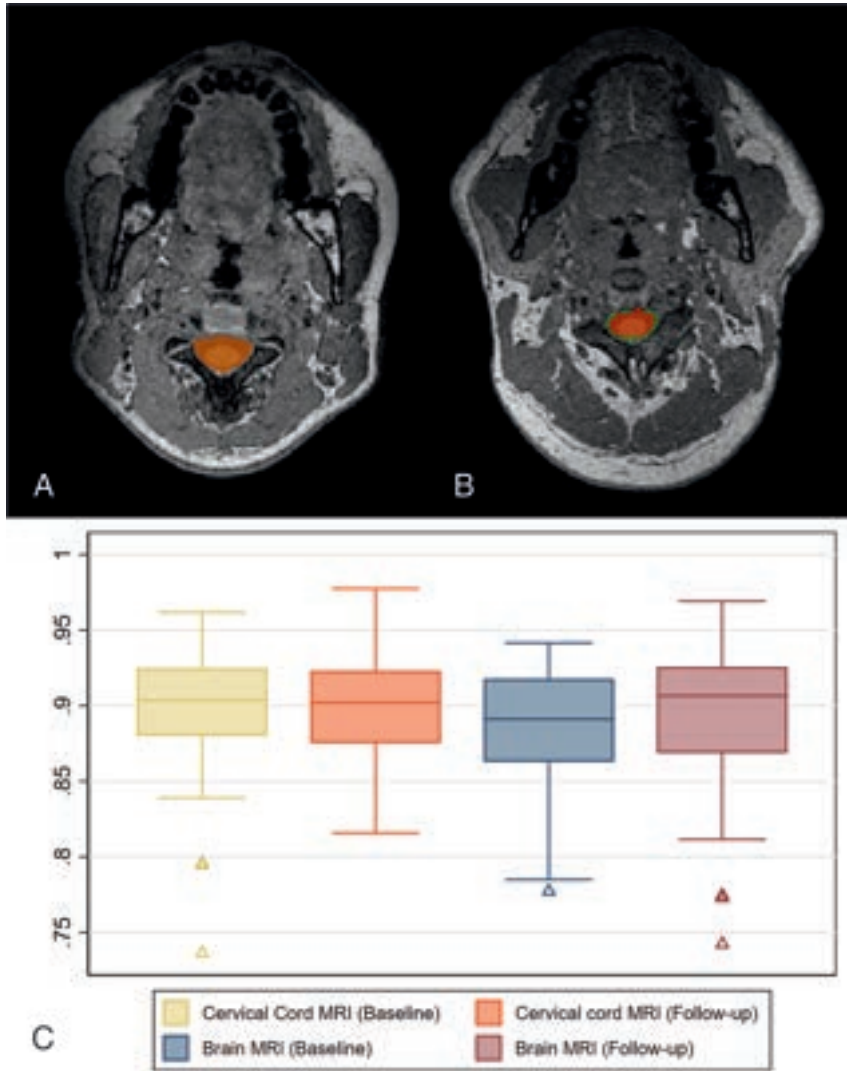


FIG 2. CCaA masks obtained with the proposed pipeline (green) versus the manual segmentation (red) in a patient with MS. A, Spinal MRI acquisition shows a Dice similarity coefficient of 0.92. B, Brain MRI acquisition shows a Dice similarity coefficient of 0.88. C, Distribution of Dice similarity coefficients between CCaA masks from the in-house pipeline and the GT across the 4 acquisitions, both in HC and patients with MS.

used to estimate the CCaA (Fig 3). However, the Bland-Altman method showed a better agreement with CCaA estimations of 17 and 11 slices, than with those obtained with 5 slices (Fig 4). When analyzing absolute means, we found minimal-but-significant

differences between CCaA estimations from brain (mean = 216.07 [SD, 3.7] mm²) and cervical MRIs (mean = 218 [SD, 5.0] mm²) (mean absolute paired difference = 2.30, $t[25] = 2.97$, $P = .006$).

DISCUSSION

In the present study, we validated a semiautomated segmentation pipeline to estimate the CCaA on the basis of the SCT by comparing the generated masks with a manual GT. The overlap was excellent, and significant differences were not found when comparing both measurement methods, indicating that the proposed pipeline seems to appropriately measure the CCaA. Additionally, we have shown that the CCaA is stable for a 1-year period in all subjects. Finally, the CCaA could be properly estimated using either brain or cervical cord MRIs.

To our knowledge, CCaA variations across time have not been analyzed before, though changes were not expected a priori.¹¹ We verified its consistency during a 1-year period by assessing the measurement in baseline and follow-up cervical T1WIs. Consequently, the CCaA could be used in future studies as a proxy for the premorbid status of the spinal cord, because stability across time is a prerequisite for such use. Because it is usually done in other cervical cord area measurement methods,¹² we considered more appropriated to calculate the mean area over several sections instead of only in 1 section. An increase in the number of sections used would reduce the variability of the measurement, but in the case of the spinal canal, variability could increase because sections may cover a region where the canal area physiologically increases toward the foramen magnum. To check what number of sections would provide the best compromise, we calculated ICCs using CCaA estimations with the SCT across 5, 7, and 11 slices centered at the midpoint of the C2–C3 vertebral disc. The study showed a good level of concordance between time points, obtaining

the highest individual ICC when using 11 and 17 slices for the analysis, compared with 5 slices. We considered that differences in the ICC between the number of slices are related to minor inaccuracies in subject repositioning; hence, the lower the number of slices used

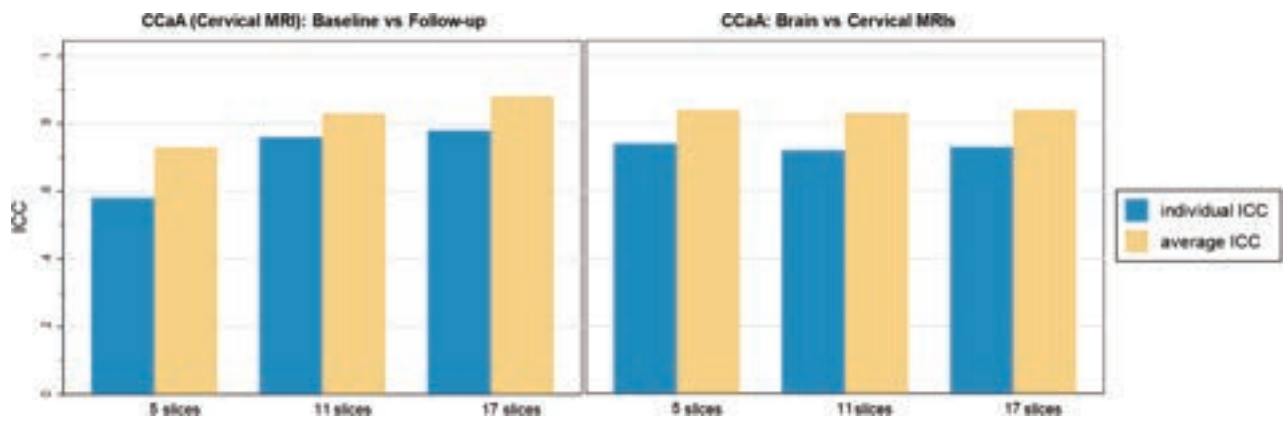


FIG 3. Representation of individual ICC (blue) and average (yellow) ICCs, calculated in 5, 11, and 17 slices. On the left, the ICC between baseline and follow-up cervical MRIs. On the right, degree of concordance of the CcA analyzed in brain and cervical acquisitions.

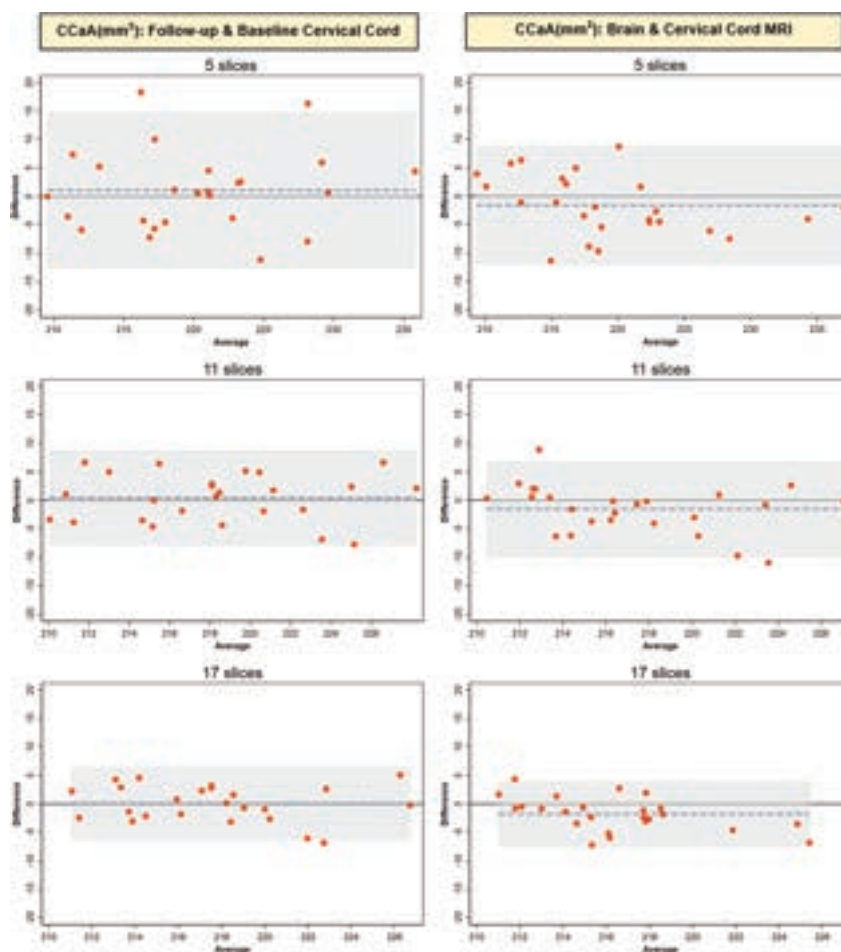


FIG 4. Bland-Altman plots showing the agreement between CcA estimations assessed in different numbers of slices. On the left, the agreement between baseline and follow-up cervical cord MRI is shown; on the right, between brain and cervical cord MRIs. Notice that the x-axis scale of the plot analyzing CcA estimations on 5 slices is larger than the others.

to calculate the CcA, the greater the variability found among patients.

Despite the spinal cord being located in the periphery of the FOV on brain T1WI, where gradient nonlinearity distortion effects are substantial,¹³ it has already been proved that it is possible to reliably measure the cervical cord area using brain

acquisitions.¹⁴ Therefore, we tested the robustness of CcA estimations obtained from brain and spine scans, obtaining good agreement between them. Similar ICC values across the different numbers of slices used to calculate the CcA may be because no repositioning is needed between brain and spine acquisitions.

Overall, ICCs obtained were lower than those reported in other validation studies.^{13,14} A possible explanation might be that the individual ICC has been reported instead of the average, which tends to minimize variations and provides higher ICCs. Moreover, although the degree of agreement between CCaA estimations from brain and cervical MRIs was not excellent and there were significant differences between both measurements, the mean difference was inferior to 3 mm² in the paired *t* test analysis. Therefore, results seem to suggest that brain CCaA estimations might be considered when dedicated cervical sequences are not available, though both acquisitions may not be fully interchangeable when analyzing the CCaA of a single subject, possibly because the cervical canal is differently located in the FOV of cervical cord and brain T1WIs. Because the in-house pipeline failed in 3 subjects when using 17 slices, it might be advisable to use the 11-slice approach, which provides similar reproducibility parameters.

Several limitations should be mentioned. First, the sample size is small and could explain the range of ICCs obtained. Second, our pipeline includes manual labeling of the C2–C3 intervertebral disc, which may be a limiting factor when dealing with large cohorts because it clearly increases processing time. Third, we performed the image acquisition with the same scanner and positioning protocol; therefore, we have not tested the pipeline under other conditions. Finally, we adjusted measurements by age and sex, but not height, because normalization using anthropometric parameters still remains controversial.^{15,16}

CONCLUSIONS

This study validates a new semiautomated algorithm to estimate the CCaA based on the SCT. An excellent agreement was obtained between the manual segmentations and those provided by the pipeline. We used this algorithm to demonstrate the consistency of CCaA measurements across time, showing no changes during a 1-year period. Finally, results suggested that brain CCaA estimations might be considered when dedicated cervical sequences are not available.

ACKNOWLEDGMENTS

We wish to thank the subjects who kindly agreed to take part in this study. We acknowledge the support of the Department of Neuroradiology and the Centre of Multiple Sclerosis of Catalonia of the Vall Hebron University Hospital (Barcelona, Spain).

Disclosure forms provided by the authors are available with the full text and PDF of this article at www.ajnr.org.

REFERENCES

1. Liu Z, Yaldizli Ö, Pardini M, et al. **Cervical cord area measurement using volumetric brain magnetic resonance imaging in multiple sclerosis.** *Mult Scler Relat Disord* 2015;4:52–57 CrossRef Medline
2. Eden D, Gros C, Badji A, et al. **Spatial distribution of multiple sclerosis lesions in the cervical spinal cord.** *Brain* 2019;142:633–46 CrossRef Medline
3. Arrambide G, Rovira A, Sastre-Garriga J, et al. **Spinal cord lesions: a modest contributor to diagnosis in clinically isolated syndromes but a relevant prognostic factor.** *Mult Scler* 2018;24:301–12 CrossRef Medline
4. Sumowski JF, Rocca MA, Leavitt VM, et al. **Brain reserve against physical disability progression over 5 years in multiple sclerosis.** *Neurology* 2016;86:2006–09 CrossRef Medline
5. Sastre-Garriga J, Rovira A, García-Vidal A, et al. **Spinal cord reserve in multiple sclerosis.** *J Neurol Neurosurg Psychiatry* 2023 Jan 23 [Epub ahead of print] CrossRef Medline
6. De Leener B, Lévy S, Dupont SM, et al. **SCT: Spinal Cord Toolbox, an open-source software for processing spinal cord MRI data.** *Neuroimage* 2017;145:24–43 CrossRef Medline
7. De Leener B, Fonov VS, Collins DL, et al. **PAM50: unbiased multimodal template of the brainstem and spinal cord aligned with the ICBM152 space.** *Neuroimage* 2018;165:170–79 CrossRef Medline
8. Tukey JW. *Exploratory Data Analysis.* Addison-Wesley; 1977:43–44
9. Zou KH, Warfield SK, Bharatha A, et al. **Statistical validation of image segmentation quality based on a spatial overlap index 1.** *Acad Radiol* 2004;11:178–89 CrossRef Medline
10. Koo TK, Li MY. **A guideline of selecting and reporting intraclass correlation coefficients for reliability research.** *J Chiropr Med* 2016;15:155–63 CrossRef Medline
11. Kato F, Yukawa Y, Suda K, et al. **Normal morphology, age-related changes and abnormal findings of the cervical spine, Part II: magnetic resonance imaging of over 1,200 asymptomatic subjects.** *Eur Spine J* 2012;21:1499–507 CrossRef Medline
12. Rocca MA, Valsasina P, Meani A, et al; MAGNIMS Study Group. **Clinically relevant cranio-caudal patterns of cervical cord atrophy evolution in MS.** *Neurology* 2019;93:e1852–66 CrossRef Medline
13. Papinutto N, Bakshi R, Bischof A, et al; North American Imaging in Multiple Sclerosis Cooperative (NAIMS). **Gradient nonlinearity effects on upper cervical spinal cord area measurement from 3D T1-weighted brain MRI acquisitions.** *Magn Reson Med* 2018;79:1595–601 CrossRef Medline
14. Liu Y, Lukas C, Steenwijk MD, et al. **Multicenter validation of mean upper cervical cord area measurements from head 3D T1-weighted MR imaging in patients with multiple sclerosis.** *AJNR Am J Neuroradiol* 2016;37:749–54 CrossRef Medline
15. Oh J, Seigo M, Saidha S, et al. **Spinal cord normalization in multiple sclerosis.** *J Neuroimaging* 2014;24:577–84 CrossRef Medline
16. Papinutto N, Schlaeger R, Panara V, et al. **Age, gender and normalization covariates for spinal cord gray matter and total cross-sectional areas at cervical and thoracic levels: a 2D phase sensitive inversion recovery imaging study.** *PLoS One* 2015;10:e0118576–18 CrossRef Medline

The Development and Application of a Cost-Effective Cervical Spine Phantom for Use in Fluoroscopically Guided Lateral C1–C2 Spinal Puncture Training

V. Risner, B. Huang, K. McCullagh, T. Benefield, and Y.Z. Lee



ABSTRACT

BACKGROUND AND PURPOSE: Lateral C1–C2 spinal punctures are uncommon procedures performed by radiologists for access to CSF and contrast injection when a lumbar approach is contraindicated and an alternate method of access becomes necessary. There are limited opportunities to learn and practice the technique. We aimed to develop and assess the efficacy of a low-cost, reusable cervical spine phantom for training in fluoroscopically guided lateral C1–C2 spinal puncture.

MATERIALS AND METHODS: The phantom was constructed with a cervical spine model, an outer tube representing the thecal sac, an inner balloon representing the spinal cord, and polyalginate to replicate soft tissue. The total cost of materials was approximately US \$70. Workshops were led by neuroradiology faculty experienced in the procedure using the model under fluoroscopy. Survey questions were assessed on a 5-point Likert scale. Participants were given pre- and postsurveys assessing comfort, confidence, and knowledge of steps.

RESULTS: Twenty-one trainees underwent training sessions. There was significant improvement in comfort level (Δ : 2.00, SD: 1.00, P value < .001); confidence (Δ : 1.52 points, SD: 0.87, P value < .001); and knowledge (Δ : 2.19, SD: 0.93, P value < .001). Eighty-one percent of participants found the model “very helpful” (5/5 on Likert scale), and all participants were “very likely” to recommend this workshop to others.

CONCLUSIONS: This cervical phantom model is affordable and replicable and demonstrates training utility to prepare residents for performing lateral C1–C2 spinal puncture. This is a rare procedure, so the use of a phantom model before patient encounters is invaluable to resident education and training.

Lateral C1–C2 spinal punctures are uncommon procedures performed by radiologists under fluoroscopic guidance for various purposes, including CSF collection and contrast injection when a lumbar approach is contraindicated.¹ A 2009 survey of neuroradiology program directors showed that 14.3% of programs have <1 C1–C2 spinal puncture performed, on average, every year, and that 47.6% average between 1 and 5 C1–C2 spinal punctures annually.² Due to the infrequency of this procedure, there are limited opportunities for trainees to learn and practice the technique.³ While lateral C1–C2 spinal puncture is considered a safe procedure when performed by a skilled radiologist, with <0.05% of cases having a major complication such as an arterial bleed, epidural hematoma, intramedullary contrast injection,

permanent neurologic deficit, or death, these potential complications have high morbidity.^{1,4} The potentially major or fatal consequences of this procedure if performed incorrectly make it difficult for trainees to gain experience with the procedure without a form of simulation training. Additionally, due to the rarity of this procedure, along with potentially serious complications, it is often found that a single neuroradiologist will be trained at an institution and will perform all lateral C1–C2 spinal punctures at the institution, further limiting training opportunities for other faculty and residents.

To enrich education and training of medical professionals while also improving patient safety, throughout all phases of medical training, simulation training has become increasingly popular for teaching and practicing techniques before using them on a patient.⁵ Research has shown that simulation training improves reported confidence levels and success rates of the first procedure performed by the student on a patient.⁶ Fluoroscopically compatible anthropomorphic head, cervical spine, and spinal cord phantoms are available for purchase. However, the price of commercially available fluoroscopically compatible models exceeds US \$6000, and these models do not include components mimicking CSF that can be used to replicate C1–C2 spinal punctures.⁷ Due to the infrequency of

Received February 25, 2023; accepted after revision May 21.

From the Department of Radiology, University of North Carolina at Chapel Hill School of Medicine, Chapel Hill, North Carolina.

Please address correspondence to Yueh Z. Lee, MD, PhD, The University of North Carolina at Chapel Hill School of Medicine, Department of Radiology, 2000 Old Clinic CB No. 7510, Chapel Hill, NC 27599-9500; e-mail: leey@med.unc.edu

Indicates article with online supplemental data.

<http://dx.doi.org/10.3174/ajnr.A7908>

these procedures, a costly model is not practical for training. Additionally, the current models available on the market for phantom fluoroscopic cervical spines would require modifications to mimic CSF. There have been cost-effective phantom models created for practicing lumbar punctures under fluoroscopic guidance,^{8,9} but no cost-effective fluoroscopically compatible cervical phantoms with simulated CSF have been created to date. We aimed to develop and assess the efficacy of a low-cost, reusable cervical spine phantom for use in fluoroscopically guided lateral C1–C2 spinal puncture training.

MATERIALS AND METHODS

Model Construction

A more detailed guide on the materials and step-by-step instructions to create the model can be found in the Online Supplemental Data. To summarize, the phantom was constructed using a modified polyvinyl chloride cervical spine model: an outer latex tubing with 1.58-mm-thick walls, similar in thickness to spinal dura mater (mean, 1.106 [SD, 0.244] mm); an outer diameter of 15.875 mm (0.625 inches), similar to that in a study by Ulbrich et al¹⁰ examining the typical diameter of a normal cervical spinal canal at the C1 level (range, 10.7–19.7 mm) and an inner diameter of 12.7 mm; an inner latex modeling balloon with an approximate diameter of 7.5 mm after being filled with 10 mL of fluid representing the spinal cord, also similar to the estimated anterior-posterior diameter of the spinal cord at the C1–C2 level (mean, 8.2 [SD, 1.6] mm); and an alginate substance encompassing the model to replicate soft tissue.^{11,12}

The commercially available cervical spine model used was meant for patient education and anatomic training. The spinal cord portion of the cervical model was removed, and the outer latex tubing was fed through the spinal canal. A polyvinyl chloride on/off valve for an 0.5-inch-tube inner diameter was placed on one end of the outer tubing, and a hemostat was used to secure the other end. The outer tube was filled with clear water, and the tube was sealed by closing the valve and using a hemostat on the opposite end to maintain the pressure and shape of the canal. The model was then placed in a cylindrical container approximately the diameter of a neck (in our model, we used part of a standard 2-L soft drink bottle, but other containers can be used), and the container was filled with the polyalginate molding mixed at a 1/4 ratio of powder to water (by weight, ie, 60 g of powder per 240 g [1 cup] water). To extend curing time, we used refrigerated water (at 35°F), and allowed the mixture to cure for approximately 10–15 minutes in the cylindrical container. After we removed it from the cylindrical container, the outer latex tube was unsealed and drained, and the inner latex modeling balloon was passed through the outer tubing using a metal rod and then filled with approximately 15–20 mL of water dyed with red food coloring so that the spinal tap would reveal dyed water if the spinal cord was punctured (Fig 1).

Additional clamps were secured to the outer tubing, posterior to the inner balloon to ensure anterior placement of the balloon to better mimic the anatomic positioning of the spinal cord. Then, the outer tubing was refilled with clear water. This tube-within-a-tube approach enabled refilling of the spinal canal and replacement of the latex balloon “spinal cord” if the balloon was punctured in a previous attempt. Before use in training sessions, the model was wrapped in plastic wrap to retain moisture and



FIG 1. Puncturing the spinal cord. The photograph demonstrates the result of puncturing the inner latex balloon, which represents the spinal cord. Red dye returns from the spinal needle.

kept refrigerated at 4°C. We found that the model lasts 7–10 days refrigerated before the alginate begins to mold, requiring recasting. Ideally, the model should be assembled in close time proximity to training sessions to prevent expiration of the alginate. The total cost of materials for 1 model was approximately US \$70. We have also developed an alternate approach with silicone material that will resist spoiling but at a greater cost. A list of materials and costs is available in the Online Supplemental Data. Immediately before use, the open end of the outer dural tube was mildly pressurized by injecting an extra 10–15 mL of fluid into the model. The final phantom construction can be seen in Fig 2.

Assessment of Training Efficacy

Training sessions were held at a single institution, conducted using the phantom model under fluoroscopic guidance and led by 1 neuroradiology faculty member with >15 years of experience with lateral C1–C2 spinal punctures. A fluoroscopic image of the phantom model during training sessions can be seen in Fig 3, with a real-life fluoroscopic image during a lateral C1–C2 spinal puncture provided in Fig 4 for comparison. Each session comprised 4–6 trainees, including radiology assistant students, medical students, radiology residents, and attending physicians. Training sessions began with a group demonstration of a C1–C2 spinal puncture by the neuroradiology faculty member facilitating the training using the phantom under fluoroscopy, followed by individual practice by training participants. Attempts of C1–C2 spinal puncture by participants were directly supervised by the neuroradiologist leading the training, with direct feedback provided during training to ensure competency of trainees.



FIG 2. Constructed cervical phantom model. The photograph shows the fully-constructed phantom model. The cervical spine model is covered with polyalginate. There is a latex tube running through the spinal canal of the cervical model, with an inner latex balloon within the tube. The inner latex balloon is filled with dyed water, and the outer tube is filled with clear water. Two hemostats on either end of the phantom are occluding the posterior third of the latex tube to ensure that the balloon is in a more accurate anatomic position relative to the spinal cord. The hemostat at the distal end of the latex tube is used to maintain water pressure within the latex tube.

Participants were provided with a pre- and posttraining survey completed immediately before and after participating in training sessions. An example of the pre- and postsurveys given to workshop participants can be seen in the Online Supplemental Data.

Surveys assessed prior experience in witnessing or performing a lateral C1–C2 spinal puncture, comfort level in performing a C1–C2 spinal puncture before and after the training session with the model, confidence in performing a successful C1–C2 spinal puncture before and after the training session, and the perception of current knowledge of the steps in a C1–C2 spinal puncture before and after the training session. Pre- and postworkshop ratings of comfort level, current knowledge, and confidence in performing a C1–C2 spinal puncture were assessed using a 5-point Likert scale, with 1 being not comfortable, no knowledge, and not confident, respectively, and 5 being very comfortable, having extensive knowledge, and feeling very confident, respectively. Each trainee was expected to correctly orient the model in the lateral position, select an appropriate entry point, and advance the needle into the posterior canal at the C1–C2 level under fluoroscopy. Successful access to the CSF space was evident when clear CSF was returned through the 3.5-inch spinal needle. Penetrating the spinal cord would result in a return of red fluid.

Participants were also surveyed on the helpfulness of the workshop, the usefulness of the information learned in the workshop, and the likeliness of recommending this workshop to others. Survey questions were assessed on a 5-point Likert scale, with 1 being not helpful, not useful, and not likely to be recommended, respectively, and 5 being very helpful, very useful, and very likely to be recommended, respectively.

We assessed whether there were differences between pre- and postworkshop ratings of comfort level, current knowledge, and

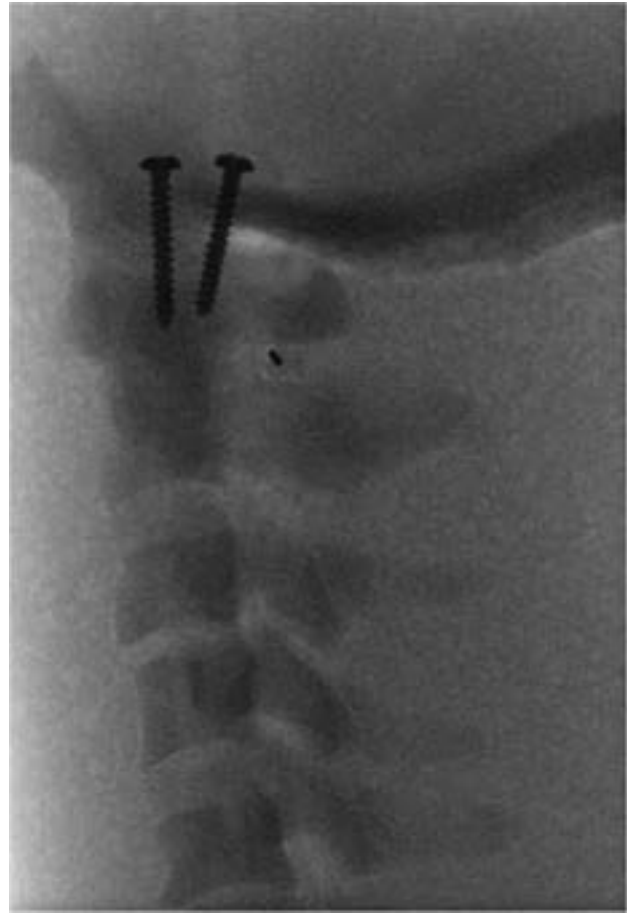


FIG 3. Fluoroscopic visualization of the phantom model shows the appearance of the model under fluoroscopy during a training session. The spinal needle can be seen within the C1–C2 space. The 2 screws seen in this image connect the skull base to the cervical spine and could not be removed in order to preserve integrity of the phantom.

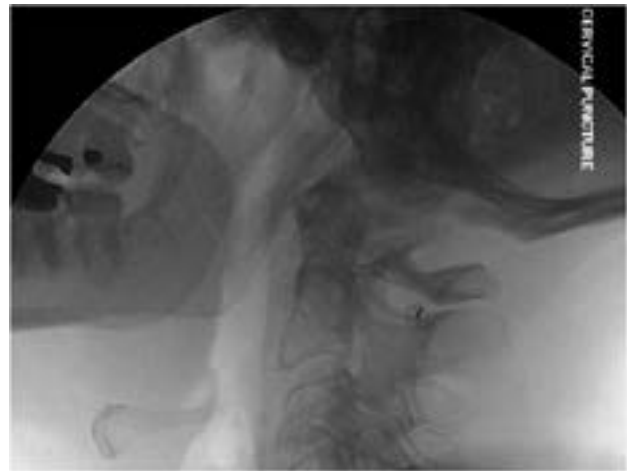


FIG 4. Real example of a fluoroscopic image of a lateral C1–C2 spinal puncture that shows a lateral view of a C1–C2 spinal puncture performed on a patient for comparing the performance of the phantom in replicating fluoroscopic views during the procedure.

confidence using a Wilcoxon signed-rank test. We considered a P value $< .05$ as evidence of a difference in medians pre- versus postworkshop.

Comparison of phantom performance in replicating actual lateral C1–C2 spinal punctures

Component of Phantom/ Procedure	Comparison with Real-Life Experience of Lateral C1–C2 Spinal Punctures
Feel of alginate/soft tissue Positioning of phantom/ patient	Similar Different: The patient is usually positioned prone for this procedure, while the training simulated the patient being in the lateral decubitus position due to constraints of the fluoroscopy room available for training (not related to the phantom itself)
Force required to penetrate outer latex tubing/dura	Different: The amount of pressure required to pop through the outer latex tube dura was greater than in real life; this difference was emphasized to the trainees who participated
Landmarks visualized under fluoroscopy Speed of CSF egress	Similar Variable: depending on how much pressure we applied to outer latex tubing via a syringe and the PVC on/off valve; future directions include construction of a model with a pressure gauge so that we could fill the tubing to match normal CSF pressure (~15 cm H ₂ O)

Note:—PVC indicates polyvinyl chloride.

RESULTS

In comparing the phantom's performance at simulating the actual lateral C1–C2 spinal puncture procedure, the neuroradiology faculty member with >15 years of experience who led the training sessions noted similarities and differences of the phantom to real punctures (Table). Four training sessions were held at a single institution during a 6-month time span. The sample size of the training group was 21, with 1 resident participating in 2 training sessions, but only the first workshop attendance of this participant was included in analyses. Participants were at various stages of training, from radiology assistant and medical students to attending physicians. Distributions of the training levels of participants can be found in Fig 5. Two-thirds of participants were either postgraduate year 6 residents or attending physicians; 71.4% (15/21) of training session participants had never seen a lateral C1–C2 spinal puncture procedure performed; and 90.5% (19/21) of participants had never performed a lateral C1–C2 spinal puncture before attending training sessions.

Figure 6 summarizes pre- and postworkshop ratings of comfort, confidence, and knowledge performing a C1–C2 spinal puncture. The mean difference in comfort level in performing a C1–C2 spinal puncture for post- versus preworkshop was 2.00 (SD, 1.00) (an increase from 1.29 to 3.29). The mean difference in confidence in the ability to successfully perform a C1–C2 spinal puncture for post- versus preworkshop was 1.53 (SD, 0.87) (an increase from 1.76 to 3.29). The mean differences in the perception of current knowledge for post- versus preworkshop was 2.19 (SD, 0.93) (an increase from 1.86 to 4.05). There was evidence

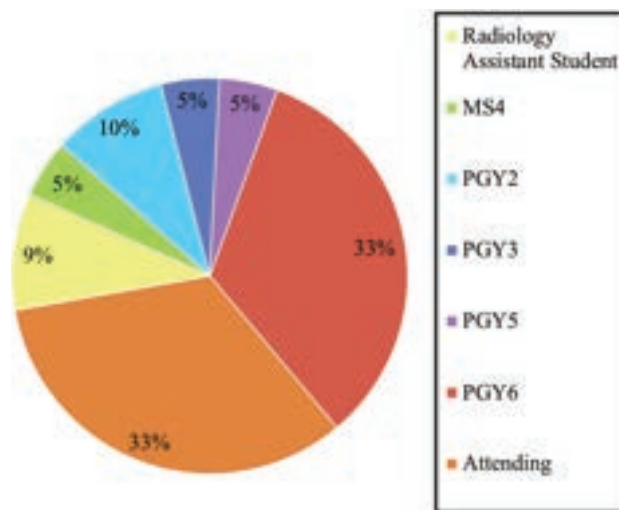


FIG 5. Stages of training of workshop participants. The graph shows the distribution of participant training levels during lateral C1–C2 spinal puncture training. A total of 21 individuals participated in training workshops, with 1 resident participating in 2 training workshops. PGY indicates postgraduate year; MS4, fourth-year medical student.

that these outcomes were higher postworkshop for all 3 outcomes ($P < .001$ for all). Eighty-one percent of participants found the phantom to be very helpful (5/5 on Likert scale), and all participants were very likely (5/5 on Likert scale) to recommend that others sign up for this workshop. Ninety-one percent of participants rated the likeliness of using knowledge gained in the workshop in the future at either a 4 or 5 on the Likert scale.

DISCUSSION

Simulation-based training workshops have been increasingly used among a wide variety of specialties—including anesthesiology, surgery, and radiology—to train residents and fellows on the steps of a procedure and to provide them with the opportunity to practice these methods before their clinical use.^{13–16} More common radiologic procedures, such as fluoroscopically guided lumbar puncture, have had low-cost phantom models created for simulations for training medical professionals to learn and practice procedures.^{8,9} However, a fluoroscopically compatible C1–C2 spinal puncture with functional CSF has not been demonstrated thus far. Because this procedure is rare, residents and fellows needed to learn the procedure of lateral C1–C2 spinal punctures on real patients, which creates a risk to the patient secondary to the inadequate training. Worse yet, practitioners may not have even had a chance to see these procedures during training and are not adequately prepared to provide this service to patients, which is sometimes necessary to obtain critical diagnostic information. Additionally, lateral C1–C2 spinal punctures are often not the first-choice procedure and are frequently chosen due to the complexities of a patient and contraindications to lumbar puncture, so these cases are often not straightforward procedures and carry inherent risks not due to infrequency of the procedure being performed.⁴ These factors make it even more important for trainees to

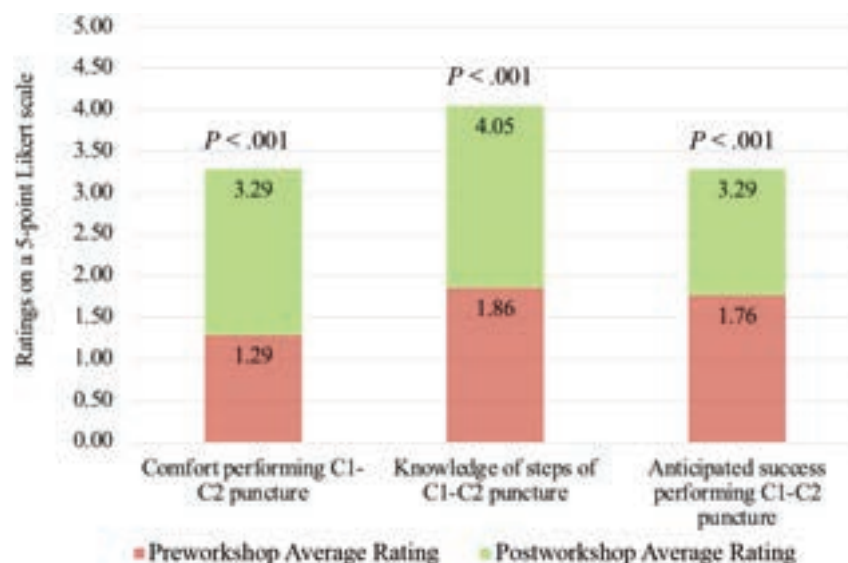


FIG 6. Pre- and postworkshop ratings of comfort, knowledge, and confidence of C1–C2 lateral cervical puncture. The image shows pre- and post-survey results of participants' ratings of their comfort performing, knowledge of steps, and anticipated success of lateral C1–C2 spinal puncture before and after taking part in an educational workshop using the cervical model developed in this article. Ratings were on a 5-point Likert scale.

have nonpatient opportunities to learn and practice this procedure to gain more experience before clinical application.

This cervical phantom model successfully provided residents and fellows with a simulation of an uncommon procedure, lateral C1–C2 spinal puncture, at a low cost with little technical expertise needed to recreate the model. Considering the improvement in comfort with the procedure, confidence in having a successful procedure, and knowledge of the steps of the procedure, this model delivers a high benefit-to-cost ratio for lateral C1–C2 spinal puncture training. By providing step-by-step instructions for creating a cervical model, this project provides easily accessible, low-cost, highly effective training opportunities for other programs interested in implementing similar training. We have also begun to use similar approaches in phantom design for other procedural phantoms. The model is somewhat “self-healing,” allowing at least 10 trainees to participate on the same model. We did not have any difficulty with model degradation with 13 trainees participating in a single session. The latex tube dura simulant was also resistant to leaking due to the resealing nature of the latex rubber under low pressures.

This project has limitations related to application at a single institution. Because all trainees came from our institution, there is concern for selection bias. However, this project has shown that a low-cost homemade model can have clinical utility in the training of our medical professionals. This particular model is moderately prone to spoiling due to the polyalginate material because we did not add any form of preservative. In our experience, this model is useful for approximately 7–10 days if preserved in a refrigerator when not in use. Future directions for this project include working with other neuroradiology programs to develop these training workshops with the C1–C2 phantom at other institutions. The how-to guide will enable other programs to create a replica of the phantom and conduct training sessions at their own institutions. The intent of expanding to other institutions would be to increase the sample size of the project if we

conduct a meta-analysis in the future. We have also begun to recreate this model using a more stable soft-tissue replica material, adding a pressure gauge to more accurately represent normal CSF pressure (15 cm H₂O) and have started to expand these methods to other radiologic procedures to increase simulation teaching at our institution.

This article discusses training on the procedure of lateral C1–C2 spinal puncture under fluoroscopic guidance. Some neuroradiologists prefer using other imaging modalities, such as CT or MR imaging, for guidance during this procedure. These modalities are not covered under the scope of this project, and the model has not been formally assessed for similarity to the human cervical spine under CT or MR imaging. However, additional future directions for this phantom include assessing the potential utility of this model under other imaging modalities for training using CT or MR imaging guidance. There are 2 metal screws in the model that had to remain in place to maintain integrity between the base of the skull and the cervical spine. These would have to be replaced with screws made from an MR imaging-compatible metal to safely visualize this model using MR imaging.

CONCLUSIONS

Simulation teaching is increasingly being used at teaching institutions to expand training for medical procedures before interactions with patients. This low-cost cervical spine model helped bridge the gap in clinical training for fluoroscopically guided lateral C1–C2 spinal punctures. The phantom and educational workshops enabled participants to gain hands-on, low-pressure experience practicing techniques for a relatively uncommon procedure, which increased participants' knowledge of the steps of the procedure, comfort in performing the procedure, and confidence in having success in the procedure. The release of open-access guidelines for creation of this model will increase training opportunities for using a low-cost training phantom at other

institutions and increase the replicability of this project. Simulation training in radiology can be a useful educational tool in all stages of training.

Disclosure forms provided by the authors are available with the full text and PDF of this article at www.ajnr.org.

REFERENCES

1. Daniels SP, Schweitzer AD, Baidya R, et al. **The lateral C1–C2 puncture: indications, technique, and potential complications.** *AJR Am J Roentgenol* 2019;212:431–42 CrossRef Medline
2. Yousem DM, Gujar SK. **Are C1–2 punctures for routine cervical myelography below the standard of care?** *AJNR Am J Neuroradiol* 2009;30:1360–63 CrossRef Medline
3. Gibbs WN, Skalski MR, Kim PE, et al. **C1–2 puncture: a safe, efficacious, and potentially underused technique.** *Neurographics* 2017;7:1–8 CrossRef
4. Robertson HJ, Smith RD. **Cervical myelography: survey of modes of practice and major complications.** *Radiology* 1990;174:79–83 CrossRef Medline
5. Higham H, Baxendale B. **To err is human: use of simulation to enhance training and patient safety in anaesthesia.** *Br J Anaesth* 2017;119:i106–14 CrossRef Medline
6. Gaubert S, Blet A, Dib F, et al. **Positive effects of lumbar puncture simulation training for medical students in clinical practice.** *BMC Med Educ* 2021;21:18 CrossRef Medline
7. Universal Medical. **RSD Anthropomorphic Head Phantom With Complete Cervical Spine (C1–C7).** https://www.universalmedicalinc.com/rsd-anthropomorphic-head-phantom-with-complete-cervical-spine-c1-c7.html?campaignid=1486031167&adgroupid=60330479187&adid=284325986593&gclid=Cj0KCQjw2_OWbDqARIsAAUNTTH
8. Lerner DJ, Gifford SE, Olafsen N, et al. **Lumbar puncture: creation and resident acceptance of a low-cost, durable, reusable fluoroscopic phantom with a fluid-filled spinal canal for training at an academic program.** *AJNR Am J Neuroradiol* 2020;41:548–50 CrossRef Medline
9. Faulkner AR, Bourgeois AC, Bradley YC, et al. **A robust and inexpensive phantom for fluoroscopically guided lumbar puncture training.** *Simul Healthc* 2015;10:54–58 CrossRef Medline
10. Ulbrich EJ, Schraner C, Boesch C, et al. **Normative MR cervical spinal canal dimensions.** *Radiology* 2014;271:172–82 CrossRef Medline
11. Nagel SJ, Reddy CG, Frizon LA, et al. **Spinal dura mater: biophysical characteristics relevant to medical device development.** *J Med Eng Technol* 2018;42:128–39 CrossRef Medline
12. Frostell A, Hakim R, Thelin EP, et al. **a review of the segmental diameter of the healthy human spinal cord.** *Front Neurol* 2016;7:238 CrossRef Medline
13. Lorello GR, Cook DA, Johnson RL, et al. **Simulation-based training in anaesthesiology: a systematic review and meta-analysis.** *Br J Anaesth* 2014;112:231–45 CrossRef Medline
14. Schlottmann F, Tolleson-Rinehart S, Kibbe MR, et al. **Status of simulation-based training in departments of surgery in the United States.** *J Surg Res* 2020;255:158–63 CrossRef Medline
15. Giannotti E, Jethwa K, Closs S, et al. **Promoting simulation-based training in radiology: a homemade phantom for the practice of ultrasound-guided procedures.** *Br J Radiol* 2022;95:20220354 CrossRef Medline
16. Patel R, Dennick R. **Simulation based teaching in interventional radiology training: is it effective?** *Clin Radiol* 2017;72:266.e7–266.e14 CrossRef Medline

In the article “Dual-Layer Detector Cone-Beam CT Angiography for Stroke Assessment: First-in-Human Results (the Next Generation X-ray Imaging System Trial)” (Ståhl F, Almqvist H, Kolloch J, et al, *AJNR Am J Neuroradiol*, 2023;44:523–29), the correct ethics approval number is 2020-04467.

The authors regret this error.

<http://dx.doi.org/10.3174/ajnr.A7898>